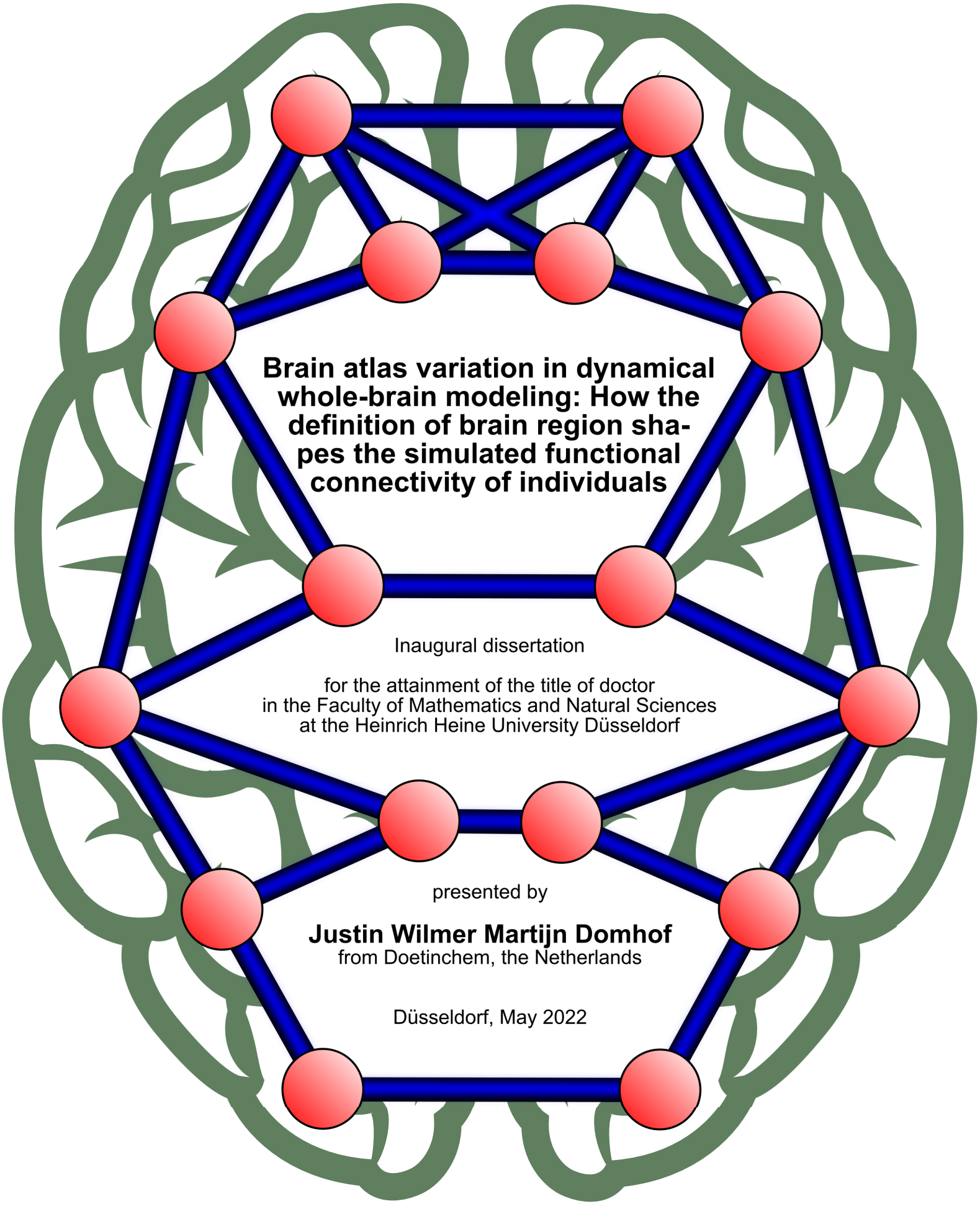

Brain atlas variation in dynamical whole-brain modeling: How the definition of brain region shapes the simulated functional connectivity of individuals

Inaugural dissertation

for the attainment of the title of doctor
in the Faculty of Mathematics and Natural Sciences
at the Heinrich Heine University Düsseldorf

presented by

Justin Wilmer Martijn Domhof
from Doetinchem, the Netherlands

Düsseldorf, May 2022

from the Institute for Systems Neuroscience
at the Heinrich Heine University Düsseldorf

and

the Institute of Neuroscience and Medicine, Brain and Behaviour (INM-7)
of Forschungszentrum Jülich

Published by permission of the
Faculty of Mathematics and Natural Sciences at
Heinrich Heine University Düsseldorf

Supervisor: PD Dr. Oleksandr V. Popovych
Co-supervisor: Prof. Dr. Markus Kollmann

Date of the oral examination: 4 November 2022

Affidavit

I declare under oath that I have produced my thesis independently and without any undue assistance by third parties under consideration of the 'Principles for the Safeguarding of Good Scientific Practice at Heinrich Heine University Düsseldorf'. The thesis has not been presented to any other faculty or institution.

Düsseldorf, 31 May 2022

Justin Wilmer Martijn Domhof

Acknowledgements

This dissertation would not have been completed had I not enjoyed the support of some special people. Here, I would like to express my gratitude towards them.

First, I thank my supervisor Oleksandr Popovych for giving me the opportunity to pursue this PhD. I am happy to have been a member of his group, and greatly acknowledge the resources that he secured and made available. They were indispensable for the individual studies comprising this dissertation. In my opinion, his feedback was always constructive and thorough, and vastly improved the quality of the results and the narratives. Last but not least, his enthusiastic and supporting attitude provided me perspective whenever I had the idea that the project was going nowhere.

I also thank my co-supervisor Markus Kollmann for his aid on the thesis. It was great to have a conversation on the progress of the project with someone outside the field of neuroimaging from time to time. Our discussions were productive and helped me to identify the concepts in the thesis that seemed self-explanatory to me but actually needed elucidation. This improved the accessibility of the dissertation to the broader scientific audience considerably. Additionally, his comments further enhanced the presentation and interpretation of the results.

With regard to supervision, I am very thankful for the valuable feedback from Simon Eickhoff as well. His contributions increased the quality of the individual publications included in this thesis tremendously. Moreover, he really helped me to develop professional soft skills such as writing an accessible and convincing rebuttal.

Besides my supervisors, I would like to thank the other contributors to the work presented in this thesis. The expertise and consultations of Kyesam Jung and Shufei Zhang on neuroimaging data processing were highly appreciated, especially since I had no experience with it at the start of the project. I additionally thank Kyesam Jung for carrying out the whole-brain tractography computations, and for his detailed feedback on the paper that he co-authored.

Of course, I am grateful for getting to know the other members of our group: Shraddha Jain, Michael Rüdiger, Alexander Silchenko, Jinmeng Sun and Kevin Wischnewski. I thank them a lot for their feedback on the progress, but even more for the personal talks that we had. Those conversations helped me to get rid of the frustrations that unavoidably arise while working on a project as large as a PhD.

Furthermore, I thank Sam Vickery for organizing Journal Club together with me. With regard to Journal Club, I also thank Sofie Valk and Felix Hoffstaedter for their help on the organization of the gradients versus parcellations debate; it was really fun to have such a structured discussion on a scientific topic.

In general, I am grateful to have been a part of INM-7, and therefore thank all of its members. I would like to express some special thanks to Jona Fischer and Alex Waite for their excellent support from the side of the digital and computational infrastructure, Julia Mans for her help on the administrative requirements (which were a little overwhelming at the start), Christian Häusler

for the inappropriate laughs and Sami for his social initiatives during times of home office. Last but not least, I thank all others for the nice lunch time and coffee break get-togethers.

I am particularly grateful for the support from my personal environment. Therefore, I would like to express my gratitude towards my parents and brothers who were always there when I needed them. The same applies to my friends (Aline, Coen, Denise, Dion, Ian, Jasper, Laura, Maaike, Rianne, Sandra, Stijn, Thyrza, Wieske and Youp). They gave me an outlet whenever I had to blow off some steam. Also, I would like to thank Paul Tiesinga and Marjolijn Roeters for their advice when I needed it most. Last but certainly not least, I would like to express special thanks to Aniek. She supported me a lot when I was feeling anxious or stressed in the months leading up to the submission of the thesis and its defense. Of course, I am also very thankful for her and Sandra's organization of the events surrounding the defense, which apparently I am not supposed to put together myself.

Abstract

How the various parts of the brain are mutually connected can be expressed through the concepts of the structural connectivity (SC) and the functional connectivity (FC). Here, the SC describes how different brain areas are interlinked by anatomical connections that facilitate the propagation of electrical signals. Alternatively, the FC reflects which distinct brain regions are consistently and synchronously co-activated. The structure-function relationship as determined by the correlation coefficient between the SC and FC is moderate at best. Hence, many neuroimaging studies have investigated how these two types of connectivity can be better associated to one another.

Some of these studies employ dynamical whole-brain models. These models aim to replicate the FC as best as possible given the information stored in the SC. Indeed, dynamical whole-brain models have been shown to explain an amount of variance that exceeds straightforwardly correlating the SC and FC. Furthermore, studies suggest that these models are promising candidates for future clinical applications. However, the high computational loads associated with dynamical whole-brain models require the modeled system to be low-dimensional, while the SC and the FC are typically derived from high-dimensional magnetic resonance imaging (MRI) data. Hence, the dimensionality of the MRI images must be reduced.

A so-called brain atlas or parcellation dividing the brain into a (low) number of brain regions may be used for this purpose. Many brain atlases have been constructed on a variety of methods and neurobiological data reflecting brain organization. It has been shown that a change of parcellation may considerably alter the results of analyses involving only empirical data. Nevertheless, a systematic assessment of the effect of the brain atlas on dynamical whole-brain modeling results is lacking. This thesis contains such an investigation.

The first study of this thesis shows that a change of brain parcellation can considerably alter the accuracy with which the dynamical whole-brain models are able to replicate the FC. It also shows that this parcellation-induced variance in the validity of the models can be explained by group-averaged deviations in the network properties of the empirical connectomes, i.e. the SC and FC that are derived from MRI data. In contrast, the within-parcellation, between-subject variations in the quality of model fit could not be explained by the inter-individual differences in those network properties. In short, the study shows that the dynamical whole-brain modeling results are susceptible to the technique used to construct a particular parcellation, and identifies deviations in the network properties of the empirical SC and FC as the cause for this sensitivity.

The second study additionally shows that the parcellation influences the reliability and the subject specificity of the modeling results to a higher degree than what is observed for the empirical FC. In addition, it shows that the FC generated by a dynamical whole-brain model can share subject-specific connectivity patterns with both the empirical SC and FC after model fitting. Moreover, it is shown that the acquired results critically depend on the exact implementation of the modeling paradigm. Hence, the study shows that not only the parcellation but also the model implementation can affect the reliability and subject specificity of the modeling results.

The results comprising this thesis are highly relevant given the current focus on the personalization and the clinical application of dynamical whole-brain models. They provide a possible explanation for the personalized fits of the models to the empirical data. More importantly, they show that the choice of the brain parcellation could be more important for findings involving these models than for straightforward analyses of the empirical SC and FC. Finally, the thesis presents information that could be used by future dynamical whole-brain modeling studies for the appropriate, well-informed selection of the brain atlas.

Table of contents

Chapter 1

Thesis overview

One frequently studied aspect of the human brain is its large-scale connectivity, which encompasses the entirety of connections throughout the central nervous system (Popovych et al., 2019; Suárez et al., 2020). This property can be investigated from the diverging viewpoints of the structural connectivity (SC) and the functional connectivity (FC). The SC is the anatomical interpretation of the concept of connectivity as it characterizes how different parts of the brain are physically connected by axon bundles that facilitate the transmissions of electrical signals (Maier-Hein et al., 2017; Sotiropoulos & Zalesky, 2019; Yeh et al., 2021). Alternatively, the FC identifies whether distinct brain areas are activated concurrently and hence form an apparent functional connection (Bolt et al., 2017; van den Heuvel & Hulshoff Pol, 2010). In other words, the SC indicates whether any two regions within the brain are physically connected, whereas the FC reflects the extent to which they exhibit synchronized co-activations and thus are connected from a functional perspective.

The SC and the FC, also referred to as the structural and functional connectome, respectively, exhibit a correspondence that is moderate at best: At most half of the variation in the FC can be accounted for by correlating it with the SC (Honey et al., 2009; Suárez et al., 2020). Three main classes of models have been used to explain the residual amounts of variance in both connectomes: statistical, communication and dynamical whole-brain models (Suárez et al., 2020). The statistical models aim to link the SC to the FC via multivariate and non-linear regression models (Messé et al., 2014; Mišić et al., 2016; Suárez et al., 2020), whereas the communication models use concepts from network science and telecommunication research to tighten the gap between both types of connectomes (Crofts & Higham, 2009; Goñi et al., 2014; Graham & Rockmore, 2011; Mišić et al., 2015; Suárez et al., 2020). The dynamical whole-brain models as the third model type link SC and FC through a biophysically-inspired procedure: They replicate the FC by simulating brain activity on the basis of the structural connectome (Breakspear, 2017; Honey et al., 2007; Sanz-Leon et al., 2015; Suárez et al., 2020).

Dynamical whole-brain models are well-studied (Suárez et al., 2020). They have indeed been shown to explain an additional amount of variance beyond the direct correlation between the SC and the FC (Honey et al., 2009). In addition, they have demonstrated that resting-state brain activity, which is observed when a subject is neither performing a predefined task nor receiving a specific stimulus (B. B. Biswal, 2012), is associated with a maximally metastable brain state (Deco et al., 2017). They have furthermore shown the importance of an appropriate amount of system noise and fitting signal transmission efficiency and latency for the proper functioning of the brain at rest (Ghosh et al., 2008; Deco et al., 2009). More recently, they also have been used to investigate neurobiological phenomena and neuropsychiatric diseases at a personalized level (Aerts et al., 2020; Deco & Kringelbach, 2014; Hahn et al., 2019; Iravani et al., 2021; Jirsa et al., 2017; Ritter et al., 2013). In fact, the results of dynamical whole-brain models

have been used to distinguish clinical patients from healthy subjects with an accuracy that could outperform classification paradigms that make use of purely empirical data (Zimmermann, Perry, et al., 2018). Hence, besides narrowing the gap between the SC and the FC, dynamical whole-brain models may have a clinical application as well.

However, the computational loads associated with the simulations of dynamical whole-brain models impose a constraint on their design: The modeled system must be relatively low-dimensional in order to keep the calculations tractable (Popovych et al., 2019). In contrast, the SC and the FC are often derived from high-dimensional magnetic resonance imaging (MRI) data in the form of diffusion-weighted MRI (dwMRI) and functional MRI (fMRI) sequences, respectively (Bandettini et al., 1993; B. Biswal et al., 1995; van den Heuvel & Hulshoff Pol, 2010; Maier-Hein et al., 2017; Sotiropoulos & Zalesky, 2019; Yeh et al., 2021). Hence, the dimensionality of the MRI data must be reduced for the model simulation computations to be evaluable. One reduction method relies on so-called brain atlases or parcellations that partition the brain into a limited number of brain areas or regions by considering neurobiological data reflecting brain organization (Amunts & Zilles, 2015; Eickhoff, Yeo, & Genon, 2018; Eickhoff, Constable, & Yeo, 2018). This biological basis has the additional advantage that the resulting structural and functional connectomes can be more interpretable with regard to the neuroscientific context than when they are reconstructed through data-driven dimensionality reduction techniques; see Ayesha et al. (2020) for a review on such data-driven approaches.

A large number of parcellations exists nowadays, and they all have been constructed on the basis of different methodologies and principles of brain organization (Amunts & Zilles, 2015; Eickhoff, Yeo, & Genon, 2018; Eickhoff, Constable, & Yeo, 2018; de Reus & van den Heuvel, 2013; Thirion et al., 2014). Two examples are the Schaefer parcellation, which has been constructed by maximizing the intra-regional homogeneity of the voxel-wise FC (Schaefer et al., 2018), and the von Economo-Koskinas atlas, which is based on spatially localized differences in the cytoarchitecture of the cerebral cortex (von Economo & Koskinas, 1925). The vastly varying parcellation techniques may have considerable effects on the resulting brain regions and thus on the region-based SC and FC that are reconstructed through the use of brain atlases (Arslan et al., 2018; Thirion et al., 2014). Indeed, a change of parcellation may substantially affect the network structures of the SC and the FC and the relation between both types of connectivity (Arslan et al., 2018; Messé, 2020; J. Wang et al., 2009; Zalesky et al., 2010; Zimmermann, Griffiths, et al., 2018). However, even though dynamical whole-brain models are constructed and validated on the basis of the SC and the FC, respectively (Popovych et al., 2019; Suárez et al., 2020), the effect of the brain atlas on their results remains relatively unexplored. Notably, some studies have shown that the choice of parcellation indeed may influence the modeling results (Jung et al., 2021; Popovych et al., 2021; Proix et al., 2016), but a thorough investigation is currently lacking. This thesis provides such a systematic assessment of the influence of the parcellation on dynamical whole-brain modeling outcomes.

First, the concepts underlying the individual studies of this thesis are explained. This theoretical background generally discusses reported brain parcellation techniques and includes a list of the publicly available brain atlases used throughout this thesis (Section 2.1: Brain atlases or parcellations). In addition, the different types of large-scale brain connectivity are described in more detail. This explanation also includes a brief statement on the MRI data used for their reconstruction and a commentary on the relationship between the SC and the FC (Section 2.2: Brain connectivity). Furthermore, a comprehensive elaboration on the general idea behind dynamical whole-brain models is included, where a particular focus is put on how this concept is implemented in the studies of this thesis (Section 2.3: Dynamical whole-brain models). The theoretical background also comprises a brief introduction to graph theory, as one of the individual studies uses this mathematical framework to explain parcellation-induced differences in the modeling results (Section 2.4: Graph theory). An explanation on principal component analysis

is given as well, because this dimensionality reduction method is used in that same study (Section 2.5: Principal component analysis). Finally, the intraclass correlation is introduced and discussed, since it is used to characterize the reliability of the modeling results (Section 2.6: Intraclass correlation).

Subsequently, the two studies of this thesis are presented (Chapter 3 and Chapter 4). The first study entitled "*Parcellation-induced variation of empirical and simulated brain connectomes at group and subject levels*" (Chapter 3) addresses how the brain atlas affects the accuracy with which dynamical whole-brain models can replicate the FC. It shows that the correspondence between the FC derived from fMRI data and the one simulated by the models can vary considerably when the parcellation is changed. Additional analyses demonstrate that this parcellation-induced variance may be independent of the exact implementation of the dynamical whole-brain modeling paradigm. Furthermore, the effect of the brain atlas on the modeling results cannot be explained by a mere dependence on the granularity (number of parcels included in the brain atlas). Eventually, graph-theoretical measures extracted from the MRI-based SC and FC are shown to explain most of the group-averaged, parcellation-induced differences in the modeling results. However, the variations in the modeling results observed between individual subjects cannot be explained by the inter-individual differences in those same measures at the level of a single parcellation. In sum, the study not only demonstrates that the modeling results are sensitive to the method on which a brain atlas is based, but additionally identifies parcellation-induced divergences in the network properties of the empirical SC and FC as the origin of this sensitivity.

The second study ("*Reliability and subject specificity of personalized whole-brain dynamical models*"; Chapter 4) investigates how reliable and subject specific the modeling results are. The results show that both the reliability and the subject specificity of a diversity of modeling results (among others the FC simulated by the models) are relatively sensitive to the choice of parcellation when compared to the MRI-based FC. In addition, they demonstrate that, after model fitting, the FC generated by dynamical whole-brain models can share subject-specific connectivity patterns with both the SC and the FC that are reconstructed from MRI data. Finally, it is demonstrated that the model implementation can have significant effects on the acquired results. The amount of model personalization exerts a particular influence in this respect. Taken together, the study illustrates that the reliability and the subject specificity of the modeling results are not only susceptible to the choice of parcellation, but are also influenced by the exact implementation of the dynamical whole-brain modeling concept.

As generally discussed in Chapter 5, these results are highly relevant given the contemporary attention on the personalization of dynamical whole-brain models and their clinical application (Aerts et al., 2020; Bansal et al., 2018; Iravani et al., 2021; Zimmermann, Perry, et al., 2018). They start to mechanistically explain how the personalized fits of the models are established. Future investigations can build on these results in order to unravel the full mechanism of this process, which may then be used to formulate best practices when distinguishing clinical patients from healthy subjects through modeling results. The findings also indicate that the brain atlas can have a larger effect on the dynamical whole-brain models than on the empirical connectomes. It may therefore be worthwhile to sample any findings involving these models for multiple parcellations to investigate whether those results critically depend on the particular choice of the brain atlas. Notably, the findings presented in this thesis do not propose that a specific parcellation suits the dynamical whole-brain modeling paradigm best. Instead, they provide additional information that can be used alongside other considerations (e.g., the parcellation technique) in the proper, well-informed selection of the brain atlas for the study at hand; see also the conclusion of Chapter 6.

Chapter 2

Background theory

The individual studies included in this thesis rely on concepts that may not be well known to the broader scientific audience. This general introduction therefore provides the theoretical background required to interpret the results presented in this thesis. First, a definition of the brain atlas or parcellation is included, which is complemented by a general discussion on the various techniques that have been used to delineate distinct brain regions and by an inventory of the publicly available parcellations used in the studies comprising this thesis (Section 2.1: Brain atlases or parcellations). Subsequently, the structural connectivity (SC) and the functional connectivity (FC) are explained in more detail, where specific attention is paid to the types of magnetic resonance imaging (MRI) data used for their derivations and to the relationship that the SC and the FC have with respect to one another (Section 2.2: Brain connectivity). The introductions of these topics allow for the presentation of the general idea behind dynamical whole-brain modeling, which is followed by the descriptions of the models that return in this thesis (Section 2.3: Dynamical whole-brain models). Two brief explanations on graph-theoretical analysis and principal component analysis are also included as these two analysis methods are used in the first study of this thesis (Chapter 3) to explain the variance observed in the modeling results (Section 2.4: Graph theory; Section 2.5: Principal component analysis). Finally, the intraclass correlation is introduced and discussed, because it is used in the second study of this thesis (Chapter 4) to characterize the reliability of a variety of modeling results (Section 2.6: Intraclass correlation).

2.1 Brain atlases or parcellations

The organization of the brain is one of the main topics in neuroscience, and is considered at multiple levels. Studies exploring microscopic brain organization, for instance, have shown that different types of neurons exhibit specific connectivity patterns with respect to one another (Tremblay et al., 2016; Pfeffer et al., 2013). Likewise, the large-scale organization of the entire human brain has also been investigated frequently (Eickhoff, Yeo, & Genon, 2018; Eickhoff, Constable, & Yeo, 2018). Brain atlases or parcellations are the results of these macroscopic brain mapping studies: They indicate which parts of the human brain are homogeneous with respect to one of its many features (Fig. 2.1A). A variety of neurobiological data can be used to construct parcellation schemes, and the homogeneity of the selected data type can be characterized through diverging paradigms as well (Amunts & Zilles, 2015; Eickhoff, Yeo, & Genon, 2018; Eickhoff, Constable, & Yeo, 2018). This section includes a general discussion on those different parcellation techniques, and lists the brain atlases used in the studies of this thesis.

2.1.1 Methods for brain parcellations

Neurobiological data reflecting brain organization

Parcellations of the human brain have been derived by considering either *post-mortem* brain tissue or MRI data (Amunts & Zilles, 2015; Eickhoff, Constable, & Yeo, 2018; Eickhoff, Yeo, & Genon, 2018). The former was the primary source of information for the earliest brain mapping studies, which reported specific positions on the cortical surface where the histology of the cerebral cortex strongly changed (Brodmann, 1909; Campbell, 1905; von Economo & Koskinas, 1925; Flechsig, 1920; Smith, 1907). Even though nowadays new parcellations are still derived from *ex-vivo* brain tissue (Amunts et al., 2020), the advent of MRI provided the human brain mapping community with new avenues to explore (Eickhoff, Constable, & Yeo, 2018; Eickhoff, Yeo, & Genon, 2018). Despite having a spatial resolution that is too coarse for the delineation of brain regions on the basis of diverging cellular and molecular properties (Edlow et al., 2019; Stucht et al., 2015), MRI images indeed were found to have considerable advantages over the histological data that can perform such delineations. For instance, a parcellation derived from MRI data may be based on more subjects as the images can be acquired and analyzed faster than *post-mortem* human brains can be sliced, stained and scrutinized (Amunts & Zilles, 2015; Eickhoff, Yeo, & Genon, 2018). In addition, the non-invasiveness of MRI facilitates the construction of brain parcellations that reflect the functional differentiations of brain regions in alive and healthy subjects (Dadi et al., 2020; Huth et al., 2015, 2016).

The neurobiological markers derived from *post-mortem* brain tissue or MRI images can reflect either a structural or a functional aspect of brain organization. Here, the structural viewpoint

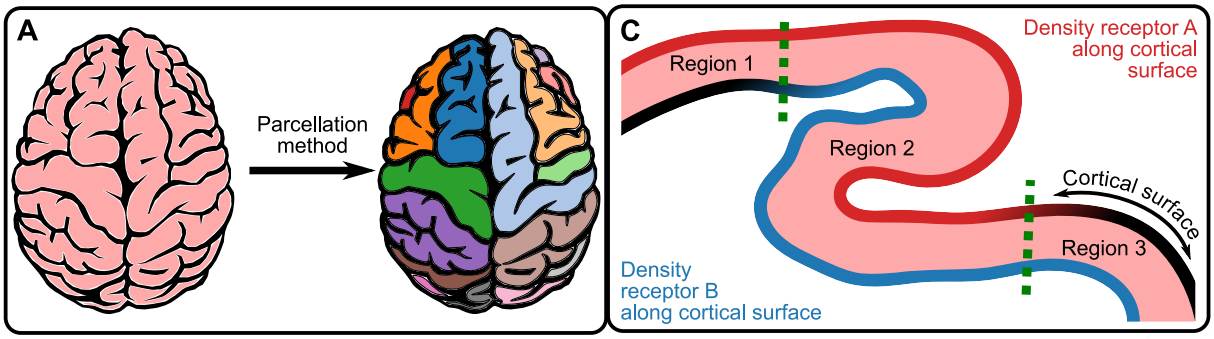

B

	Structural		Functional	
	Local	Connectivity	Local	Connectivity
Brain tissue	Cyto-, myelo- and receptorarchitecture, immunohistochemistry, in situ hybridisation	Axon tracing, Myelin mapping	Post-mortem lesion mapping, calcium imaging	Calcium imaging
Magnetic Resonance Imaging	Structural images, Structural covariances	Diffusion-weighted magnetic resonance imaging	Functional mapping	Coactivation patterns (resting-state and task-based)

Fig. 2.1. **(A)** A brain atlas divides the brain into several brain regions depending on the parcellation method. **(B)** General options when selecting the neurobiological data for a brain parcellation. In addition, example data types are provided where "calcium imaging" is highlighted in gray as it may be used in animal but not human brain mapping studies (Amunts & Zilles, 2015; Eickhoff, Constable, & Yeo, 2018; Eickhoff, Yeo, & Genon, 2018; Grienberger & Konnerth, 2012; Kleist, 1934). **(C)** Illustration of the boundary detection method for the delineation of brain regions. A slice of cortex is drawn with above and below characterizations of the densities of the hypothetical receptors A (red) and B (blue), respectively, along the cortical surface, where brighter colors correspond to higher densities. The boundaries between brain regions are depicted by the green dotted lines marking the positions where either one of the two receptor densities exhibits a spatially localized gradient.

encompasses physical features of the brain, such as neuron and receptor densities when examining *ex-vivo* brain tissue (Amunts & Zilles, 2015; Amunts et al., 2020) and cortical folding patterns when considering MRI images (Auzias et al., 2013, 2016; Desikan et al., 2006; Destrieux et al., 2010; Faillenot et al., 2017; Frazier et al., 2005; Goldstein et al., 2007; Gousias et al., 2008; Hammers et al., 2003; Makris et al., 2006; Rolls et al., 2015; Tzourio-Mazoyer et al., 2002). On the other hand, the brain's functional organization describes the coordination of brain activity, and can be captured by e.g. function mapping: the identification of brain areas associated with a particular cognitive function through the inspection of spatial activation patterns (Dadi et al., 2020; Huth et al., 2015, 2016; Kleist, 1934). Furthermore, even though it cannot be used in human subjects due to its invasiveness, calcium imaging may be used to investigate the functional organization of the brain at a cellular level in animal studies (Ju et al., 2021); see Grienberger & Konnerth (2012) for a review.

The previous examples of neurobiological data only considered local structural or functional properties: Cortical folding patterns, cytoarchitectural differences and function mappings are all spatially constrained to one particular part of the brain. However, brain parcellations may not only be derived from local, but also from connectivity data reflecting the relation between spatially separated parts of the brain. This is explicitly demonstrated by the many brain mapping studies that constructed parcellations on the basis of the structural and the functional connectivity patterns derived from MRI data (Craddock et al., 2012; Fan et al., 2016; Gordon et al., 2016; Joliot et al., 2015; Schaefer et al., 2018; Shen et al., 2013; Urchs et al., 2019); see also Section 2.2: Brain connectivity. Structural connectivity may also be evaluated from brain tissue using axon tracers (Saleeba et al., 2019), and, even though it is unfit for investigating the human brain, calcium imaging has been used to create brain maps of the functional connectivity in the fruit fly *Drosophila* (Mann et al., 2017).

In sum, the neurobiological data used for the construction of parcellations generally involve either brain tissue samples or MRI images, reflect either structural or functional aspects of brain organization, and consider either local properties or connectivity patterns (Amunts & Zilles, 2015; Eickhoff, Constable, & Yeo, 2018; Eickhoff, Yeo, & Genon, 2018). These notions have been summarized in Fig. 2.1B, which schematically shows different types of neurobiological data that can reflect brain organization. Notably, parcellations can also be constructed using a methodology that combines a multitude of these data types (Glasser et al., 2013).

Brain region delineation via boundary detection and clustering

Given a particular type of neurobiological data, two methods can be employed to delineate brain regions: boundary detection and clustering (Eickhoff, Yeo, & Genon, 2018). The former involves the identification of spatially localized changes in the selected data (Amunts & Zilles, 2015; Eickhoff, Yeo, & Genon, 2018). Fig. 2.1C provides a schematic illustration of this technique. The boundaries between brain regions are drawn at those positions where the densities of the hypothetical receptors A and B exhibit strong gradients (Fig. 2.1C). As a consequence, three brain regions can be distinguished: Region 1 is characterized by high and low densities, and region 3 by low and high quantities of the receptors A and B, respectively, whereas region 2 has high expressions for both (Fig. 2.1C).

In contrast, clustering or factorization algorithms define the brain regions by considering similarities rather than strong, localized differences (Eickhoff, Yeo, & Genon, 2018). Various unsupervised learning algorithms from the field of pattern recognition and machine learning have been used to construct brain atlases through this principle (Bishop, 2006; MacKay, 2003). For example, brain parcellations have been constructed by applying non-negative matrix factorization to structural covariance data (Varikuti et al., 2018) and k-means clustering to functional connectivity data (Joliot et al., 2015).

Brain regions can thus be delineated by considering strong and local gradients (boundary detection) or by maximizing the within-region and minimizing the between-area similarity (clustering) with regard to a particular brain feature (Amunts & Zilles, 2015; Eickhoff, Yeo, & Genon, 2018). Similar to parcellation methods combining different types of neurobiological data, brain atlases may also be constructed through a paradigm combining boundary detection and clustering (Schaefer et al., 2018).

2.1.2 Brain atlases used in the studies of this thesis

Parcellations have thus been constructed on the basis of a vast variety of approaches. However, the dynamical whole-brain models could only be simulated for a restricted number of parcellations given the computational demand associated with the model simulations; see Section 5.3.1: Computational costs for a discussion. Below, the parcellations used in the individual studies of this thesis are listed alphabetically, and are provided with a short statement on their derivations to enhance the interpretability of the results and to place them within the general framework discussed above (Section 2.1.1: Methods for brain parcellations). These particular brain atlases were selected to harmonize between parcellations derived from functional and structural data. More details of these parcellations are included in the Supplementary Method of Chapter 3.

AAL atlas The Automated Anatomical Labeling (AAL) atlas considered cortical folding patterns that were detected using the sulci delineation software Voxeline (Diallo et al., 1998). The initial version of the parcellation counted 90 cortical areas (Tzourio-Mazoyer et al., 2002) and 26 cerebellar regions that were adopted from Schmahmann et al. (1999). A second version of the atlas was generated by implementing a new subdivision of the orbitofrontal cortex (Chiavaras & Petrides, 2000; Chiavaras et al., 2001), which resulted in a whole-brain parcellation consisting of 120 parcels in total (Rolls et al., 2015). Additionally, more detailed parcellations of the anterior cingulate cortex and several subcortical regions were adopted, which yielded the third version of the AAL atlas comprising 170 parcels (Rolls et al., 2020).

Brainnetome atlas The Desikan-Killiany atlas was used as a starting point (Desikan et al., 2006; Fan et al., 2016); see below. Subsequently, spectral clustering was applied to the structural connectivity data of 40 subjects to create this parcellation consisting of 210 cortical parcels (Fan et al., 2016).

Craddock parcellations The functional connectivity data of 41 subjects were subjected to spectral clustering (Shi & Malik, 2000; von Luxburg, 2007). The result comprised 44 parcellations that can contain 10 to 1,000 parcels (Craddock et al., 2012).

Desikan-Killiany atlas Desikan et al. (2006) considered the cortical folding patterns of 40 subjects for the generation of this parcellation. The atlas consists of 70 gyral-based parcels (Desikan et al., 2006).

Destrieux atlas The atlas was generated by investigating the curvature and convexity values of the cortical folding patterns of 12 subjects while taking into account prior labeling probabilities and neighboring labels (Destrieux et al., 2010). The resulting parcellation counted 150 parcels (Destrieux et al., 2010).

Harvard-Oxford atlas The 96 cortical brain regions in this parcellation were delineated probabilistically using the cortical folding patterns of 37 subjects (Desikan et al., 2006; Frazier et al., 2005; Goldstein et al., 2007; Makris et al., 2006). The parcellation covers the cerebral cortex, can include subcortical areas, and has been constructed using multiple probability thresholds (Desikan et al., 2006; Frazier et al., 2005; Goldstein et al., 2007; Jenkinson et al., 2012; Makris et al., 2006).

MIST parcellations The Multiresolution Intrinsic Segmentation Template (MIST) parcellations were derived by applying hierarchical agglomerative clustering to the functional connectivity data of 198 subjects (Urchs et al., 2019). The resulting whole-brain parcellations have 7 to 444 parcels (Urchs et al., 2019).

Schaefer parcellations The Schaefer parcellations were constructed by considering the functional connectivity data of 1489 subjects from the Brain Genomics Superstruct Project (A. J. Holmes et al., 2015; Schaefer et al., 2018). A gradient-weighted Markov Random Field model implementing both boundary detection and clustering was applied to the data to generate several cortical parcellations that contained 100 to 1,000 parcels (Schaefer et al., 2018).

Shen 2013 parcellations Multigraph K-way clustering, a method related to the K-way normalized cut algorithm from Yu & Shi (2003), was applied to the functional connectivity data of 79 subjects (Shen et al., 2013). The forthcoming parcellations counted 100, 200 and 300 parcels (Shen et al., 2013).

von Economo-Koskinas atlas von Economo & Koskinas (1925) created this brain parcellation by detecting gradients in the cytoarchitecture of 20 human brains *post-mortem*. The atlas has been digitized and made publicly available by Scholtens et al. (2018). Recently, the same group has publicly released digitizations of other historical parcellations (Pijnenburg et al., 2021).

2.2 Brain connectivity

Dynamical whole-brain models have been designed to tighten the gap between the SC and the FC of the brain (Honey et al., 2007). Hence, in order to interpret the results of the model simulations, there first must be an understanding of what the SC and the FC entail in principle. This section provides this background information, and additionally explains how the structural and the functional connectomes can be derived from diffusion-weighted MRI (dwMRI) and functional MRI (fMRI) data, respectively. Finally, the relationship between the SC and the FC is discussed in detail, where an explicit statement is provided as to why (non-linear) dynamical whole-brain models are well suited to investigate this relationship.

2.2.1 Structural connectivity

The structural connectome reflects how the brain is internally wired by physical connections (Sporns et al., 2005). The SC at the microscopic scale, for instance, considers the axonal projections between individual neurons in microcircuits (DeFelipe, 2010; Kadirvelu et al., 2017; Verstraelen et al., 2018; Sporns et al., 2005). A courser consideration of the structural connectome yields its mesoscopic variant, which exhibits specific connectivity patterns with respect to the different layers of the cerebral cortex (Douglas & Martin, 2004; Felleman & Van Essen, 1991; Olivas et al., 2012; Sporns et al., 2005). However, dynamical whole-brain models consider the macroscopic SC that may characterize how entire brain regions are connected by white matter fiber tracts as illustrated in Fig. 2.2A (Ambrosen et al., 2020; Bastiani & Roebroeck, 2015; Craddock et al., 2013; Sporns et al., 2005). These fibers constitute bundles of axons, and hence facilitate the transmission of electrical signals across the entire cortical space (Fields, 2010). The macroscopic SC can thus be viewed as a representation of the physical framework that the brain may employ to coordinate its activity at a larger spatial scale in order to process information and undertake appropriate action as a response.

This macroscopic version of the SC can be derived from dwMRI sequences (Behrens et al., 2003; Conturo et al., 1999; Le Bihan, 2003). This type of MRI data exploits the anisotropic diffusion of water in the axons of neurons (Jbabdi et al., 2015; Le Bihan et al., 1988; Makris et al., 1997). Fig. 2.2C illustrates this concept: In the axon, the water molecules predominantly

diffuse along the axis of the cell membrane, whereas their movements are not as directionally restricted in the cell body of a neuron. If many axons are aligned, as is the case in white matter fiber tracts (Abdollahzadeh et al., 2019), this principle leads to detectable signals that can be used by so-called tractography algorithms to reconstruct those fibers throughout the entire brain (Fillard et al., 2011; Yeh et al., 2021; Zhan et al., 2015). Importantly, these algorithms can infer the presence of connections but are not able to specify the directionality of information flow, and hence are considerably limited in this respect (Kale et al., 2018).

The results of the tractography comprise a predefined number of reconstructed white matter fibers or streamlines (Tournier et al., 2019; Yeh et al., 2021). This information can be compressed by using a brain atlas. Given a particular parcellation with N brain regions, such a compression would produce two $N \times N$ matrices. The first, named the counts or SC matrix, contains the number of streamlines connecting the individual pairs of brain regions, and the other, called the path length (PL) matrix, accommodates the average lengths of those streamlines (Tournier et al., 2019; Yeh et al., 2021). The dynamical whole-brain models are constructed on the basis of this compressed information: They use the elements of the SC and PL matrices as proxies for the efficiencies and latencies with which signals are transmitted between the brain

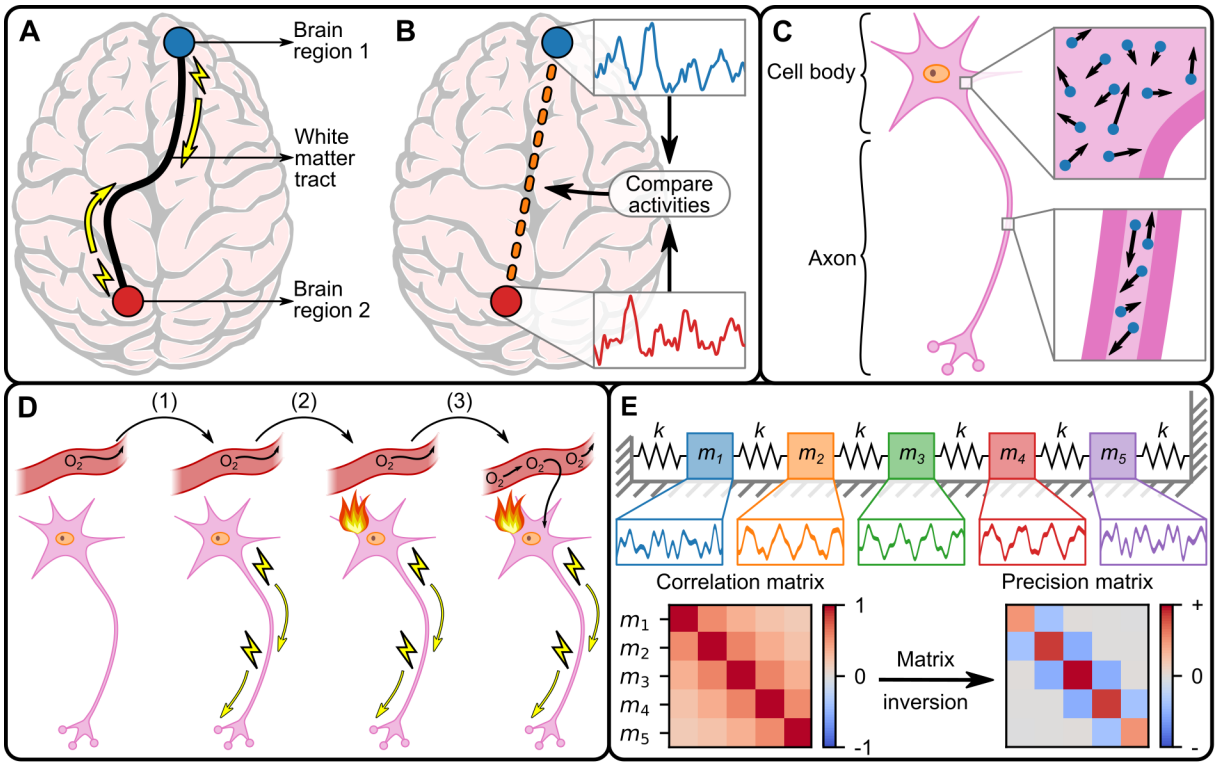

Fig. 2.2. **(A-B)** Illustrations explaining (A) the structural connectivity (SC) and (B) the functional connectivity (FC) of the brain. The SC considers the white matter fiber tracts physically facilitating the transmission of electrical signals between brain regions, whereas the FC reflects statistical dependencies betwixt the regional activities. **(C)** Schematic depiction of isotropy and anisotropy in a neuron. In the axon, the (water) molecules diffuse predominantly along the direction of the fiber (anisotropy), while their movements are not so restricted in the cell body (isotropy). **(D)** Illustration explaining the origin of the blood-oxygen-level-dependent (BOLD) signal. First, (1) neurons are activated. As a consequence, (2) they start to consume energy. Eventually, (3) continued activation necessitates the oxygen-demanding production of new energy which requires oxygenated blood to flow into the activated brain region. **(E)** Demonstration of how the SC can be derived from the FC in a system that can be modeled via a (linear) multivariate Gaussian process. The example system is an adaptation of the mass-spring system shown in Das et al. (2017). Five masses are coupled by identical springs as depicted in the top panel, and are perturbed by Gaussian white noise. Simulations of this system yield the positions of these masses over time (fragments of these traces are shown in the top panel), which can be correlated to yield the correlation matrix shown on the bottom left. Inversion of this matrix yields the precision matrix shown on the bottom right, which only reflects conditional statistical dependencies.

regions, respectively; see Section 2.3: Dynamical whole-brain models. Since the tractography algorithms cannot infer the directionality of the connections from the dwMRI sequences, the SC and PL matrices are symmetric, and so the models assume that information flows from brain region A to area B with the same efficiency and latency as for the reversed direction.

2.2.2 (Resting-state) functional connectivity

The functional connectome is conceptually distinct from the SC, because it does not consider physical connections but statistical dependencies between activities instead (Craddock et al., 2013; van den Heuvel & Hulshoff Pol, 2010; Rogers et al., 2007). In other words, the FC reflects how similar the activation patterns of two brain regions are over time (Fig. 2.2B). Even though this correspondence can be evaluated through a number of analyses, it traditionally involves calculating the correlation coefficient between the activity time series (Farahani et al., 2019; Marrelec et al., 2016; H. E. Wang et al., 2018). In fact, it has been argued that this approach is a suitable choice when fMRI data are used for the inference of the functional connectome (H. E. Wang et al., 2014), as is the case throughout this thesis. Albeit the FC might change over time (Brovelli et al., 2017; Heitmann & Breakspear, 2018; Hutchison et al., 2013; Preti et al., 2017), it currently is not clear which analytical procedures applied to fMRI data yield time-dependent FC fluctuations that actually reflect neurobiologically-relevant brain state variations (Hindriks et al., 2016; Honari et al., 2019; Leonardi & Van De Ville, 2015; Lurie et al., 2020; Zhang, Baum, et al., 2018). Because of this ongoing debate, the functional connectome is assumed to be static in this thesis.

The FC of the brain can thus be derived from fMRI sequences. That is because fMRI measures the amount of oxygenated blood that may serve as a proxy for the activity of a brain region (Bandettini et al., 1992; Kwong et al., 1992; Ogawa et al., 1992). The theoretical principle linking oxygenated blood to brain activity is captured by the concept of the blood-oxygen-level-dependent (BOLD) response illustrated in Fig. 2.2D. When a group of nerve cells becomes activated and starts to generate action potentials, the individual neurons start to consume more energy (Fig. 2.2D; Attwell & Laughlin, 2001; Harris et al., 2012). As a consequence, additional energy in the form of adenosine triphosphate (ATP) must be generated within the cells, which requires oxygenated blood to flow to the activated brain area (Fig. 2.2D; Schmidt-Rohr, 2020; Vergara et al., 2019). These indirect measurements of neural activity and the relatively low sampling rates ($\sim$1 s per brain volume) are the main disadvantages of fMRI, whereas the benefits are its spatial resolution (voxels are approximately 2 mm $\times$ 2 mm $\times$ 2 mm) and its non-invasiveness (Uğurbil et al., 2013).

Dynamical whole-brain models often consider the FC corresponding to resting-state brain dynamics, which is observed when the subject is neither performing a particular task nor receiving a specific stimulus (B. B. Biswal, 2012; Deco et al., 2011; Popovych et al., 2019; Suárez et al., 2020). In fact, throughout this thesis, the FC is assumed to have been derived from resting-state data unless explicitly specified otherwise. Even though this type of brain activity was historically thought to merely constitute unstructured noise, there nowadays is consensus that it actually reflects ongoing mental processes (van den Heuvel & Hulshoff Pol, 2010; Deco et al., 2011; Cabral et al., 2014; Popovych et al., 2019). Resting-state fMRI data can even portray activation patterns that are similar to those found in task-based settings, presumably because those mental processes require a careful coordination of brain activity (B. Biswal et al., 1995; Cole et al., 2014; Bolt et al., 2017). Furthermore, considering the brain activity at rest has practical advantages over the investigation of task-induced dynamics. As they can be acquired in the absence of an experimental paradigm, resting-state data can be sampled more readily than task-based brain activity, which necessitates the engagement of a subject with a predefined task or stimulus (M. D. Fox & Greicius, 2010; Lv et al., 2018; Popovych et al., 2019; Smitha et al., 2017). Additionally, the FC associated with a specific experimental design could strongly

rely on the task at hand, and may thus be less generalizable and reusable than the functional connectome obtained from resting-state data (Popovych et al., 2019; Smitha et al., 2017).

The (resting-state) fMRI data is 4-dimensional as it constitutes 3-dimensional brain volumes sampled at several consecutive time points. To derive the region-based FC from the time series, a parcellation can be used to pool the BOLD signals of all the voxels comprising a particular brain region together for every individual time point by calculating, e.g., the mean or first eigenvariate of the BOLD signals across those voxels (Jenkinson et al., 2012). This operation yields N time series where N is the number of brain regions in the considered parcellation. The FC may then be calculated from these temporal activation patterns by determining their statistical dependencies through a selected measure (H. E. Wang et al., 2014). The final result is the $N \times N$ FC matrix describing the extent to which the individual pairs of brain regions are co-activated.

2.2.3 Correspondence between structural and functional connectivity

The SC and the FC of the human brain exhibit a linear relationship that explains a moderate amount of the variance (<50%) in the connectomes at best (Honey et al., 2009; Suárez et al., 2020). This discrepancy between the SC and the FC matrices may be induced by the emergence of correlations between pairs of brain regions that do not exhibit a structural connection but are physically connected to a common source (Das et al., 2017). When a system can be modeled via a multivariate Gaussian process in the form of the well-known Ornstein-Uhlenbeck model (Bishop, 2006; Galán, 2008; Saggio et al., 2016), and a sufficiently large number of samples is available, these indirect functional connections can be removed by inverting the FC (correlation) matrix to yield the precision matrix which only contains the direct or conditional statistical dependencies (Das et al., 2017; Dawid, 1979; Dempster, 1972); see Fig. 2.2E for an illustration. Comparing the SC reconstructed from dwMRI images with the functional precision matrix derived from fMRI sequences can indeed tighten the link between the structural and the functional connectomes, but the relationship nevertheless remains imperfect even if many hours of resting-state data are used for the calculations (Liégeois et al., 2020; Marrelec et al., 2016). These findings therefore suggest that the relationship between the SC and the FC may not be accurately described by a multivariate Gaussian process in the form of a linear dynamical system (Bishop, 2006).

Three types of models have been proposed to explain the remaining variability in the empirical data. Some studies have used (multivariate) statistical models to provide a tighter link between the SC and the FC (Deligianni et al., 2016; Messé et al., 2014; Mišić et al., 2016; Suárez et al., 2020; Vázquez-Rodríguez et al., 2019). Others have used principles from network and telecommunication science to achieve the same goal (Avena-Koenigsberger et al., 2018; Crofts & Higham, 2009; Goñi et al., 2014; Graham & Rockmore, 2011; Mišić et al., 2015). However, this thesis considers the third class of dynamical whole-brain models that replicate the FC by simulating resting-state brain dynamics on the basis of the SC (Deco & Kringelbach, 2014; Popovych et al., 2019; Suárez et al., 2020). These models are well suited to investigate the non-linear interactions that presumably underlie the relationship between the SC and the FC (see above), because they may incorporate a wide variety of non-linearities; see below.

2.3 Dynamical whole-brain models

The first studies investigating dynamical whole-brain models were published more than a decade ago (Honey et al., 2007; Ghosh et al., 2008; Honey et al., 2009). Ever since, these models have been used to study a wide variety of aspects regarding the human brain. For example, they demonstrated that proper resting-state brain dynamics require an appropriate amount of system noise as well as a fitting coupling strength and delay in the transmission of signals between brain regions (Deco et al., 2009, 2011; Ghosh et al., 2008). Eventually,

these investigations led to the conclusion that the brain at rest is characterized by a state of maximal metastability (Deco et al., 2012; Deco & Jirsa, 2012; Deco et al., 2017). Whole-brain models were also used to study the temporal variations of the FC discussed in Section 2.2.2 (E. C. A. Hansen et al., 2015), and some recent studies even embedded additional region-specific information (beyond the regional connectivity profiles included in the SC and FC) in the models to explain a variety of neurobiological phenomena (Deco, Cruzat, et al., 2018; Deco et al., 2019, 2021; Demirtaş et al., 2019; Kringelbach et al., 2020).

There is a growing body of evidence that dynamical whole-brain models may not only be used to study general neurobiological principles underlying brain functioning, but that they can also be a personalized representation of the (resting-state) brain dynamics of a particular individual (Bansal et al., 2018). This is explicitly demonstrated by one study that used the toolbox of The Virtual Brain (Jirsa et al., 2017; Ritter et al., 2013; Sanz-Leon et al., 2015) to show the predictive capacity of dynamical whole-brain modeling results outperforming that of the empirical connectomes when distinguishing between healthy subjects and patients with Alzheimer's disease (Zimmermann, Perry, et al., 2018). Furthermore, the models have been used to identify attention deficit hyperactivity disorder (ADHD) patient subtypes (Iravani et al., 2021), and to estimate the impact of tumor resection on brain dynamics (Aerts et al., 2020). In sum, even though dynamical whole-brain models were initially designed to understand general aspects of the brain by investigating its structure-function relationship, they nowadays are also used to identify differences between individuals corresponding to distinct cohorts.

Fig. 2.3 schematically depicts the general analysis pipeline associated with dynamical whole-brain models. Prior to the modeling, the brain is divided into N brain regions by a particular

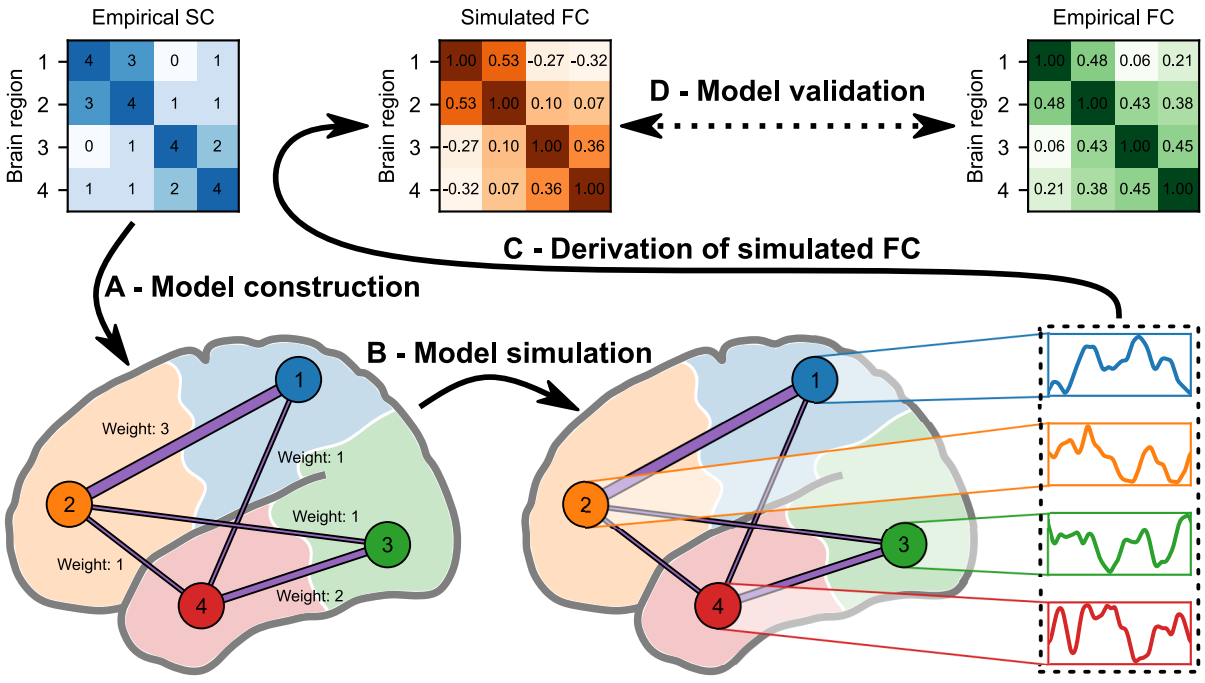

Fig. 2.3. The various stages in dynamical whole-brain modeling. **(A)** A network graph is constructed on the basis of the (empirical) structural connectivity (SC). In this graph, the nodes represent the brain regions, and are connected by weighted edges as prescribed by the SC matrix. This matrix is symmetric when it is derived from MRI data (Section 2.2.1: Structural connectivity), and so the edges are undirected. **(B)** The mean-field activities of all brain regions are modeled via a particular model of local dynamics that includes a coupling term enabling connected brain regions to interact. Subsequently, the model is simulated in order to sample the (simulated) activity time traces of each individual region. **(C)** A functional connectivity (FC) matrix is calculated from the simulated activities by following the same procedure used to derive the empirical FC from the (empirical) BOLD signals. **(D)** Finally, the model is validated by determining the similarity between the simulated and the empirical FC.

parcellation, and the corresponding $N \times N$ *empirical SC* and *empirical FC* matrices are derived from dwMRI and fMRI data, respectively. Subsequently, a network graph is constructed on the basis of the empirical SC (Fig. 2.3A). The nodes of this graph represent the individual brain regions, and pairs of nodes are connected by edges if the corresponding element of the empirical SC is non-zero. These edges are undirected because the empirical SC matrix is symmetric (Section 2.2.1: Structural connectivity), and are assigned a weight that is equal to the value of their associated elements in the empirical SC matrix; see the example of the connection between brain regions 1 and 2 in Fig. 2.3, which has a weight of 3. The constructed structural network includes all the connections that the model can use to coordinate the activities of the individual brain regions.

Then, the mean-field activities of all brain regions are sampled by simulating the dynamics of the network model (Fig. 2.3B). Here, a single set of differential equations with a known dynamical behavior is used to describe the local dynamics of each individual brain region. Such systems of equations summarize the complex interactions between the many neurons within those regions through a few state variables; see below for examples. When implementing these local models in dynamical whole-brain models, a coupling term is added to the equations to enable the (mean-field) activities of distinct brain regions to interact in accordance with the constructed structural network. Hence, dynamical whole-brain models are network models that mimic how the regional activities following a well-defined pattern in isolation affect one another when (structural) connections are added.

Next, the *simulated FC* is calculated from the (simulated) activity time traces by employing the same procedure that was used to derive the empirical FC from the regional BOLD signals (Fig. 2.3C; Section 2.2.2: (Resting-state) functional connectivity). Finally, the simulated and the empirical FC are compared by calculating an index of the similarity (e.g., the Pearson correlation coefficient) between them (Fig. 2.3D). This index indicates how well the model is able to replicate the empirical FC and can thus be regarded as a measure of the validity of the model. Dynamical whole-brain models can have a number of free parameters, and the settings of these parameters may influence the network dynamics and incidentally (the similarity between the empirical and) the simulated FC. Therefore, in order to provide a definite estimate of the fit of the model to the empirical data, the free parameters of the models should first be optimized such that the similarity index is maximized.

Dynamical whole-brain modeling studies have proposed a vast variety of models for local dynamics that can have diverging conceptual underpinnings and interpretations (Abeysuriya et al., 2018; Bick et al., 2020; Deco et al., 2012, 2013; Deco, Ponce-Alvarez, et al., 2014; Deco et al., 2017; Ghosh et al., 2008; E. C. A. Hansen et al., 2015). However, two of these models return in both studies of this thesis, which are the Kuramoto model of coupled phase oscillators (Cabral et al., 2011; Kuramoto, 1984; Ponce-Alvarez et al., 2015; Popovych et al., 2021) and a system of coupled Wilson-Cowan neural mass models (Abeysuriya et al., 2018; Deco et al., 2009; Muldoon et al., 2016; Wilson & Cowan, 1972). These models are therefore introduced and examined in more detail below. The second study of this thesis also makes use of the (linear) Ornstein-Uhlenbeck model that was mentioned in Section 2.2.3: Correspondence between structural and functional connectivity. With respect to this model, it nevertheless suffices to mention that it simply describes the (linear) diffusion of noise over the (anatomical) network structure; see Bishop (2006) and Galán (2008) for more details on this model, and Saggio et al. (2016) for its analytical solution in the context of dynamical whole-brain modeling.

2.3.1 Kuramoto model

Oscillations are omnipresent in the brain. They can be found in the collective activities of large neuronal ensembles (Baria et al., 2011; Cohen, 2017; Scheeringa et al., 2016) as well as in the

fluctuating membrane potentials of individual nerve cells (Stiefel & Ermentrout, 2016). These oscillation generating (populations of) neurons may be connected by synapses, which leads to the formation of networks of coupled neural oscillators. Then, the Kuramoto model may be used to approximate the (phase) dynamics of such networks (Bick et al., 2020; Cumin & Unsworth, 2007; Breakspear et al., 2010). After all, this dynamical model was designed to study synchronization in any system of coupled (phase) oscillators (Acebrón et al., 2005; da Fonseca & Abud, 2018; Kuramoto, 1984; Strogatz, 2000); for a comprehensive review see Rodrigues et al. (2016).

The Kuramoto model describes the dynamics of an individual oscillator $i \in \{1, ..., N\}$ in a network of N oscillators by considering only its phase $\varphi_i(t)$ as a function of time t. In dynamical whole-brain models, the phase of each oscillator follows the dynamic equation (Cabral et al., 2011; Popovych et al., 2021)

$$\frac{d\varphi_i(t)}{dt} = \dot{\varphi}_i(t) = 2\pi f_i + \sigma\nu_i(t) + \sum_{j=1}^{N} C_{ij} \sin\left(\varphi_j(t - \tau_{ij}) - \varphi_i(t)\right). \tag{2.1}$$

The first term on the right hand side of this equation indicates that oscillator i has an intrinsic or natural frequency f_i, which means that it oscillates with that particular frequency in the absence of any perturbations. The second term characterizes that the phase of the oscillator is perturbed by noise with an intensity of σ through the stochastic variable $\nu_i(t)$. The third and final term defines how the oscillator is coupled to all other oscillators in the network. Here, the phase of oscillator j influences that of the considered oscillator i after a delay of τ_{ij} and with a strength of C_{ij}. This is different from the original model proposed by Kuramoto (1984), where the network is fully and homogeneously connected. This divergence from the original formulation is required to implement the prior information included in the SC into the network model. Here, the empirical SC and PL matrices can be used for the derivation of the coupling strengths C_{ij} and delays τ_{ij}, respectively (Section 2.2.1: Structural connectivity).

It must be mentioned here that dynamical whole-brain models based on the Kuramoto model disregard the neurophysiological principles underlying neural oscillations. Indeed, the Kuramoto model is an abstract model that can be used to study (de)synchronization in any network of coupled phase oscillators (Kuramoto, 1984). However, this high level of abstraction is achieved by simply assuming the existence of the oscillations and ignoring their origin (Eq. 2.1). In reality, neural oscillations typically emerge from the interplay between neurons through a variety of mechanisms (Tiesinga & Sejnowski, 2009; Vijayan & Kopell, 2012; Viriyopase et al., 2016). Moreover, the Kuramoto model presumes that the activities of the brain regions oscillate with a fixed natural frequency (Eq. 2.1). This aspect of the model deviates fundamentally from the finding that neural oscillations may vary considerably in terms of time scale (Buzsáki, 2006), which may be caused by the involvement of distinct inhibitory neuron subtypes in these rhythms (J. W. M. Domhof & Tiesinga, 2021; Kopell et al., 2000).

Alternatively, dynamical whole-brain models may be based on biologically-plausible models for local dynamics. These models explicitly consider the interactions between the activities of separate (ensembles of) neurons. As a consequence, the network dynamics enjoy a stronger neurobiological motivation, but they may also be more complex. Examples of such biologically-realistic models include the Jansen-Rit model (Jansen et al., 1993; Jansen & Rit, 1995), the (reduced) Wong-Wang model (Deco, Ponce-Alvarez, et al., 2014; Wong & Wang, 2006) and the Wilson-Cowan model considered in this thesis and described in more detail below (Wilson & Cowan, 1972).

2.3.2 Wilson-Cowan model

Fig. 2.4A shows the network architecture that is typically employed when the Wilson-Cowan model characterizes the regional dynamics in a dynamical whole-brain model (Abeysuriya et

al., 2018; Deco et al., 2009; Hellyer et al., 2016; Messé et al., 2014). Given a network of N brain regions, the variables $E_i(t)$ and $I_i(t)$ represent the collective activities of all the excitatory and inhibitory neurons in brain region $i \in \{1, ..., N\}$, respectively (Wilson & Cowan, 1972). These variables can be interpreted as the average firing rates of the neuron ensembles, i.e. the proportion of excitatory and inhibitory cells generating an action potential within a unit of time, respectively. In the studies of this thesis, the activity of an individual brain region i is then modeled via the coupled differential equations

$$\mu_E \dot{E}_i(t) = -E_i(t) + \kappa \mathcal{S}\left(\sum_{j=1}^{N} C_{ij} E_j\left(t - \tau_{ij}\right) - w_{EI} I_i(t) + I_b\right) + \sigma \nu_i(t) \quad \text{and} \tag{2.2}$$

$$\mu_I \dot{I}_i(t) = -I_i(t) + \kappa \mathcal{S}\left(w_{IE} E_i(t)\right) + \sigma \nu_i(t), \tag{2.3}$$

where $\mu_E = \mu_I = 20$ ms determine the time scales of the excitatory and inhibitory dynamics, respectively. The first terms in the right hand sides of Eqs. 2.2 and 2.3 ($-E_i(t)$ and $-I_i(t)$, respectively) characterize that the activities of both populations decay in the absence of any input. Their last terms ($\sigma\nu_i(t)$ for both expressions) indicate that both neuronal ensembles receive the same noise with intensity σ.

The middle terms in both equations define the inputs arriving at the separate populations. The pool of inhibitory neurons only receives an excitatory input from the excitatory cells located in the same brain region that is scaled by a factor $w_{IE} = 0.6$ (Eq. 2.3; Fig. 2.4A). In contrast, a number of inputs arrive at the excitatory cells. One of these inputs is a constant background input I_b. In addition, they receive an inhibition from the inhibitory cells located in the same region that is scaled by a factor $w_{EI} = 1.5$. Furthermore, the excitatory cells residing in the same area of the brain excite one another, and this excitation is scaled by a factor $C_{ii} = w_{EE} = 1.0$. Moreover, the excitatory cells in any other brain region j can excite those located in brain region i after a delay of τ_{ij} and with a strength of C_{ij}. Fig. 2.4A schematically depicts these connectivity patterns for three brain regions. The sums of the inputs elicit a change in the activations of the individual pools of neurons via the non-linear, sigmoid-shaped activation function

$$\mathcal{S}(x) = \frac{1}{1 + \exp\left(-\lambda(x - \gamma)\right)} - \frac{1}{1 + \exp(\lambda\gamma)}, \tag{2.4}$$

where $\lambda = 20.0$ and $\gamma = 0.3$ determine the width and the position of its inflexion point, respectively. This function satisfies $\mathcal{S}(0) = 0$ for any combination of λ and γ, and $\kappa = (1 + \exp(\lambda\gamma))/\exp(\lambda\gamma)$ ensures that $\kappa\mathcal{S}(x) = 1$ as $x \to \infty$.

In the absence of inter-regional coupling and noise, the model described by Eqs. 2.2 - 2.4 and

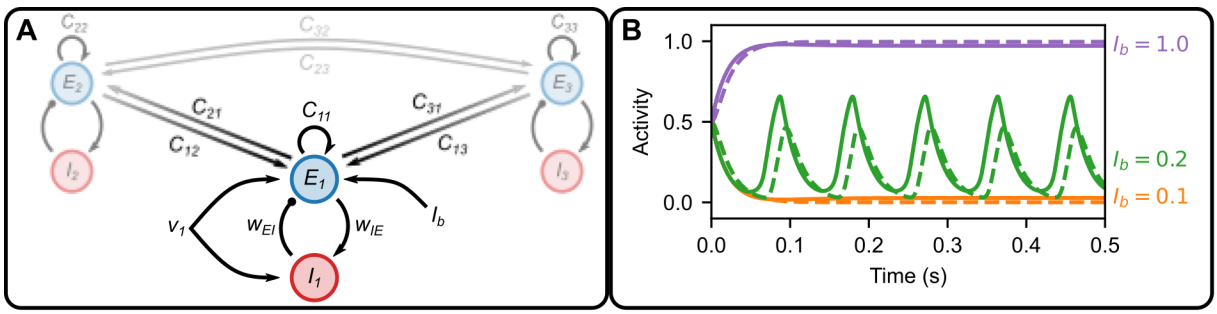

Fig. 2.4. **(A)** Schematic of a dynamical whole-brain model that uses the Wilson-Cowan model for local dynamics and comprises three brain regions. The input details are only shown for the region in the middle. Arrows and dots represent excitatory and inhibitory interactions, respectively. Eqs. 2.2 - 2.3 and the associated text explain the depicted symbols. **(B)** Sample activity time series of the excitatory ($E_i(t)$, solid lines) and inhibitory ($I_i(t)$, dashed lines) neuron populations for distinct settings of the constant background input arriving at the excitatory population I_b in the absence of inter-regional coupling and noise.

associated parameter values exhibits the behavior displayed in Fig. 2.4B. If the background input I_b is too low and too high, the model converges to a low and high activity state, respectively (Fig. 2.4B, orange and purple). However, between these states, the model produces oscillations (Fig. 2.4B, green). These oscillations have an alpha-band ($\sim$10 Hz) frequency (Foster et al., 2017), which is the predominant frequency in the electroencephalography (EEG) measuring large-scale fluctations in the electrical potentials of the resting human brain (Fraga González et al., 2018; Spitoni et al., 2013). Even though the Wilson-Cowan model may also feature multistability and hysteresis besides the oscillatory behavior (Wilson & Cowan, 1972), the model was designed to generate these (alpha-band frequency) oscillations because these rhythms have been associated with the BOLD signals captured by fMRI data (Mayhew et al., 2013; Scheeringa et al., 2016)

It should be noted that the exact implementation of the Wilson-Cowan model in dynamical whole-brain models may vary between studies (Abeysuriya et al., 2018; Daffertshofer & van Wijk, 2011; Deco et al., 2009; Hellyer et al., 2016; Messé et al., 2014; Muldoon et al., 2016). Furthermore, recent studies suggest that the model described by Fig. 2.4A and Eqs. 2.2 - 2.4 may not be entirely accurate from a biophysical point of view: Inhibitory neurons have been shown to inhibit one another and to form long-range connections (Melzer & Monyer, 2020; Pfeffer et al., 2013). However, as this thesis focuses on the influence of the parcellation on dynamical whole-brain modeling results, the model is formulated with the objective to enhance its comparability with the pre-existing literature. Hence, it is based on the model by Deco et al. (2009), which regularly also forms the basis for other dynamical whole-brain models using the Wilson-Cowan model as the model for local dynamics (Abeysuriya et al., 2018; Hellyer et al., 2016; Messé et al., 2014)

2.4 Graph theory

The previous section already demonstrated that the SC and FC may be represented by network graphs. In such graphs, the brain regions are portrayed by the network nodes or vertices that are connected to one another by edges as prescribed by the considered connectivity matrix; see Fig. 2.3A for an example. Consequently, concepts from the mathematical field of graph theory may be used to study these networks and characterize them in terms of a variety of network properties (Bullmore & Sporns, 2009; Rubinov & Sporns, 2010). Such graph-theoretical statistics have, for example, been used to better understand how neuropathologies affect brain functioning (Bullmore & Sporns, 2009; Guye et al., 2010; Z. Wang et al., 2021). In this section, the main classes of network properties that are frequently used to study brain networks are discussed globally. In particular, the properties of node centrality, functional integration and functional segregation are introduced (Rubinov & Sporns, 2010). Additionally, each of these brief introductions is accompanied by concrete examples of graph-theoretical measures reflecting that specific network property. Here it should be noted that some of these metrics are also used in one of the studies of this thesis to explain the observed parcellation-induced variations in the modeling results (Chapter 3).

2.4.1 Centrality of network nodes

Individual nodes may play specific roles in a network; in fact, one vertex may be more important for its functioning than another. The concept of centrality provides a ranking of the influences that the individual nodes can have on (the dynamics of) the network (Borgatti, 2005; Borgatti & Everett, 2006). Here, relatively important nodes or brain regions are supposed to promote the integration of information distributed throughout the (brain) network and to protect network functioning from improper behavior following small network architectural changes or even degradation (Rubinov & Sporns, 2010). Experimental studies have demonstrated a practical implication of this theoretical notion: Deviations in node centrality have indeed been

associated with neurological diseases (Lynall et al., 2010; Rubinov et al., 2009). Interestingly, these empirical findings received additional theoretical support from an investigation wielding dynamical whole-brain models (Cabral et al., 2012).

The centrality measure that is perhaps most often used in brain network research is the nodal degree (Rubinov & Sporns, 2010). It is the sum of all the connections that link a particular vertex to the rest of the network (Diestel, 2012; Rubinov & Sporns, 2010). However, the centrality may also be expressed in terms of shortest paths or geodesics, i.e. the combinations of network edges that minimize the costs of traveling between any two nodes in the network (Cherkassky et al., 1996; Rubinov & Sporns, 2010). One measure expressing the centrality in terms of geodesics is the closeness centrality of a node, which is the reciprocal of the average length of all shortest paths connecting that node to the other vertices in the network (Freeman, 1978; Rubinov & Sporns, 2010). Another example is the nodal betweenness centrality, which is the fraction of all shortest paths in a given network that involve the considered vertex (Brandes, 2001; Freeman, 1978; Rubinov & Sporns, 2010). Of these three measures, the degree and closeness centrality are used in the first study of this thesis (Chapter 3).

2.4.2 Functional integration

Measures of functional integration reflect the extent to which a (brain) network facilitates the swift assimilation of segregated flows of information (Latora & Marchiori, 2001; Rubinov & Sporns, 2010; Watts & Strogatz, 1998). Indeed, information may be distributed over spatially separated parts of the brain. For instance, the area of the cerebral cortex that processes visual information is located in the occipital lobe based at the rearmost part of the brain (Tong, 2003). Concurrently, somatosensory input is processed in a portion of the brain adjacent to the central sulcus that can be found approximately in the middle of the anterior-posterior axis (Sanchez-Panchuelo et al., 2010). It has been proposed that the assimilation of different types of (sensory) information could underlie higher-order cognitive functions (Oizumi et al., 2014; Toker & Sommer, 2019). In fact, experimental findings suggest that the capacity of the brain for functional integration is related to the intelligence scores of individual subjects (van den Heuvel et al., 2009).

In brain network research, the ability of a network to quickly integrate diverse streams of functional information is typically reflected by two measures (Rubinov & Sporns, 2010). The first, the characteristic path length, is calculated as the mean length of all shortest paths in the network, and a larger value for this quantity indicates a lower capacity for fast assimilation (Watts & Strogatz, 1998). The second, the (global) efficiency, is the mean across the inverted lengths of all geodesics; here, a higher efficiency reflects an increased ability to quickly integrate distributed information (Latora & Marchiori, 2001). It has been argued that the efficiency outperforms the characteristic path length when considering brain networks (Achard & Bullmore, 2007). Nevertheless, both measures are used in the first study of this thesis (Chapter 3).

2.4.3 Functional segregation

As discussed in the previous paragraph, information indeed may be distributed across the brain (Tong, 2003; Sanchez-Panchuelo et al., 2010), and the network architecture may reflect this segregation as well. Visual information, for instance, is initially relayed the to primary visual cortex, but is ultimately processed by the ensemble of neighboring brain regions (Freud et al., 2016). Measures of functional segregation characterize the extent to which the (brain) network consists of separate clusters of nodes, where many and few connections are found between nodes belonging to the same and different clusters, respectively (Rubinov & Sporns, 2010, 2011; Watts & Strogatz, 1998). The amount of functional segregation in a brain network can thus be interpreted as the degree to which the brain regions can be divided into groups that presumably perform specific tasks (Rubinov & Sporns, 2010).

In brain network studies, functional segregation is typically characterized by the clustering coefficient or the modularity (Rubinov & Sporns, 2011; J. Wang et al., 2009; Zalesky et al., 2010), although the transistivity may also be used for this purpose (Rubinov & Sporns, 2010). The clustering coefficient is defined at the nodal level and can be interpreted as the portion of the neighbors of the considered node that also connect to each other (Onnela et al., 2005; Rubinov & Sporns, 2010; Watts & Strogatz, 1998). Calculating the mean across the nodal clustering coefficients then yields a measure representing how connectivity is clustered around the individual nodes of the network on average (Rubinov & Sporns, 2010). When the nodal clustering coefficients are instead collectively normalized, the transistivity is obtained (Newman, 2003; Onnela et al., 2005; Rubinov & Sporns, 2010). In contrast to the clustering coefficient and transistivity, the modularity is calculated for the entire network and not on a nodal basis (Newman & Girvan, 2004; Rubinov & Sporns, 2010, 2011). It aims to divide the network nodes into a number of modules so that the connectivity within and between modules is maximized and minimized, respectively (Newman & Girvan, 2004; Rubinov & Sporns, 2010, 2011). Finding the exact optimal modular structure quickly becomes computationally intractable as the number of nodes increases, and so this optimization problem is typically solved by algorithms specifically designed for this purpose (Blondel et al., 2008; Danon et al., 2005; Newman, 2006). In the first study of this thesis, only the clustering coefficient and the modularity are considered (Chapter 3).

2.5 Principal component analysis

Nowadays, neuroscience research often involves the analysis of high-dimensional datasets comprising many samples that all consist of multiple variables (Pang et al., 2016). In animal studies, for example, calcium imaging can be used to simultaneously record the activity of thousands of nerve cells on a vast number of points in time (Ohki et al., 2005; Stosiek et al., 2003). Depending on the research question, it may be helpful to reduce the dimensionality of such datasets prior to further analyses in order to enhance the interpretability of the forthcoming results (Pang et al., 2016). Such dimensionality reductions can be performed using techniques from the field of pattern recognition and machine learning (Bishop, 2006).

Principal component analysis is one of these techniques (Ayesha et al., 2020; Bishop, 2006; Pang et al., 2016). It is rather well known and often used by the neuroimaging community (Finn & Bandettini, 2021; Thirion et al., 2014; Zhan et al., 2015). It aims to construct a set of mutually orthogonal axes within the feature space of the dataset, where each subsequent axis is a linear combination of the original variables and explains as much as possible of the remaining variance in the data (Hotelling, 1936; Pearson, 1901; Stewart, 1992); see Fig. 2.5 for an illustration. This goal is achieved by calculating the covariance matrix for the dataset and subsequently determining and normalizing the eigenvalues and eigenvectors of that matrix (Bishop, 2006). In one of the studies of this thesis, this is done numerically by making use of the relationship between singular value decomposition and principal component analysis; see Wall et al. (2003) and Chapter 3 for details. Ultimately, the actual reduction of the dimensionality is then attained by only considering the first (few) principal component(s) in further analyses (Ayesha et al., 2020; Pang et al., 2016).

2.6 Intraclass correlation

The reliability of a metric essentially characterizes its consistency across different measurements that were performed under similar if not equal conditions. In neuroimaging studies, for instance, the investigation of the reliability of a particular observable often involves the acquisition of data for the same subject at different moments in time (Shehzad et al., 2009; Muldoon et al., 2016; Noble et al., 2017, 2019; Taxali et al., 2021). Then, the intraclass correlation (ICC) can

be used to quantify the reliability of the considered measure, because it may reflect the inter-individual variability of the measure relative to the total variance; see below (Fig. 2.6; Bartko, 1966; G. Chen et al., 2018; Noble et al., 2019; Shrout & Fleiss, 1979). Numerous neuroimaging studies used the ICC to characterize the reliability of the empirical FC derived from fMRI data (Birn et al., 2013; Noble et al., 2017, 2019; Pannunzi et al., 2017; Shehzad et al., 2009; Taxali et al., 2021; Zhang, Baum, et al., 2018). Also the second study of this thesis employs this statistic in order to estimate the reliability of the modeling results (Chapter 4).

Although the ICC has different forms depending on the number of confounds to account for, the second study of this thesis uses its most simple variant characterizing the absolute agreement in the considered metric (G. Chen et al., 2018; Noble et al., 2017, 2019); see Chapter 4 for a justification of this selection. This form of the ICC can be calculated by making use of the analysis of variance (ANOVA) framework (McGraw & Wong, 1996; Shrout & Fleiss, 1979). In this analysis, the observable x is modeled via the relationship

$$x_{s,m} = \mu + a_s + \varepsilon_{s,m}, \tag{2.5}$$

where $x_{s,m}$ is the observable determined using measurement m of subject s, and μ is the mean over all measurements of all subjects. Additionally, a_s is the effect induced in the observable by subject s, and $\varepsilon_{s,m}$ is the residual noise included in the measurement. The ICC reflecting the absolute agreement in x ($ICC(1,1)$) then follows the expression (G. Chen et al., 2018; Noble et al., 2019)

$$ICC(1,1) = \frac{\sigma_a^2}{\sigma_a^2 + \sigma_\varepsilon^2}, \tag{2.6}$$

where σ_a and σ_ε are the "true" standard deviations of a and ε, respectively. These standard deviations and hence the ICC can be estimated from the data at hand using the procedures described in Liljequist et al. (2019), which were also employed in the second study of this thesis (Chapter 4).

Cicchetti & Sparrow (1981) suggested to interpret the ICC either as being "poor" ($ICC(1,1) < 0.40$; Fig. 2.6A), "fair" ($0.40 \leq ICC(1,1) < 0.60$; Fig. 2.6B), "good" ($0.60 \leq ICC(1,1) < 0.75$; Fig. 2.6C) or "excellent" ($ICC(1,1) \geq 0.75$; Fig. 2.6D). These classifications were adopted by

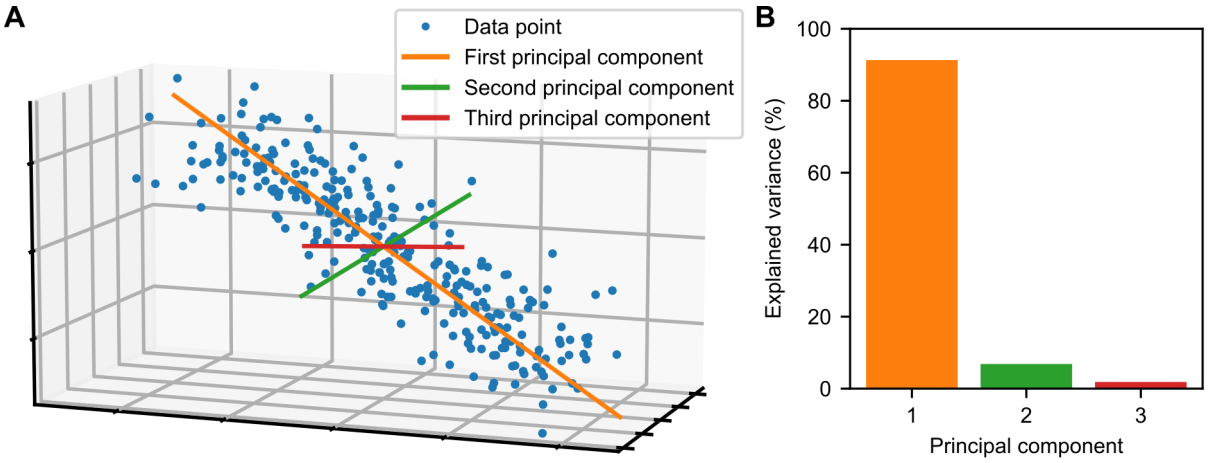

Fig. 2.5. Principal component analysis applied to a three-dimensional toy dataset. **(A)** Individual data points (blue dots) projected in a three-dimensional space. Principal component analysis yields the three (mutually orthogonal) principal components represented by the colored lines. The legend explains the color coding. **(B)** Percentages of variance explained by the individual principal components shown in panel A. In order to reduce the dimensionality of the depicted dataset, only the first principal component could be considered in further analyses since it explains most of the variance in the data (>90%).

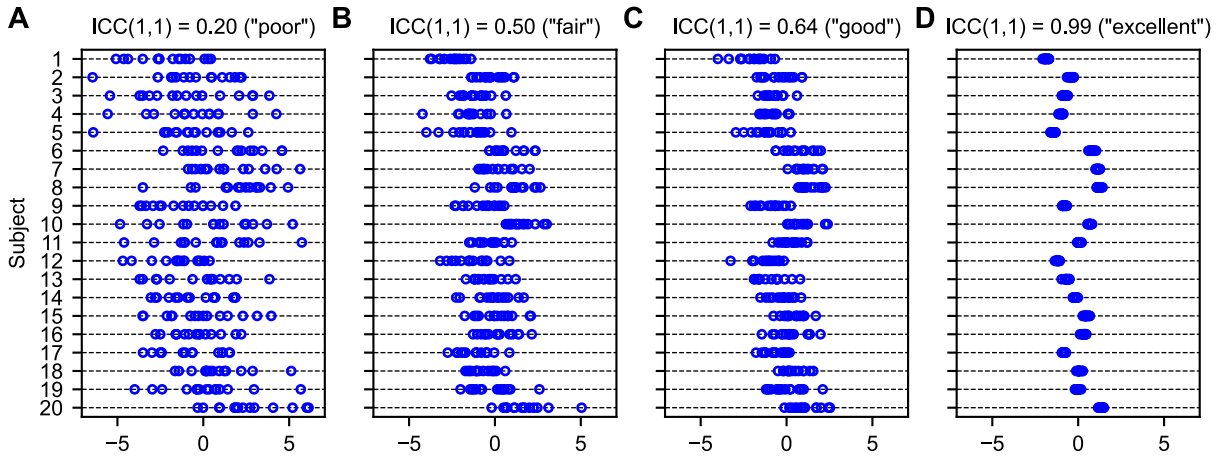

Fig. 2.6. Illustration of the concept behind the intraclass correlation (ICC). For each panel, a toy data set was generated that comprised 20 subjects, which all had 15 measurements of a hypothetical quantity. The subject means are the same for all panels, and were sampled from a Gaussian distribution with a mean of zero and a standard deviation of $\sigma_a = 1.00$. The individual measurements were sampled using those subject means and a residual standard deviation of (A) $\sigma_\varepsilon = 2.00$, (B) $\sigma_\varepsilon = 1.00$, (C) $\sigma_\varepsilon = 0.75$ and (D) $\sigma_\varepsilon = 0.10$. Individual measurements are plotted as blue circles. The titles display the ICCs associated with the individual panels as calculated through Eq. 2.6.

the second study of this thesis as well (Chapter 4). Nonetheless, another interpretation has been proposed by Koo & Li (2016).

Chapter 3

Study 1: Parcellation-induced variation of empirical and simulated brain connectomes at group and subject levels

Justin W. M. Domhof [1,2], Kyesam Jung [1,2], Simon B. Eickhoff [1,2] and Oleksandr V. Popovych [1,2]

[1]Institute of Neuroscience and Medicine, Brain and Behaviour (INM-7), Research Centre Jülich, Jülich, Germany
[2]Institute for Systems Neuroscience, Medical Faculty, Heinrich Heine University Düsseldorf, Düsseldorf, Germany

First published in Network Neuroscience (2021; https://doi.org/10.1162/netn_a_00202)
under a Creative Commons Attribution 4.0 International License (CC BY 4.0)
© 2021 Massachusetts Institute of Technology

Own contributions according to CRediT (70%):

- **Conceptualization** (design of the study)
- **Data curation** (data management)
- **Formal analysis** (analysis of modeling results and their relation with network properties)
- **Investigation** (reconstruction of connectomes and acquisition of results)
- **Methodology** (inventory of models and graph-theoretical measures to consider)
- **Software** (implementation of computational procedures)
- **Validation** (comparison of results with the literature)
- **Visualization** (design of figures)
- **Writing - original draft**
- **Writing - review and editing**

Abstract

Recent developments of whole-brain models have demonstrated their potential when investigating resting-state brain activity. However, it has not been systematically investigated how alternating derivations of the empirical structural and functional connectivity, serving as the model input, from MRI data influence modeling results. Here, we study the influence from one major element: the brain parcellation scheme that reduces the dimensionality of brain networks by grouping thousands of voxels into a few hundred brain regions. We show graph-theoretical statistics derived from the empirical data and modeling results exhibiting a high heterogeneity across parcellations. Furthermore, the network properties of empirical brain connectomes explain the lion's share of the variance in the modeling results with respect to the parcellation variation. Such a clear-cut relationship is not observed at the subject-resolved level per parcellation. Finally, the graph-theoretical statistics of the simulated connectome correlate with those of the empirical functional connectivity across parcellations. However, this relation is not one-to-one, and its precision can vary between models. Our results imply that network properties of both empirical connectomes can explain the goodness-of-fit of whole-brain models to empirical data at a global group but not a single-subject level, which provides further insights into the personalization of whole-brain models.

3.1 Introduction

The structure-function relationship in the human brain has been a topic of interest in many neuroimaging studies (Suárez et al., 2020). Here, the structural connectivity (SC) and functional connectivity (FC), which reflect the physical connections and patterns of synchronized coactivation throughout the brain, respectively, do not exhibit a perfect association (Honey et al., 2009). One effort to close this gap in the structure-function relationship involves the employment of dynamical whole-brain models that use SC as prior knowledge to simulate resting-state brain activity (Honey et al., 2009). These models indeed successfully explain an additional amount of variance beyond the direct comparison of SC and FC (Honey et al., 2009). They also demonstrate that the brain at rest operates at a state of maximal metastability (Deco et al., 2017). Other studies even suggested that the vast parameter space of the models can be exploited to reproduce resting-state brain activity on a personalized level (Ritter et al., 2013; Sanz-Leon et al., 2015; Zimmermann, Perry, et al., 2018).

Throughout the past decade, the workflow associated with dynamical whole-brain models investigating resting-state brain activity has matured (Bansal et al., 2018; Deco et al., 2011; Popovych et al., 2019). When these models are derived and validated using magnetic resonance imaging (MRI) data, region-based SC and FC are typically calculated from diffusion-weighted MRI (dwMRI) and functional MRI (fMRI) sequences, respectively, so that the computations remain tractable (Bandettini et al., 1992; Kwong et al., 1992; Ogawa et al., 1992; Popovych et al., 2019; Yeh et al., 2021). The reconstruction of these connectomes requires the use of a so-called brain parcellation or brain atlas, which describes which voxels should be included in which brain region. Over the years, many brain atlases have been constructed upon conceptually distinct underpinnings, where each of these methodologies incorporates its own biological knowledge and assumptions (e.g. the number of parcels or *granularity*) into the parcellation (Amunts & Zilles, 2015; Eickhoff, Constable, & Yeo, 2018; Eickhoff, Yeo, & Genon, 2018).

Because region-based SC and FC are reconstructed on the basis of a particular brain parcellation, it to a large extent determines the SC and FC matrices. The used brain parcellation may thus exert a substantial influence on the results of region-based neuroimaging studies. Earlier works examined the influence of parcellations on graph-theoretical measures derived from region-based SC and FC (J. Wang et al., 2009; Zalesky et al., 2010) and on direct SC-FC comparisons (Messé, 2020). The impact of the granularity of a brain atlas on modeling results

was also investigated for the Desikan-Killiany atlas (Desikan et al., 2006) and variations of it, wherein the brain regions were split into a number of smaller subregions (Proix et al., 2016). Nevertheless, a systematic investigation of the influence of the brain parcellation is, to the best of our knowledge, currently lacking when it comes to dynamical whole-brain models replicating resting-state brain activity.

Here, we investigate this influence by using the methodology outlined in Fig. 3.1. We first extracted the SCs and FCs, henceforth referred to as the *empirical SCs* and *empirical FCs*, respectively, from the MRI data of 200 healthy subjects using 19 freely available state-of-the-art brain parcellations (Fig. 3.1, green). We constructed the models corresponding to the SC and two qualitatively different models for the local dynamics of individual brain regions that were based on phase oscillators and a neural mass model (Fig. 3.1, blue). By comparing between the two models, we could evaluate whether any observed effects were model-dependent. The resting-state brain activity was individually simulated for every combination of parcellation, model and subject. Then FCs were derived from the simulated brain activity, which will henceforth be referred to as *simulated FCs*. The correlations between the simulated and empirical FCs were calculated and maximized through model parameter variations to quantify how well the models could reproduce the empirical FCs (Fig. 3.1, blue). Finally, we compared the maximized correlations or *goodness-of-fits* with graph-theoretical measures calculated from the empirical SC and FC (Fig. 3.1, red and orange), so that any observation regarding the modeling results could be interpreted in terms of the properties of the empirical networks used to construct and validate our models.

We found large deviations in the goodness-of-fit as brain parcellations vary. In addition, most of the group-averaged interparcellation variance in the goodness-of-fit could be attributed to variations in the graph-theoretical metrics. Such a well-pronounced relationship was practically absent when we considered within-parcellation, interindividual differences. Finally, we show that the models (inaccurately) map the empirical SC to a simulated functional network that has similar network properties as the empirical FC. Our investigation therefore illustrates how the results produced by a dynamical whole-brain modeling workflow are influenced by the brain parcellation, and reveals some of its current limitations and open issues. The reported results are relevant when considering personalized models of resting-state brain dynamics in the framework of precision medicine.

3.2 Materials and methods

In this study, we systematically investigated the influence of the brain atlas on the validation of dynamical whole-brain models by using the methodology outlined in Fig. 3.1. First, we extracted the empirical SC and FC matrices corresponding to a particular parcellation from the dwMRI and fMRI data, respectively (Fig. 3.1, green). The result of the empirical SC reconstruction comprised two matrices: one with the number of streamlines and one with the average length of the streamlines between each pair of brain regions, which are referred to as the actual structural connectivities (SCs) and the path lengths (PLs), respectively. The empirical FC matrix contained the Pearson correlation coefficients across the BOLD response time series extracted from the fMRI data.

Subsequently, the empirical SC and PL matrices were fed to the model as prior knowledge, while the empirical FC matrix was compared with the simulated FC matrix produced by the model simulations (Fig. 3.1, blue). Two models (a phase oscillator and a neural mass model) were used for the acquisition of the simulation results, and we simulated both models for a broad range of global parameter settings to maximize the fit between the empirical and simulated FC. We also extracted some graph-theoretical metrics from the empirical SC and PL and the empirical and simulated FC matrices (Fig. 3.1, red). To be specific, we determined the degree distribution

and the modularity of the empirical SC and both types of FC to characterize their centrality and segregation, respectively. In addition, we calculated the closeness centrality distribution and the global efficiency of the PL matrix as representations of its centrality and integration, respectively. The latter two metrics calculated from the PL matrix are based on the streamline path lengths between brain regions and allow a natural interpretability of the obtained quantities (see below). Furthermore, we calculated the clustering coefficients from the empirical SC and FC and the characteristic path lengths from the empirical PL and FC matrices. These latter two metrics can also be used to compare our results with the literature investigating the influence of the brain parcellation on graph-theoretical metrics extracted from empirical SC and FC (J. Wang et al., 2009; Zalesky et al., 2010).

Finally, we sought to find correlations between the model simulation results and the extracted graph-theoretical metrics using univariate and multivariate regression approaches (Fig. 3.1, orange). In the remainder of this section, we discuss the procedures employed at each step in detail. The source code of our analyses and connectome data have been made available elsewhere (https://jugit.fz-juelich.de/inm7/public/parcellation-modelling and https://doi.org/10.25493/81EV-ZVT; J. W. M. Domhof et al., 2021; J. Domhof, 2021).

3.2.1 Extraction of empirical connectomes

Empirical connectomes were extracted for 200 (96 males, age 28.5 $\pm$ 3.5 years) healthy, unrelated subjects from the HCP S1200 release dataset (http://www.humanconnectomeproject.org) (Van Essen et al., 2013, 2012) using 19 different brain parcellations. The local ethics committee of the HCP WU-Minn gave its approval for the study and written, informed consent was given by all subjects. Here, we discuss the extraction of empirical SC and PL from dwMRI data and empirical FC from fMRI data, and present the brain atlases for which we extracted the region-based connectomes.

SC extraction from dwMRI

For the extraction of the empirical SC matrices from dwMRI data, we used a workflow developed in-house which consisted of four stages: (1) preprocessing of dwMRI images, (2) calculation

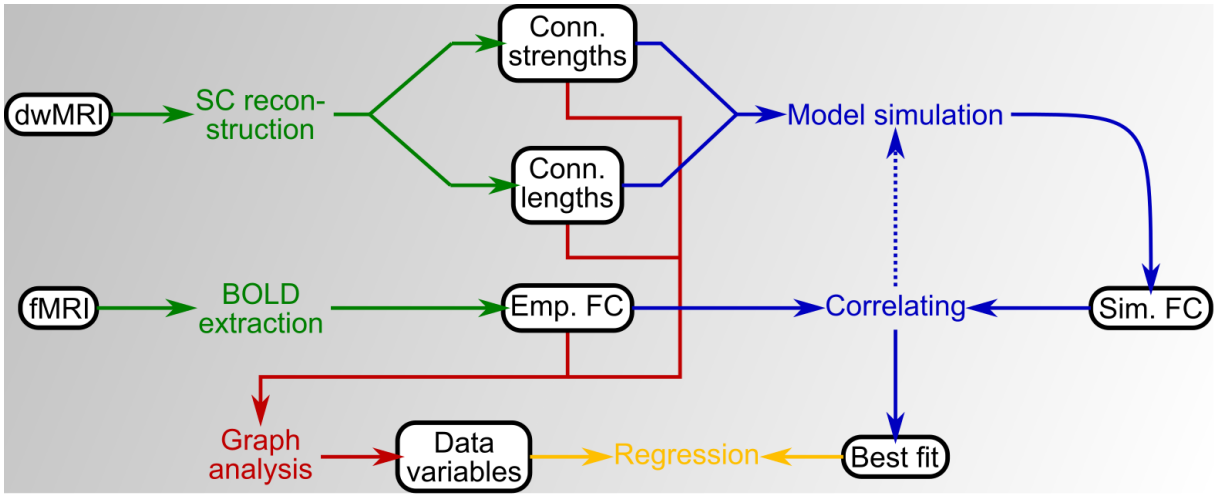

Fig. 3.1. Summary of the methods used in this study. Connectome extraction (green) comprises the construction of the empirical structural (SC) and functional connectivity (FC) from the diffusion-weighted (dwMRI) and functional magnetic resonance imaging (fMRI) data, respectively. Both connectomes serve as input for the modeling stage (blue), where the model parameters are optimized to maximize the correlation between simulated and empirical data (dotted arrow). Graph-theoretical metrics were extracted from the empirical and simulated connectomes (red) and regressed with the model fitting results (orange).

of the whole-brain tractography (WBT), (3) transformation of the atlas images and (4) reconstruction of the empirical SC. The workflow included functions from the ANTs (Tustison et al., 2010), FreeSurfer (Dale et al., 1999), FSL (Jenkinson et al., 2012) and MRtrix3 (Tournier et al., 2019) software packages. Computations were performed on the JURECA high-performance computing cluster (Jülich Supercomputing Centre, 2018).

(1) In the preprocessing stage, we used FreeSurfer functions to perform the following operations on the T1-weighted images: bias field correction, tissue segmentation, cortical (surface) reconstruction, volume-surface conversion, and surface deformation. We also used FreeSurfer functions to correct the dwMRI images with regard to head motions and eddy current distortions, while MRtrix3 functions were employed to denoise them and perform bias field correction. The dwMRI images were then registered to the T1-weighted images using the linear and non-linear transformation functions included in FSL; afterwards, tissue segmentation was performed for these images as well. (2) Subsequently, WBT was calculated using exclusively MRtrix3 functions. A multi-shell, multi-tissue constrained algorithm (Jeurissen et al., 2014) estimated the response functions for spherical deconvolution, which were subsequently used to determine the fiber-oriented distributions from the dwMRI data. The WBT was then completed through a second-order integration over the fiber-oriented distributions using a probabilistic algorithm (Tournier et al., 2010), where we used 10M streamlines and the following other tracking parameter settings: step size = 0.625 mm, angle = 45^{o}, min. length = 2.5 mm, max. length = 250 mm, FOD amplitude for terminating tract = 0.06, max. attempts per seed = 50, max. number of sampling trials = 1000, and down-sampling = 3 mm. (3) Next, the images of the brain atlases used in this study (see below) were linearly and non-linearly transformed from the standard space (in which they were all sampled) to the native space using FSL functions. (4) Finally, we reconstructed the empirical SCs and PLs for all pairs of parcels included in a particular parcellation by using the MRtrix3 function `tck2connectome`.

FC extraction from fMRI

To construct the empirical FC matrix, BOLD signals of the resting-state brain activity were first extracted from fMRI data that were preprocessed using the ICA-FIX approach as provided by the HCP repository (Griffanti et al., 2014), which eliminated the motion parameter but not the global signal effect from the images. Here, the brain atlas images were used to calculate the mean voxel intensity across each parcel per volume resulting in one BOLD signal time series per parcel. Individual time series were linearly detrended and z-scored before we constructed the empirical FC matrix by calculating the Pearson correlation coefficients across the time series for each pair of parcels. Four resting-state fMRI sessions were available in the HCP dataset for every subject (two phase encoding directions scanned on two days), each one comprising 1,200 volumes sampled with a repetition time of 720 ms. We thus calculated four different empirical FCs per subject that were used for the validation of our models.

Brain parcellations

In our study, we performed the whole workflow outlined in Fig. 3.1 for the 19 parcellations included in Table 3.1. As the aim of this study is to compare the modeling results for a variety of brain atlases, we ensured their comparability such that only cortical areas were considered and that all parcellations had similar volumes and were sampled to the MNI152 non-linear template space (Grabner et al., 2006). For more details on the preprocessing of the used atlases; see the Supplementary method.

3.2.2 Graph-theoretical analysis of empirical connectomes

The empirical SC, PL and both the empirical and simulated FC matrices were subjected to graph-theoretical analyses in order to extract data variables portraying the properties of the

networks they represent. In these analyses, the connectivity matrices represented a (network) graph in which the brain regions were the nodes and the individual matrix elements were undirected weighted edges between them. Since self-connections inferred from the empirical SC and FC extraction procedures did not influence the model simulation results (see below), we removed them from the connectivity matrices prior to the graph-theoretical analyses by setting their diagonal elements to 0. From the empirical SC and both types of FC matrices, we extracted the (weighted) degree distribution and the modularity. We selected these measures because they characterized respectively the network centrality and segregation (Rubinov & Sporns, 2010) when only the signal transmission efficiencies within the network were taken into account. The PL matrix may also provide information about the network properties from the point of view of signal transmission latencies. Here, we used the closeness centrality distribution and the global efficiency as indicators of network centrality and integration, respectively.

The degree for empirical SC and both types of FC and closeness centrality for empirical PL indicate how strongly and how quickly a node may influence the network dynamics, respectively. Accordingly, the global efficiency describes (for empirical PL) how quickly signals may be integrated throughout the network, and the modularity portrays (for empirical SC and both types of FC) to what extent the network is segregated into separate modules that have many or strong

Table 3.1. Overview of the used brain parcellation schemes with the index for reference in this study, the number of parcels after image processing, and associated publications. In addition to this table, we have included a Supplementary data sheet that includes (a number of statistics of) the connectomes that were extracted through the use of these parcellations.

Index	Name	No. of parcels	Refs.
1	MIST	31	Urchs et al. (2019)
2		56	
3		103	
4		167	
5	Craddock	38	Craddock et al. (2012)
6		56	
7		108	
8		160	
9	Shen 2013	79	Shen et al. (2013)
10		156	
11	Schaefer	100	Schaefer et al. (2018)
12		200	
13	Harvard-Oxford	48	Frazier et al. (2005); Desikan et al. (2006); Makris et al. (2006); Goldstein et al. (2007)
14		96	
15	Desikan-Killiany	70	Desikan et al. (2006)
16	von Economo-Koskinas	86	von Economo & Koskinas (1925); Scholtens et al. (2018)
17	AAL (version 2)	92	Tzourio-Mazoyer et al. (2002); Rolls et al. (2015)
18	Destrieux	150	Destrieux et al. (2010)
19	Brainnetome	210	Fan et al. (2016)

intramodular and few or weak intermodular connections.

Besides the modularity and the global efficiency, we also calculated the clustering coefficient as a measure of segregation from the empirical SC and FC and the characteristic path length as a measure of integration from the empirical PL and FC matrices. Even though the modularity and global efficiency are more state-of-the-art techniques, the calculation of the clustering coefficient and characteristic path length enabled the comparison of our study with the literature investigating the influence of the brain parcellation on the graph-theoretical measures of empirical SC and FC (J. Wang et al., 2009; Zalesky et al., 2010).

In the remainder of this section, we explain in detail how and why these particular metrics were calculated. Any calculations were carried out using the Python programming language (Python Software Foundation, https://www.python.org/) in combination with the SciPy (Virtanen et al., 2020), NumPy (van der Walt et al., 2011) and NetworkX (Hagberg et al., 2008) modules.

Degree distribution

Let a symmetric $N \times N$ coupling matrix $\mathbf{W}$ determine how the N network nodes are connected by undirected, weighted edges. Here, the assumption of symmetry is justified because the empirical SC and empirical and simulated FC matrices inferred from WBT and (simulated) BOLD signal time series correlations, respectively, are symmetric as well. The degree d_j of node j can be calculated by taking the sum over the j^{th} row of $\mathbf{W}$ leading to N values for the entire network corresponding to the number of parcels included in the used brain parcellation. We actually used the degree as opposed to other measures of centrality because of this simple summation: It makes the degree distribution easy to calculate and straightforwardly interpretable with respect to the neurobiology of the brain (Rubinov & Sporns, 2010). The degrees could be directly calculated from the empirical SC matrices. The empirical and simulated FCs were first thresholded at 0, and the Fisher Z-transforms (Fisher, 1921, 1915) of the positive elements were subsequently calculated before determining the degrees.

To compare the degree distributions across parcellations, we fitted them to the gamma ($\mathrm{Gamma}(x|k,\theta)$) parametric probability distribution. The gamma distribution is defined for positive real numbers ($x > 0$) by the following equation:

$$\mathrm{Gamma}(x|k,\theta) = \frac{1}{\theta^k \Gamma(k)} x^{k-1} \exp\left(-\frac{x}{\theta}\right), \tag{3.1}$$

where $\Gamma(x)$ represents the gamma function and k and θ are free parameters commonly referred to as the shape and scale parameter, respectively. The former determines to what extent the distribution function has a shape resembling an exponential decay or a bell curve, and the latter scales the probabilities with respect to the x-axis (see Fig. S3.1 in the Supplementary Results for an illustration). The fitting result for SC and FC matrices comprised the fitted shape and scale parameters denoted by $Degree_{shape}^{SC/FC}$ and $Degree_{scale}^{SC/FC}$, respectively. In addition to these fitted parameters, we also calculated the Kolmogorov-Smirnov statistics between the fitted cumulative gamma distributions and the cumulative empirical degree distributions, and the mean and the standard deviation of the degree.

We used the gamma distribution to characterize the degree distribution for several reasons. First, we acknowledge that the degree can practically assume semi-infinite values because it cannot be smaller than zero for the empirical SC as well as for the thresholded and Fisher Z-transformed empirical and simulated FC. Then, modeling the distribution by the gamma distribution is more applicable to this situation than, for example, by the Gaussian distribution. In particular, the shape parameter of the gamma distribution may reflect the variable concentrations of degrees close to zero that are observed for the different parcellations; see the Supplementary data sheet. Second, studies investigating the influence of the brain parcellation on graph-theoretical measures extracted from empirical SC and FC have used the truncated

power law model to characterize degree distributions (J. Wang et al., 2009; Zalesky et al., 2010). The truncated power law model essentially is an unnormalized version of the gamma distribution (see J. Wang et al., 2009; Zalesky et al., 2010; and Eq. 3.1). Therefore, the parameters of the gamma distribution and the truncated power law model are practically the same. Using the gamma distribution to characterize the degree distribution thus enhances the comparability of our study with the literature. Nevertheless, we deviate from the use of the (unnormalized) truncated power law model as the normalization condition enables the comparison of the fitting errors between the empirical and fitted distributions across parcellations. The latter is our third and final reason to use the gamma distribution to model the degree distributions. In sum, the gamma distribution suits the problem at hand given that the degrees can only assume values larger than or equal to 0. In addition, it enables the comparison of all the fitting results across parcellations, and enhances the comparability of our results with the literature.

Modularity

The modularity of a network was obtained by maximizing its expression (Rubinov & Sporns, 2011):

$$Modularity = \frac{1}{w^+}\sum_{i=1}^{N}\sum_{j=1}^{N}(W_{ij}^+ - e_{ij}^+)\delta_{M_i,M_j} - \frac{1}{w^+ + w^-}\sum_{i=1}^{N}\sum_{j=1}^{N}(W_{ij}^- - e_{ij}^-)\delta_{M_i,M_j}. \tag{3.2}$$

Here i and j both represent the number of a particular network node. Additionally, W_{ij}^+ and W_{ij}^- are the positive and negative elements of $\mathbf{W}$ respectively (i.e. if $W_{ij} > 0$ then $W_{ij}^+ = W_{ij}$ and $W_{ij}^- = 0$; otherwise $W_{ij}^+ = 0$ and $W_{ij}^- = -W_{ij}$). Then $w^\pm$ represents the total sum over $W_{ij}^\pm$, and $e_{ij}^\pm$ is defined by

$$e_{ij}^\pm = \frac{\sum_{j=1}^{N} W_{ij}^\pm \sum_{i=1}^{N} W_{ij}^\pm}{w^\pm}. \tag{3.3}$$

Finally, M_i denotes the module to which node i belongs and δ_{M_i,M_j} is the Kronecker delta, meaning $\delta_{M_i,M_j} = 1$ if $M_i = M_j$ and $\delta_{M_i,M_j} = 0$ otherwise. By changing the modular structure of the network (i.e. changing M_i), the modularity can be maximized. Since evaluating all possible module configurations is too computationally expensive, we used the Louvain algorithm to solve this optimization problem (Blondel et al., 2008).

The modularity was selected from other measures of segregation (e.g. the clustering coefficient and local efficiency) because of its more sophisticated design especially in light of the negative correlations an FC matrix can have (Rubinov & Sporns, 2011, 2010). Additionally, it allows for an in-depth examination of the modular network structure after the maximization has been performed, for instance, to determine the strength of community structure for a given network (Newman & Girvan, 2004).

Closeness centrality

Signals propagating throughout the network from one node to another can traverse several edges that have associated weights representing the cost of crossing them. The minimal cost of traveling between nodes i and j is termed the shortest path length l_{ij}. For the empirical PL matrix, the calculated shortest path length literally estimated the minimal distance that the signals have to cover along the white matter fibers connecting two brain regions. The closeness centrality L_j of node j is then defined as the inverse of the mean shortest path length between that node and all other nodes in the network (Rubinov & Sporns, 2010):

$$L_j = \frac{N-1}{\sum_{i=1}^{N} l_{ij}}, \quad \text{where} \quad l_{ii} = 0. \tag{3.4}$$

We calculated the closeness centrality for all nodes to determine the network's closeness centrality distribution. Subsequently, we fitted this distribution to the gamma probability distri-

bution (Eq. 3.1) because also the closeness centrality could not assume values below 0, which resulted in the fitted gamma distribution shape and scale parameters denoted by $Centr._{shape}^{PL}$ and $Centr._{scale}^{PL}$, respectively. Just as with the degree distribution, we also calculated the Kolmogorov-Smirnov statistics between the fitted cumulative gamma distributions and the cumulative empirical closeness centrality distributions, and the mean and the standard deviation of the closeness centrality.

Also the degree or betweenness centrality could have been used to analyze the empirical PL matrix (Rubinov & Sporns, 2010). Nevertheless, we selected the closeness centrality as opposed to these alternatives. The degree calculated on the basis of the empirical PL does not have the same neurobiological interpretation as with the empirical SC and both types of FC (see above). The betweenness centrality has the disadvantage that it discards any information about the shortest path lengths themselves (Rubinov & Sporns, 2010).

Global efficiency

The global efficiency of a network was also defined in terms of the shortest path lengths (Rubinov & Sporns, 2010):

$$Efficiency = \frac{1}{N}\sum_{i=1}^{N}\frac{\sum_{j=1}^{N} l_{ij}^{-1}}{N-1}, \quad \text{where} \quad l_{ii} = 0. \tag{3.5}$$

It can thus be interpreted as the mean of the inverted shortest path lengths across all pairs of network nodes. An alternative measure of integration is the characteristic path length (Rubinov & Sporns, 2010), but it has been argued that global efficiency may be superior when investigating brain networks (Achard & Bullmore, 2007).

Clustering coefficient

For weighted graphs, which we consider in our study, several variants of the clustering coefficient exist. We use the expression of the clustering coefficient proposed by Onnela et al. (2005):

$$Cluster = \frac{1}{N}\sum_{i=1}^{N}\frac{\sum_{j=1}^{N}\sum_{k=1}^{N}(\hat{W}_{ij}\hat{W}_{ik}\hat{W}_{jk})^{1/3}}{d_i(d_i-1)}. \tag{3.6}$$

Here, $\hat{W}_{ij} = W_{ij}/\max(\mathbf{W})$ are the elements of the connectivity matrix normalized by their maximum and d_i represents the degree of node i.

The clustering coefficient is a rather simple measure of segregation and its expression has not been optimized for FC matrices. Therefore, we consider the modularity to be a more accurate statistic for network segregation. Nevertheless, as previous work studying the influence of brain parcellations on graph-theoretical measures extracted from empirical connectomes included this measure (J. Wang et al., 2009; Zalesky et al., 2010), we have added it to our calculations. We calculated the clustering coefficient from the empirical SC matrix and from the thresholded and Fisher's Z-transformed empirical FC matrix (see also the case with the degree).

Characteristic path length

The characteristic path length is obtained by averaging the shortest path length across all pairs of nodes (Rubinov & Sporns, 2010):

$$Char.\,PL = \frac{1}{N}\sum_{i=1}^{N}\frac{\sum_{j=1}^{N} l_{ij}}{N-1}, \quad \text{where} \quad l_{ii} = 0 \tag{3.7}$$

Analogous to the modularity and the clustering coefficient describing the network segregation, the global efficiency and the characteristic path length are both measures of network integration. As mentioned above, the global efficiency is superior in brain network research (Achard

& Bullmore, 2007). However, we also included the characteristic path length to ameliorate the comparability of our work with other studies investigating the influence of the brain parcellation on region-based SC and FC by means of this metric (J. Wang et al., 2009; Zalesky et al., 2010). We calculated the characteristic path length associated with the structural connectivity by using the PL matrix. For the functional connectivity we used the thresholded and Fisher Z-transformed empirical FC matrix with inverted elements. The latter inversion was done after the Z-transformation to convert the functional association strengths to estimations of the link lengths, where link strengths and lengths are inversely related (Rubinov & Sporns, 2010).

3.2.3 Model simulations

In the modeling stage of our workflow, the brain was once again seen as a network of brain regions (network nodes) parcellated according to a given brain atlas. We subsequently used a system of coupled oscillators to model the collective dynamics of the mean-field activities of the individual brain regions. The coupling between network nodes was defined by the extracted empirical SC, where the SC matrix determined how strongly one region influenced the other. The PL matrix was used to evaluate the latency in the signal propagation between the nodes. By simulating the dynamics of the whole-brain models, we sampled the activity time series of the N nodes included in the network. We subsequently correlated these time series with one another and constructed a simulated FC matrix. Finally, the similarity between the simulated and the empirical FC matrices was quantified by vectorizing the upper triangular parts of both matrices excluding the diagonal and subsequently calculating the Pearson correlation coefficient between the resulting two vectors. By exploring the parameter space of the model via a grid search, the maximal similarity between the empirical and simulated FC matrices could be found, which is henceforth also referred to as the *goodness-of-fit* of the model.

In this study, we modeled the local dynamics of the brain regions from different perspectives by considering two different models. The first model was the Kuramoto system of coupled phase oscillators (Kuramoto, 1984), and the other was an ensemble of Wilson-Cowan type neural mass models (Wilson & Cowan, 1972). These two models were chosen because of their major conceptual differences, which increased the likelihood of finding cross-model deviations. These models have also been used in previous studies investigating the brain's structure-function relationship by dynamical whole-brain models (Deco et al., 2009; Messé et al., 2014; Ponce-Alvarez et al., 2015).

Phase oscillator model

In the Kuramoto model (Kuramoto, 1984), the mean-field activity of brain region $i \in \{1, 2, ..., N\}$ (N is the number of brain regions in a given parcellation) is assumed to oscillate with a region-specific frequency f_i, and the dynamics of its phase $\varphi_i(t)$ are governed by the differential equation

$$\dot{\varphi}_i(t) = 2\pi f_i + \sum_{j=1}^{N} C_{ij} \sin(\varphi_j(t - \tau_{ij}) - \varphi_i(t)) + \sigma_p \nu_i(t). \tag{3.8}$$

Here $\nu_i(t)$ is independent Gaussian white noise with zero mean and unit variance, and $\sigma_p = 0.17$ is the noise intensity. Furthermore, C_{ij} and τ_{ij} represent the individual coupling strength and delay values between brain regions, respectively. These were derived from the empirical SC and PL matrices via

$$C_{ij} = \begin{cases} 0 & \text{if } i = j \\ G \cdot \frac{\mathrm{SC}_{ij}}{N\langle \mathbf{SC} \rangle} & \text{otherwise} \end{cases} \quad \text{and} \quad \tau_{ij} = \begin{cases} 0 & \text{if } i = j \\ \tau \cdot \frac{\mathrm{PL}_{ij}}{\langle \mathbf{PL} \rangle} & \text{otherwise} \end{cases}. \tag{3.9}$$

Here, the operator $\langle \cdot \rangle$ returns the mean over all elements of the matrix, and G and τ are scaling factors referred to as the global coupling and global delay.

Although the Kuramoto model has been used in different paradigms in relation to large-scale whole-brain models (e.g., Messé et al., 2014 vs. Ponce-Alvarez et al., 2015), we adopted the approach wherein the ultra slow phase dynamics of the BOLD signals was directly modeled by $\varphi_i(t)$. Then the simulated BOLD signals $\cos(\varphi_i(t))$ were used for the calculation of the simulated FC matrix. The region-specific oscillation frequencies f_i in the range [0.01, 0.1] Hz were derived from the empirical BOLD signal time series via spectral density estimation. For this analysis, we subjected those signals to Welch's method (`welch` function implemented in the SciPy module; Virtanen et al., 2020) while using a 1,024 time points long Hamming window function with 95% (972 time points) overlap between segments. We used the frequencies corresponding to the largest peaks in the spectra and heterogenized them a little by adding Gaussian white noise with zero mean and 0.002 Hz standard deviation. Finally, G and τ were considered to be free parameters and were optimized in order to maximize the similarity between empirical and simulated FC.

Neural mass model

The neural mass model used in this study was a Wilson-Cowan model (Wilson & Cowan, 1972) adapted from the paper by Deco et al. (2009). It models the interaction between the excitatory and inhibitory neuron ensembles of the i^{th} brain region, where their mean firing rates $E_i(t)$ and $I_i(t)$, that is, the proportion of cells firing within a unit of time, respectively, are modeled via the following coupled differential equations:

$$\mu_E \dot{E}_i(t) = -E_i(t) + \kappa \mathcal{S}\left(\sum_{j=1}^{N} C_{ij} E_j(t-\tau_{ij}) - c_{EI} I_i(t) + I_b\right) + \sigma_n \nu_i(t) \quad \text{and} \tag{3.10}$$

$$\mu_I \dot{I}_i(t) = -I_i(t) + \kappa \mathcal{S}\left(c_{IE} E_i(t)\right) + \sigma_n \nu_i(t). \tag{3.11}$$

In these equations, μ_E and μ_I are the decay time constants of the excitatory and inhibitory activity, respectively. Both populations received the same zero-mean, independent Gaussian white noise of intensity σ_n. Parameters c_{EI} and c_{IE} regulate the inhibition of the excitatory cells by the inhibitory pool and the excitation of the inhibitory cells by the excitatory pool, respectively. $\mathcal{S}(x)$ is a sigmoid function defined by

$$\mathcal{S}(x) = \frac{1}{1+\exp(-\lambda(x-\gamma))} - \frac{1}{1+\exp(\lambda\gamma)}, \tag{3.12}$$

where λ and γ determine its width and the position of its inflexion point, respectively. Additionally, I_b is a constant external input to the excitatory neurons, and $\kappa = (1+\exp(\lambda\gamma)) \,/\, \exp(\lambda\gamma)$ scales $\mathcal{S}(x)$ such that $\kappa\mathcal{S}(x) = 1$ as $x \to \infty$. Finally, C_{ij} and τ_{ij} have the same interpretations and similar associated expressions as with the Kuramoto model (Eq. 3.9):

$$C_{ij} = \begin{cases} c_{EE} & \text{if } i = j \\ G \cdot \frac{\mathrm{SC}_{ij}}{N\langle \mathbf{SC} \rangle} & \text{otherwise} \end{cases} \quad \text{and} \quad \tau_{ij} = \begin{cases} 0 & \text{if } i = j \\ \tau \cdot \frac{\mathrm{PL}_{ij}}{\langle \mathbf{PL} \rangle} & \text{otherwise} \end{cases}, \tag{3.13}$$

where c_{EE} is a parameter scaling the self-excitation of the excitatory pool.

We set the model parameters to the values listed in Table 3.2. As for the Kuramoto model, parameters G and τ were regarded as free parameters and were varied to maximize the simi-

Table 3.2. Parameter settings of the neural mass model.

Parameter	Value	Parameter	Value	Parameter	Value
μ_E	20 ms	λ	20.000	c_{EE}	1.000
μ_I	20 ms	γ	0.300	c_{EI}	1.500
I_b	0.100	σ_n	0.002	c_{IE}	0.600

larity between the empirical and simulated FC matrix. The considered parameter configurations resulted in a low activity state of disconnected nodes ($G = 0$) and generation of limit-cycle oscillations with an alpha-band frequency when the individual regions were coupled ($G > 0$). The modeled alpha oscillations have been shown to be dominant in EEG of human resting-state brain activity (Fraga González et al., 2018; Spitoni et al., 2013) and to interact with BOLD responses (Mayhew et al., 2013).

Simulating the neural mass model yielded neuronal signal time series that are not directly comparable with the empirical BOLD responses extracted from fMRI data. To account for this, the neuronal signals of the excitatory pool were converted to BOLD responses by the Balloon-Windkessel model from Friston et al. (2003), a procedure that has also been used elsewhere (Havlicek et al., 2015). The resulting (simulated) BOLD signals were subsequently used to construct the simulated FC matrix.

Implementation, simulation and parameter variation

The Python (Python Software Foundation, https://www.python.org/) and C++ (Standard C++ Foundation, https://isocpp.org/) programming languages were selected for the implementation of the model simulations; here, we also used the SciPy (Virtanen et al., 2020) and Numpy (van der Walt et al., 2011) modules. Simulation and analysis computations were carried out on the JURECA high-performance computing cluster (Jülich Supercomputing Centre, 2018). The temporal integration of both models as well as the neuronal to BOLD signal conversion followed Heun's method. For both models, we optimized the free parameters by simulating the models using a dense grid of 64 $\times$ 48 parameter points for the global coupling and delay, respectively, and subsequently selecting the parameters maximizing the correlation between the empirical and simulated FC (goodness-of-fit). Regarding the phase oscillator model, the global coupling and delay were varied using $G \in \{0.000, 0.015, 0.030, ..., 0.945\}$ and $\tau \in \{0\ \mathrm{s}, 1\ \mathrm{s}, 2\ \mathrm{s}, ..., 47\ \mathrm{s}\}$. For every parameter setting, we then simulated 70 min of network dynamics with a 60-ms integration time step and disregarded the first 10 min so that the initial conditions did not influence the results. For the neural mass model we used $G \in \{0.000, 0.018, 0.036, ..., 1.134\}$ and $\tau \in \{0.0\ \mathrm{ms}, 1.5\ \mathrm{ms}, 3.0\ \mathrm{ms}, ..., 70.5\ \mathrm{ms}\}$ for the global coupling and delay, sampled 510 s of network activity with an integration step size of 2 ms and removed the first 150 s prior to analysis. The differences in the simulation parameters (simulated time and integration time step size) between both models were adapted to the ultra-slow timescale and alpha frequency oscillations of the phase oscillators and the neural mass model, respectively. The simulations above were performed individually for each combination of the 200 subjects, the 2 models and the 19 considered parcellations listed in Table 3.1.

3.2.4 Analysis

Analysis of interparcellation variations

We observed differences across brain parcellations when examining the graph-theoretical measures and goodness-of-fit. We determined whether these deviations were consistent across subjects; in other words, we assessed whether altering the parcellation changes the patterns of the values across all subjects. To this end, we gathered the values of the considered graph-theoretical measure for the individual subjects into separate data vectors for each parcellation and calculated the Pearson correlation coefficient corresponding to each pair of vectors and thus parcellations. The same approach was used to investigate goodness-of-fit correlations across subjects for different models, where separate data vectors were constructed for every combination of brain atlas and model for local dynamics to also assess the effect of the model in this respect.

Then, we studied whether covariations between the graph-theoretical metrics and the goodness-of-fit existed by combining principal component analysis with ordinary least squares re-

gression. We built a dataset with the granularities (number of parcels N), the median values across subjects of 13 considered graph-theoretical measures extracted from the empirical SC, PL and FC matrices and the Pearson correlation coefficient between the empirical SC and empirical FC such that we obtained a 15 $\times$ 19 matrix in which each row was associated with one of those statistics and each column held the values of those metrics for a particular parcellation from Table 3.1. The dataset was z-scored to ensure the comparability of the individual metrics to one another and subsequently decomposed into the scores and loadings corresponding to the principal components (PCs) through the use of singular value decomposition as performed by the `linalg.svd` function in NumPy (van der Walt et al., 2011). Finally, the scores of the PCs were regressed with the median values of the goodness-of-fit across subjects for every brain atlas for both model types separately. Here, we considered both a univariate and multivariate approach, in which we used the scores of only the first PC and those of multiple PCs, respectively, to explain the variance in the goodness-of-fit for varying brain parcellation via ordinary least squares regression.

Detection of within-parcellation, between-subject correlations

We checked whether the covariations found between the group-averaged graph-theoretical measures and the goodness-of-fit across parcellations were also present when considering intraparcellation, interindividual variations. Hence, we investigated whether graph-theoretical metrics could also explain interindividual differences when considering a specific parcellation in isolation. First, we wielded the same approach from the previous paragraph for this investigation. For each brain atlas, we built a 14 $\times$ 800 data matrix, in which each row corresponded to one of the data variables mentioned in the previous paragraph excluding the granularity and each column held the values of these statistics for a specific subject and fMRI session pair. For the HCP dataset used in our study, four resting-state fMRI sessions were available for each subject, which led to the 200 (subjects) $\times$ 4 (fMRI sessions) = 800 columns in the datasets. In order to keep the matrix dimensions the same also for the SC matrices, the same SC characteristics were repeated in the dataset for the individual fMRI sessions per subject. We calculated the z-scored dataset, extracted the first PC and regressed its scores with the goodness-of-fits of the individual subjects.

We also checked whether a multivariate approach could substantially improve the explained interindividual variance in the goodness-of-fit across subjects for a given brain parcellation. To do so, we directly regressed the z-scored dataset with the goodness-of-fits of the individual subjects and sessions via (multivariate) ordinary least squares regression for the two models separately.

3.3 Results

In this study, we investigated the effect of the brain atlas on the goodness-of-fit of dynamical whole-brain models. For this inquiry, we first extracted the empirical SC, PL, and FC matrices from the dwMRI and fMRI data of 200 subjects included in the HCP S1200 release dataset using the 19 parcellations in Table 3.1 and subsequently subjected them to graph-theoretical analyses. Next, we sampled the modeling results associated with those empirical SC and FC matrices for the Kuramoto system (Eq. 3.8 - Eq. 3.9) of coupled phase oscillators (Kuramoto, 1984) and the ensemble (Eq. 3.10 - Eq. 3.13) of Wilson-Cowan type neural mass models (Wilson & Cowan, 1972). Finally, we investigated through principal component analysis and linear regressions whether differences in network properties could explain the variance in modeling results.

3.3.1 Parcellation-induced heterogeneity of empirical connectomes

We found a high variability in the graph-theoretical network properties of the empirical SC for varying parcellations (Fig. 3.2). Note, however, that the shape and scale parameters of the de-

gree distributions of the empirical SC should be considered with some reservation as they may not fully capture all differences in these distributions across parcellations; see Supplementary data sheet. Nevertheless, we on average obtained better fit with the gamma distribution for all approximated network metrics than with the Gaussian distribution.

The shape parameter of the degree distribution of the empirical SC, for instance, had a median value ranging from 1.1 for the von Economo-Koskinas atlas (atlas index 16) to 8.1 for the Craddock parcellation with 56 parcels (atlas index 6) (Fig. 3.2A). Its scale parameters exhibited an opposing trend with respect to the variation of the parcellation when compared to the shape parameters: Relatively large values for the shape parameter were accompanied by relatively small values for the scale parameter when considering an individual atlas (Fig. 3.2B). This opposing trend was also observed for the shape parameter and scale parameters describing the closeness centrality distribution of the empirical PL matrix (Fig. 3.2E-F). The modularities derived from the empirical SC matrix showed an increasing trend when the number of parcels grew (Fig. 3.2C). On the other hand, the clustering coefficients showed an opposing trend (Fig. 3.2D). This is a rather striking observation, because both measures reflect net-

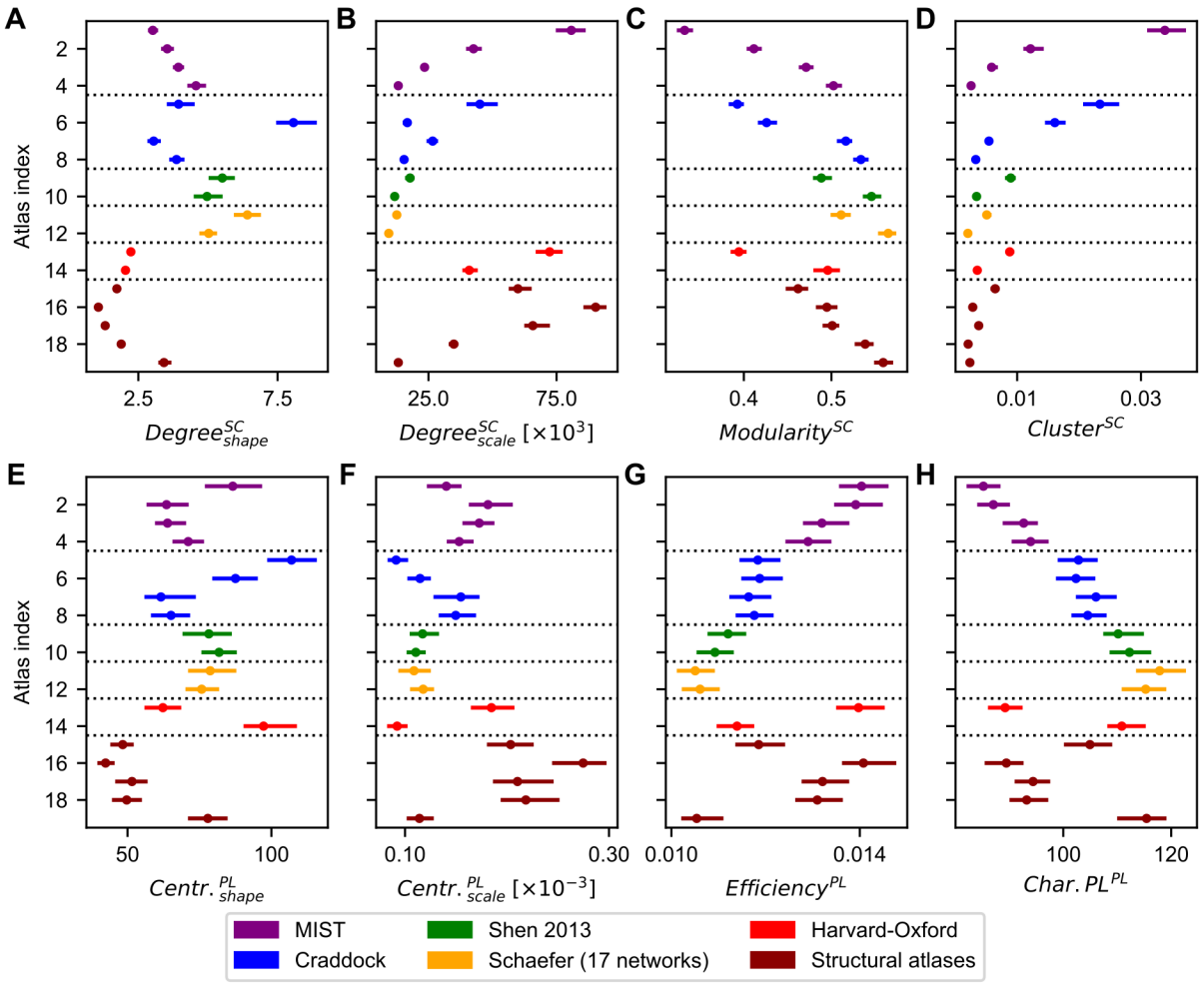

Fig. 3.2. Heterogeneity of graph-theoretical properties of empirical structural networks across parcellations. **(A-D)** Statistics extracted from the structural connectivity (SC) matrices, which are the shape (A) and scale (B) parameters of the degree distributions, the modularities (C) and the clustering coefficients (D). **(E-H)** Statistics extracted from the path length (PL) matrices, which are the shape (E) and scale (F) parameters of the closeness centrality distributions, the global efficiencies (G) and the characteristic path lengths (H). Dots and lines depict the medians and interquartile ranges across subjects, respectively. The atlas indices on the vertical axes correspond to those in Table 3.1 which contains the information about the used parcellations. Abbreviations: Centr. = closeness centrality, Char. PL = characteristic path length.

work segregation. However, the modularity is calculated through a consideration of the entire network (Eq. 3.2), whereas the clustering coefficient is determined on a node-by-node basis (Eq. 3.6). These findings therefore demonstrate that parcellations with higher granularities may yield structural networks that contain more pronounced subnetworks, but have fewer triplets of nodes that are strongly interconnected. The decreasing trend of the (raw) clustering coefficient with increasing granularity was also observed in other studies investigating the empirical SC (Zalesky et al., 2010). Simple dependencies on the granularity were found neither for the parameters of the degree distribution (Fig. 3.2A-B) nor for the graph-theoretical metrics derived from the empirical PL matrix (Fig. 3.2E-H).

Analogous to the modularity and the clustering coefficient, the global efficiency and characteristic path length of the PL matrix also exhibited opposing trends (Fig. 3.2G-H). These opposing trends were expected: Longer characteristic path lengths reflect slower integration of signals throughout the network, which agrees with a lower global efficiency. In addition to the fitted gamma distribution parameters of the degree and closeness centrality distributions shown in Fig. 3.2A-B and Fig. 3.2E-F, respectively, we also calculated the means and standard deviations of the degrees and closeness centralities and the Kolmogorov-Smirnov statistics characterizing the qualities of the gamma distribution fittings; these are included in the Supplementary results (Fig. S3.2A-F).

The shape parameter of the degree distribution of the empirical FC matrix exhibited similar variations across parcellations when compared to its structural counterpart (Fig. 3.2A vs. Fig. 3.3A), though using the Craddock parcellation with 38 parcels (atlas index 5) and the Schaefer parcellation with 100 parcels (atlas index 11) did result in some notably larger values for this statistic (Fig. 3.3A). The scale parameter, on the other hand, seemed to mostly depend on the granularity (number of brain regions) of the parcellations (Fig. 3.3B). Just as with the SC matrix, the modularity and the clustering coefficient of the FC matrix exhibited opposing trends, and again appeared to mostly depend on the granularity (Fig. 3.3C-D). The characteristic path length calculated from the empirical FC did not exhibit such a general trend (Fig. 3.3E). We also calculated

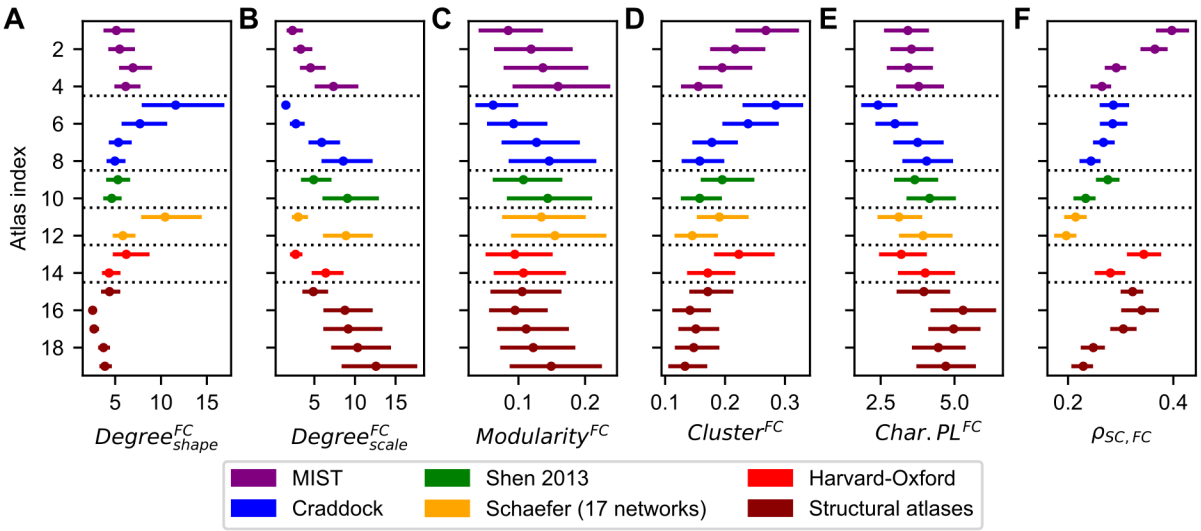

Fig. 3.3. Heterogeneity of graph-theoretical properties of the empirical functional connectivity (FC) across parcellations. **(A-E)** Statistics extracted from the empirical FC matrices, which are the shape (A) and scale (B) parameters of their degree distributions, their modularities (C), their clustering coefficients (D), and their characteristic path lengths (E). **(F)** Pearson correlation coefficients corresponding to the structure-function relationship between the upper triangular parts (excluding diagonal) of the empirical SC and FC matrices. Dots and lines depict the medians and interquartile ranges across subjects, respectively. The atlas indices on the vertical axes correspond to those in Table 3.1, which contains the information about the used parcellations. Abbreviations: Char. PL = characteristic path length.

the strength of the structure-function relationship as given by the Pearson correlation coefficient between the empirical SC and FC matrices ($\rho_{SC,FC}$). It seemed to demonstrate similarities with the scale parameters of the degree distributions of the empirical SC and the scale parameters of the closeness centrality distributions and the global efficiencies of the PL matrix as the parcellation varies (Fig. 3.2B,E,F, Fig. 3.3D).

So far, we observed trends for some graph-theoretical statistics that exhibited large dependencies on the parcellation granularity. We therefore investigated this effect in more detail. The literature shows that (graph-theoretical) statistics extracted from empirical SC and FC may be inversely related to the number of parcels included in a parcellation (Messé, 2020; Zalesky et al., 2010). We therefore plotted the median of each considered measure as a function of the inverted number of parcels for each parcellation, which revealed high dependencies on the granularity for some statistics (Fig. 3.4A-N). Indeed, the modularity and clustering coefficient reflecting the segregation of the empirical SC and FC are highly influenced by the parcellation

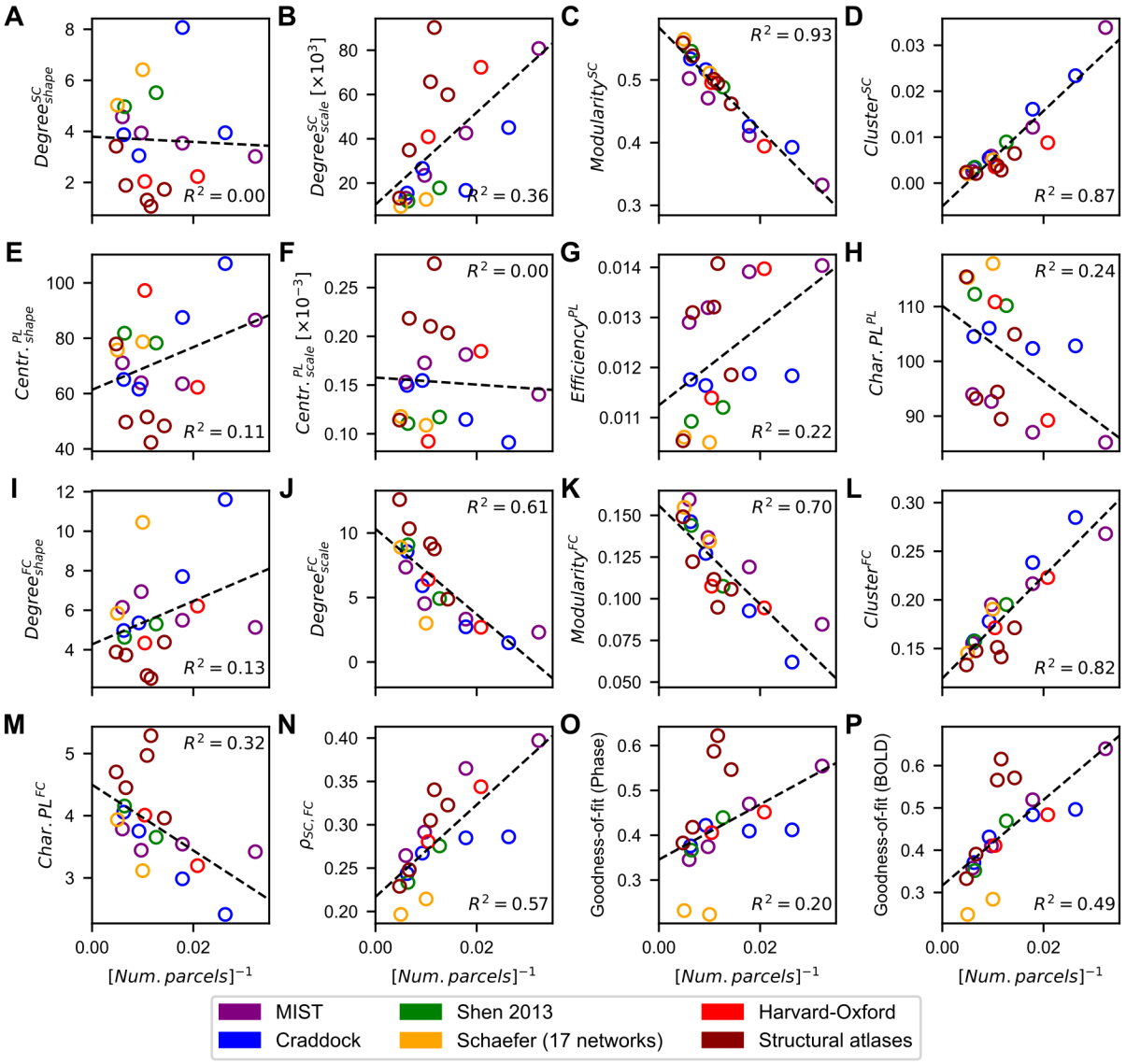

Fig. 3.4. Scatterplots of all the measures shown in Fig. 3.2 (A-H), Fig. 3.3 (I-N) and Fig. 3.6A (O-P) as a function of the inverse of the number of parcels included in the considered parcellations. Each dot corresponds to a particular atlas and the dashed lines show the least squares linear regressions between these points. The coefficients of determination are also displayed in each plot. Abbreviations: Centr. = closeness centrality, Char. PL = characteristic path length, Num. = number of.

granularity (Fig. 3.4C,D,K,L). The structure-function relationship $\rho_{SC,FC}$ is also governed by the number of regions to a large extent (Fig. 3.4N), which is in agreement with the results of Messé (2020). However, most of the other network properties only weakly to moderately correlate with parcellation granularity. In addition to the inverted relationship, we checked whether the granularity effect could be modeled better by a linear dependence on the number of parcels. The opposite was true: A linear treatment of the granularity effect did not lead to higher explained variances, and for many measures it even resulted in lower coefficients of determination.

To investigate how the considered measures depend on the parcellations beyond the granularity effect, we regressed this effect out by fitting the data to an inverse relationship ($y = a/N + b$) and examined the residuals. As expected, the residuals of the modularities and clustering coefficients exhibited differences between brain atlases that had a lower scale than the raw data; see for example Fig. 3.4C,D,K,L vs. Fig. S3.5C,D,K,L in the Supplementary results. The other residuals still exhibited differences across parcellations of the same magnitude; see Fig. S3.3, Fig. S3.4, and Fig. S3.5A-N in the Supplementary results. In sum, even though the granularity of a parcellation can greatly influence some of the network statistics extracted from the empirical data, the observed parcellation-induced deviations typically go beyond such a simple relationship. We further analyze this dependence below (Interparcellation variations of empirical connectomes and modeling results).

Subsequently, we investigated how the graph-theoretical network properties of the individual subjects correlated between each pair of the considered brain atlases; see Materials and methods (Analysis) for details of this analysis. Following this procedure, we evaluated whether the interindividual differences in the empirical network statistics exhibited similar patterns between the parcellations used for the extraction of the empirical connectomes. We found that these correlations were highest for the global efficiency and characteristic path length of the empirical PL matrix (Fig. 3.5D), for the modularity, clustering coefficient and characteristic path length of the empirical FC matrices (Fig. 3.5F,G), and for the correlation between empirical SC and FC (Fig. 3.5G). Such correspondences were generally lower for the parameters of the degree and closeness centrality distributions (Fig. 3.5A,C,E), and the modularity and clustering coefficient of the empirical SC (Fig. 3.5B). These network metrics of the corresponding connectivity matrices are thus sensitive to a selected brain parcellation. At the individual level, network segregation properties of the empirical FC and network integration statistics thus seemed to be influenced much less by the brain parcellation than measures reflecting the centrality and the network segregation of empirical SC.

3.3.2 Parcellation-induced heterogeneity of modeling results

In this section we present the results of the model simulations for all brain atlases in Table 3.1 and the two considered whole-brain models of coupled phase oscillators (Eq. 3.8 - Eq. 3.9) and neural mass models (Eq. 3.10 - Eq. 3.13). For each combination of subject, parcellation and model, the optimal values of the global coupling and delay parameters were found by maximizing the Pearson correlation between the empirical and simulated FC matrices, which provided the goodness-of-fit of the model illustrated in Fig. 3.6A for both models. For varying parcellations we observed a high variability of the fitting results, implying that the extent of correspondence between simulated and empirical FC strongly depended on the selected parcellation. Here, the MIST parcellation with 31 parcels, the Desikan-Killiany atlas, the von Economo-Koskinas atlas, and the AAL atlas yielded the highest goodness-of-fits independently of the model type (Fig. 3.6A, atlas indices 1, 16, 17 and 18, respectively). Interestingly, the interindividual variance of the goodness-of-fit had approximately the same range as the structure-function relationship between the empirical SC and FC matrices (Fig. 3.3). It also appeared as if the patterns of the goodness-of-fit versus parcellations were similar to each other for different models (Fig. 3.6A).

To quantify the mentioned similarity, we considered the medians of the goodness-of-fit calculated over all subjects corresponding to the phase oscillators and regressed them across parcellations with those of the neural mass model. This resulted in a regression with a coefficient of determination of 0.88 (Fig. 3.6C), suggesting a model-independent impact of a given brain parcellation on the (group-averaged) goodness-of-fit. As with the graph-theoretical measures, we investigated the effect of granularity on the goodness-of-fit by plotting its median across subjects against the inverse of the number of parcels included in the parcellations. The corresponding plots exhibited moderate correlations (Fig. 3.4O-P), where the impact of granularity on the fitting results for the phase model is much smaller than that for the neural mass model. To quantify the parcellation-induced influence on the goodness-of-fit beyond the dependence on the granularity, the effect of the (inverted) granularity was regressed out. The residual goodness-of-fits

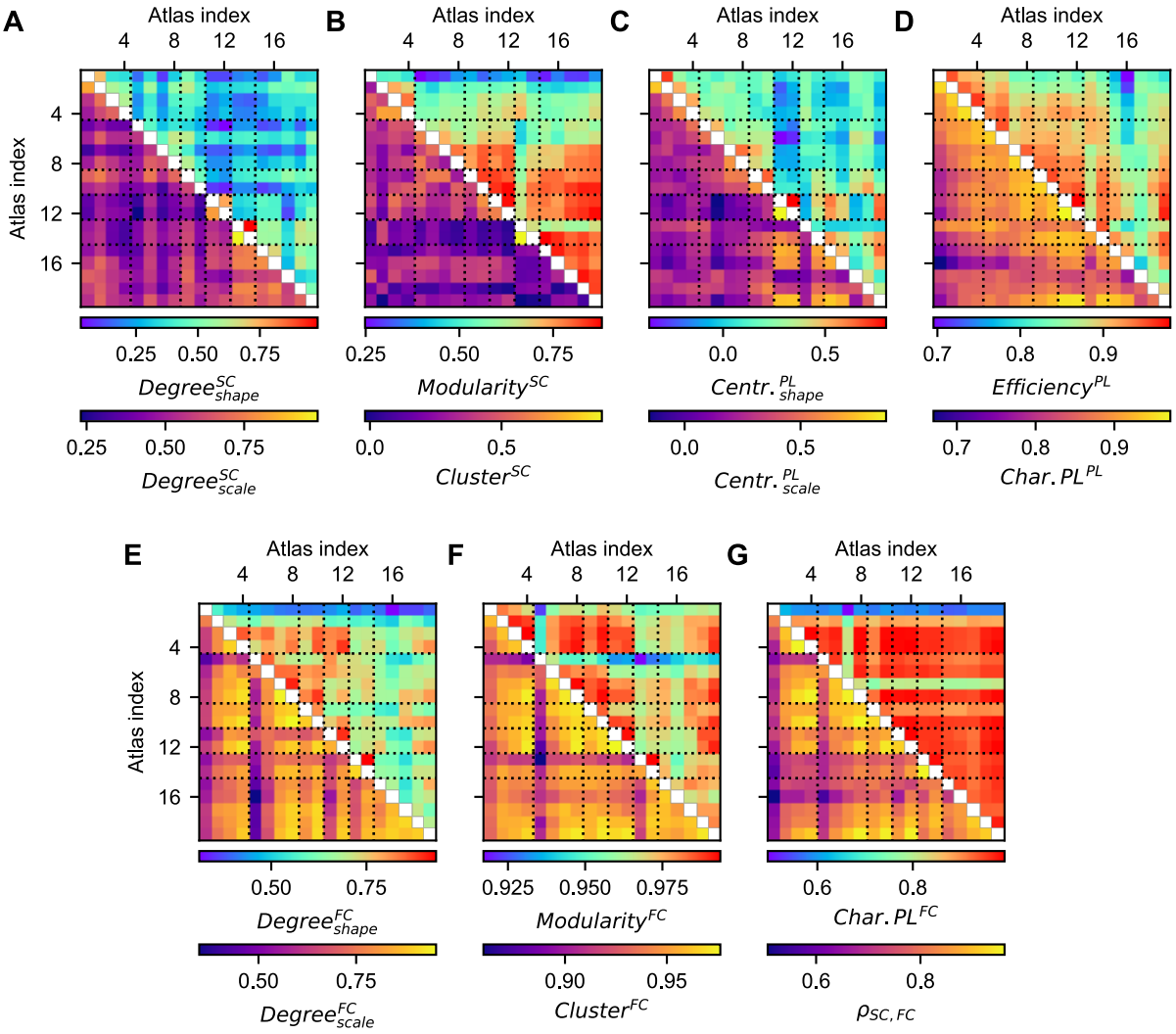

Fig. 3.5. Cross-correlations across subjects of the network statistics derived from the empirical structural and functional connectomes for different parcellations. The correlations between parcellations were calculated for **(A)** the shape (upper triangle) and scale (lower triangle) parameters of the degree distributions of the empirical SC matrix, **(B)** the modularities (upper triangle) and clustering coefficients (lower triangle) of the empirical SC, **(C)** the shape (upper triangle) and scale (lower triangle) parameters of the closeness centrality distributions of the empirical PL matrix, **(D)** the global efficiencies (upper triangle) and characteristic path lengths (lower triangle) of the empirical PL matrix, **(E)** the shape (upper triangle) and scale (lower triangle) parameters of the degree distribution of the empirical FC matrix, **(F)** the modularities (upper triangle) and clustering coefficients (lower triangle) of the empirical FC, and **(G)** the characteristic path lengths of the empirical FC (upper triangle) and the Pearson correlation between the empirical SC and FC (lower triangle). The atlas indices correspond to those in Table 3.1 which contains the information about the used parcellations. Abbreviations: Centr. = closeness centrality, Char. PL = characteristic path length.

exhibited variations across parcellations that had similar magnitudes as the original data; see for example Fig. 3.4O-P vs. Fig. S3.5O-P in the Supplementary results. In addition, the agreement between models was further enhanced; see Fig. 3.6C vs. Fig. S3.6C. In conclusion, the granularity influences the goodness-of-fit to a limited extent, implying that the parcellation-induced deviations cannot exclusively be explained by this quantity.

The goodness-of-fit was also correlated across individual subjects between the considered parcellations and models to evaluate how similar the patterns of the model fitting over all subjects were for different parcellations and models; see Materials and methods (Analysis) for details of this analysis. The results showed relatively high correspondence of the fitting patterns across individual subjects for many of the parcellation combinations for the same as well as for different models, which is illustrated in Fig. 3.6B. Nevertheless, we also observed generally lower correlations for the Schaefer and also the Harvard-Oxford atlases, both within and across models (Fig. 3.6B, atlas indices 11-14). Note that we did not find such clear, generally decreased values when considering the correlations of the empirical graph-theoretical statistics across parcellations (Fig. 3.5). For the empirical FC matrices, the Craddock atlas with 38 parcels could however be distinguished in this respect (Fig. 3.5E-F, atlas index 5), and only a slight indication of a lower correlation could be found for the scale parameter of the degree distribution of the empirical FC for the Schaefer atlas with 100 parcels and Harvard-Oxford atlas with 48 parcels (Fig. 3.5E, atlas indices 11 and 13).

Taken together, the modeling results as represented by the goodness-of-fit between empirical and simulated FC showed pronounced heterogeneity with respect to the variation of the brain atlas. Additionally, we found that the intersubject variability of the fitting results exhibited similar

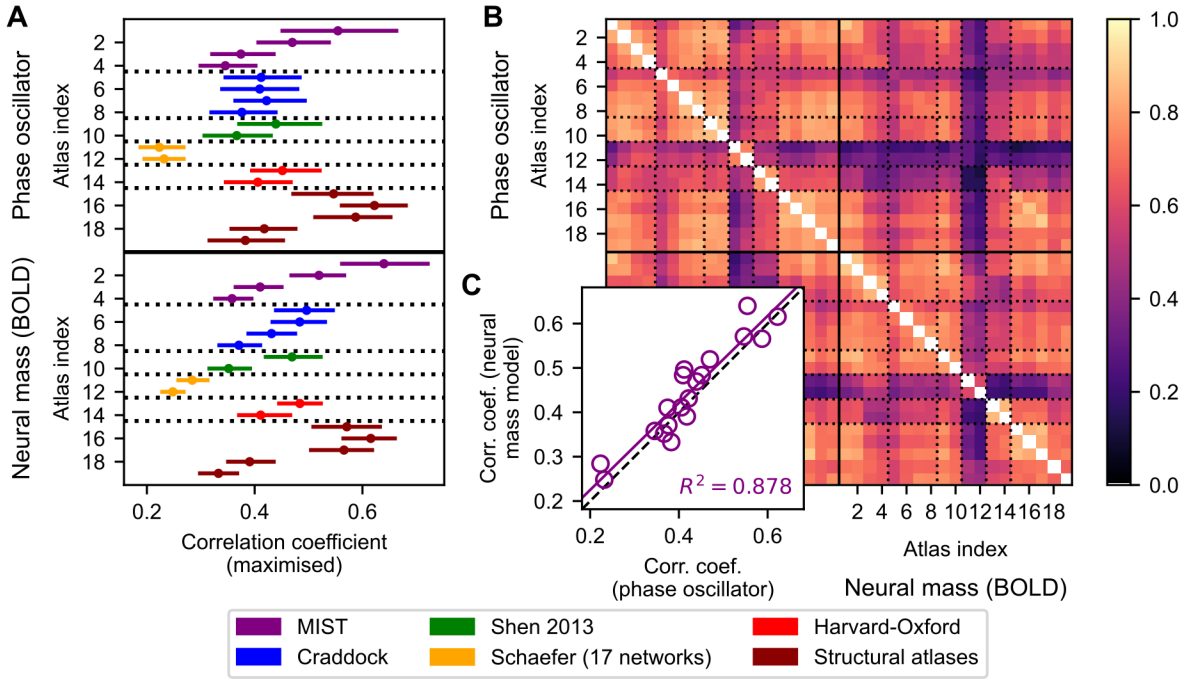

Fig. 3.6. Goodness-of-fit of the whole-brain models based on coupled phase oscillators and neuronal mass models and their interrelations for the considered parcellation schemes. **(A)** Maximized correlations (goodness-of-fit) between the empirical and simulated FC matrices for the brain parcellation schemes and models investigated in this study as indicated on the vertical axes. Dots and lines depict the medians and interquartile ranges across subjects, respectively. **(B)** Correlations across subjects of the goodness-of-fit of the model between the considered parcellations and models. Table 3.1 contains the parcellation information corresponding to the atlas indices used in the plots. **(C)** Scatterplot of the medians of the goodness-of-fit corresponding to the phase oscillator (x-axis) and neural mass model (y-axis) across subjects. Each dot corresponds to a particular parcellation, the purple line portrays the linear regression between both types of goodness-of-fit and the black dashed line corresponds to $x = y$.

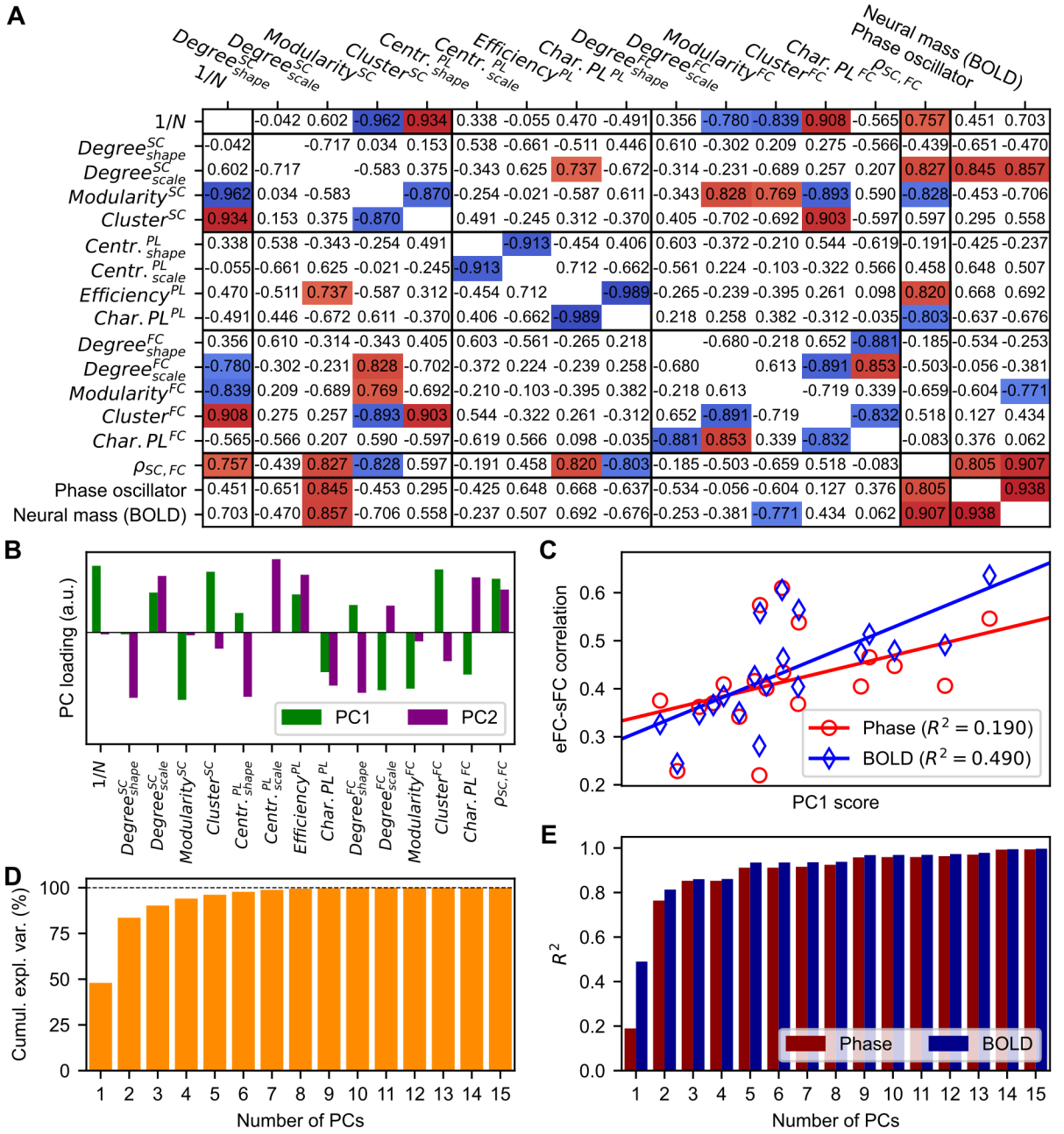

Fig. 3.7. Relationship between the interparcellation variations of the empirical graph-theoretical metrics and the goodness-of-fit. **(A)** Cross-correlations among the inverted granularities, the graph-theoretical measures of the empirical connectomes (network properties depicted in Fig. 3.2 and Fig. 3.3), the structure-function relationship and the goodness-of-fit of the models to the empirical data. The correlation was calculated across parcellations between the median values over all subjects. Significant correlations are highlighted by colors ($p<0.05$, two-sided, Bonferroni corrected). **(B)** Loadings of the first (PC1) and the second (PC2) principal components of the group-averaged graph-theoretical metrics, that is, the contributions of the original empirical data variables to PC1 and PC2. **(C)** Regressions of the PC1 scores with the medians of the goodness-of-fit between empirical (eFC) and simulated (sFC) functional connectivity. The medians were calculated across subjects for each considered parcellation for the phase oscillator (red) and the neural mass model (blue) as indicated in the legend together with the fraction of the explained variance. The symbols stand for the individual parcellations from Table 3.1. **(D)** Cumulative amount of explained variance in the group-averaged graph-theoretical measures as a function of the number of included PCs. **(E)** Fraction of the interparcellation variance of the goodness-of-fit being explained by the (multivariate) linear regression model as a function of the number of PCs included in the model. Other abbreviation: a.u. = arbitrary unit, cumul. = cumulative, expl. = explained, var. = variance.

patterns for most of the considered parcellations, although we also observed some exceptions for which this correspondence is limited (the Schaefer and Harvard-Oxford atlases).

3.3.3 Interparcellation variations of empirical connectomes and modeling results

To understand the effects observed at the group level, the patterns of the extracted graph-theoretical statistics across parcellations (Fig. 3.2, Fig. 3.3, median values) were compared with one another and with those obtained for the goodness-of-fit of both models (Fig. 3.6A, median values). Significant correlations were observed for some of the tested combinations, which are shown in Fig. 3.7A. This in particular concerned the correlations of the inverted number of parcels with the subject medians of the modularities and clustering coefficients of both the empirical SC and FC, the scale parameters of the degree distributions of the empirical FC, and the correlations between empirical SC and FC (Fig. 3.7A, top row/first column). In such a way the dependencies of these measures on granularity were demonstrated, which were already observed in Fig. 3.4. Furthermore, the scale parameters of the degree distributions of the empirical SC and the structure-function relationship between the empirical SC and FC exhibited significant correlations with the fitting results for both models. Interestingly, the modularity of the empirical FC significantly anti-correlated with fitting results for the neural mass model (i.e., smaller modularity implies better fitting), but not for the phase model (Fig. 3.7A).

We thus found that the network properties of the empirical connectomes (Fig. 3.2, Fig. 3.3) and the quality of the model validation as given by the goodness-of-fit of the simulated FC to the empirical FC (Fig. 3.6) in some cases demonstrated a pronounced and significant correlation with one another across parcellations (Fig. 3.7A). To quantify this relationship further, we combined principal component analysis with ordinary least squares linear regression to take into account the contributions from all graph-theoretical statistics; see Materials and methods (Analysis) for details of this analysis. The first principal component (PC1) extracted from the group-averaged graph-theoretical statistics was found to explain 48% of the variance in the data variables across parcellations (Fig. 3.7D), and the signs of its relative loadings (Fig. 3.7B) were in accordance with previous results (see e.g., Fig. 3.7A). Subsequently, we regressed the PC1 scores with the medians of the goodness-of-fit calculated across subjects for every brain atlas. We found that this PC explained about 19% and 49% of the interparcellation variance in the goodness-of-fit for the phase oscillators and the neural mass models, respectively (Fig. 3.7C). We again observed stronger contribution of empirical data to the fitting results of the neuronal mass model; see also Fig. 3.4O,P.

The second principal component (PC2) explained an additional 35% of the variance in the data variables (Fig. 3.7D). We included this component in the linear regression model, which made it multivariate. This improved the association between the data variables and the goodness-of-fit to 77% and 81% of explained variance for the phase oscillator and neural mass model, respectively (Fig. 3.7E). Including more principal components in the linear regression model led to an even better explanation of the goodness-of-fit variance by the empirical data (Fig. 3.7D,E). Note, however, that using too many PCs in the regression may lead to an overfitting for the considered 19 parcellations. Finally, we investigated the effect of the granularity on these results by regressing this effect out of all the quantities used in this investigation while following the same procedure as described above. The results of this inquiry are shown in Fig. S3.7 in the Supplementary results, and they demonstrate that after the removal of the granularity effect already the first principal component sufficed to get approximately the same associations between the data variables and the goodness-of-fit as observed in Fig. 3.7 for 2 PCs. Also the difference between models was inverted and reduced.

With these results, we demonstrated that most of the interparcellation variation observed in the modeling results at the group level (Fig. 3.6A) could be explained by the network properties

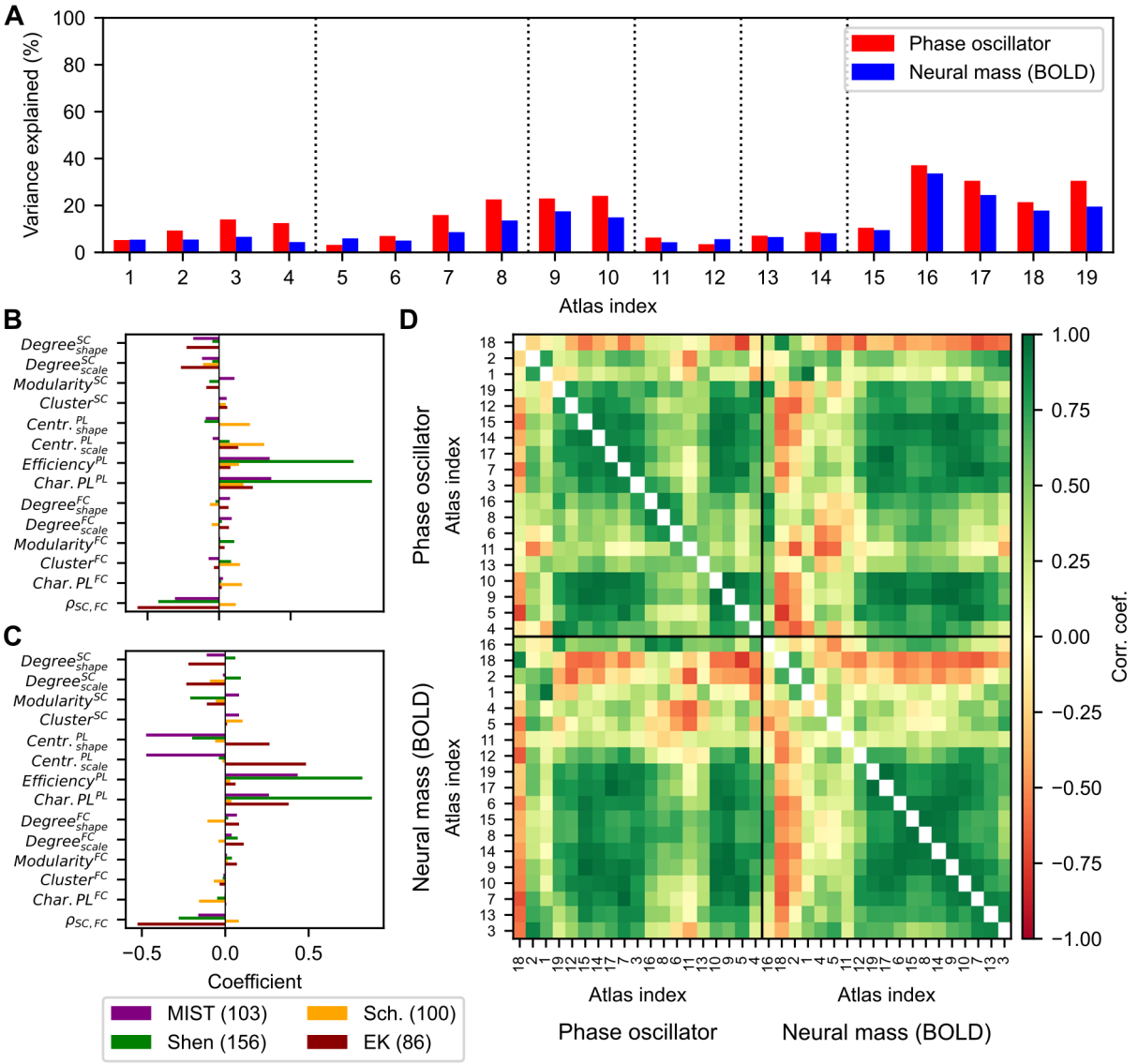

Fig. 3.8. Relationship between the interindividual variations of the empirical graph-theoretical metrics and modeling results for different parcellations. **(A)** Amounts of within-parcellation, between-subject variance in the modeling results (goodness-of-fit to empirical data) being explained via multivariate ordinary least squares linear regression utilizing the z-scored graph-theoretical statistics of the empirical connectomes per parcellation. Modeling results were sampled by using the systems of coupled phase oscillators (red) and neural mass models (blue). **(B-C)** Regression coefficients corresponding to the data variables (network properties) depicted in Fig. 3.2 and Fig. 3.3 for four selected brain parcellations as indicated in the legend and for the phase oscillators (B) and the neural mass models (C) leading to the regression results in panel A. The abbreviations MIST (103), Shen (156), Sch. (100), and EK (86) correspond to the parcellations in Table 3.1 and in panel A with indices 3, 10, 11, and 16, respectively. **(D)** Pearson correlation coefficients across the regression coefficients per pair of brain parcellation and model type. Table 3.1 contains the parcellation information corresponding to the atlas indices. Abbreviations: coef. = coefficient, corr. = correlation.

of and the relationship between empirical SC and FC used to inform and validate the models. Furthermore, we showed which metrics derived from the empirical connectomes contributed positively and negatively to the goodness-of-fit of the simulated FC produced by the model to the empirical FC (Fig. 3.7B). Lastly, our results confirm that the parcellation exerts an influence on the graph-theoretical measures and the goodness-of-fits that can only partially be explained by the granularity. This especially becomes evident when considering the high PC1 loading of the inverse of the number of parcels in relation to the relatively low association of this PC with the modeling results (Fig. 3.7B,D); see also Fig. S3.7 in the Supplementary results, where the granularity was regressed out.

3.3.4 Interindividual differences of empirical connectomes and modeling results

As shown above, the group averages of the graph-theoretical statistics and the modeling results obtained using different brain atlases tightly related to one another (Fig. 3.7). Nevertheless, as dynamical whole-brain models seem to be a promising model-based approach for studying interindividual differences (Ritter et al., 2013; Sanz-Leon et al., 2015; Zimmermann, Perry, et al., 2018), we investigated whether the within-parcellation, between-subject variances observed in our modeling results could also be attributed to variations of the data variables extracted from the empirical SC and FC. To do so, we adopted the approach from the previous section, where, for each individual parcellation, we built a separate dataset containing the corresponding graph-theoretical network properties; see Materials and methods (Analysis) for details. Using this dataset, we initially checked how individual empirical graph-theoretical statistics correlated with the interindividual variability of the goodness-of-fit, and found no clear correspondences except for the structure-function relationship $\rho_{SC,FC}$ (Fig. S3.8). It is interesting to observe here, that $\rho_{SC,FC}$ correlated negatively with the goodness-of-fit of the models to the empirical data for most of the considered parcellations. Given that this bivariate approach did not yield positive results in the form of clear (anti)correlations for the investigated network metrics, we resorted to multivariate analyses.

As before, we calculated the PC1 of the consequent dataset of z-scored individual data variables (network properties) and subsequently regressed the PC1 scores with the corresponding goodness-of-fits of the model across individual subject-session pairs for every one of the considered brain atlases. The obtained results showed that the amount of variance in the modeling results across subjects explained by PC1 was low (<3%; see Fig. S3.9A in the Supplementary results), even though the data variables extracted using different parcellations exhibited similar co-variations as reflected by the PC1 loadings and corresponding correlations, which exhibited some form of clustering (Fig. S3.9B-C). Because of the weak explanatory power observed at this approach (Fig. S3.9A), the used methodology based on the principal component analysis of network properties of empirical connectomes might be inappropriate to assess interindividual differences in the model validation.

We therefore employed a different approach, where the z-scored data variables representing the network properties of empirical SC and FC were directly regressed with the z-scored goodness-of-fits of the models across individual subjects via multivariate ordinary least squares regression. The regression results obtained for individual parcellations indicated a variable amount of explained between-subject variance in the goodness-of-fit for different parcellations (Fig. 3.8A). The strongest influences of the empirical connectomes on the interindividual variations in the goodness-of-fit were observed for the von Economo-Koskinas, AAL and Brainnetome atlases (indices 16, 17, and 19 in Fig. 3.8A, respectively), which however still did not exceed 40% of explained variance. For other parcellations based on, for example, the Schaefer or Harvard-Oxford atlases (indices 11-14 in Fig. 3.8A), the results of the model fitting for an individual subject practically did not depend on the network properties of the used empirical connectomes.

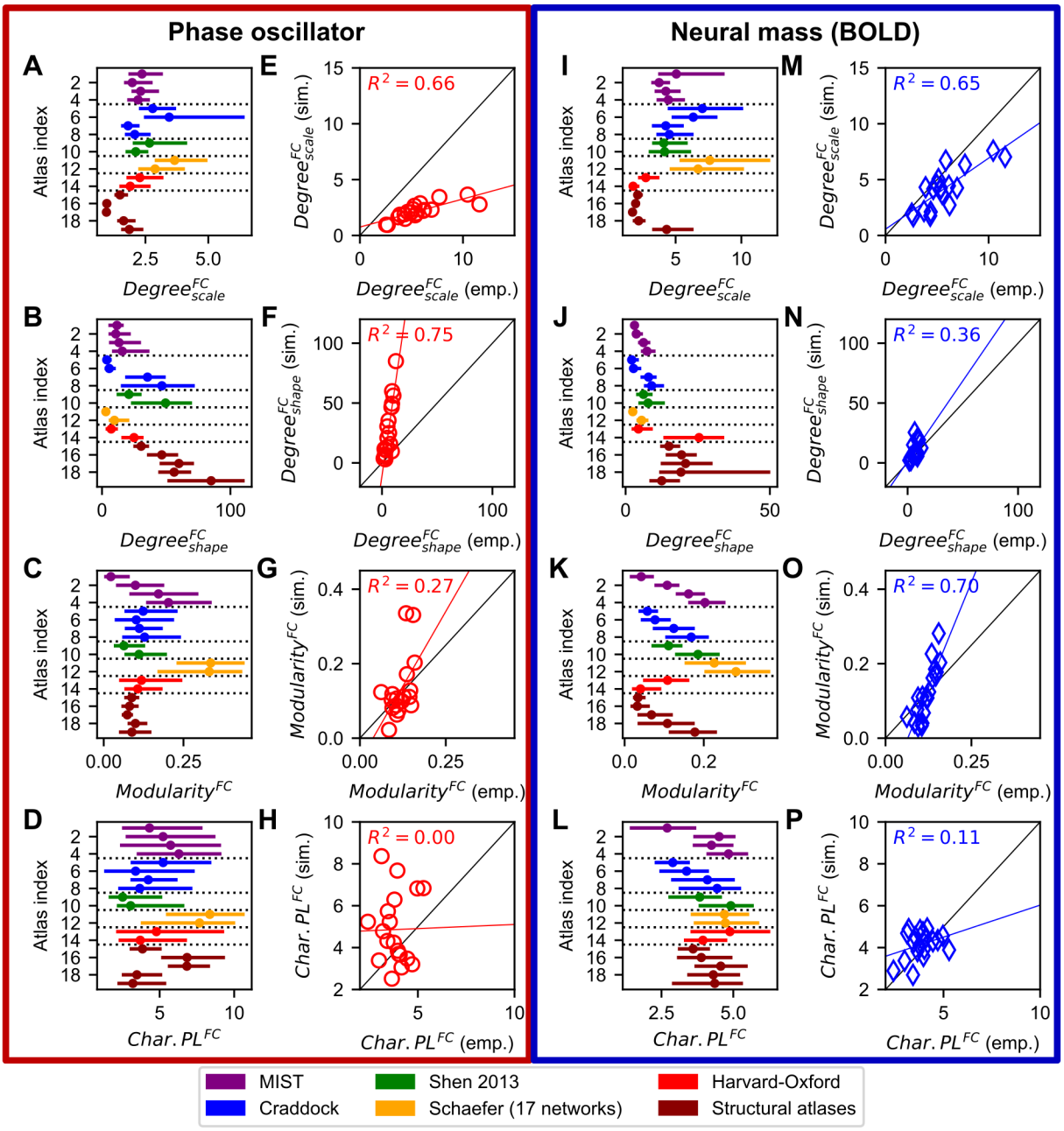

Fig. 3.9. Relationship between the graph-theoretical statistics of empirical and simulated FC matrices at the group level. Network properties of the simulated FCs providing the best fits to the empirical FC and the scatterplots of the corresponding median values calculated across subjects are illustrated for phase oscillator model (A-F) and neural mass model (G-L). The shape (A, E, I, M) and scale (B, F, J, N) parameters of the degree distributions, the modularities (C, G, K, O) and the characteristic path lengths (D, H, L, P) are depicted for the parcellations in Table 3.1, where dots and lines in panels A-D and I-L depict the medians and interquartile ranges across subjects, respectively. Symbols, colored and black lines in the scatterplots (E-H) and (M-P) of the simulated network metrics versus empirical ones stand for individual parcellations, regression lines and the diagonal $x = y$, respectively.

Interestingly, in most cases the phase oscillators exhibited a somewhat stronger dependence on the considered data variables (Fig. 3.8A, red bars), which contrasts with the interparcellation variation of the medians (Fig. 3.7E). We observed low consistency between parcellations and between models regarding the regression coefficients assigned to the corresponding data variable by this multivariate regression analysis (Fig. 3.8B-C). This is reflected by the Pearson correlations across the coefficients per model and parcellation pair illustrated in Fig. 3.8D, which shows a clustering that is inconsistent across models.

Taken together, these results demonstrated that the contributions of the graph-theoretical statistics derived from the empirical connectomes to the interindividual differences in the modeling results were limited.

3.3.5 Network properties of simulated functional connectomes

We established that between-parcellation variances in the model fitting results could largely be explained by the variation of the network properties taken from the empirical SC and FC (Fig. 3.7). However, we also found that such a relationship was hardly applicable to the explanation of the intraparcellation, between-subject variations. In this case, for any parcellation, the interindividual differences in the goodness-of-fit only weakly to moderately correlated with the graph-theoretical properties of empirical networks for individual subjects (Fig. 3.8).

Here we evaluate how similar the empirical FC matrices were in terms of the graph-theoretical statistics to the simulated ones that provided the best fits based on Pearson's correlation. To do so, the simulated FC matrices were subjected to the same graph-theoretical analyses as the empirical FCs; see Fig. 3.9A-D,I-L for results. The medians of the network properties calculated across subjects for the empirical and simulated FCs were correlated with each other over all considered parcellations. The results showed that relationships between the network properties of the empirical and simulated FCs existed, which indicated that the models on average preserved most of the considered network properties of the empirical functional connectome; only the characteristic path length exhibited low coefficients of determinations for both models (Fig. 3.9E-H,M-P). The results for the clustering coefficient have not been shown in Fig. 3.9 as they resembled those of the modularity. We also found that the empirical and simulated functional networks agreed with each other to very different extents for the two considered models except for the shape parameter of the degree distribution (Fig. 3.9E,M). More variance in the scale parameters of the degree distributions of the simulated FC across parcellations could be explained by that of the empirical FC when the phase oscillators rather than the neural mass models were used for the generation of the former (Fig. 3.9F,N). The opposite is true for the modularity and characteristic path length; here, the neural mass model led to more explained variance (Fig. 3.9G-H,O-P). From these results, we can conclude that the accuracy of the transformation of the empirical SC to simulated FC by the considered dynamical whole-brain models can depend on the model used for the simulation of the local mean activity of the brain regions. These findings furthermore indicated that, even though different models may lead to comparable goodness-of-fits (Fig. 3.6C), the correspondence of the network structures of the simulated FCs to those of the empirical ones may vary considerably across models.

Finally, we investigated how the latter analysis performed at the level of individual subjects and individual parcellations. Hence, we correlated the network properties derived from the empirical and simulated FCs across subjects for each individual parcellation. The obtained results, illustrated in Fig. 3.10A-D, revealed that the highest correspondences between the network properties of the empirical and simulated FC could be found for the modularity and characteristic path length (Fig. 3.10G-H). No general patterns could be found as to which model led to higher explained variances between empirical and simulated FC (Fig. 3.10E-H). Still, we observed relatively large deviations of the explained variance between the two considered models

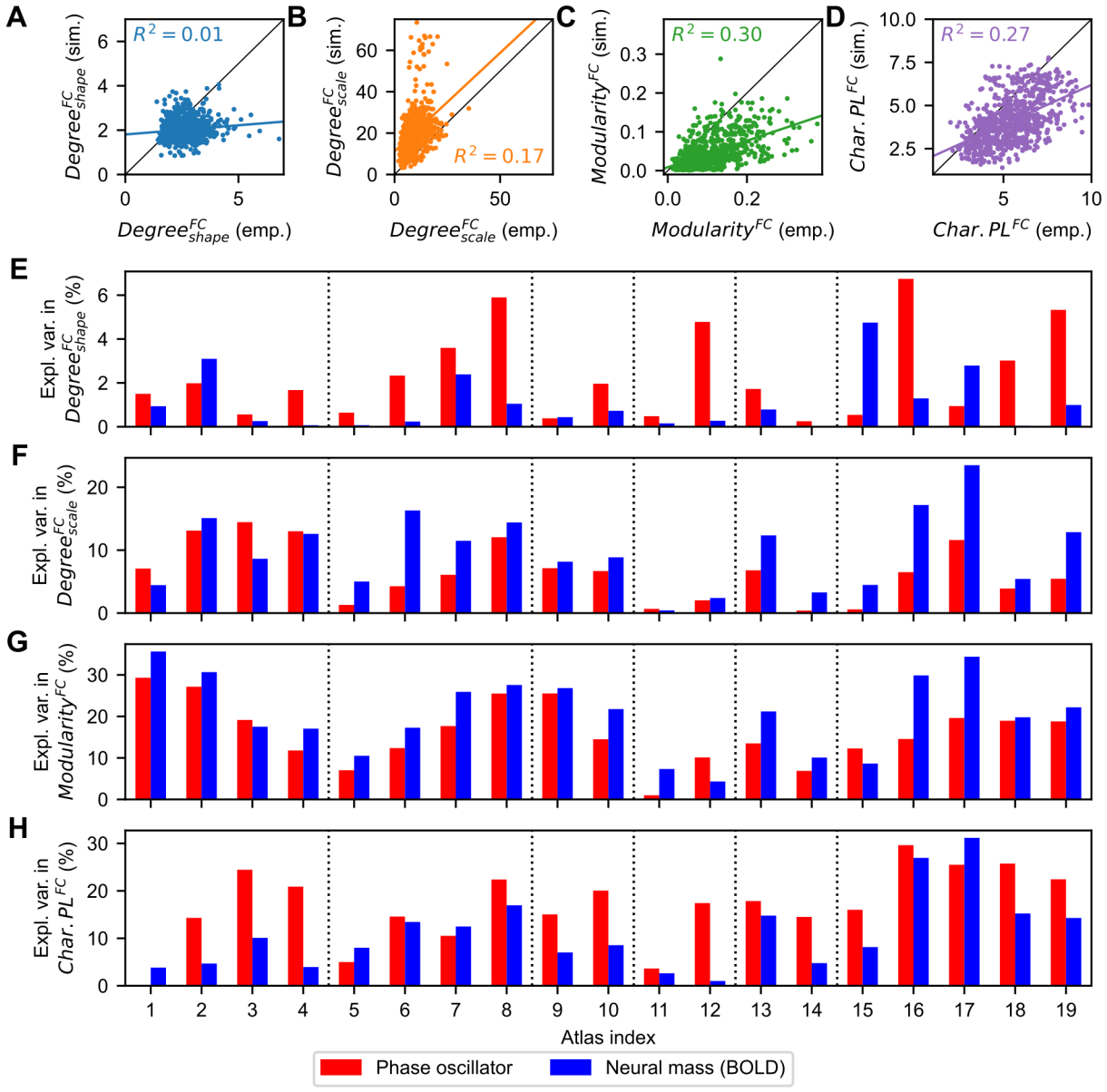

Fig. 3.10. Relationship between the graph-theoretical statistics of empirical and simulated FC matrices at the subject level. **(A-D)** Scatterplots of the shape (A) and scale (B) parameters of the degree distributions, the modularities (C) and the characteristic path length (D) of the empirical and simulated (by neural mass model) FCs within a single parcellation as given by the von Economo-Koskinas atlas (index 16 in Table 3.1). Every dot represents a subject-session pair, the colored lines depict the ordinary least squares linear regression solution and the black lines correspond to $x = y$. **(E-H)** Proportion of intersubject variance of the network properties of the best-fit simulated FCs generated by the phase oscillators (red) and the neural mass model (blue) that is explained by the network properties of the empirical FCs for a given parcellation indicated on the horizontal axes. Table 3.1 contains the parcellation information corresponding to the atlas indices used in the plots. Other abbreviations: expl. = explained, var. = variance.

for the individual parcellations, where the largest differences between the models could reach around 20% of explained variance (Fig. 3.10E-H, differences between red and blue bars).

These results show that network properties of the empirical and simulated FCs could be a good measure of the model validation, and allow to distinguish different models at the level of individual subjects (Fig. 3.10) as well as at the group level (Fig. 3.9). This seemed not to be the case for the correlative model fitting, where the models were practically indistinguishable at the group level and could be differentiated only at the subject levels. The latter claim can be seen in the amount of variance in the goodness-of-fit that is explained by the network properties derived from the empirical data when comparing between- and within-parcellation variations (see Fig. 3.7, Fig. 3.8).

3.4 Discussion

In this study, we used a selection of 19 parcellations constructed through 10 different approaches. They were selected with an attempt to balance between parcellations derived from functional data, comprising the atlases described by Craddock et al. (2012), Shen et al. (2013), Schaefer et al. (2018), and Urchs et al. (2019), and structural information, constituting the other parcellations included in Table 3.1. Furthermore, the investigated parcellations were compiled using distinct methodologies such as boundary detection algorithms, histological stainings, and diverse clustering approaches (see the Supplementary method for details). While more brain parcellations are available in the literature and were used for data-driven analyses (Dadi et al., 2020; Messé, 2020; Schaefer et al., 2018), the tested parcellations and the variation regarding the number of parcels in them are representative for the state-of-the-art brain parcellations, and can support the derived conclusions concerning the reported relationship between the model simulation results and the empirical data.

3.4.1 Influence of parcellation on graph-theoretical statistics and goodness-of-fit

Significant (anti)correlations were found across parcellations when comparing the parcellation granularity with individual graph-theoretical statistics and the goodness-of-fit of the whole-brain models (Fig. 3.7). This clearly evidenced the granularity substantially affecting the network properties of the empirical FC and SC and the model fitting results regardless of the method used to construct the parcellation. Still, as the parcellation varied, graph-theoretical statistics as well as the goodness-of-fit exhibited pronounced variations (Fig. 3.2, Fig. 3.3, Fig. 3.4, Fig. 3.6) that persisted after we corrected for the effect of the granularity (Fig. S3.3, Fig. S3.4, Fig. S3.5, Fig. S3.6). We were not able to reliably distinguish between results derived from e.g. functionally and structurally derived parcellations, even after the granularity correction was performed. Hence, as parcellation-induced variances in the goodness-of-fit were shown to be related to the variations in the empirical SC and FC, the question still remains how the parcellations induce the pronounced differences in the graph-theoretical statistics.

The reported parcellation-induced variances emphasize the importance of a well-advised selection of the parcellations in region-based neuroimaging studies using graph-theory or whole-brain models to analyze the data. A recent study by Messé (2020) already showed this to be true when examining the structure-function relationship of the brain from a statistical perspective. Also studies by J. Wang et al. (2009) and Zalesky et al. (2010) demonstrated the prominent influence the brain parcellation may have on the network properties of the empirical FC and SC, respectively. Our study added further modern graph-theoretical measures to the analysis for both empirical SC and FC as well as simulated FC. In sum, these findings can complement other considerations (e.g., the biological interpretation of the atlas) in the selection of the proper parcellation for the study at hand. After all, the question concerning an optimal parcellation is a difficult problem given many possible parcellation techniques and optimization criteria.

3.4.2 Important factors with respect to model fitting

We found that most of the interparcellation variance in the goodness-of-fit at the group level could be explained by the graph-theoretical statistics derived from the empirical SC and FC (Fig. 3.7). By examining the PC1 and PC2 loadings in Fig. 3.7B, the graph-theoretical measures associated with a high goodness-of-fit can be identified. Here, the PC1 loadings clearly reflected the effect of granularity in the graph-theoretical statistics, and demonstrated that a finer granularity leads to a lower goodness-of-fit. The loadings of PC2, which explained a large amount of variance in the modeling results for both models, did not exhibit such a general relation. The parameters of the degree and closeness centrality distributions as well as the global efficiency are heavily loaded onto this PC. Here, the shape parameters of all the fitted gamma distributions exhibited negative loadings, implying that a small shape parameter leads to a high goodness-of-fit (see also Fig. S3.7). Given Eq. 3.1 and Fig. S3.1, this implies that the modeling workflow prefers that most nodes have a low centrality and a select few nodes have a high centrality for the empirical SC as well as FC, because then the density is high close to 0 and decreases with incrementing degree. The positive PC2 loading of the global efficiency, furthermore, implies that the whole-brain models can replicate the functional networks better if the structural networks facilitate the integration of signals.

The network architecture of the brain itself is believed to comprise a multi-level modular structure and a heterogeneity with respect to the degree of individual nodes (Avena-Koenigsberger et al., 2018; van den Heuvel & Sporns, 2019). Although the modularity did not exhibit a strong relationship with the goodness-of-fit other than their shared dependence on the granularity (Fig. 3.7, Fig. S3.7), our results show that dynamical whole-brain models indeed favor such a heterogeneity in the degree distribution. After all, the goodness-of-fit was ameliorated by a higher diversity with regard to the degree distribution in the SC and FC (as illustrated in Fig. S3.10A-E).

3.4.3 Within-parcellation, between-subject variances and the personalization of whole-brain models

Previous studies suggested that dynamical whole-brain models are able to simulate the resting-state brain activity on a personalized level (Bansal et al., 2018; Deco et al., 2017; Ritter et al., 2013; Sanz-Leon et al., 2015; Zimmermann, Perry, et al., 2018). How this personalization is achieved is not known. In this study, we have provided evidence that interindividual differences in the goodness-of-fit do not reliably relate to the subject-specific deviations in the graph-theoretical measures (Fig. 3.8, Fig. S3.9). In addition, we have shown that the network structures of the simulated FC map onto those of the empirical FC when considering group-averages, but not within-parcellation, interindividual variances (Fig. 3.9, Fig. 3.10). Taken together, the personalization of whole-brain models does not seem to use subject-specific deviations in the network properties. How personalization of whole-brain models then actually is achieved requires further investigation.

To account for the interindividual variations of the modeling results, other data variables may for example be considered out of the class of the considered network properties. In such investigations, special attention must be paid to the limitations in the reconstruction of the structural connectome. Studies namely have shown substantial amounts of inaccuracies (e.g., false positives or negatives) infecting the empirical SC when it is extracted from dwMRI data (Bassett et al., 2011; Lindquist, 2020; Maier-Hein et al., 2017; Schilling et al., 2019; Sotiropoulos & Zalesky, 2019). These inaccuracies can have a systematic effect on the network properties of the empirical SC (Zalesky et al., 2016). In order to reduce these inaccuracies, the whole-brain tractography should be calculated with high density by state-of-the-art techniques, as we did in this study, which can enhance its reproducibility (Roine et al., 2019).

The patterns of the intersubject differences in the graph-theoretical statistics and the modeling

results may vary across parcellations (Fig. 3.5, Fig. 3.6B), which implies that the network structures of the empirical connectomes and the modeling results depend on the used parcellation also at the level of individual subjects. This is a relevant implication as it may have consequences for computational modeling studies investigating clinical traits (Cabral et al., 2012; Saenger et al., 2017). Observed differences between groups and individual subjects may deviate when another parcellation is used and may therefore reflect artefacts induced through the use of a particular parcellation rather than actual deviations in the structure-function relationship of distinct cohorts, as also discussed by Betzel & Bassett (2017).

3.4.4 Perspectives and outlook

Further brain parcellations, datasets, models, and (graph-theoretical) analyses variations might be considered to verify and confirm the obtained results, especially when more computationally powerful resources become available. In the end, the simulations and optimizations of dynamical whole-brain models are computationally costly. The computational costs also inhibit the estimation of biases in the model simulation results via, for example, null models. Future studies should be devoted to devising strategies that could estimate these biases without a full evaluation of the model dynamics through simulations.

Related to these computational costs is the notion that our results can contribute to the development of informed expectations concerning the quality of the model validation for a given brain parcellation. For this, a few network properties of the empirical connectomes calculated for this parcellation can be examined before running time and resource consuming model simulations. Additionally, this concept may be exploited to distinguish between data-induced and model-induced deviations in the modeling results. Such an investigation may estimate to what extent the empirical data already predicted the differences in modeling results between, for example, healthy and clinical cohorts; the contribution of the model is consequently represented by the remaining between-group variance.

Finally, the inaccurate mappings of empirical SC to simulated FC by both tested models for local, mean-field activity highlight their current limitations with respect to the replication of empirical resting-state brain dynamics. How well other types of models can replicate the empirical FC on the basis of the empirical SC remains to be seen and should be investigated further. Such an investigation would typically comprise the application of the framework of this study to other model types such as the Jansen-Rit model (Jansen et al., 1993; Jansen & Rit, 1995), the (reduced) Wong-Wang model (Deco & Kringelbach, 2014; E. C. A. Hansen et al., 2015; Wong & Wang, 2006), different types of limit-cycle oscillators (Deco, Cabral, et al., 2018; Deco et al., 2017; Ghosh et al., 2008) and a more recently developed neural mass model that incorporates plasticity dynamics (Abeysuriya et al., 2018). Taken together, this implies that, even though the tested models yield results that are related to the empirical data in terms of more than one statistic, they are far from perfect and hence there is room for improvement.

Acknowledgements

We thank M. Kollmann for his consultation on the manuscript and S. Zhang for his consultation on the parcellation image processing. This study was made possible through the Portfolio Theme Supercomputing and Modeling for the Human Brain of the Helmholtz Association (https://www.helmholtz.de/en), and through the European Union's Horizon 2020 Research and Innovation Program (grant agreements 785907 (HBP SGA2), 945539 (HBP SGA3) and 826421 (VirtualBrainCloud)). The funders had no role in study design, data collection and analysis, decision to publish, or preparation of the manuscript. Also, the authors gratefully acknowledge the computing time granted through JARA on the supercomputer JURECA at Forschungszentrum Jülich.

Supplementary data sheet

Every datasheet contains nine plots. The top row contains examples of the structural connectivity, path length and functional connectivity matrices (from left to right). These examples were constructed using the same subject of the HCP dataset. Modularity and modular structure were calculated from the structural and functional connectivity matrices and subsequently matrix rows and columns were sorted on the basis of these results. The modularity index and the number of modules are also displayed within the structural and functional connectivity matrices and the global efficiency calculated from the PL matrix is displayed in that matrix. The middle row contains the densities of the individual elements of the corresponding matrices calculated across the 200 subjects from the HCP dataset used in this study. The bottom row shows (from left to right) the degree distribution of the empirical SC matrix, the closeness centrality of the empirical PL matrix and the degree distribution of the empirical FC matrix. These distributions were calculated across the 200 subjects from the HCP dataset used in this study. In addition, the gamma and normal distributions that best fitted the empirical distribution at hand are drawn into the plots. The legends explain which line corresponds to which distribution. Additionally, they also display the Kolmogorov-Smirnov statistic (in parentheses), which characterises the quality of the fit of the parametric distribution to the empirical data as reflected by the distance between the cumulative distribution functions. A lower value of this statistic implies a better fit.

MIST

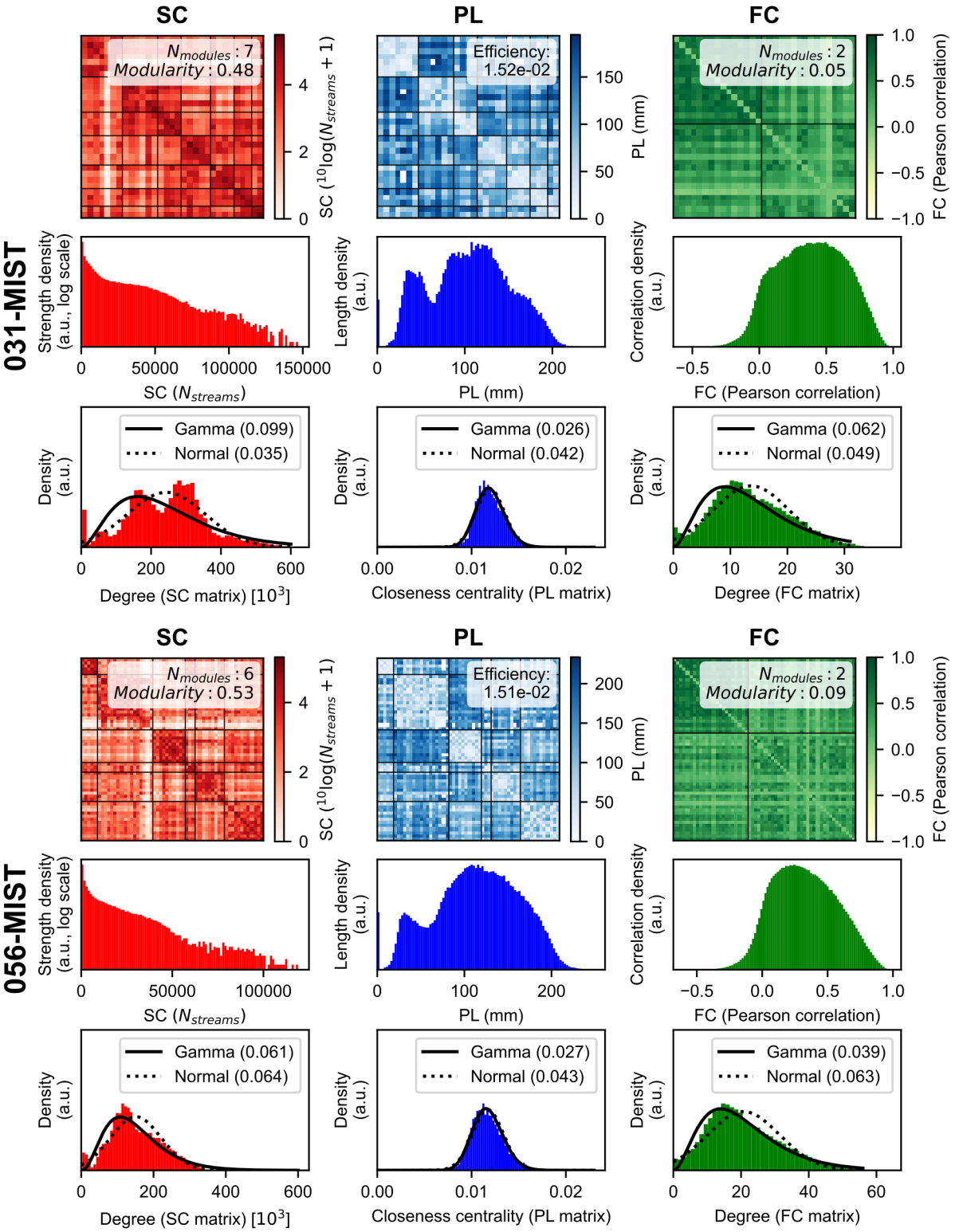
SC
PL
FC
031-MIST
$N_{modules}$: 7
Modularity : 0.48
Efficiency: 1.52e-02
$N_{modules}$: 2
Modularity : 0.05
SC (^{10}log($N_{streams}$ + 1))
PL (mm)
FC (Pearson correlation)
Strength density (a.u., log scale)
Length density (a.u.)
Correlation density (a.u.)
SC ($N_{streams}$)
PL (mm)
FC (Pearson correlation)
Gamma (0.099)
Normal (0.035)
Gamma (0.026)
Normal (0.042)
Gamma (0.062)
Normal (0.049)
Density (a.u.)
Degree (SC matrix) [10^3]
Closeness centrality (PL matrix)
Degree (FC matrix)
SC
PL
FC
056-MIST
$N_{modules}$: 6
Modularity : 0.53
Efficiency: 1.51e-02
$N_{modules}$: 2
Modularity : 0.09
SC (^{10}log($N_{streams}$ + 1))
PL (mm)
FC (Pearson correlation)
Strength density (a.u., log scale)
Length density (a.u.)
Correlation density (a.u.)
SC ($N_{streams}$)
PL (mm)
FC (Pearson correlation)
Gamma (0.061)
Normal (0.064)
Gamma (0.027)
Normal (0.043)
Gamma (0.039)
Normal (0.063)
Density (a.u.)
Degree (SC matrix) [10^3]
Closeness centrality (PL matrix)
Degree (FC matrix)

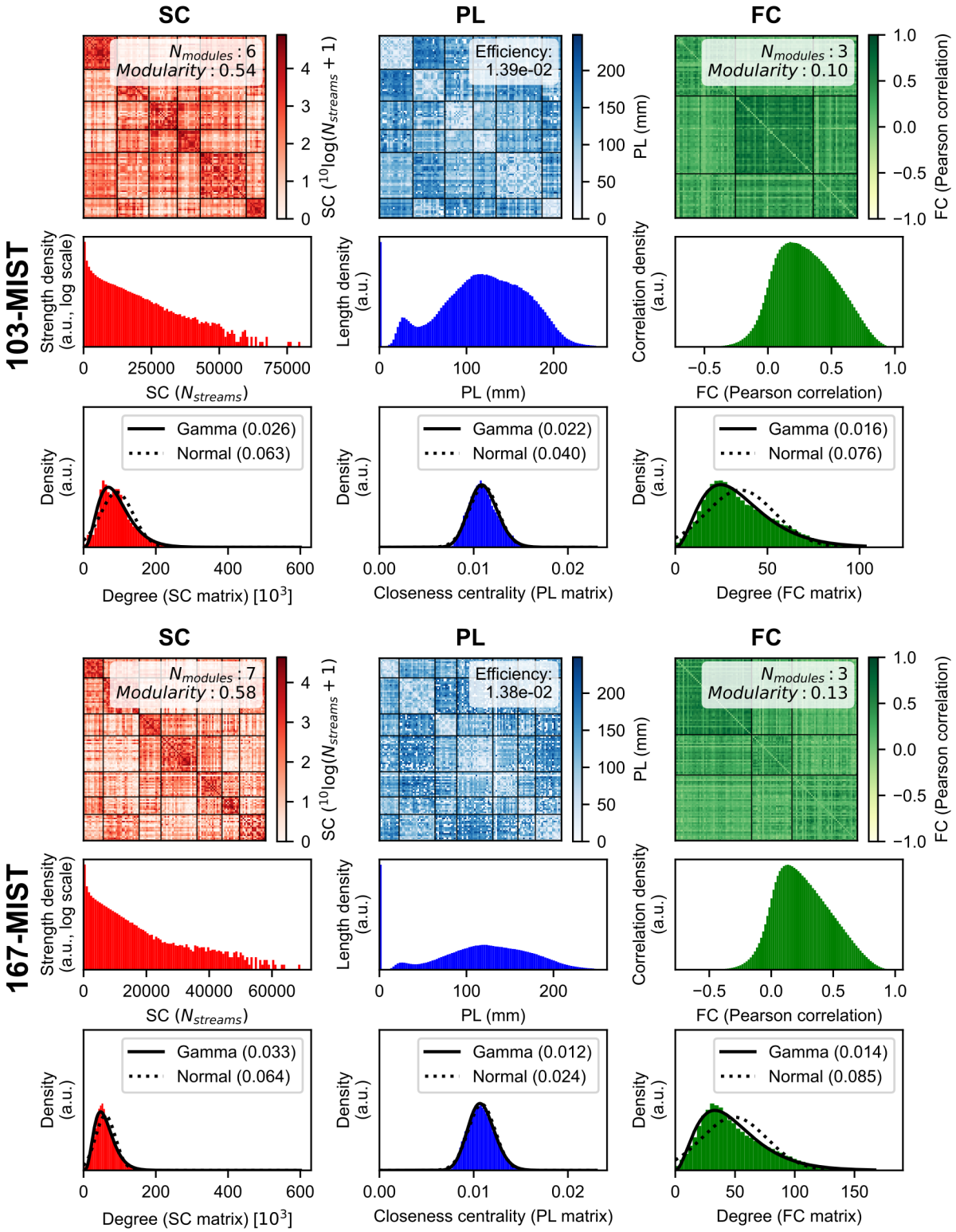
103-MIST
SC
PL
FC
$N_{modules}$: 6
Modularity : 0.54
Efficiency: 1.39e-02
$N_{modules}$: 3
Modularity : 0.10
SC (^{10}log($N_{streams}$ + 1))
PL (mm)
FC (Pearson correlation)
Strength density (a.u., log scale)
SC ($N_{streams}$)
Length density (a.u.)
PL (mm)
Correlation density (a.u.)
FC (Pearson correlation)
Gamma (0.026)
Normal (0.063)
Gamma (0.022)
Normal (0.040)
Gamma (0.016)
Normal (0.076)
Density (a.u.)
Degree (SC matrix) [10^3]
Closeness centrality (PL matrix)
Degree (FC matrix)
167-MIST
SC
PL
FC
$N_{modules}$: 7
Modularity : 0.58
Efficiency: 1.38e-02
$N_{modules}$: 3
Modularity : 0.13
SC (^{10}log($N_{streams}$ + 1))
PL (mm)
FC (Pearson correlation)
Strength density (a.u., log scale)
SC ($N_{streams}$)
Length density (a.u.)
PL (mm)
Correlation density (a.u.)
FC (Pearson correlation)
Gamma (0.033)
Normal (0.064)
Gamma (0.012)
Normal (0.024)
Gamma (0.014)
Normal (0.085)
Density (a.u.)
Degree (SC matrix) [10^3]
Closeness centrality (PL matrix)
Degree (FC matrix)

CraddockSCorr2Level

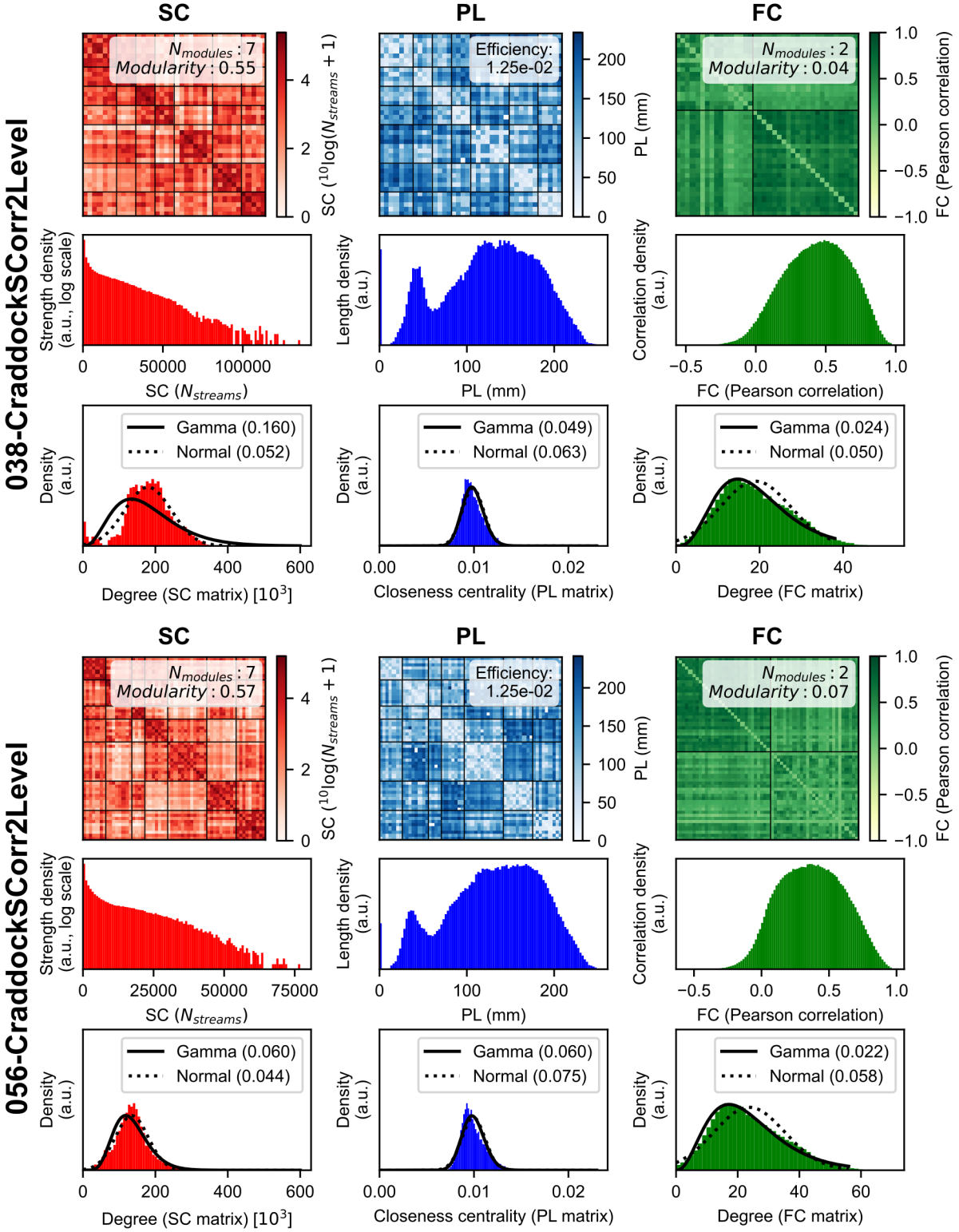

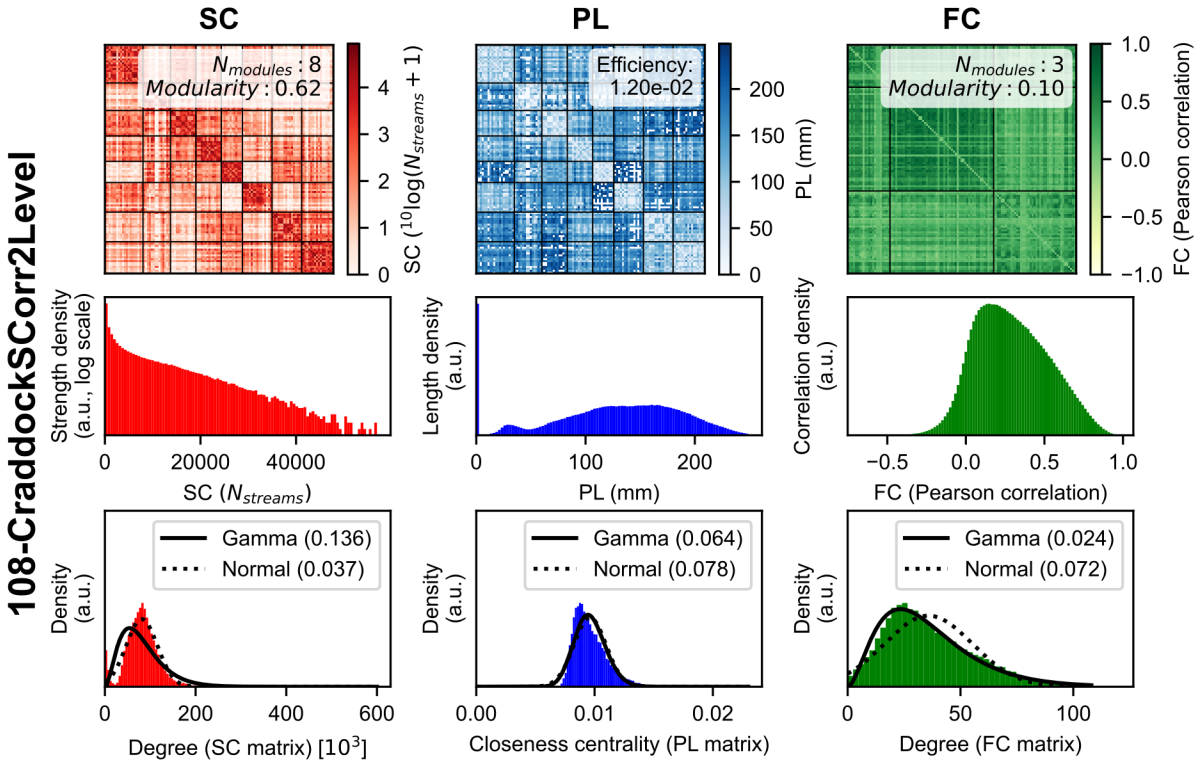
108-CraddockSCorr2Level
SC
PL
FC
$N_{modules}$: 8
Modularity : 0.62
Efficiency: 1.20e-02
$N_{modules}$: 3
Modularity : 0.10
SC (^{10}log($N_{streams}$ + 1))
PL (mm)
FC (Pearson correlation)
Strength density (a.u., log scale)
SC ($N_{streams}$)
Length density (a.u.)
PL (mm)
Correlation density (a.u.)
FC (Pearson correlation)
Density (a.u.)
Gamma (0.136)
Normal (0.037)
Degree (SC matrix) [10^3]
Gamma (0.064)
Normal (0.078)
Closeness centrality (PL matrix)
Gamma (0.024)
Normal (0.072)
Degree (FC matrix)

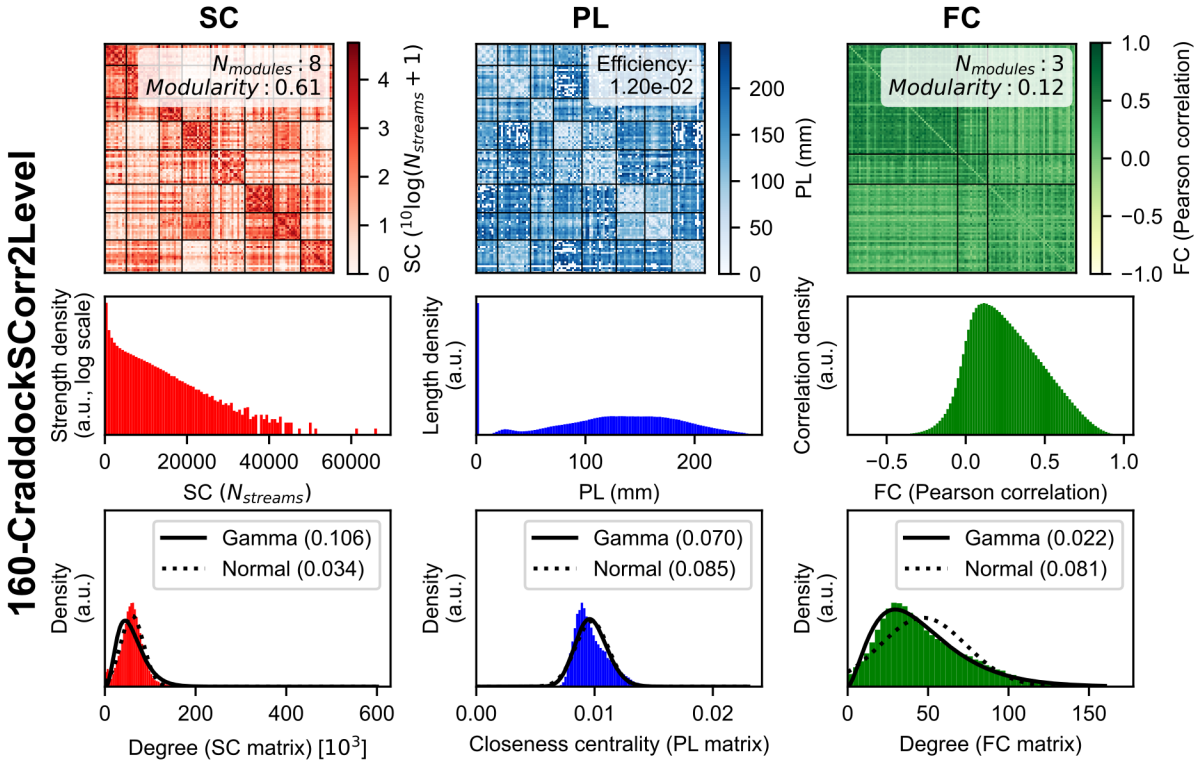
160-CraddockSCorr2Level
SC
PL
FC
$N_{modules}$: 8
Modularity : 0.61
Efficiency: 1.20e-02
$N_{modules}$: 3
Modularity : 0.12
SC (^{10}log($N_{streams}$ + 1))
PL (mm)
FC (Pearson correlation)
Strength density (a.u., log scale)
SC ($N_{streams}$)
Length density (a.u.)
PL (mm)
Correlation density (a.u.)
FC (Pearson correlation)
Density (a.u.)
Gamma (0.106)
Normal (0.034)
Degree (SC matrix) [10^3]
Gamma (0.070)
Normal (0.085)
Closeness centrality (PL matrix)
Gamma (0.022)
Normal (0.081)
Degree (FC matrix)

Shen2013

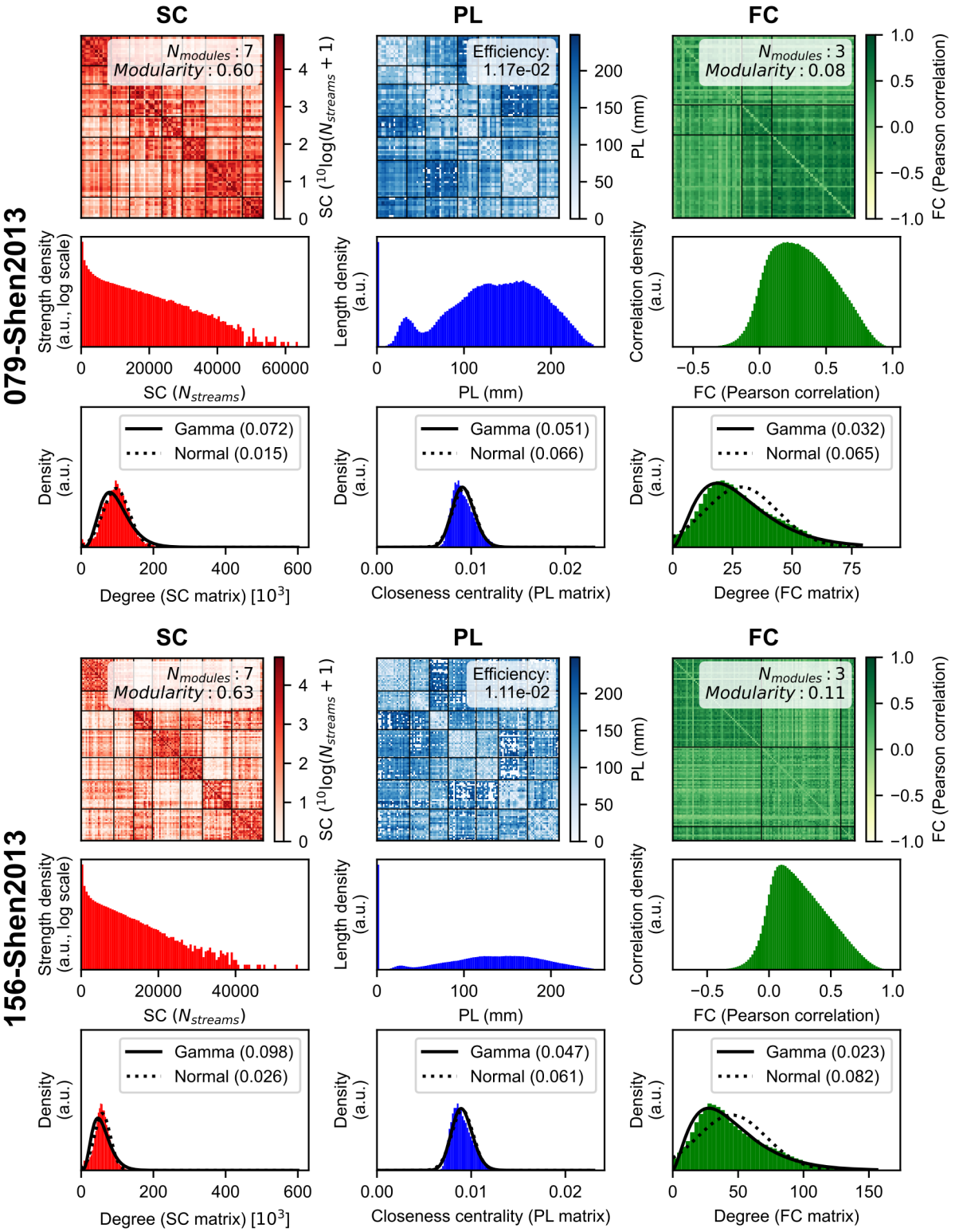
SC
PL
FC
079-Shen2013
$N_{modules}$: 7
Modularity : 0.60
Efficiency: 1.17e-02
$N_{modules}$: 3
Modularity : 0.08
SC (^{10}log($N_{streams}$ + 1))
PL (mm)
FC (Pearson correlation)
Strength density (a.u., log scale)
SC ($N_{streams}$)
Length density (a.u.)
PL (mm)
Correlation density (a.u.)
FC (Pearson correlation)
Gamma (0.072)
Normal (0.015)
Gamma (0.051)
Normal (0.066)
Gamma (0.032)
Normal (0.065)
Density (a.u.)
Degree (SC matrix) [10^3]
Closeness centrality (PL matrix)
Degree (FC matrix)
156-Shen2013
$N_{modules}$: 7
Modularity : 0.63
Efficiency: 1.11e-02
$N_{modules}$: 3
Modularity : 0.11
Gamma (0.098)
Normal (0.026)
Gamma (0.047)
Normal (0.061)
Gamma (0.023)
Normal (0.082)

Schaefer17Networks

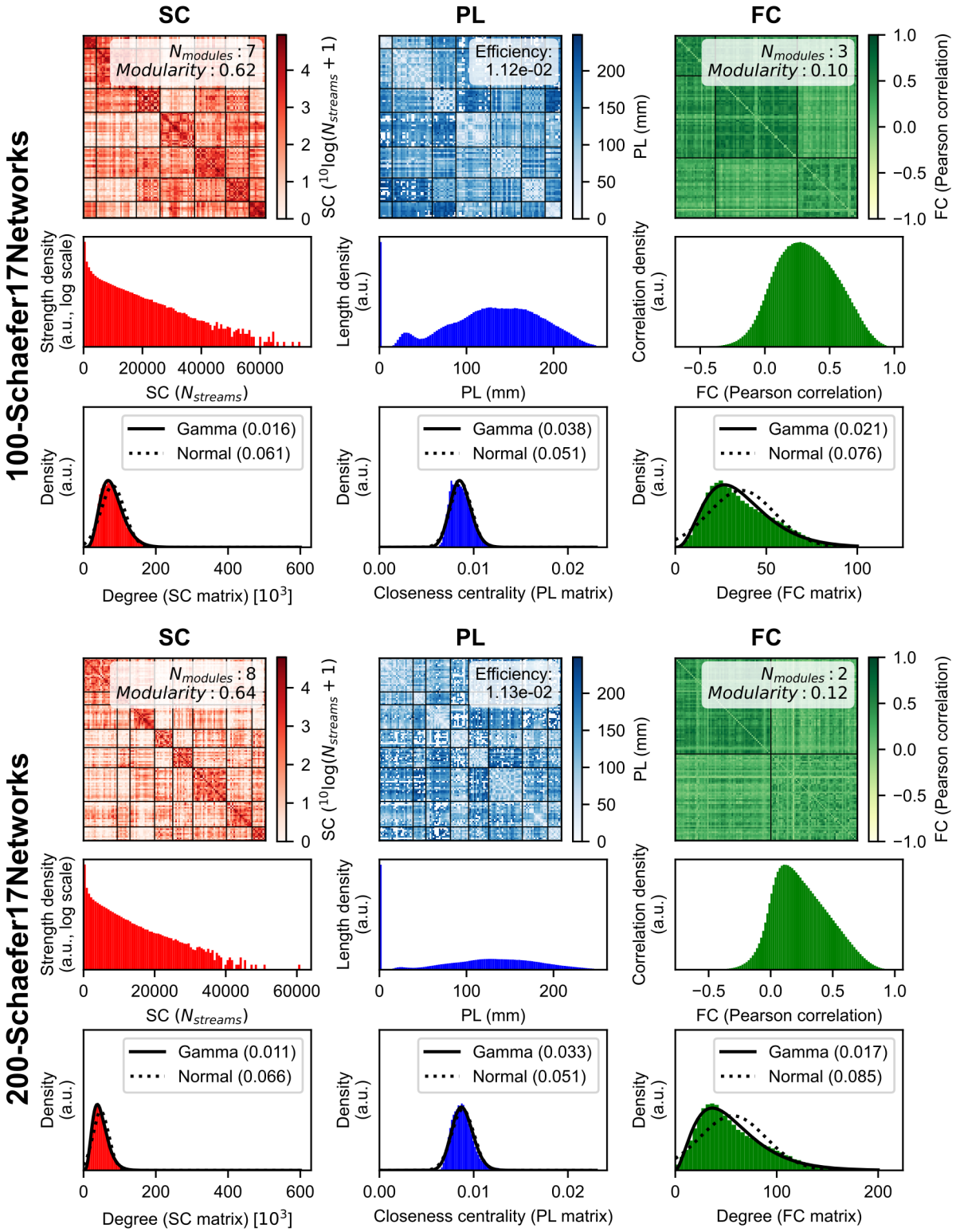

HarvardOxfordMaxProbThr0

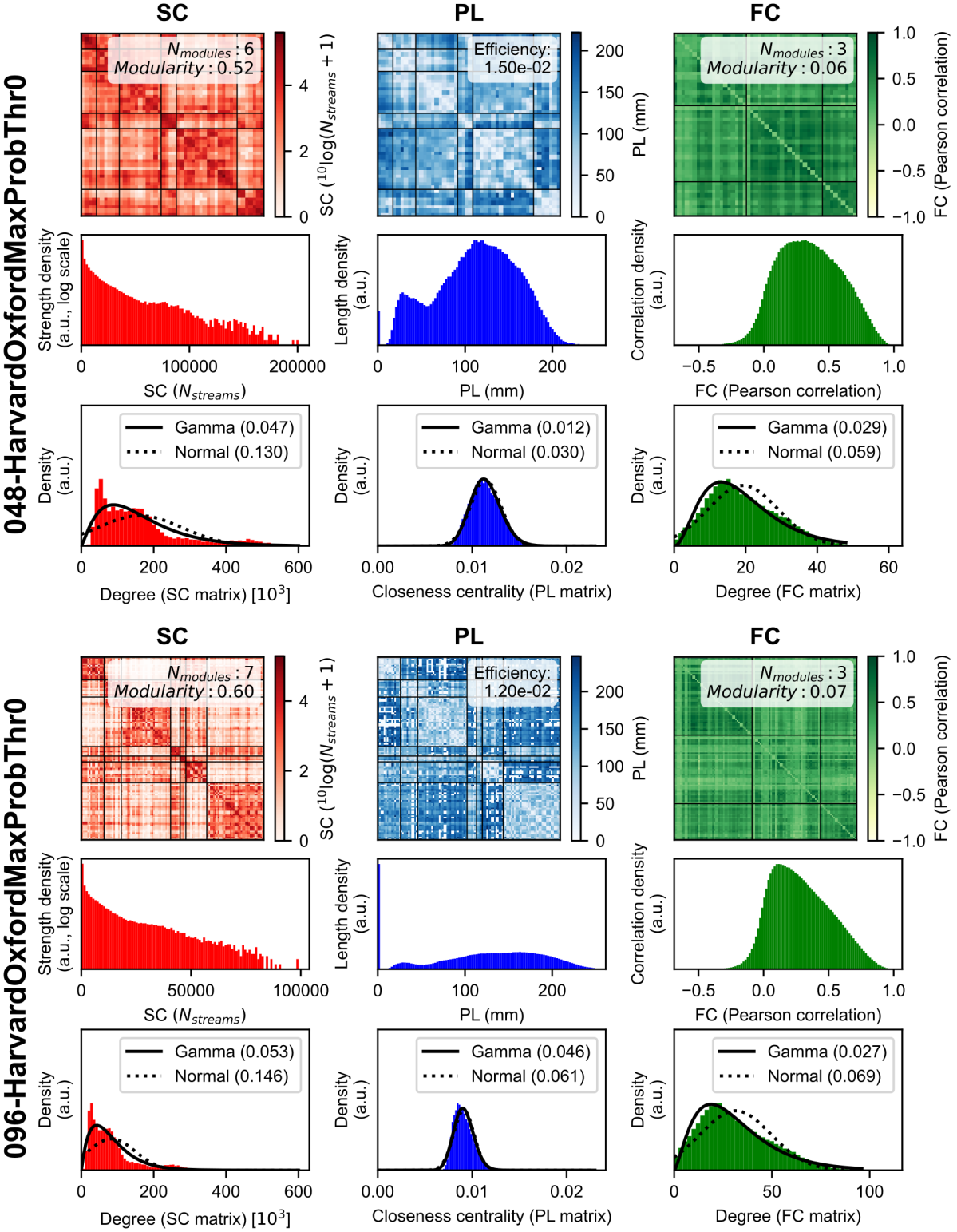

Structural atlases

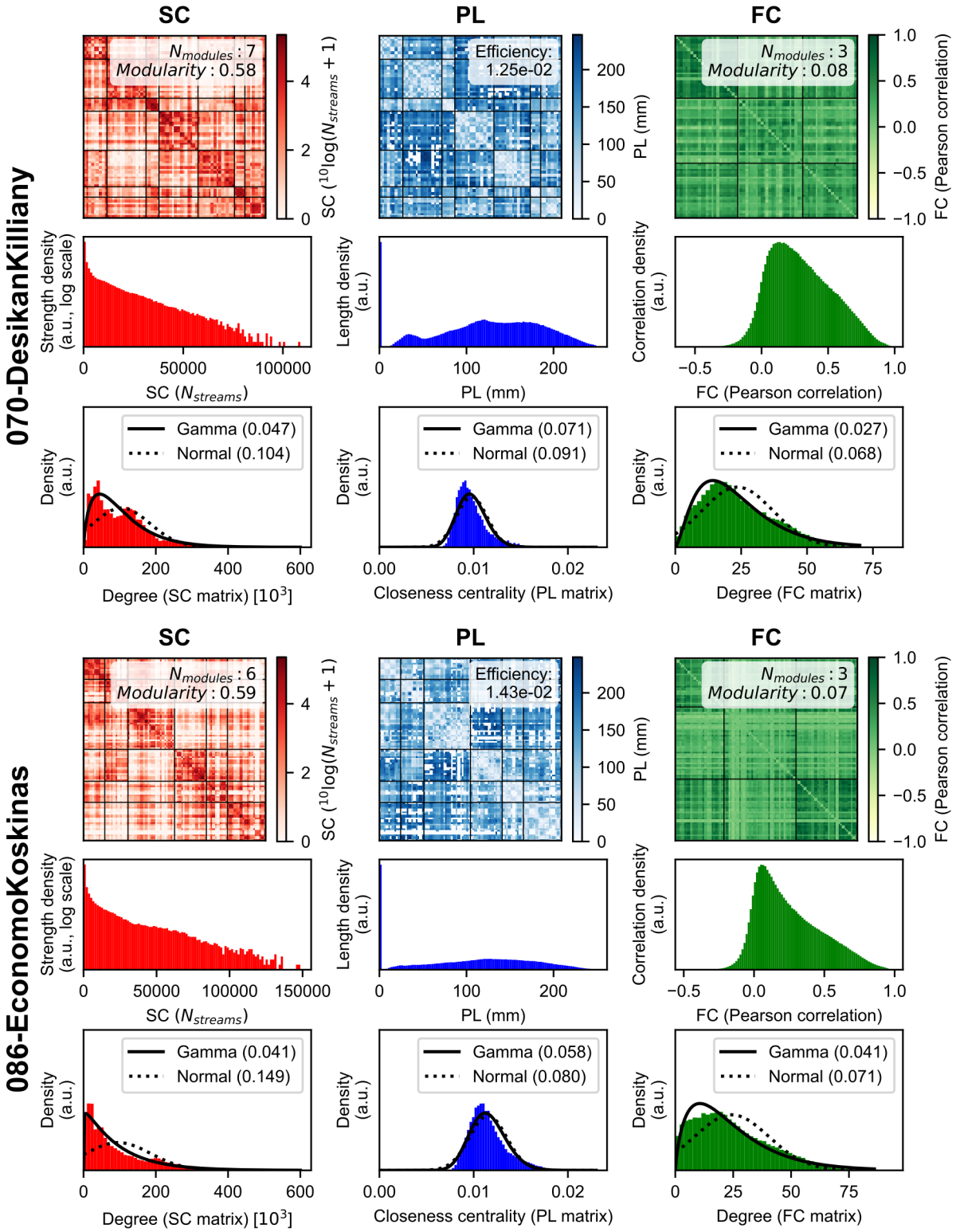

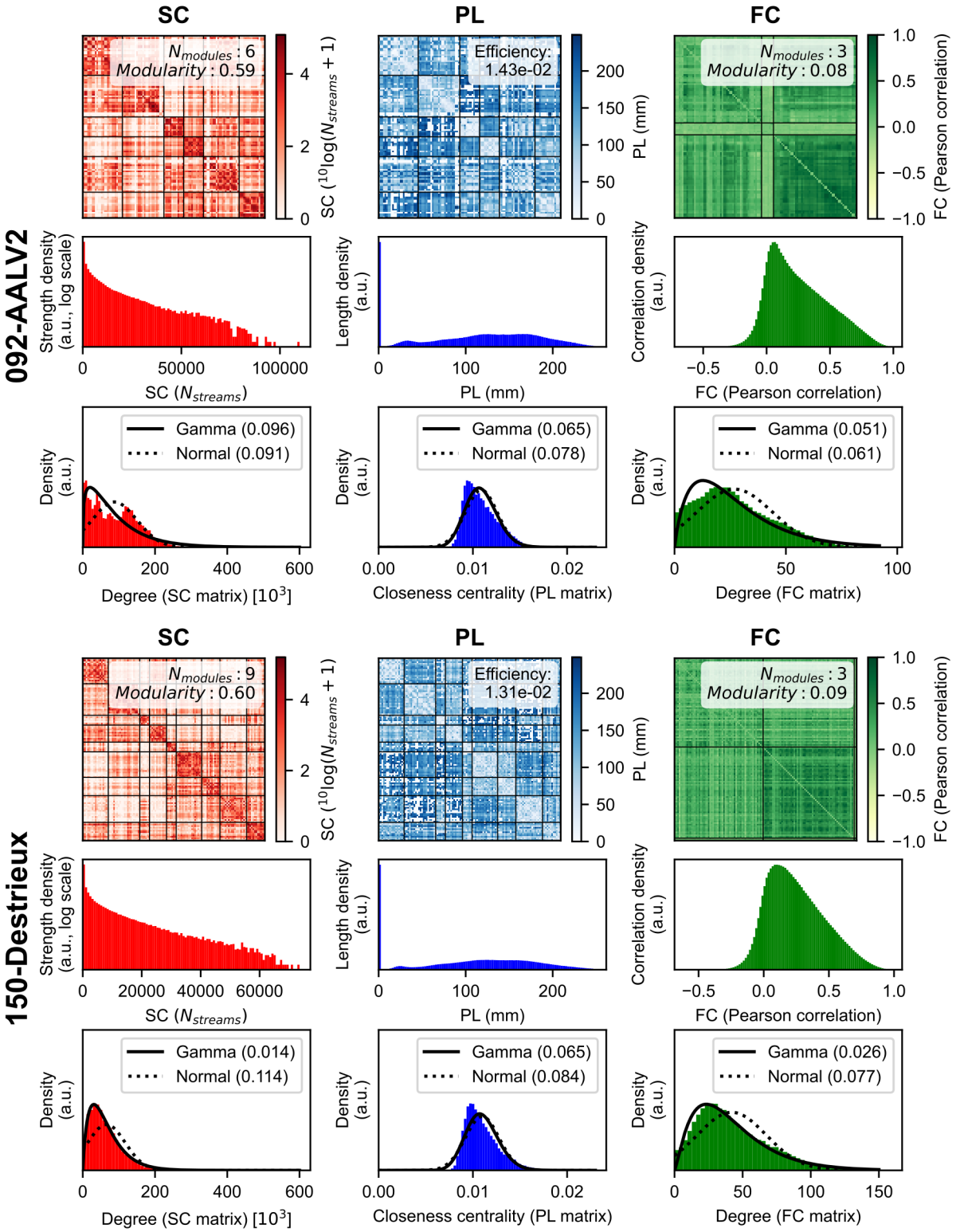
092-AALV2
SC
PL
FC
$N_{modules}$: 6
Modularity : 0.59
Efficiency: 1.43e-02
$N_{modules}$: 3
Modularity : 0.08
SC (^{10}log($N_{streams}$ + 1))
PL (mm)
FC (Pearson correlation)
Strength density (a.u., log scale)
SC ($N_{streams}$)
Length density (a.u.)
PL (mm)
Correlation density (a.u.)
FC (Pearson correlation)
Gamma (0.096)
Normal (0.091)
Gamma (0.065)
Normal (0.078)
Gamma (0.051)
Normal (0.061)
Density (a.u.)
Degree (SC matrix) [10^3]
Closeness centrality (PL matrix)
Degree (FC matrix)
150-Destrieux
SC
PL
FC
$N_{modules}$: 9
Modularity : 0.60
Efficiency: 1.31e-02
$N_{modules}$: 3
Modularity : 0.09
SC (^{10}log($N_{streams}$ + 1))
PL (mm)
FC (Pearson correlation)
Strength density (a.u., log scale)
SC ($N_{streams}$)
Length density (a.u.)
PL (mm)
Correlation density (a.u.)
FC (Pearson correlation)
Gamma (0.014)
Normal (0.114)
Gamma (0.065)
Normal (0.084)
Gamma (0.026)
Normal (0.077)
Density (a.u.)
Degree (SC matrix) [10^3]
Closeness centrality (PL matrix)
Degree (FC matrix)

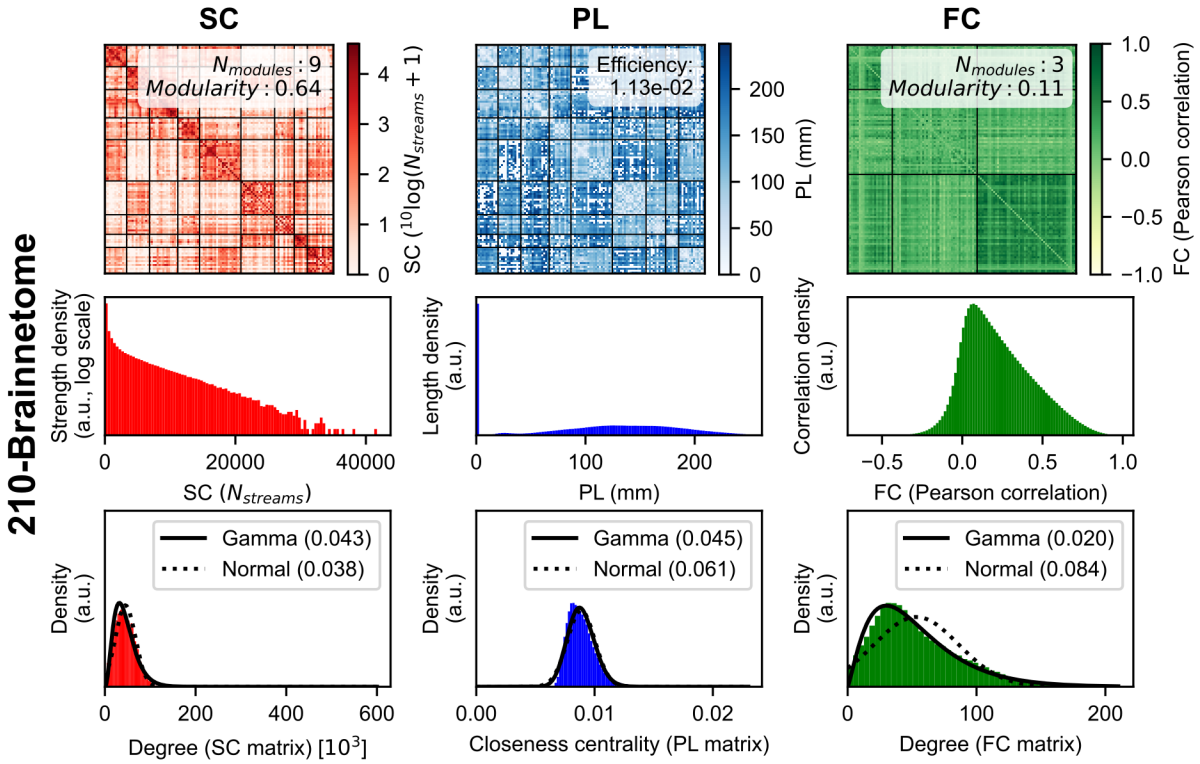
210-Brainnetome
SC
PL
FC
$N_{modules}$: 9
Modularity : 0.64
Efficiency: 1.13e-02
$N_{modules}$: 3
Modularity : 0.11
SC (^{10}log($N_{streams}$ + 1))
PL (mm)
FC (Pearson correlation)
Strength density (a.u., log scale)
SC ($N_{streams}$)
Length density (a.u.)
PL (mm)
Correlation density (a.u.)
FC (Pearson correlation)
Gamma (0.043)
Normal (0.038)
Density (a.u.)
Degree (SC matrix) [10^3]
Gamma (0.045)
Normal (0.061)
Closeness centrality (PL matrix)
Gamma (0.020)
Normal (0.084)
Degree (FC matrix)

Supplementary method

Table 3.1 includes the parcellation schemes that are compared with one another in this study. Here, we provide a summary on the construction of the parcellation schemes, i.e. what methodology was applied to what type of data to construct them. Additionally, we disclose how we modify each brain parcellation image for the purpose of enhancing the comparability between parcellations. These modifications typically comprise the following five steps:

- checking whether the image was sampled to MNI152 non-linear template space,
- ensuring that its spatial resolution was 1 mm (resolution of dwMRI images in the HCP dataset) and that its coordinates were compliant with FSL standards,
- performing any transformations to warp the image to the MNI152 non-linear template space,
- removing any cerebellar and subcortical regions and
- down-sampling the image to a 2 mm spatial resolution (resolution of the fMRI data in the HCP dataset).

In order to ease the procedures required in any of these steps, FreeSurfer's `recon_all` function is applied to acquire the tissue segmentation result corresponding to the MNI152 non-linear template image. From the results of this tissue segmentation, we compile a grey matter mask spanning both hemispheres which we dilute with a 3 mm box kernel. Subsequently, we ensure that the diluted mask is compliant with FSL standards.

MIST atlas parcellations (Urchs et al., 2019)

In order to construct these whole-brain, volume-based parcellations, the functional connectivity data from 198 subjects was clustered using a hierarchical agglomerative clustering algorithm. In this study, we use the 36, 64, 122 and 197 parcels variants of the atlas. However, the comparability enhancing image modifications left respectively 31, 56, 103 and 167 parcels in the images. The details of these modifications are described below.

1. The parcellation images are in the MNI152 non-linear template space.
2. The images have a resolution of 3 mm. To correct for this mismatch, we
    - reorient the images to FSL's standard orientation,
    - make a 3 mm resolution variant of the MNI152 non-linear template image by down-sampling the 1 mm resolution original,
    - co-register the parcellation images to this 3 mm variant,
    - linearly transform the 3 mm resolution MNI152 non-linear template image to its 1 mm resolution original and
    - warp the parcellation images to obtain their 1 mm variant.
3. As the parcellation images are now already in the appropriate MNI152 non-linear template space, we are not required to perform any additional transformations.
4. The parcellation images contain cerebellar and subcortical regions, which are eliminated by multiplying the atlas images with the diluted grey matter mask (see above) and subsequently removing invaluable labels from the parcellation images; here, the total volume occupied by a parcel is required to be at least 500 voxels.
5. The parcellation images are down-sampled to a spatial resolution of 2 mm.

Craddock atlas parcellations (Craddock et al., 2012)

In order to construct these whole-brain, volume-based parcellations, the functional connectivity data from 41 subjects was clustered using a spectral clustering algorithm. We consider the parcellations that were realised by applying a two-level group clustering scheme to the spatial

correlations between functional connectivity maps. We take the 40, 60, 120 and 180 parcels variants and modify them to enhance their comparability; respectively 38, 56, 108 and 160 parcels still remain in the parcellation images after these modifications. The details of these modifications are described below.

1. The parcellation images are in the MNI152 non-linear template space.
2. The images have a resolution of 4 mm. To correct for this mismatch, we
    - first dilute the images with a 12 mm box kernel to account for the rather poor resolution,
    - reorient the images to FSL's standard orientation,
    - make a 4 mm resolution variant of the MNI152 non-linear template image by down-sampling the 1 mm resolution original,
    - co-register the parcellation images to this 4 mm variant,
    - linearly transform the 4 mm resolution MNI152 non-linear template image to its 1 mm resolution original and
    - warp the parcellation images to obtain their 1 mm variant.
3. As the parcellation images are now already in the appropriate MNI152 non-linear template space, we are not required to perform any additional transformations.
4. The parcellation images contain cerebellar and subcortical regions, which are eliminated by multiplying the atlas images with the diluted grey matter mask (see above) and subsequently removing invaluable labels from the parcellation images; here, the total volume occupied by a parcel is required to be at least 500 voxels.
5. The parcellation images are down-sampled to a spatial resolution of 2 mm.

Shen 2013 atlas parcellations *(Shen et al., 2013)*

In order to construct these whole-brain, volume-based parcellations, the functional connectivity data from 79 subjects was clustered using a multigraph k-way clustering algorithm. In this study, we take the 100 and 200 parcels variants and modify them to enhance their comparability; respectively 79 and 156 parcels still remain in the parcellation images after these modifications. The details of these modifications are described below.

1. The parcellation images are in the MNI152 non-linear template space.
2. The images have a resolution of 1 mm, but the coordinates and folding patterns are not consistent with the MNI152 non-linear template. To correct for these mismatches, we
    - first dilute the images with a 3 mm box kernel to account for the incompatible folding patterns,
    - reorient the images to FSL's standard orientation,
    - co-register the parcellation images to the 1 mm MNI152 non-linear template image.
3. As the parcellation images are now already in the appropriate MNI152 non-linear template space, we are not required to perform any additional transformations.
4. The parcellation images contain cerebellar and subcortical regions, which are eliminated by multiplying the atlas images with the diluted grey matter mask (see above) and subsequently removing invaluable labels from the parcellation images; here, the total volume occupied by a parcel is required to be at least 500 voxels.
5. The parcellation images are down-sampled to a spatial resolution of 2 mm.

Schaefer atlas parcellations *(Schaefer et al., 2018)*

Voxels were grouped together by applying a gradient-weighted Markov Random Field to the functional connectivity data from 1489 subjects. The result was published as a cortical, surface-based atlas. In this study, we use the 100 and 200 parcels variants. Because the parcellations are surface-based, we sample these parcellations in the volumetric MNI152 non-linear template

space using the results from the `recon_all` function that was applied to the MNI152 non-linear template image. The rest of the parcellation image modifications is described below.

1. The parcellation images are already in the right standard space, because the atlas is sampled through the use of the MNI152 non-linear template image.
2. The spatial resolution is correct, but the coordinates are not consistent with FSL standards.The parcellation images are assigned the right coordinates through the use of the results from the `recon_all` function.
3. As the parcellation images are now already in the appropriate MNI152 non-linear template space, we are not required to perform any additional transformations.
4. The parcellation images do not contain cerebellar or subcortical regions; still, the parcels are thinner than the other parcellation images and are therefore diluted with a 3 mm box kernel to ensure they cover a similar cortical volume.
5. The parcellation images are down-sampled to a spatial resolution of 2 mm.

Harvard-Oxford atlas parcellations *(Desikan et al., 2006; Frazier et al., 2005; Goldstein et al., 2007; Makris et al., 2006)*

In order to construct these volumetric parcellations, the cortical folding patterns of 37 subjects were analysed using semi-automated tools developed by the Harvard-Center for Morphometric Analysis. We use the maximum probability, 0% threshold, cortical variants with 48 (without hemispheric separation) and 96 (with hemispheric separation) parcels. The details of the modifications applied to these parcellations are listed below.

1. The parcellation images are in the MNI152 non-linear template space.
2. The images have a resolution of 1 mm and their coordinates are consistent with the MNI152 non-linear template.
3. The parcellation images are already in the appropriate MNI152 non-linear template space.
4. The parcellation images do not contain cerebellar and subcortical regions. Still, parcels occupy a relatively large cortical volume. To correct for this, we multiply the parcellation images with the diluted grey matter mask (see above).
5. The parcellation images are down-sampled to a spatial resolution of 2 mm.

Desikan-Killiany atlas *(Desikan et al., 2006)*

The structural MRI data of 40 subjects were analysed by a registration procedure that aligns the cortical folding patterns to create this surface-based parcellation. Because the parcellation is surface-based, the same procedures as described for the Schaefer atlas are applicable here.

Von Economo-Koskinas atlas *(Scholtens et al., 2018; von Economo & Koskinas, 1925)*

20 human brains were analysed using histological tools in order to identify strong, spatial gradients regarding cytoarchitectonic properties. These gradients were then assumed to represent the boundaries of cortical regions. The original parcellation has been digitised and is available as a surface-based parcellation. Because the parcellation is surface-based, the same procedures as described for the Schaefer atlas are applicable here.

AAL atlas (version 2) *(Rolls et al., 2015; Tzourio-Mazoyer et al., 2002)*

The structural MRI data of 1 subject was analysed by a boundary detection algorithm called VoxeLine to create this volume-based parcellation. The original parcellation contains 120 parcels, but after we modified its image in order to enhance comparability only 92 cortical parcels remained. The details of these modifications are described below.

1. The parcellation image is not in the MNI152 non-linear template space, but in the Colin27 linear template space.
2. As the atlas is not in the MNI152 non-linear template space, checking its coordinates and resolution is irrelevant.
3. Since the atlas is not in the MNI152 non-linear template space, it first has to be transformed to it. In order to do this we
    - reorient the parcellation and its original template image to FSL standards,
    - extract the brain from the original template image by multiplying it with its mask,
    - decrease the spatial resolution of the original template to 2 mm to ease the non-linear transformation to the MNI152 non-linear template space,
    - co-register the original template brain with the MNI152 non-linear template brain image with 2 mm resolution,
    - non-linearly transform the original template brain to the MNI152 non-linear template brain image with 2mm resolution,
    - warp the parcellation image to the MNI152 non-linear template space with 2 mm resolution,
    - co-register the MNI152 non-linear 2 mm template brain with its 1 mm variant and, finally,
    - warp the parcellation image to the 1 mm MNI152 non-linear template space.
4. The parcellation image contains cerebellar and subcortical regions, which are eliminated by multiplying the atlas images with the diluted grey matter mask (see above) and subsequently removing invaluable labels from the parcellation images; here, the total volume occupied by a parcel is required to be at least 500 voxels.
5. The parcellation images are down-sampled to a spatial resolution of 2 mm.

Destrieux atlas *(Destrieux et al., 2010)*

The structural MRI data of 12 subjects was analysed in order to divide the brain into gyral and sulcal regions. This division was performed through a consideration of surface curvature and convexity values as well as prior labelling probabilities and neighbouring labels. The parcellation is surface-based and therefore the same procedures as described for the Schaefer atlas are applicable here.

Brainnetome atlas *(Fan et al., 2016)*

The structural connectivity data from 40 subjects was clustered using a spectral clustering algorithm to create this parcellation. We use the surface-based cortical version of the parcellation. Because the parcellation is surface-based, the same procedures as described for the Schaefer atlas are applicable here.

Supplementary results

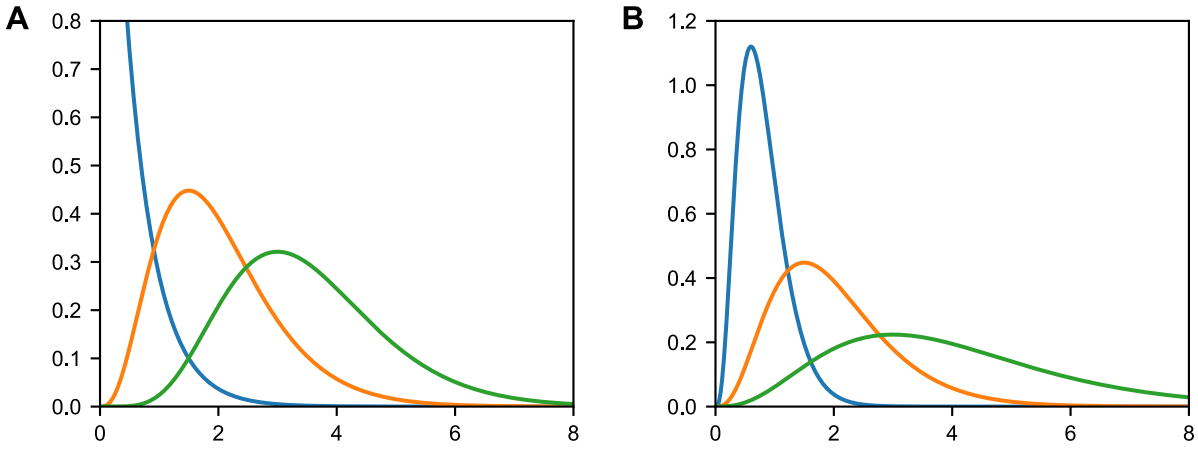

Fig. S3.1. (A) Gamma probability distribution function for fixed scale parameter $\theta = 0.5$ and varying shape parameter k. Blue, orange and green correspond to $k = 1$, $k = 4$ and $k = 7$, respectively. **(B)** Gamma probability distribution function for fixed shape parameter $k = 4$ and varying scale parameter θ. Blue, orange and green correspond to $\theta = 0.2$, $\theta = 0.5$ and $\theta = 1.0$, respectively.

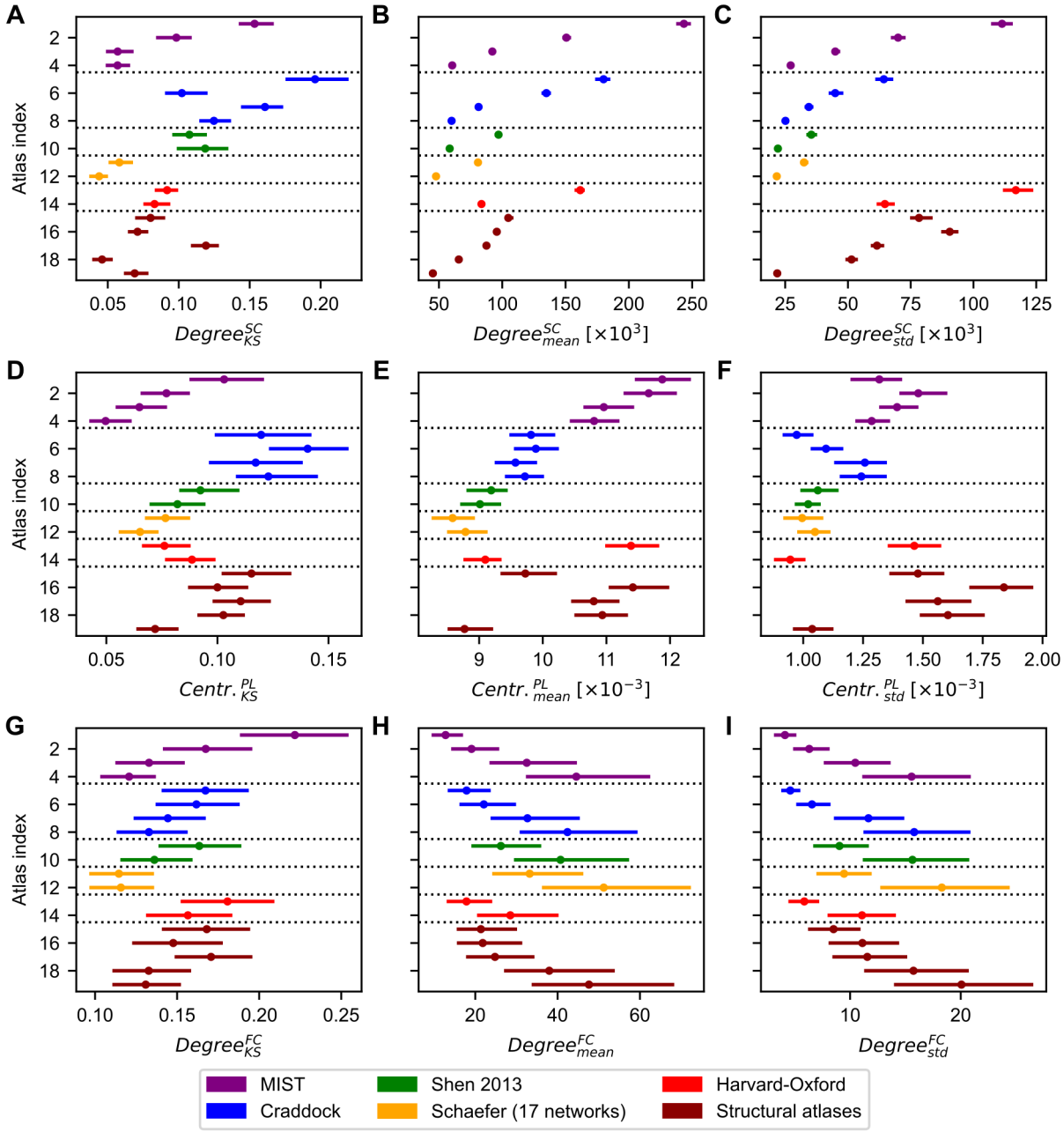

Fig. S3.2. **(A-C)** Kolmogorov-Smirnov (KS) statistics of the fit of the gamma distribution to the empirical degree distribution of the structural connectivity (SC) (A) and the mean (B) and the standard deviation (C) of that type of degree. **(D-F)** Same quantities as in panel A to C but for the closeness centrality of the path length (PL) matrix. **(G-I)** Same quantities as in panel A to C but for the degree of the functional connectivity (FC) matrix. Dots and lines depict the medians and interquartile ranges across subjects, respectively, and the atlas indices on the vertical axes correspond to those in Table 3.1 which contains the information about the used parcellations. Abbreviations: centr. = closeness centrality.

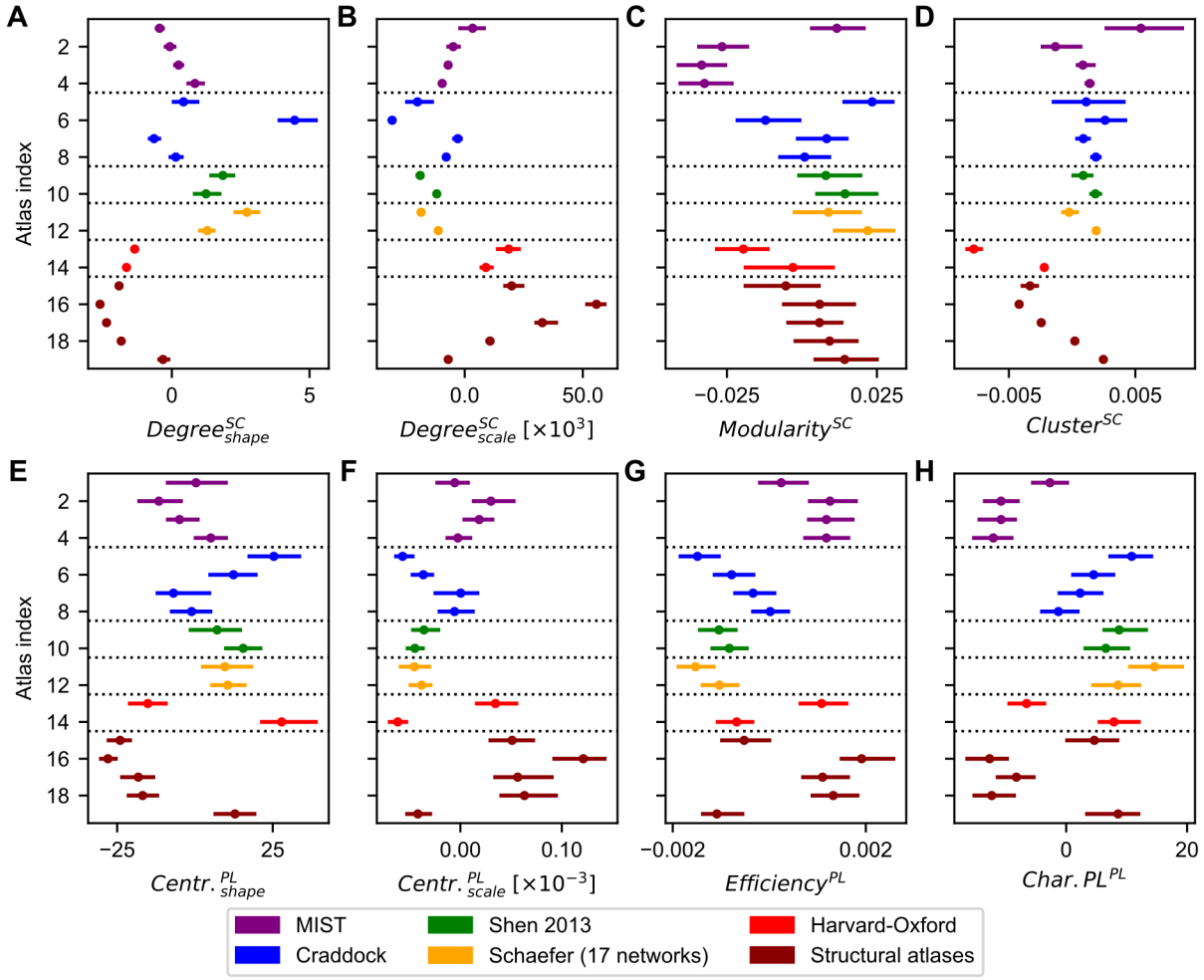

Fig. S3.3. (A-D) Statistics extracted from the structural connectivity (SC) matrices, which are the shape (A) and scale (B) parameters of the degree distributions, the modularities (C) and the clustering coefficients (D). **(E-H)** Statistics extracted from the path length (PL) matrices, which are the shape (E) and scale (F) parameters of the closeness centrality distributions, the global efficiencies (G) and the characteristic path lengths (H). Dots and lines depict the medians and interquartile ranges across subjects, respectively. The atlas indices on the vertical axes correspond to those in Table 3.1 which contains the information about the used parcellations. The difference between these plots and those shown in Fig. 3.2 is that here the effect of granularity has been regressed out. Abbreviations: Centr. = closeness centrality, Char.PL = characteristic path length.

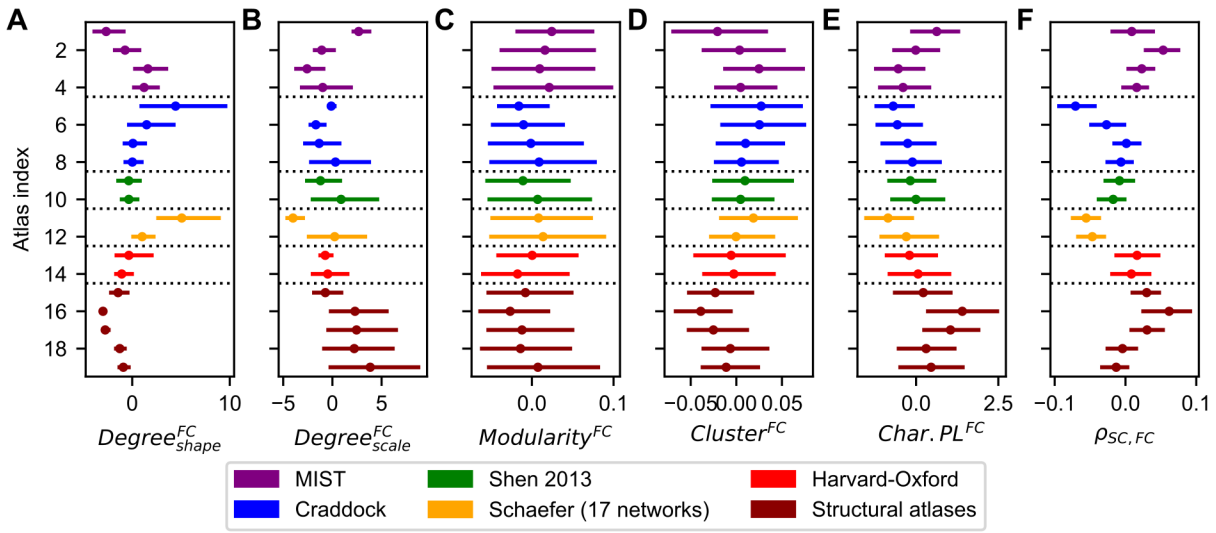

Fig. S3.4. (A-E) Statistics extracted from the empirical FC matrices, which are the shape (A) and scale (B) parameters of their degree distributions, their modularities (C), their clustering coefficients (D) and their characteristic path lengths (E). **(F)** Pearson correlation coefficients corresponding to the structure-function relationship between the upper triangular parts (excluding diagonal) of the empirical SC and FC matrices. Dots and lines depict the medians and interquartile ranges across subjects, respectively. The atlas indices on the vertical axes correspond to those in Table 3.1 which contains the information about the used parcellations. The difference between these plots and those shown in Fig. 3.3 is that here the effect of granularity has been regressed out. Abbreviations: Char.PL = characteristic path length.

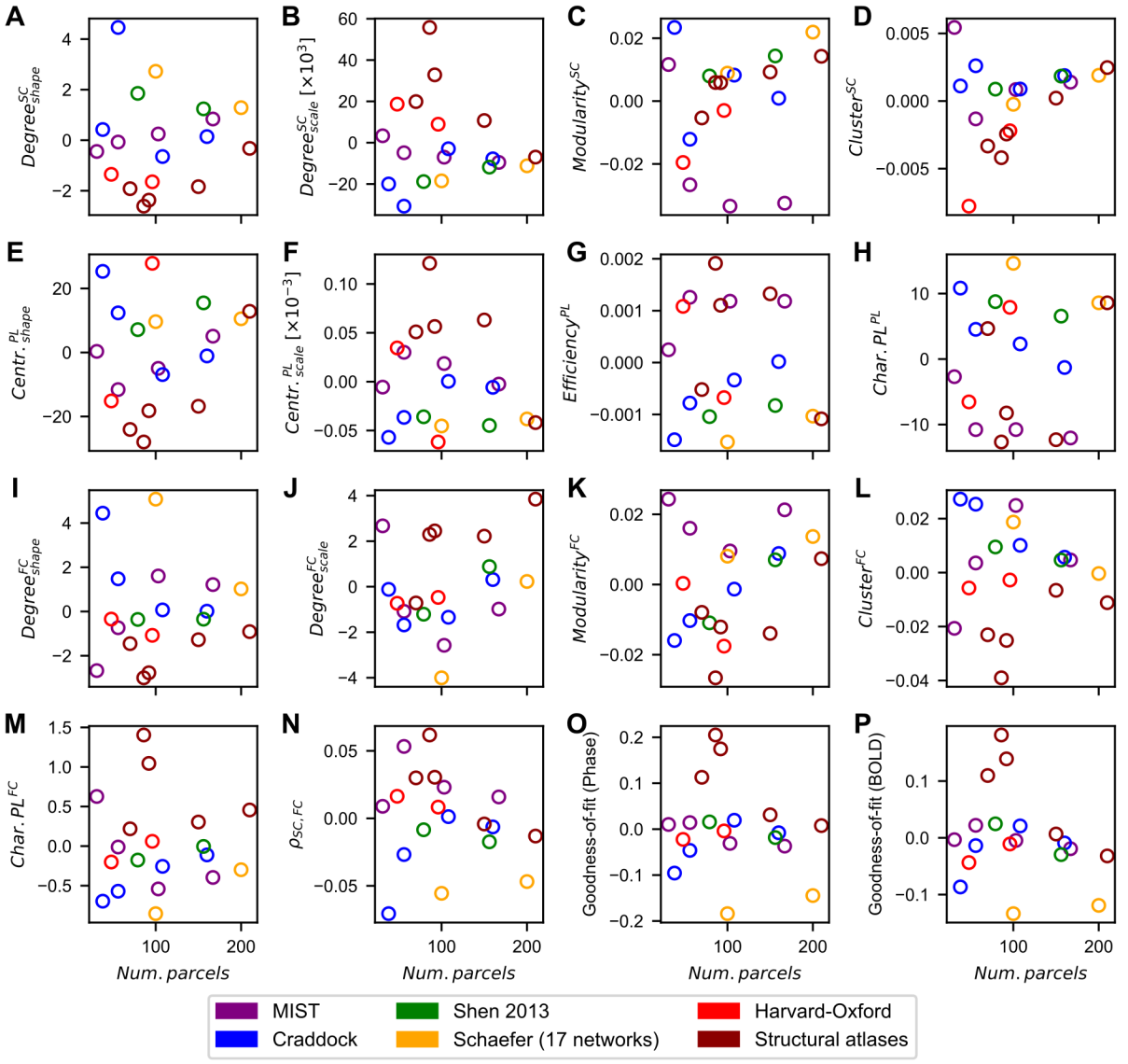

Fig. S3.5. Same as Fig. 3.4, though with the difference that in these plots the measures are plotted as functions of the number of parcels instead of its inverse and that the granularity effects displayed in Fig. 3.4 have been regressed out. Each dot corresponds to a particular atlas. Abbreviations: Centr. = closeness centrality, Char.PL = characteristic path length.

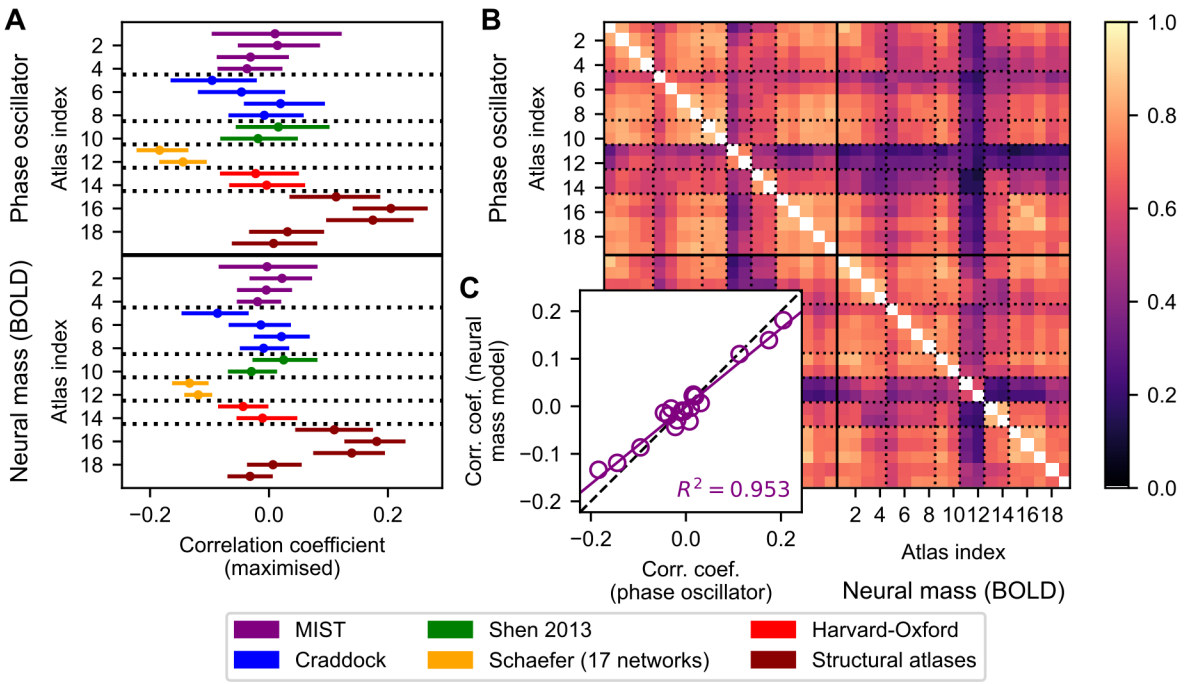

Fig. S3.6. **(A)** Maximised correlations (goodness-of-fit) between the empirical and simulated FC matrices for the brain parcellation schemes and models investigated in this study as indicated on the vertical axes. Dots and lines depict the medians and interquartile ranges across subjects, respectively. **(B)** Correlations across subjects of the goodness-of-fit of the model between the considered parcellations and models. Table 3.1 contains the parcellation information corresponding to the atlas indices used in the plots. **(C)** Scatter plot of the medians of the goodness-of-fit corresponding to the phase oscillator (x-axis) and neural mass model (y-axis) across subjects. Each dot corresponds to a particular parcellation, the purple line portrays the linear regression between both types of goodness-of-fit and the black dashed line corresponds to $x = y$. The difference between these plots and those shown in Fig. 3.6 is that here the effect of granularity has been regressed out.

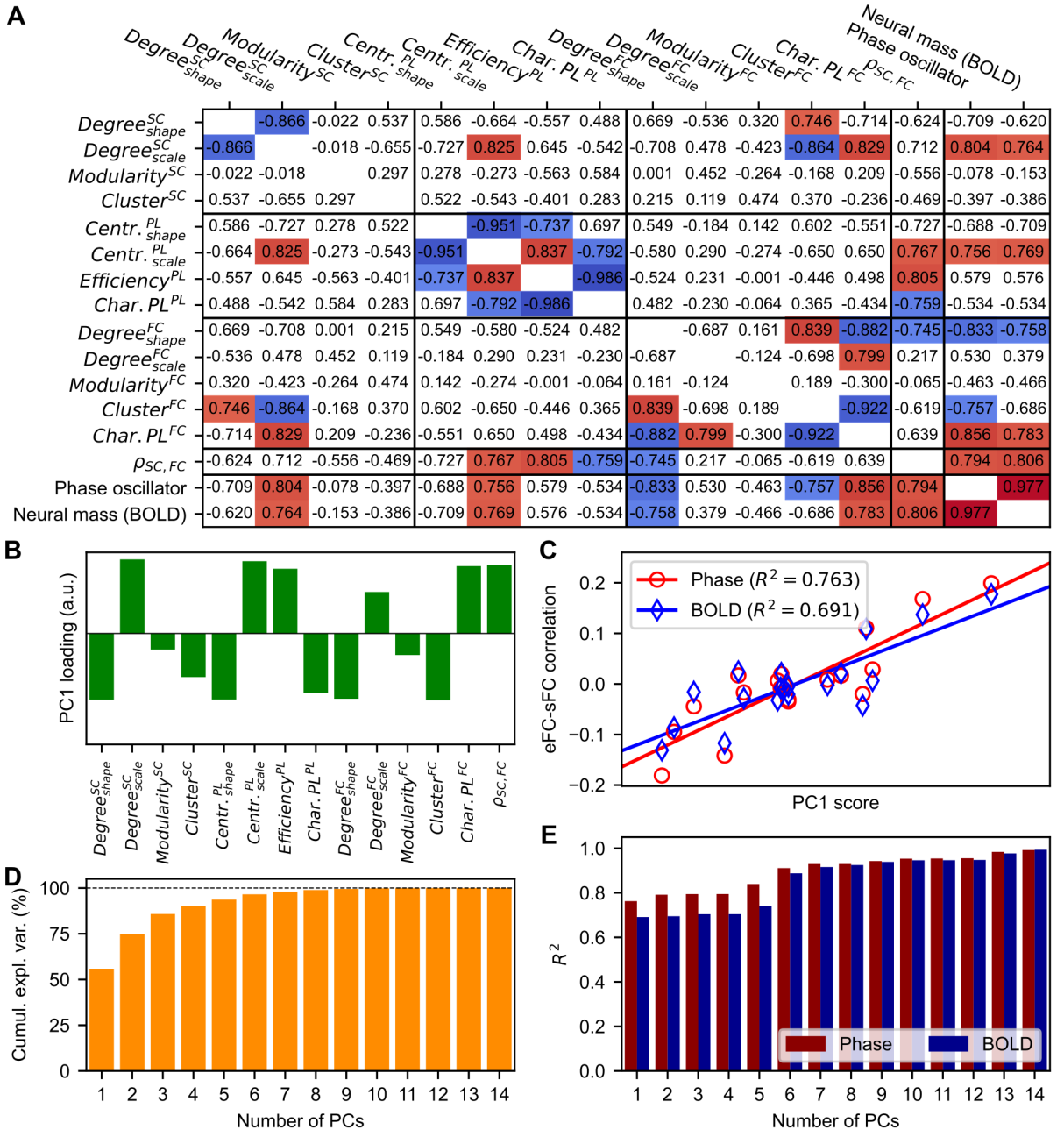

Fig. S3.7. **(A)** Cross-correlations among the graph-theoretical measures of the empirical connectomes (network properties depicted in Fig. 3.2 and Fig. 3.3), the structure-function relationship and the goodness-of-fit of the models to the empirical data. The correlation was calculated across parcellations between the median values over all subjects. Significant correlations are highlighted by colours ($p<0.05$, two-sided, Bonferroni corrected). **(B)** Loadings of the first (PC1) principal component of the group-averaged graph-theoretical metrics, i.e. the contributions of the original empirical data variables to PC1. **(C)** Regressions of the PC1 scores with the medians of the goodness-of-fit between empirical (eFC) and simulated (sFC) functional connectivity. The medians were calculated across subjects for each considered parcellation for the phase oscillator (red) and the neural mass model (blue) as indicated in the legend together with the fraction of the explained variance. The symbols stand for the individual parcellations from Table 3.1. **(D)** Cumulative amount of explained variance in the group-averaged graph-theoretical measures as a function of the number of included PCs. **(E)** Fraction of the interparcellation variance of the goodness-of-fit being explained by the (multivariate) linear regression model as a function of the number of PCs included in the model. The difference between these plots and those shown in Fig. 3.7 is that here the effect of granularity has been regressed out. Other abbreviation: a.u. = arbitrary unit, cumul. = cumulative, expl. = explained, var. = variance.

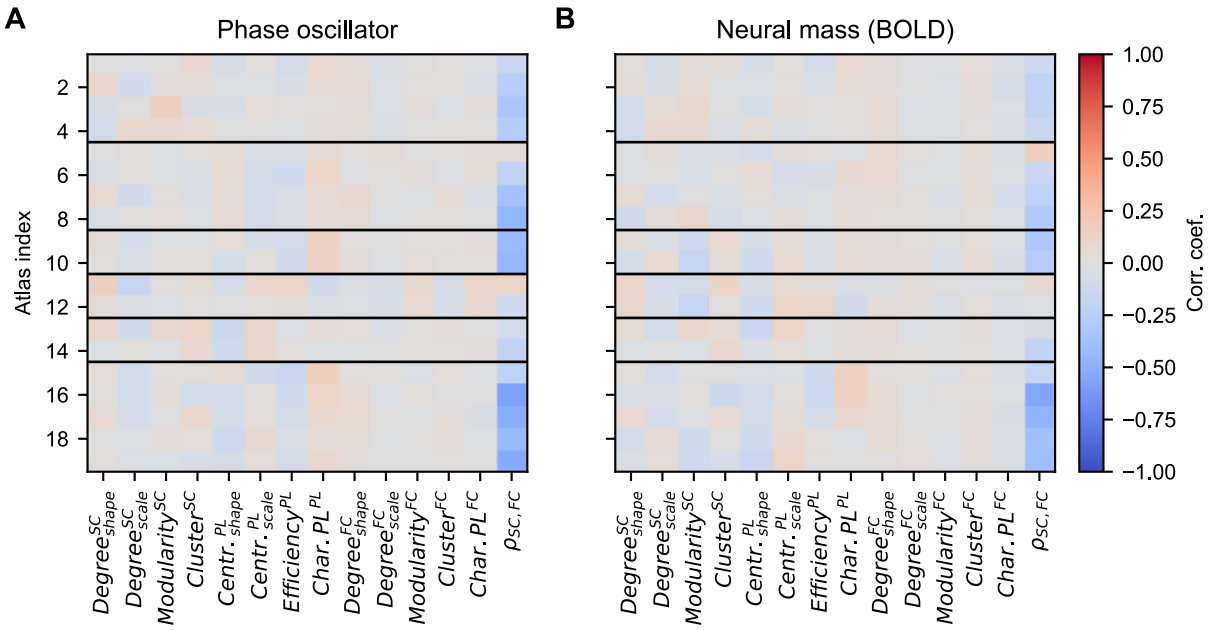

Fig. S3.8. Pearson correlation coefficients between the goodness-of-fit and the empirical data variables shown in Fig. 3.2 and Fig. 3.3 across subjects per parcellation for the phase oscillator (A) and the electrical model (B). Table 3.1 contains the parcellation information corresponding to the atlas indices used in the plots. Abbreviations: coef. = coefficient, corr. = correlation.

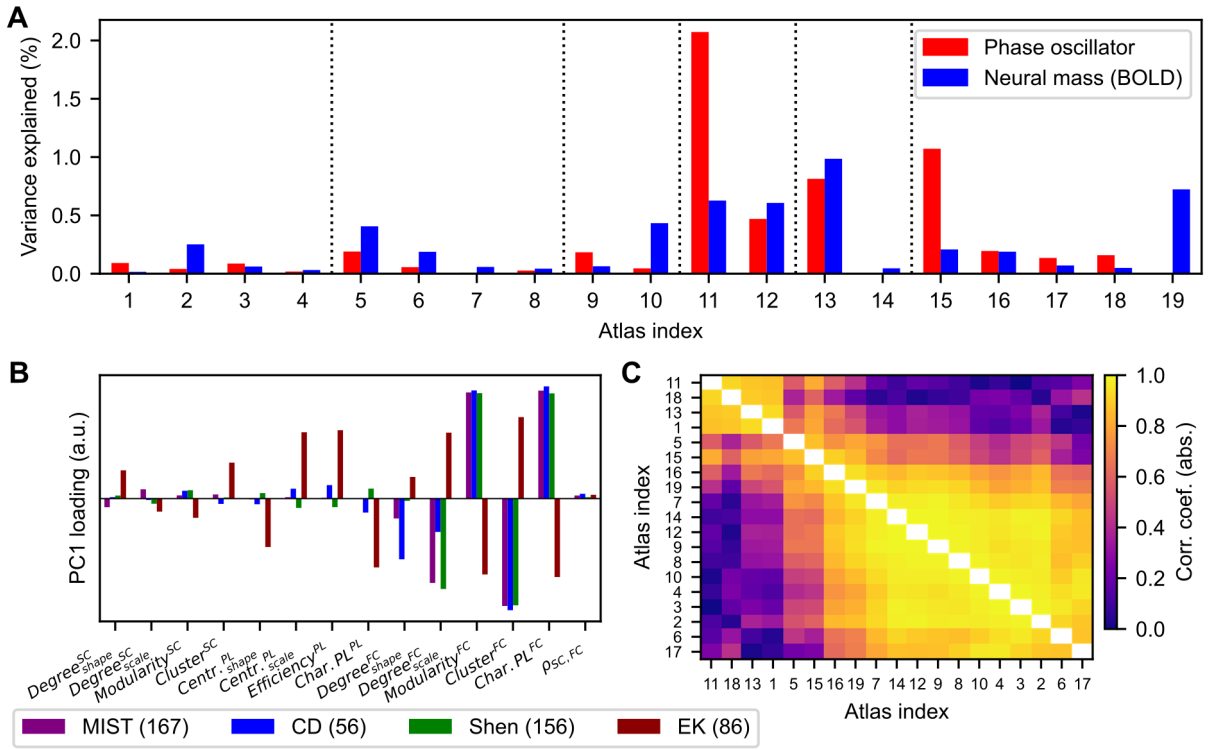

Fig. S3.9. **(A)** Amounts of within-parcellation, between-subject variance in the modeling results being explained by the combination of principal component analysis with univariate, ordinary least squares linear regression (same approach as in Fig. 3.7B-E) per parcellation. Modeling results are sampled by using the coupled phase oscillators (red) and neural mass models (blue) and comprise the maximised correlation coefficients between the upper triangles of the empirical and simulated functional connectivity matrices excluding the diagonals. **(B)** Loadings of the first principal component (PC1) corresponding to the data variables depicted in Fig. 3.2 and Fig. 3.3 for a selection of 4 brain parcellation schemes. The abbreviations "Shen (79)", "Sch. (100)", "HO (96)" and "EK (86)" correspond to the parcellations in Table 3.1 with indices 9, 11, 14 and 16, respectively. **(C)** Absolute values of the Pearson correlation coefficients across the loadings per pair of brain parcellation. Table 3.1 contains the parcellation information corresponding to the atlas indices used in the plots. Other abbreviations: abs. = absolute value, coef. = coefficient, corr. = correlation.

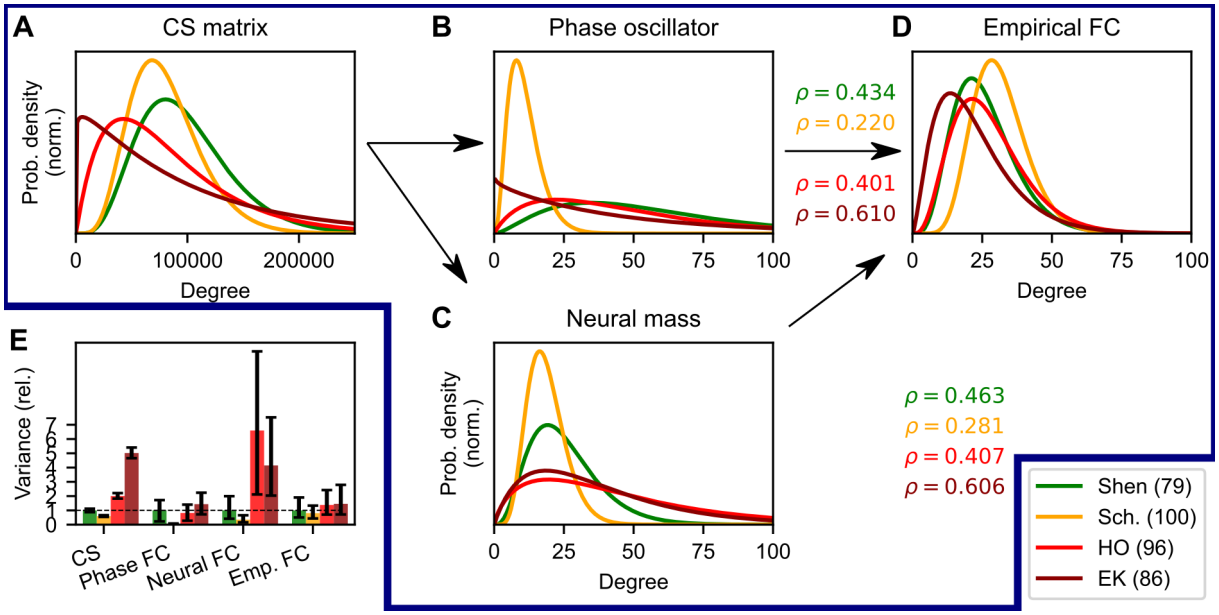

Fig. S3.10. (A) Characteristic degree distributions of the connection strength (CS) matrices for a selection of 4 parcellation schemes. **(B-D)** Same as panel A but here the empirical (emp. FC, D) and simulated functional connectivity matrices corresponding to the phase oscillator (phase FC, B) and neural mass (neural FC, C) models that provided the best fit are considered. Distributions are shown as normalised probability density functions and are constructed using the medians of their corresponding parameters across subjects. Coloured texts denote the median maximised correlation coefficients. **(E)** Relative variances included in the degree distributions. Bars and errorbars depict the medians and interquartile ranges across subjects. The abbreviations "Shen (79)", "Sch. (100)", "HO (96)" and "EK (86)" correspond to the parcellations in Table 3.1 with indices 9, 11, 14 and 16, respectively.

Chapter 4

Study 2: Reliability and subject specificity of personalized whole-brain dynamical models

Justin W. M. Domhof [1,2], Simon B. Eickhoff [1,2] and Oleksandr V. Popovych [1,2]

[1]Institute of Neuroscience and Medicine, Brain and Behaviour (INM-7), Research Centre Jülich, Jülich, Germany
[2]Institute for Systems Neuroscience, Medical Faculty, Heinrich Heine University Düsseldorf, Düsseldorf, Germany

First published in NeuroImage (2022; https://doi.org/10.1016/j.neuroimage.2022.119321)
under a Creative Commons Attribution 4.0 International License (CC BY 4.0)
© 2022 Domhof, Eickhoff & Popovych

Own contributions according to CRediT (75%):

- **Conceptualization** (design of the study)
- **Data curation** (data management)
- **Formal analysis** (analysis of modeling results and their relation with empirical data)
- **Investigation** (acquisition of connectomes and results)
- **Methodology** (inventory of models and statistics to consider)
- **Software** (implementation of computational procedures)
- **Validation** (comparison of results with the literature)
- **Visualization** (design of figures)
- **Writing - original draft**
- **Writing - review and editing**

Abstract

Dynamical whole-brain models were developed to link structural (SC) and functional connectivity (FC) together into one framework. Nowadays, they are used to investigate the dynamical regimes of the brain and how these relate to behavioral, clinical and demographic traits. However, there is no comprehensive investigation on how reliable and subject specific the modeling results are given the variability of the empirical FC. In this study, we show that the parameters of these models can be fitted with a ”poor” to ”good” reliability depending on the exact implementation of the modeling paradigm. We find, as a general rule of thumb, that enhanced model personalization leads to increasingly reliable model parameters. In addition, we observe no clear effect of the model complexity evaluated by separately sampling results for linear, phase oscillator and neural mass network models. In fact, the most complex neural mass model often yields modeling results with ”poor” reliability comparable to the simple linear model, but demonstrates an enhanced subject specificity of the model similarity maps. Subsequently, we show that the FC simulated by these models can outperform the empirical FC in terms of both reliability and subject specificity. For the structure-function relationship, simulated FC of individual subjects may be identified from the correlations with the empirical SC with an accuracy up to 70%, but not vice versa for non-linear models. We sample all our findings for 8 distinct brain parcellations and 6 modeling conditions and show that the parcellation-induced effect is much more pronounced for the modeling results than for the empirical data. In sum, this study provides an exploratory account on the reliability and subject specificity of dynamical whole-brain models and may be relevant for their further development and application. In particular, our findings suggest that the application of the dynamical whole-brain modeling should be tightly connected with an estimate of the reliability of the results.

4.1 Introduction

The neuroscientific literature generally distinguishes between three types of macroscopic connectivity in the human brain: the structural (SC), functional (FC) and effective connectivity (Deco, McIntosh, et al., 2014; Robinson, 2012). Here, the SC assumes an anatomical viewpoint and reflects how different parts of the brain are connected via axonal projections bundled into white matter fibers (Maier-Hein et al., 2017; Sotiropoulos & Zalesky, 2019; Yeh et al., 2021). FC, on the other hand, uses synchronized co-activations as proxies for stable functional connections (Bolt et al., 2017; Deco et al., 2013; van den Heuvel & Hulshoff Pol, 2010). Finally, effective connectivity considers the causality or the directionality of the information flow between various parts of the brain (Friston, 2011; Gilson et al., 2016; Robinson et al., 2014; Valdes-Sosa et al., 2011). Studies have shown that SC and FC exhibit a complex relationship, which is demonstrated by the relatively low correlations between them, and many approaches have been proposed to infer the FC from the SC or vice versa (Honey et al., 2009; Larson-Prior et al., 2013; Saggio et al., 2016; Suárez et al., 2020; Woolrich & Stephan, 2013).

Dynamical whole-brain models are one of the main methodologies used to link SC and FC together into one comprehensive framework (Breakspear, 2017; Deco et al., 2011; Popovych et al., 2019; Sanz-Leon et al., 2015; Suárez et al., 2020). These models explain an additional amount of variance beyond a direct correlation between SC and FC, and have been used to study the dynamical properties of the resting-state human brain (Deco et al., 2017; Ghosh et al., 2008; Honey et al., 2009). Moreover, the models can be employed to study the mechanisms underlying neurobiological phenomena and neural disorders at a personalized level and suggest an approach for hypothesis testing in silico (Deco et al., 2019; Deco & Kringelbach, 2014; Hahn et al., 2019; Jirsa et al., 2017; Ritter et al., 2013; Zimmermann, Perry, et al., 2018).

Studies have assessed how varying preprocessings of magnetic resonance imaging (MRI) data influence the results of dynamical whole-brain models. They showed that the models are sen-

sitive to variations in the pipelines reconstructing the SC and the FC from diffusion-weighted MRI (dwMRI) and resting-state functional MRI (fMRI) images, respectively (Aquino et al., 2022; Jung et al., 2021), and how the model fitting may depend on the properties of the empirical data used for model derivation and validation (Chapter 3; Popovych et al., 2021). Nevertheless, the methodological aspects of the (test-retest) reliability and the subject specificity of the modeling results and their relation to the empirical data have not been extensively investigated so far. In contrast, the reliability of the FC derived from fMRI data, which is used for model validation, has been scrutinized in many studies over a period longer than a decade (Birn et al., 2013; Noble et al., 2017, 2019; Pannunzi et al., 2017; Shehzad et al., 2009; Van Dijk et al., 2010). Its subject specificity reflected by, for example, fingerprinting analysis has received much attention as well (Amico & Goñi, 2018; Finn et al., 2015; Li et al., 2021; Peña-Gómez et al., 2018; Sarar et al., 2021; Waller et al., 2017). Also the subject specificity of the empirical structure-function relationship has been considered in the literature (Messé, 2020; Zimmermann, Griffiths, et al., 2018). Hence, comprehensive assessments of the reliability and the subject specificity of the modeling results and their relation with the empirical data are due.

This study therefore critically assesses the reliability and subject specificity of the results of the model validation and their relations with the empirical connectomes across a wide variety of conditions for model construction such as model definition and wielded parcellation. In short, it demonstrates that the results of the model fitting may be more reliable and subject specific than the empirical data. However, our results also show that this finding highly depends on the modeling conditions. In fact, for some of the tested circumstances we found a reliability and subject specificity that are substantially lower for the modeling results than for the empirical data. Moreover, we explicitly show that the models can integrate various types of subject-specific information extracted from empirical data into their output. This makes our study relevant for application, especially, given the current focus on the involvement of dynamical whole-brain models in clinical investigations, for example, in the framework of precision medicine.

4.2 Materials and methods

In the current study, we assessed the reliability and the subject specificity of the fits of the dynamical whole-brain models to the empirical FC. We first constructed such models on the basis of the *empirical SC* derived from dwMRI data (Fig. 4.1). Subsequently, we independently fitted them to different realizations of the *empirical FC* (the FC derived from resting-state fMRI data) of individual subjects by optimizing the (global) model parameters through a grid search paradigm (Fig. 4.1). By doing so, we obtained the optimal model parameters that were used by the models to generate the associated *simulated FCs* that provided the best fits of the model to these separate realizations of empirical FC.

We subsequently calculated the intraclass correlation (ICC) of the individual optimal model parameters as characterizations of their reliability. Additionally, we calculated the same quantity for the individual (undirected) edges of the empirical and fitted simulated FCs, and inspected the distribution of these ICCs across connections to examine the reliabilities of those connectomes. We also computed the *single-modal connectome correlations*, where different realizations of the empirical and the fitted simulated FCs were separately compared with each other for the same subject (within-subject) or different subjects (between-subject) to determine how variable the connectivity patterns are for the same and different subjects (Fig. 4.1, blue arrows). Furthermore, we determined the within- and between-subject, cross-modal connectome correlations to study how the different types of connectivity related to one another. Here we named the correlations calculated between the empirical SC and both types of FC (empirical and simulated) the *structure-function correlations* (Fig. 4.1, red arrows), and those computed between the empirical and the simulated FC the *model-fit correlations* (Fig. 4.1, brown arrows). Finally,

we considered all values of similarity (Pearson correlation) between the empirical and simulated FC established at the model validation by the parameter grid search, which are referred to as a similarity map. We examined how the similarity maps relate to one another within and between subjects.

We repeated our calculations using 8 distinct parcellations for the reconstruction of the empirical SC and FC from the MRI data to determine whether a change of brain atlas could critically alter the conclusions. In addition, we repeated our computations for 6 distinct dynamical whole-brain model implementations to investigate whether varying model personalization and model complexity may yield qualitatively different results.

Below we describe the wielded procedures in detail. The code used for the simulation of the brain network dynamics, the analysis and the visualization can be found here: https://jugit.fz-juelich.de/inm7/public/specificity-modeling.

4.2.1 Empirical connectomes

In this work, we used the empirical connectomes that we have already published elsewhere (J. W. M. Domhof et al., 2021). This repository contains the empirical SC and FC matrices of 200 healthy, unrelated subjects (96 males, 104 females, aged 28.5 $\pm$ 3.5 years) from the Human Connectome Project (HCP) S1200 release dataset (Van Essen et al., 2012, 2013). The local ethics committee of the HCP approved the study, and the informed consent of all subjects was collected. The connectomes were reconstructed for 19 different parcellation schemes, where the original parcellation images were first modified to increase the comparability of results across brain atlases. In particular, the modifications ensured the images only included cortical parcels and were sampled to the MNI152 non-linear template space (Grabner et al., 2006).

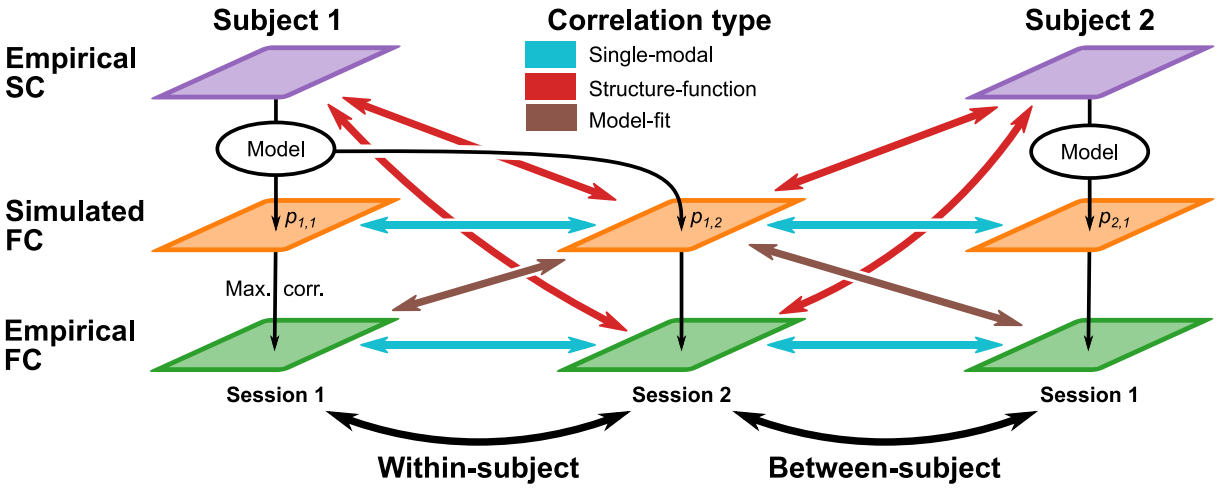

Fig. 4.1. Schematic illustration of the methodology used in this study. The empirical structural connectivity (SC) and the empirical functional connectivity (FC) were calculated from dwMRI and resting-state fMRI data, respectively. Dynamical whole-brain models were used to sample the simulated FC matrices that replicated each individual empirical FC as close as possible for every fMRI session by using the optimal model parameter configuration $p_{subject,session}$. This particular configuration was obtained by validating the model (fitting simulated FC to empirical FC) using a grid search in the parameter space. Subsequently, the upper triangles of the empirical SC, empirical FC and the corresponding fitted simulated FC matrices were correlated between different resting-state fMRI sessions or subjects to determine their similarities. Here, a distinction was made between three types of correlations. (1) The correlations evaluated between the same type of FC were named single-modal correlations (blue arrows). (2) Cross-modal structure-function correlations (red arrows) were calculated between the empirical SC and the empirical or simulated FC. (3) Cross-modal correlations between the empirical and simulated FC were termed model-fit correlations (brown arrows). All sessions participate in within- and between-subject comparisons, but arrows in the figure are only fully shown for session 2 of subject 1 (center column of simulated and empirical FC).

We used the empirical connectomes of 8 representative parcellations out of the available 19 brain parcellations in order to put more emphasis on varying the parcellation method rather than the granularity. Table 4.1 displays the final selection of parcellations. Below we provide a brief explanation on the derivation of the empirical SC and FC from the dwMRI and fMRI data, respectively. For a detailed description of the connectome data, we refer to the data descriptor included in the repository (J. W. M. Domhof et al., 2021) and to the associated paper (Chapter 3).

Empirical structural connectivity

The reconstruction of the empirical SC matrices from dwMRI data was carried out by a workflow developed in-house (Jung et al., 2021). The pipeline can be regarded as a wrapper around functions included in the software packages of ANTs (Tustison et al., 2010), FreeSurfer (Dale et al., 1999), FSL (Jenkinson et al., 2012) and MRtrix3 (Tournier et al., 2019), and is publicly available (https://github.com/inm7/vbc_dwmri). The result of the reconstruction consisted of the empirical SC matrix with the number of streamlines between all pairs of brain regions and the empirical path length (PL) matrix, which included the average lengths of those streamlines. For the details of the reconstruction process, we refer to the above repository hosting the workflow, to the data descriptor of the data repository (J. W. M. Domhof et al., 2021) and to the associated paper (Chapter 3).

In addition to the subjects' own (personalized) empirical SC and PL matrices, we also derived their grand-averages per parcellation, which is a common practice in modeling studies (Aquino et al., 2022; Cabral et al., 2011; Deco, Cruzat, et al., 2018; Donnelly-Kehoe et al., 2019; Iravani et al., 2021; Messé et al., 2014, 2015). However, by a straightforward averaging, the unconnected brain regions may bias the grand-averaged path lengths to lower values. Instead, we considered each edge of the empirical SC and PL matrices separately, and determined the medians of the connected edges across subjects. This variation from a straightforward averaging does not yield qualitatively different empirical SC matrices, but yields a more accurate estimation of the grand-averaged physical distance the signals have to travel; see supplementary Fig. S4.1 for illustration.

Empirical functional connectivity

The empirical FC matrices were calculated from the ICA-FIX preprocessed resting-state fMRI data as included in the HCP dataset (Griffanti et al., 2014). First, the mean intensity of the resting-state blood-oxygen-level-dependent (BOLD) signal was calculated across all voxels of

Table 4.1. Names and abbreviations of the brain parcellations used in this study together with the number of cortical parcels and associated publications. The top and bottom blocks correspond to parcellations derived using data reflecting structural and functional brain organization, respectively.

Name (abbreviation)	Parcels	References
Desikan-Killiany (DK)	70	(Desikan et al., 2006)
von Economo-Koskinas (EK)	86	(Scholtens et al., 2018; von Economo & Koskinas, 1925)
AAL (version 2) (AAL)	92	(Rolls et al., 2015; Tzourio-Mazoyer et al., 2002)
Harvard-Oxford (HO)	96	(Desikan et al., 2006; Frazier et al., 2005; Goldstein et al., 2007; Makris et al., 2006)
Shen 2013 (Shen)	79	(Shen et al., 2013)
Schaefer (Sch.)	100	(Schaefer et al., 2018)
MIST (MIST)	103	(Urchs et al., 2019)
Craddock (CD)	108	(Craddock et al., 2012)

a given brain region included in the considered parcellation, which resulted in one BOLD signal time series for each parcel. The resulting BOLD signals were recently published in a separate dataset as well (J. W. M. Domhof et al., 2022). Subsequently, the time series were linearly detrended and z-scored. Eventually, the empirical FC was derived from the time series by calculating the Pearson correlation coefficients across the time series for all pairs of brain regions.

For all considered subjects, the HCP dataset provided 4 resting-state fMRI sessions (left-to-right and right-to-left phase encoding directions scanned on 2 days) comprising 1200 volumes each (TR = 720 ms). We thus calculated 4 different realizations of the empirical FC per subject. These separate instances of the empirical FC for every individual subject enabled us to estimate the reliability of the empirical FC and hence that of the corresponding fitted simulated FC and the respective fitted model parameters as well.

4.2.2 Simulated functional connectivity

After the acquisition of the empirical connectomes, the simulated FC matrices were generated by dynamical whole-brain models. In these models, the brain was considered to be a network of nodes corresponding to the brain regions included in a particular parcellation. The mean-field activities of the brain regions were subsequently described by models for local dynamics that interact with one another according to the connectivity profile prescribed by the empirical SC. Here, the empirical SC and PL matrices were used to determine the strengths of the network connections and their associated time delays of signal propagation, respectively.

We performed our simulations for 6 different dynamical whole-brain model implementations to study how the distinct facets of *model personalization* and *model complexity* affect the results. The influence of model personalization was studied by considering multiple versions of the Kuramoto model of coupled phase oscillators (Kuramoto, 1984). In particular, the model could be constructed either on the basis of the grand-averaged or the personalized empirical SC, and could be simulated using either group-averaged or subject-specific region-specific oscillation frequencies; see below. Taken together, we considered the Kuramoto model

(1) using averaged empirical SCs and averaged frequencies,
(2) using personalized empirical SCs and averaged frequencies,
(3) using averaged empirical SCs and personalized frequencies and
(4) using personalized empirical SCs and personalized frequencies.

The first and the last modeling conditions define the least and the most personalized models considered, respectively.

The influence of model complexity was studied using three different models with similar personalizations (personalized SC). As the least complex model, we employed (5) a fully linear model. In addition, we used the results of the Kuramoto model that was simulated using the group-averaged frequency profiles (case (2) above) as a moderately complex model. Furthermore, we used (6) a Wilson-Cowan neural mass model (Wilson & Cowan, 1972), which has the most complex model description and implementation among all models wielded in this study. As mentioned above, these models were all constructed on the basis of the personalized empirical SC and PL matrices, but there were no other personalized data included in them.

The non-linear models have two free parameters: the global coupling G and the global delay τ; see below. We simulated the models, which yielded the activity time series of all N brain regions (network nodes), for broad ranges of these parameters sampled from a dense grid in the (G, τ)-parameter space. Subsequently, we derived the simulated FC from the sampled time series via the same procedure that we wielded to construct the empirical FC from the empirical BOLD signals. Conversely, the considered linear model had an analytical solution in which the global coupling is the only (relevant) free parameter (Saggio et al., 2016). Hence, we determined the simulated FC of the linear model via that solution for a broad range of global coupling values.

The correspondence between the empirical and the simulated FC matrices was then quantified by comparing both matrices through the Pearson correlation coefficient. Hence, we determined the similarity between the empirical and simulated FC as a function of the model parameters

$$\psi(G, \tau) = \mathrm{corr}[\mathbf{FC}_{emp.}, \mathbf{FC}_{sim.}(G, \tau)]. \tag{4.1}$$

Here, $\mathbf{FC}_{emp.}$ and $\mathbf{FC}_{sim.}(G, \tau)$ are vectors containing the upper triangular elements of the empirical FC and the simulated FC, respectively. In the case of the linear model, the delay parameter τ was dropped from Eq. 4.1. The function $\psi(G, \tau)$ is henceforth also referred to as the *similarity mapping* mentioned above.

For every individual realization of the empirical FC, we selected the parameter setting and associated simulated FC that provided the best fit of the model with that particular empirical FC (Fig. 4.1). In other words, for the four realizations of the empirical FC of every subject (four resting-state fMRI sessions per HCP subject), we acquired the four simulated FCs and the accompanying optimal model parameter settings that resulted in the highest value of the similarity $\psi(G, \tau)$. The actual maximum value of Eq. 4.1 is subsequently referred to as the *goodness-of-fit*. The selected optimal model parameter configurations and the corresponding fitted simulated FC matrices were subjected to further analyses together with the empirical connectomes. Below we describe the models used in this study in more detail and provide an explanation on their implementation and simulation.

Linear model

As a linear model, we used the well-known Ornstein-Uhlenbeck model approximating the diffusion of noise over the anatomical structure (Galán, 2008). Saggio et al. (2016) demonstrated that this model has an analytical solution, as it gives rise to the covariance matrix $\mathbf{K}$ via the equation

$$\mathbf{K} = -\frac{\sigma_L^2}{2}\left(-\mathbf{I} + G \cdot \overline{\mathbf{SC}}\right)^{-1}. \tag{4.2}$$

Here, σ_L is the intensity of the noise, G is the global coupling parameter and $\mathbf{I}$ is the identity matrix. Additionally, $\overline{\mathbf{SC}}$ is the personalized empirical SC matrix normalized by the maximum of its eigenvalues. This normalization makes the global coupling parameter range more comparable across subjects and parcellations as it ensures that $G = 1$ coincides with the critical coupling; for $G \geq 1$ the solution loses its stability (Saggio et al., 2016). The derived covariance matrix was converted to a (functional connectivity) correlation matrix by using the definition of the Pearson correlation coefficient $\rho_{X,Y} = \mathrm{cov}_{X,Y}/\left(\sigma_X \sigma_Y\right)$. Evidently, the noise parameter σ_L then becomes irrelevant, and hence the global coupling parameter G remains the only free parameter. We determined the simulated FC for a broad range of values for this parameter to maximize the fit between the simulated and the empirical data as given by Eq. 4.1 (without delay parameter); see below for details on this variation.

Kuramoto phase oscillator model

The Kuramoto model approximated the phase dynamics of the mean-field activity of brain region $i \in \{1, 2, ..., N\}$ (N being the number of brain regions in a particular brain atlas), where the corresponding phase $\varphi_i(t)$ was governed by the differential equation

$$\dot{\varphi}_i(t) = 2\pi f_i + \sum_{j=1}^{N} C_{ij} \sin(\varphi_j(t - \tau_{ij}) - \varphi_i(t)) + \sigma_p \nu_i(t). \tag{4.3}$$

Here, f_i is a region-specific natural frequency, and $\nu_i(t)$ is zero-mean Gaussian white noise with an intensity $\sigma_p = 0.17$. In addition, the individual coupling strengths and delays were characterized by C_{ij} and τ_{ij}, respectively. They were determined from the personalized or

grand-averaged empirical SC and PL matrices:

$$C_{ij} = \begin{cases} 0 & \text{if } i = j \\ G \cdot \frac{\mathrm{SC}_{ij}}{N\langle \mathbf{SC} \rangle} & \text{otherwise} \end{cases} \quad \text{and} \quad \tau_{ij} = \begin{cases} 0 & \text{if } i = j \\ \tau \cdot \frac{\mathrm{PL}_{ij}}{\langle \mathbf{PL} \rangle} & \text{otherwise} \end{cases}, \tag{4.4}$$

where $\langle \cdot \rangle$ returns the mean over all the elements in the matrix, and G and τ are the free parameters of the global coupling and delay scaling the individual coupling strengths and delays, respectively. The normalizations of the empirical SC and PL matrices by their mean values ensured that the coupling and delay parameter values were within similar ranges across subjects and parcellations. Other studies used a similar approach (Deco et al., 2017, 2019).

In our study, $\varphi_i(t)$ directly modeled the ultra-slow phase dynamics of the BOLD signals, which is similar to the paradigm described by Ponce-Alvarez et al. (2015) but different from Messé et al. (2014). The signal $\cos(\varphi_i(t))$ then was considered as a proxy for the simulated BOLD signals, and hence used to construct the simulated FC. We determined the simulated FC for a broad range of the parameters G and τ, which are sampled on a dense grid in the parameter space, to maximize the fit between the simulated and the empirical data; see below for details on this variation.

The oscillation frequencies f_i were determined via spectral density estimations calculated from the empirical BOLD time series. To better estimate the frequency spectra of a given subject, we first concatenated the four z-scored BOLD signals of the individual fMRI data acquisitions. The concatenated signals were analyzed using Welch's method (`welch` function in the SciPy module; Virtanen et al., 2020), where we used a Hamming window function of 1024 time points and 95% overlap between segments (972 time points). We then used the peak frequencies within the [0.01, 0.10] Hz frequency range; see supplementary Fig. S4.2 for the distributions of the frequencies across all regions and subjects that were obtained by following this procedure for each individual parcellation. We added Gaussian white noise with zero mean and 0.002 Hz standard deviation to make the peak frequencies more heterogeneous and to avoid duplicate frequencies due to discretization of the frequency values. Following this approach, a vector of frequencies was obtained for each subject separately reflecting the peak BOLD frequencies of the N individual brain regions. Two considered versions of the phase oscillator model used these subject-specific frequencies. We also repeated our calculations while using the same group-averaged, region-specific frequencies for all subjects. These frequencies were calculated as the median frequencies of the brain regions across subjects and correspond to two other considered versions of the phase oscillator model.

Neural mass model

We used a neural mass model similar to the one used by Deco et al. (2009), which was an adaptation of the model described by Wilson & Cowan (1972). The activity of brain region i was modeled by pooling the activities of the excitatory and inhibitory neurons in that region together into the variables $E_i(t)$ and $I_i(t)$, respectively. The temporal dynamics of these activities were governed by the equations

$$\mu_E \dot{E}_i(t) = -E_i(t) + \kappa \mathcal{S}\left(\sum_{j=1}^{N} C_{ij} E_j(t - \tau_{ij}) - c_{EI} I_i(t) + I_b \right) + \sigma_n \nu_i(t) \quad \text{and} \tag{4.5}$$

$$\mu_I \dot{I}_i(t) = -I_i(t) + \kappa \mathcal{S}\left(c_{IE} E_i(t) \right) + \sigma_n \nu_i(t), \tag{4.6}$$

where $\mu_E = \mu_I = 20$ ms represented the decay time constants of the excitatory and inhibitory activity, respectively. The same independent Gaussian white noise with a mean of zero and an intensity of $\sigma_n = 0.002$ was received by both neuronal populations. $c_{EI} = 1.5$ and $c_{IE} = 0.6$ scaled the inhibition of the excitatory neurons by the inhibitory population and the excitation of the inhibitory neurons by the excitatory pool, respectively. Parameter $\kappa = (1 + \exp(\lambda\gamma)) \,/\, \exp(\lambda\gamma)$

scaled the sigmoid function

$$\mathcal{S}(x) = \frac{1}{1+\exp(-\lambda(x-\gamma))} - \frac{1}{1+\exp(\lambda\gamma)} \tag{4.7}$$

so that $\kappa\mathcal{S}(x) = 1$ as $x \to \infty$. Here, $\lambda = 20.0$ and $\gamma = 0.3$ were the parameters determining the width and the position of the inflexion point of $\mathcal{S}(x)$, respectively. Finally, $I_b = 0.10$ was a constant external input arriving at the excitatory population, and C_{ij} and τ_{ij} were the individual coupling strengths and delays, respectively. Different from the Kuramoto model (Eq. 4.4), they were only derived from the personalized (hence not grand-averaged) empirical SC and PL matrices via

$$C_{ij} = \begin{cases} c_{EE} & \text{if } i = j \\ G \cdot \frac{\mathrm{SC}_{ij}}{N\langle \mathbf{SC} \rangle} & \text{otherwise} \end{cases} \quad \text{and} \quad \tau_{ij} = \begin{cases} 0 & \text{if } i = j \\ \tau \cdot \frac{\mathrm{PL}_{ij}}{\langle \mathbf{PL} \rangle} & \text{otherwise} \end{cases}. \tag{4.8}$$

In this equation, the parameter $c_{EE} = 1.0$ regulated the self-excitation of the excitatory neurons, and G and τ are the global coupling and delay parameters, respectively. These were considered as the free parameters of the model and required optimization; see below.

The model exhibited limit-cycle oscillatory behavior in the alpha frequency band when the brain regions were coupled in a network by a sufficiently large coupling parameter $G > 0$, and remained at a low activity state when the network was disconnected ($G = 0$). The modeled oscillations had alpha-band frequencies on purpose: Alpha oscillations have been associated with BOLD responses (Mayhew et al., 2013), and they dominate in human resting-state EEG (Fraga González et al., 2018; Spitoni et al., 2013).

The activities of the two neuron populations were sampled by simulating the model. However, as the fluctuations in the modeled neuronal activity took place on a much shorter time scale ($\sim$10 Hz) than the BOLD dynamics (<0.1 Hz), the simulated time series cannot be compared directly with the empirical BOLD signals. Instead, a Balloon-Windkessel model (Friston et al., 2003) was employed to convert the activities of the excitatory population to BOLD-like responses which were then used to construct the simulated FC matrix.

Model implementation and simulation

The models were implemented using the Python (Python Software Foundation, https://www.python.org) and C++ (Standard C++ Foundation, https://isocpp.org) programming languages, where we also made use of the SciPy (Virtanen et al., 2020) and NumPy (van der Walt et al., 2011) modules for Python. The extensive computations required to evaluate the model simulations and their subsequent analyses were performed on the JURECA high-performance computing cluster (Jülich Supercomputing Centre, 2018). The temporal integrations of the phase oscillator, neural mass and Balloon-Windkessel models were implemented according to Heun's method.

The linear model only required optimization of the global coupling parameter. This parameter was varied using the collection of global coupling values described by

$$G \in \{0.0005, 0.0010, 0.0015, ..., 1.0000\}. \tag{4.9}$$

Because the model had an analytical solution, the correlation matrix could directly be calculated from the empirical SC matrix using Eq. 4.2, and no computationally intensive model simulations were needed for this model.

We maximized the correspondence between the empirical and simulated FC for both the phase oscillator and the neural mass models by evaluating a dense grid search of 64 $\times$ 48 different parameter values for the global coupling G and delay τ, respectively. The phase oscillator model was simulated for the collection of global parameter values described by

$$G \in \{0.000, 0.015, 0.030, ..., 0.945\} \quad \text{and} \tag{4.10}$$

$$\tau \in \{0\,\mathrm{s}, 1\,\mathrm{s}, 2\,\mathrm{s}, ..., 47\,\mathrm{s}\}. \tag{4.11}$$

We simulated 70 minutes of phase dynamics in steps of 60 ms, and the first 10 minutes were disregarded as transient. When considering the neural mass model, the dense grid corresponded to all combinations between the collections of global coupling and delay values described by

$$G \in \{0.000, 0.018, 0.036, ..., 1.134\} \quad \text{and} \tag{4.12}$$

$$\tau \in \{0.0\,\mathrm{ms}, 1.5\,\mathrm{ms}, 3.0\,\mathrm{ms}, ..., 70.5\,\mathrm{ms}\}. \tag{4.13}$$

Also the configuration of the temporal integration was different for this model. For every parameter setting, 510 s of network activity were simulated in steps of 2 ms, and we omitted the first 150 s. These diverging simulation conditions were adapted to the alpha-frequency and ultra-slow time scales of the neural mass and the phase oscillator model, respectively.

The simulations above were performed individually for each combination of the 200 subjects, the 8 parcellations listed in Table 4.1 and the 6 model implementations; see above. These simulation conditions accumulated to over 15M model simulations used for the model validation (fitting) against empirical data on a dense parameter grid. Out of these simulations several optimal parameter settings of the closest correspondence between the simulated and empirical data were selected for further analysis of reliability and subject specificity: 4 (fMRI sessions) $\times$ 8 (parcellations) $\times$ 6 (models) $\times$ 200 (subjects) $=$ 38,400 parameter points and the respective simulated FCs generated by the models for these parameters.

4.2.3 Reliability and subject specificity

As mentioned above, for every parcellation we acquired the empirical SC and FC of $S = 200$ individuals, where $M = 4$ different realizations of the empirical FC were available for each subject. Furthermore, after the simulations of a given model we additionally had to our disposal the 200 $\times$ 4 = 800 optimal model parameter configurations and the associated simulated FC matrices that provided the best replications of the individual empirical FC matrices. We subsequently performed additional analyses to evaluate the reliability and the subject specificity of the empirical data and the modeling results. We performed the analyses independently for each combination of the 8 parcellations listed in Table 4.1 and the 6 model implementations described in "Simulated functional connectivity" to estimate their influence on the results.

Intraclass correlation

We first used the intraclass correlation (ICC) to characterize the reliability of the model parameters of the global coupling and delay as well as the connectomes. In the latter case, the ICCs were calculated for the weights (correlation coefficients) of every $N(N-1)/2$ undirected edges of the functional connectomes (empirical and simulated). The calculated ICC reflects the between-subject variance of these quantities relative to the total variance (between- and within-subject), and was given by the following expression (G. Chen et al., 2018; Liljequist et al., 2019; Noble et al., 2019; Shrout & Fleiss, 1979):

$$ICC = \frac{\sigma^2_{subject}}{\sigma^2_{subject} + \sigma^2_{\epsilon}}. \tag{4.14}$$

Here, $\sigma^2_{subject}$ is the variance of the considered quantity (parameter or connectome edge weight) that is related to the variance among the subjects, and σ^2_{ϵ} is the residual variance induced by the different fMRI acquisitions; see "Empirical functional connectivity". Such an implementation of the ICC has been recommended for the case when no convincing argument can be made that the residual noise contains additional consistent effects (G. Chen et al., 2018; Noble et al., 2019). We wielded the equations proposed by Liljequist et al. (2019) in order to calculate the ICC directly from the data.

Connectome correlations

We also examined the single- and cross-modal connectome correlations within and between subjects. Here, we first vectorized the off-diagonal upper triangles of the individual connectivity matrices corresponding to all subjects and realizations (according to the different fMRI sessions) of the FC. Subsequently, we calculated the Pearson correlation coefficients between the resulting vectors, where we distinguished between three types of correlations (Fig. 4.1). The first type is the *single-modal correlations* comprising the correlations between FCs of the same modality, i.e. empirical FC vs. empirical FC or simulated FC vs. simulated FC (Fig. 4.1, blue arrows). The second type is the *structure-function correlations*, where the cross-modal correlations of the empirical SC with the empirical or the simulated FC were calculated (Fig. 4.1, red arrows). When a model was constructed on the basis of a grand-averaged SC, the structure-function correlations nevertheless involved the correlations between the empirical or simulated FC and the personalized SC matrix of the subject to compare with the personalized simulations. The third type is the *model-fit correlations* consisting of the correlations between the empirical and the simulated FC (Fig. 4.1, brown arrows). The calculated correlations quantified the extent to which the connectomes of the same or different modalities had similar patterns for the same or different subjects.

On top of these three different types of correlations, we distinguished between within- and between-subject correlations. Here, the *between-subject correlations* included all correlations calculated between two different subjects (Fig. 4.1). In addition, the *within-subject correlations* included the correlations computed between the connectomes of the same subject (Fig. 4.1). However, the correlations calculated for the same subject and the same FC realization (fMRI session) equal one in the case of the single-modal correlations, and they correspond to the goodness-of-fit values for the model-fit correlations which means that they are maximized and may thus bias the results; see the section "Simulated functional connectivity" above. They were therefore omitted from the analyses. Table 4.2 clarifies how many distinct values each type of correlation comprised. The within- and between-subject correlations were used to subsequently characterize the reliability and the subject specificity of the (cross-modal) connectome correlations.

Within-subject correlations

The models were fitted to the empirical data by maximizing the similarity between the connectivity patterns of the empirical and simulated FC (Eq. 4.1). We therefore investigated the reliability of the empirical and simulated FCs, that is, the reproducibility of the connectivity patterns for the same subject. The approach based on the calculation of the ICC (Eq. 4.14) quantified the reliability of each individual FC edge in isolation, but did not reflect whether the entire patterns of the functional connections were congruent. Such a reliability of the connectome patterns was characterized in this study by the within-subject single-modal connectome correlations (Fig. 4.1). For the empirical FC, these correlation coefficients reflected how similar the connectivity patterns were to one another when the fMRI data used for their construction were sampled for the same subject but on different days or with different phase encodings. Analogously, for the simulated FC, these correlations characterized the replicability of the simulated connectome under

Table 4.2. Number of distinct values comprising each type of connectome correlation for S subjects that each have M distinct empirical FC realizations.

	Between-subject	**Within-subject**
Single-modal	$S \cdot (S-1) \cdot M^2/2$	$S \cdot M \cdot (M-1)/2$
Structure-function	$S \cdot (S-1) \cdot M$	$S \cdot M$
Model-fit	$S \cdot (S-1) \cdot M^2$	$S \cdot M \cdot (M-1)$

(potential) variations of the empirical FC. By comparing the replicability of the empirical and simulated FCs, we may evaluate whether the considered simulation condition (model, parcellation, etc.) led to an intra-subject variability of the simulated FC that is either enhanced or reduced relative to that of the empirical FC.

Specificity index

As mentioned above, the within-subject, single-modal correlations characterized whether model fits are realized through converging connectivity patterns of simulated FC. However, these patterns may be more similar in general, that is, also across different subjects. We therefore calculated the specificity index $Specificity$, where the mean between-subject correlation $\overline{Corr}_{between}$ was subtracted from the mean within-subject correlation $\overline{Corr}_{within}$

$$Specificity = \overline{Corr}_{within} - \overline{Corr}_{between}, \tag{4.15}$$

which is similar to the approach of Amico & Goñi (2018) and Zimmermann, Griffiths, et al. (2018). The specificity index reflects whether connectomes are indeed reproduced better (more similar to each other) within than between subjects and can be used to quantify the subject specificity. In practice, it fluctuates around zero when the considered type of correlation is not subject specific, and is (significantly) larger than zero when it is subject specific.

To assess the variations in this specificity index, we bootstrapped both mean correlations 50,000 times. Here, one bootstrap involved the resampling of the vectors containing all within- and between-subject correlations with replacement and the subsequent calculation of the means from the resampled vectors. The specificity index was then calculated for each bootstrap so that its 95% confidence interval could be constructed. If the lower bound of this interval was larger than zero, the within-subject correlations were significantly larger than the between-subject ones, and the considered relation was considered significantly subject specific. We performed this analysis separately for the single-modal, structure-function and model-fit correlations.

Connectome fingerprinting

We also adapted the fingerprinting analysis from Finn et al. (2015) to provide an additional measure for the subject specificity (or subject identifiability). The rationale behind this analysis is that a connectome is subject specific if a single subject can be identified from the full cohort on the basis of the connectome (cross-modal) correlations. For one particular connectivity matrix, we first evaluated either the single-modal, structure-function or model-fit correlations. Subsequently, we determined whether the maximum of these correlations involved a within-subject or a between-subject correlation, which implied a correct and false identification of the subject, respectively. By repeating this procedure for all connectivity matrices of that modality, we could determine the portion of correct identifications or *fingerprinting accuracy*. In addition to the fingerprinting accuracy, we calculated the *fingerprinting confidence*. Here, we first determined which subject provided the next highest correlation coefficient for each identification attempt. Subsequently, we subtracted these correlation coefficients from the maxima. Finally, we calculated the fingerprinting confidence by averaging these differences across all identification attempts. The fingerprinting confidence thus characterizes how dissimilar the next closest connectomes are to the identified connectivity matrices. In other words, larger fingerprinting confidences indicate facilitation of (correct) subject identification.

When using the structure-function correlations, a subject could be identified by the strongest correspondence between a given (empirical or simulated) FC and all empirical SC with known subjects. However, the analysis could also be performed using the opposite directionality, i.e. comparing one empirical SC with the empirical or simulated FC matrices of all subjects. Analogously, model-fit correlations were used to identify subjects by correlating one empirical FC with all simulated FC or by correlating one simulated FC with all empirical FC.

Inter- and intra-individual correspondences of the similarity maps

We also investigated how the similarity maps (Eq. 4.1) calculated between the empirical and simulated FC during the parameter grid search may relate to one another within and between subjects. In other words, we investigated how strongly these mappings change across subjects and across different empirical FC realizations of the same subject. For this analysis, we simply calculated the within- and between-subject correlations of these maps across all tested parameter settings, and inspected their distributions. Furthermore, we calculated the specificity indices and fingerprinting accuracies corresponding to these correlations analogous to the single-modal connectome correlations; see above.

4.3 Results

In this study, we used the empirical SC and FC matrices of 200 healthy subjects that were constructed on the basis of the 8 parcellations listed in Table 4.1. The empirical SCs were then used to construct dynamical whole-brain models that were based on the 6 distinct model implementations described in "Simulated functional connectivity" (Materials and methods). We optimized the free model parameters so that the similarity between the simulated FC and the empirical FC (Eq. 4.1) was maximized. Examples of this similarity as a function of the model parameters are shown in supplementary Figs. S4.3-S4.10, which are examples of similarity maps. These similarity maps provide information that may help the interpretation of our other findings; see below. For instance, the maps can have multiple regions of high similarity within the parameter space, in particular, when the neural mass model is considered. The latter indicates that the global optimum may be unstable, which could considerably impact the reliability of the fit of the model to the empirical FC.

This maximization procedure was performed individually for each combination of subject, empirical FC (4 realizations per subject), model implementation and parcellation. The corresponding goodness-of-fit values are shown in supplementary Fig. S4.11 for every combination of parcellation and model individually. In addition, the distributions of the optimal model parameter settings are shown in supplementary Figs. S4.12-S4.19. Subsequently, we investigated the reliability and the subject specificity of the empirical data and the modeling results by performing the analyses described in "Reliability and subject specificity" in Materials and methods.

4.3.1 Reliability of model parameters

We first investigated the reliability of the optimal model parameters by examining the distributions of their absolute differences between different subjects (inter-subject) and between different empirical FC realizations of the same subject (intra-subject). These distributions often appeared to be shifted closer to zero when the differences were calculated within subjects than between subjects (Fig. 4.2A-B; Fig. 4.3A-B). This might be an initial indication that the parameter variability between subjects is larger than the one within subjects. We further quantified this observation by computing the ICCs (Eq. 4.14) reflecting the variance between subjects relative to the total variance of the fitted model parameters. The results showed that the reliability of the coupling and delay parameters could range from "poor" to "good" depending on the atlas and model implementation (Fig. 4.2C-D; Fig. 4.3C-D).

We draw a specific attention to the positive influence of model personalization on the reliability of the fitted model parameters: Simulating the phase oscillator model using subject-specific frequency profiles yielded higher reliability than using group-averaged frequency profiles practically irrespective of whether the group-averaged or personalized SC was used (Fig. 4.2C-D, green vs. red and orange). However, when considering the phase oscillator model simulated

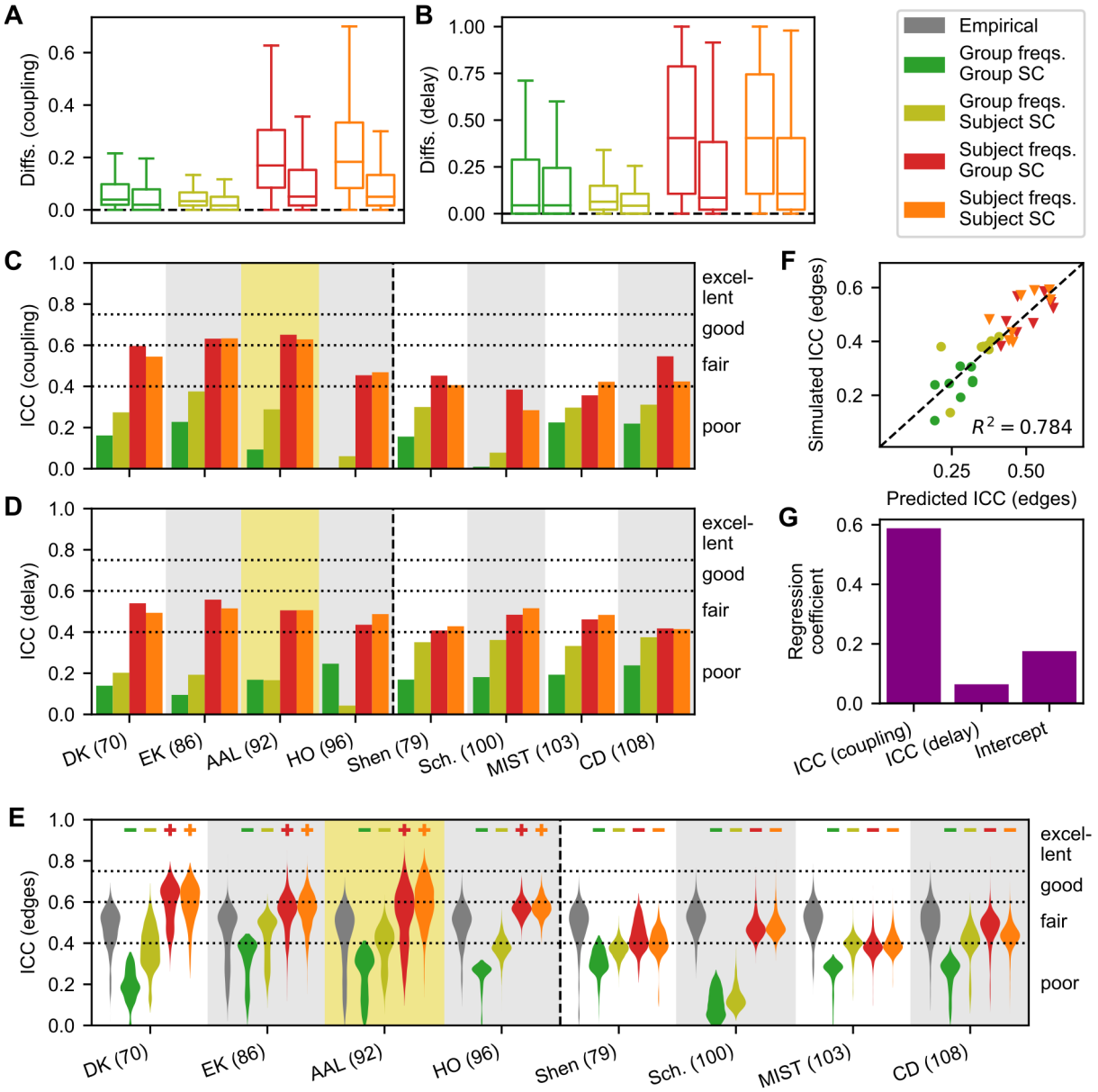

Fig. 4.2. Reliability of modeling results for varying personalization of the phase oscillator model. **(A-B)** Absolute differences (diffs.) of (A) the optimal coupling parameters and (B) the optimal delay parameters for the AAL atlas, which is also highlighted in yellow in panels C to E. The extent of the model personalization as given by the combinations of the subject-specific or group-averaged natural frequencies (freqs.) and SC is reflected by color as indicated in the legend. Left and right boxes of the same color in the plots correspond to inter- and intra-individual differences per model implementation, respectively. The differences were normalized using the maximum across all (inter- and intra-subject) parameter differences per model. **(C-D)** Intraclass correlations (ICCs; Eq. 4.14) of (C) the coupling parameters and (D) the delay parameters for all the atlases considered in this study (Table 4.1). The labels "poor", "fair", "good" and "excellent" correspond to those proposed by Cicchetti & Sparrow (1981). The vertical dashed black lines separate the brain atlases constructed on the basis of structural data (left blocks) from those based on functional data (right blocks). **(E)** Distributions of the ICCs of individual functional connections, edges of the empirical (gray) and simulated functional connectome for all the atlases considered in this study. Plus and minus signs at the top of the plot signify significantly increased and decreased ICC distributions for the respective simulated FC with respect to the one for the empirical FC, respectively ($p<0.05$, two-sided Wilcoxon paired signed-rank test, Bonferroni corrected). **(F)** Scatter plot of the intraclass correlations (ICCs) calculated from and averaged across simulated FC edges (simulated ICC, vertical axes) and their predicted values obtained from a linear regression with the ICCs of the model parameters (predicted ICC, horizontal axes). The plotted symbols represent parcellations and models as indicated in the legend. The dashed black line represents $x = y$ for comparison. **(G)** Regression coefficients corresponding to the results shown in panel F.

using group-averaged frequencies, the model parameters were also fitted with higher reliability when the personalized instead of the group-averaged SCs were used for model construction (Fig. 4.2C-D, dark vs. light green). Hence, model personalization appears to promote the reliability of the model fit to the empirical data.

More complex models seemed to yield a reliability of the model parameters that was less variant across parcellations, and higher model complexity was not immediately more reliable at the same level of personalization (Fig. 4.3C-D). In addition, the linear model fitted the coupling parameter with higher reliability than the non-linear models in most cases (Fig. 4.3C-D). We however verified whether this could be explained by the absence of the signal latency in the network of the linear model. Hence, we considered the non-linear models with zero global delay $\tau = 0$ in Eq. 4.4 and Eq. 4.8. Subsequently, we determined the optimal coupling parameter values under this constraint and calculated their ICCs. The results of this investigation confirmed that model complexity did not exert an influence on the reliability of the coupling parameter in isolation that was consistent across parcellations (supplementary Fig. S4.20). Hence, the model complexity per se does not seem to systematically influence the reliability of the fitted model parameters.

We checked whether our results critically depended on the choice of the intraclass correlation for the characterization of the reliability of the optimal model parameters. For this investigation, we calculated the (non-parametric) test-retest Spearman correlation coefficient of the optimal model parameters. The results showed a strong covariation across parcellations and model implementations (supplementary Fig. S4.21; see figure caption for specifics), which indicated that our results did not qualitatively depend on the intraclass correlation as the reliability measure.

Taken together, these findings demonstrate that whole-brain dynamical models can be fitted to the empirical FC with a ”poor” to ”good” reliability depending on the implementation of the modeling paradigm. Furthermore, we explicitly demonstrated the positive influence of the model personalization on the reliability of the fitted model parameters. Moreover, higher model complexity reduces the parcellation-induced variations in the reliability of the optimal model parameters, but it cannot credibly be associated with systematic tendencies (enhancement or reduction) of the parameters' reliability.

4.3.2 Reliability of functional connectivity edges

We also examined the reliability of the empirical and the simulated FC. First, we calculated the ICCs of all empirical and simulated FC edges (individual functional connections between brain regions) and inspected their distributions. The ICCs of the empirical functional connections remained approximately at the same (”fair”) level across parcellations (Fig. 4.2E, gray). In contrast, the edge reliability of the simulated functional connectomes varied considerably across parcellations, and ranged from ”poor” to ”good” (Fig. 4.2E; Fig. 4.3E). These findings indicate that the reliability of the empirical FC is rather stable across parcellations, while that of the simulated FC is more sensitive to the utilized brain parcellations.

Additionally, we found that the conclusions derived for the reliability of the fitted model parameters (Fig. 4.2C-D; Fig. 4.3C-D) can also be confirmed for the FC edges. Indeed, model personalization often led to an increase in the reliability of the connectome edges (Fig. 4.2E). The simulated FCs of the phase oscillator model using subject-specific regional frequencies clearly exceeded the empirical FC in terms of edge reliability for all considered structurally-derived atlases irrespective of the personalization of the empirical SC, and reached the ”good” level (Fig. 4.2E, red and orange). We regressed the ICCs of the optimal model parameters with the mean ICCs of all simulated FC edges and found that this linear regression could explain 78% of the variance for the phase oscillator model (Fig. 4.2F). The regression coefficients demonstrated a high contribution of the global coupling to the reliability of the simulated FC edges as compared to

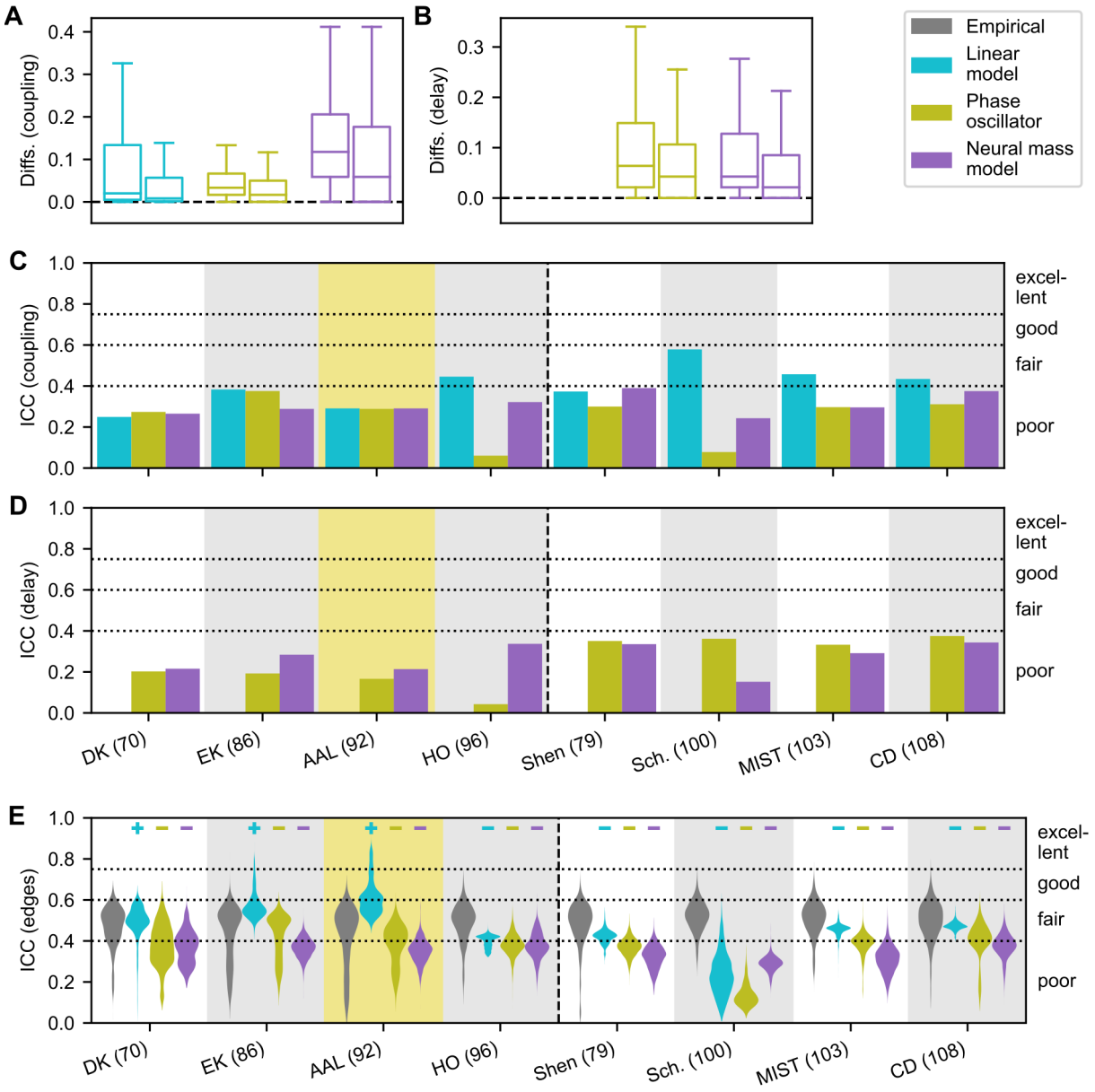

Fig. 4.3. Reliability of modeling results for varying model complexity with similar model personalization. The model implementations (2), (5) and (6) are considered; see "Simulated functional connectivity" in Materials and methods. Here (5) the linear model (blue) corresponds to a low complexity, (2) the phase oscillator model (green) to a moderate complexity and (6) the neural mass model (purple) to a high complexity. **(A-B)** Absolute differences (diffs.) of (A) the optimal coupling parameters and (B) the optimal delay parameters for the AAL atlas, which is also highlighted in yellow in panels C to E. Left and right boxes of the same color in the plots correspond to inter- and intra-individual differences per model implementation, respectively. The differences were normalized using the maximum across all (inter- and intra-subject) parameter differences per model. The results of the delay parameter are not shown for the linear model as this model did not include this parameter (Eq. 4.2). **(C-D)** Intraclass correlations (ICCs; Eq. 4.14) of (C) the coupling parameters and (D) the delay parameters for all the atlases considered in this study (Table 4.1). The labels "poor", "fair", "good" and "excellent" correspond to those proposed by Cicchetti & Sparrow (1981). The vertical dashed black lines separate the brain atlases constructed on the basis of structural data (left blocks) from those based on functional data (right blocks). **(E)** Distributions of the ICCs of the empirical (gray) and simulated functional connectome edges for all the atlases considered in this study. Plus and minus signs at the top of the plot signify significantly increased and decreased ICC distributions for the respective simulated FC with respect to the one for the empirical FC, respectively ($p<0.05$, two-sided Wilcoxon paired signed-rank test, Bonferroni corrected).

the optimal delay parameter (Fig. 4.2G). Moreover, the positive intercept of the regression also indicated that the reliability of the simulated FC edges was enhanced by the personalized phase oscillator model as compared to that of the optimal model parameters (Fig. 4.2G).

In addition, as for the reliability of the optimal model parameters, we again observed that enhanced model complexity (e.g., for the neural mass model) led to a reliability of the simulated FC edges that varied less across parcellations (Fig. 4.3E). On the other hand, the reliability of the simulated FC generated by the linear model varied considerably and significantly exceeded that of the empirical FC for the Desikan-Killiany, von Economo-Koskinas and AAL atlases (Fig. 4.3E). We also compared the reliability (ICC values) of the optimal model parameters and the simulated FC edges of the models in Fig. 4.3 by linear regression and found no consistent, strong dependencies across models (not shown).

In sum, the variation of the reliability of the simulated FC edges with respect to the extent of model personalization and the brain parcellation well agrees with that of the optimal model parameters (Fig. 4.2F). Evidently, the observed relationship between these two types of model reliability implies that they exhibit similar variations across model personalization, where an enhancement of the latter led to an improvement of the reliability of the simulated FC, possibly outperforming that of the empirical FC. Furthermore, higher model complexity has a positive effect on the consistency of the reliability of the simulated FC across parcellations, but it may not contribute to an enhancement of the reliability of individual FC edges, and a simple linear model sometimes performed better (Fig. 4.3E).

We also checked whether the different ICCs (Fig. 4.2C-E; Fig. 4.3C-E) could be related to the goodness-of-fits of the model to the empirical data. With regard to the reliability of the optimal model parameters, the tested regressions varied considerably across models in terms of the relationship (positive vs. negative) as well as variance explained (supplementary Fig. S4.22A-G). Hence, the goodness-of-fit is not a good predictor for the reliability of the model parameters when considering a particular modeling condition (parcellation and model implementation) at random. Additionally, the edge-wise reliability of the simulated FC exhibited a positive correlation with the quality of the model fit for all considered models, though also with varying fractions of explained variance (supplementary Fig. S4.22H-K).

4.3.3 Reliability and subject specificity of functional connectivity patterns

Several modeling conditions yielded simulated FCs with edges' reliability being lower than for the empirical FC (Fig. 4.2E; Fig. 4.3E). We therefore investigated whether the whole connectivity patterns of the simulated FCs were nevertheless similar given that they were fitted to different empirical FCs of the same subject. For this purpose, we evaluated the within-subject, single-modal connectome correlations (Fig. 4.1, blue arrows). A considerable number of the modeling conditions and subjects yielded simulated FC matrices that had strongly diverging connectivity motifs, which is reflected by low intra-subject correlations between simulated FCs compared to the empirical FCs (Fig. 4.4A-B). In particular, increased model complexity led to more dissimilar simulated FCs for most parcellations, especially, for the functionally-derived parcellations, where strong bimodalities were elicited in the within-subject, single-modal correlation distributions (Fig. 4.4B). Enhancing the model personalization could reduce or smooth these bimodalities (Fig. 4.4A). Hence, the fit of the model to the empirical data could on average enhance the within-subject variability of the empirical FC depending on the particular combination of model implementation and parcellation (Fig. 4.4A-B, minus signs on top of the plots).

We also checked whether the within-subject, single-modal correlations could be related to the goodness-of-fit of the model to the empirical data. Here, we found strong relationships between these two quantities for the non-linear models (supplementary Fig. S4.22M-O), but not for the linear model (supplementary Fig. S4.22L). This indicates that the FC patterns simulated by

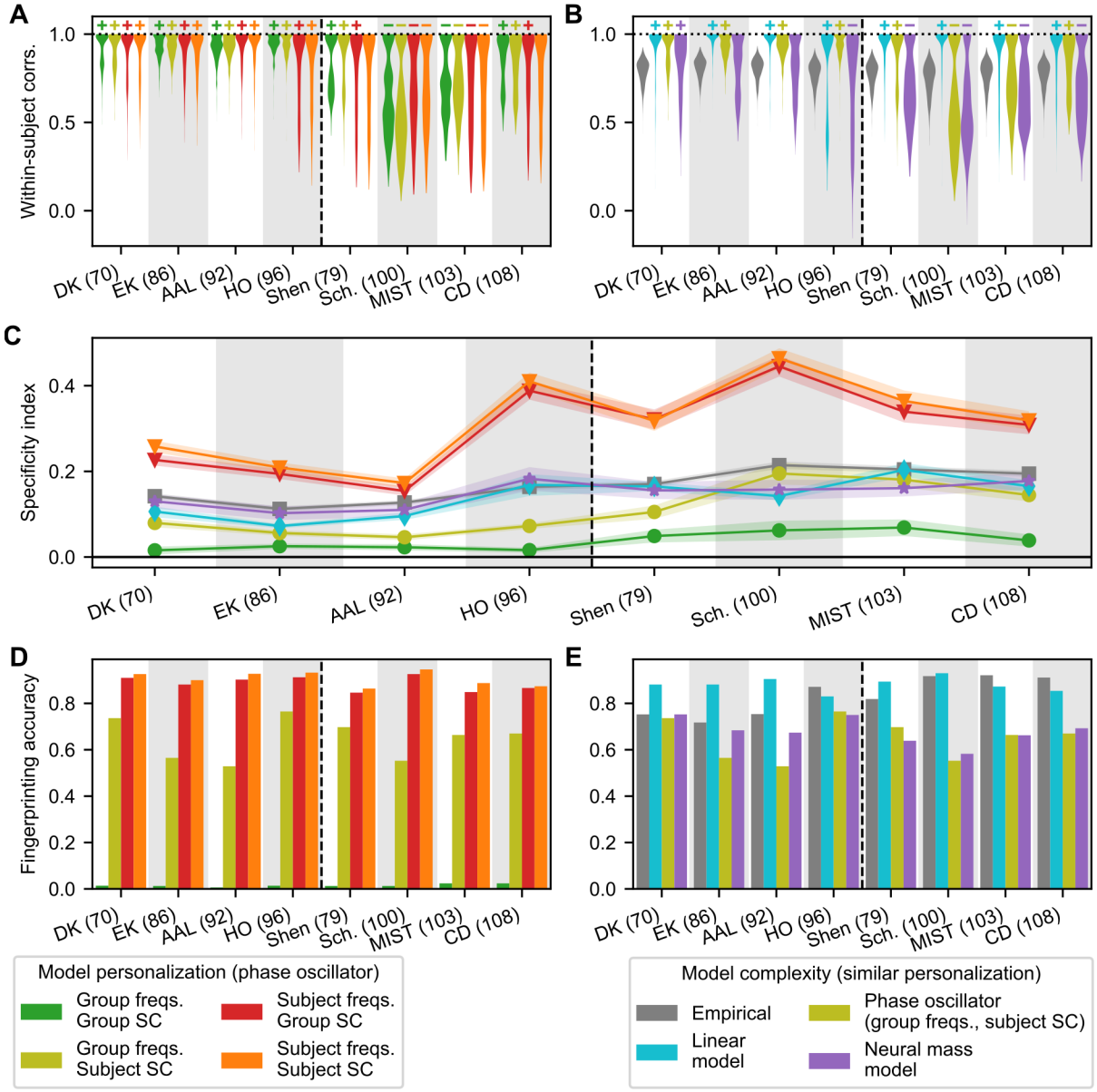

Fig. 4.4. Impact of the brain atlas, model personalization and model complexity on the reliability and subject specificity of the connectivity patterns of the empirical (gray) and simulated FC. **(A-B)** Distributions of the within-subject, single-modal correlations (corrs.) as a reliability measure of the empirical and simulated FC patterns for the various parcellations considered in this study (Table 4.1) and for varying levels of (A) model personalization and (B) model complexity. The extent of model personalization as given by the combinations of the subject-specific or group-averaged natural frequencies (freqs.) and SC is indicated in the legend shown in the lower left corner of the plot. Analogously, the level of model complexity as reflected by the linear (least complex), phase oscillator (moderately complex) and neural mass (most complex) models with similar personalization levels is indicated in the legend shown in the lower right corner. The vertical dashed black lines separate the brain atlases constructed on the basis of structural data (left blocks) from those based on functional data (right blocks). Plus and minus signs at the top of the plots indicate significantly increased and decreased within-subject correlation distributions for the respective simulated FC with respect to the one for the empirical FC (gray; panel B), respectively ($p<0.05$, two-sided Wilcoxon paired signed-rank test, Bonferroni corrected). **(C)** Specificity indices (Eq. 4.15) calculated from the single-modal correlations of the empirical FC and the simulated FC. The symbols and shaded areas mark the medians and the (Bonferroni corrected) 95% confidence intervals across the 50,000 bootstrapped specificity index estimations, respectively. **(D-E)** Fingerprinting accuracy when identifying individual subjects by comparing one of their empirical (simulated) FCs against all other empirical (simulated) FCs for varying levels of (D) model personalization and (E) model complexity.

non-linear models can exhibit higher within-subject similarity when they are fitted better to the empirical FC, but also that such a relationship is not evident for the linear model.

For most modeling conditions, we nonetheless observed that the simulated FC matrices had connectivity patterns that were significantly more similar to one another than those of the empirical FC (Fig. 4.4A-B, plus signs on top of the plots). We investigated whether these enhancements of the within-subject, single-modal correlations were realized by a general increase in the similarity of the connectivity patterns, that is, both within and between subjects. We therefore calculated the (single-modal) specificity indices (Eq. 4.15) and fingerprinting accuracies to determine the gain of the within- relative to the between-subject, single-modal correlations. We observed that enhanced model personalization induced a clear increase in the specificity index and the fingerprinting accuracy, where both these specificity measures could exceed those of the empirical FC (Fig. 4.4C-E). Fingerprinting confidences were also increased for stronger model personalization and apparently exceeded those of the empirical FC (supplementary Fig. S4.23A), which resulted in a precise and robust subject identification. On the other hand, the least personalized model with the averaged frequencies and SC exhibited an extremely low subject specificity, fingerprinting accuracy and confidence (Fig. 4.4C-D and supplementary Fig. S4.23A, dark green) at a relatively high reliability as given by the intra-subject correlation of simulated connectomes (Fig. 4.4A, dark green).

Conversely, varying the model complexity did not result in differences of the specificity indices that were consistent across parcellations (Fig. 4.4C, blue, light green and purple). The same observation held for the fingerprinting accuracies of the non-linear models, but not for those of the linear model, which were enhanced relative to the non-linear models of the same personalization and could exceed those of the empirical FC in some cases (Fig. 4.4E). Interestingly, the fingerprinting confidences of the linear model were systematically much lower than those for the neuronal mass model and in many cases also lower than for the empirical FC (supplementary Fig. S4.24A). Therefore, subject identification by a simple linear model is less erroneous but also less robust than by more complex non-linear models. Hence, model personalization (but not model complexity) had a positive effect on both single-modal subject specificity measures (specificity index and fingerprinting accuracy) that was consistent across parcellations.

In sum, most of the model implementations yielded within-subject, single-modal correlations of the simulated FC that were significantly enhanced relative to the empirical FC. However, these significant enhancements actually reflected a general increase in both the within- and between-subject single-modal correlations such that the specificity index remained comparable with that of the empirical data. This is in particular true for the linear and non-linear models with a low and moderate extent of personalization (Fig. 4.4). Only an enhanced model personalization can lead to much improvement of both the subject specificity and the subject identifiability of the simulated FC as a modeling result (Fig. 4.4).

4.3.4 Subject specificity of cross-modal connectome correlations

So far we observed that dynamical whole-brain models produce simulated FCs with a particular subject specificity. We subsequently investigated the extent to which these subject-specific connectivity patterns agree with those of the empirical SC and FC by determining the specificity indices and fingerprinting accuracies corresponding to the structure-function and model-fit correlations (Fig. 4.1, red and brown arrows). We observed that the empirical structure-function relationship was only significantly subject specific for the functionally-derived atlases, although being very small (Fig. 4.5D, gray). Model personalization through the use of the personalized SC yielded simulated FCs that had structure-function specificity indices significantly higher than zero for all functionally-derived parcellations as well as for some of the structurally-derived atlases (Fig. 4.5A, light green and orange). Conversely, deriving the models from a grand-average

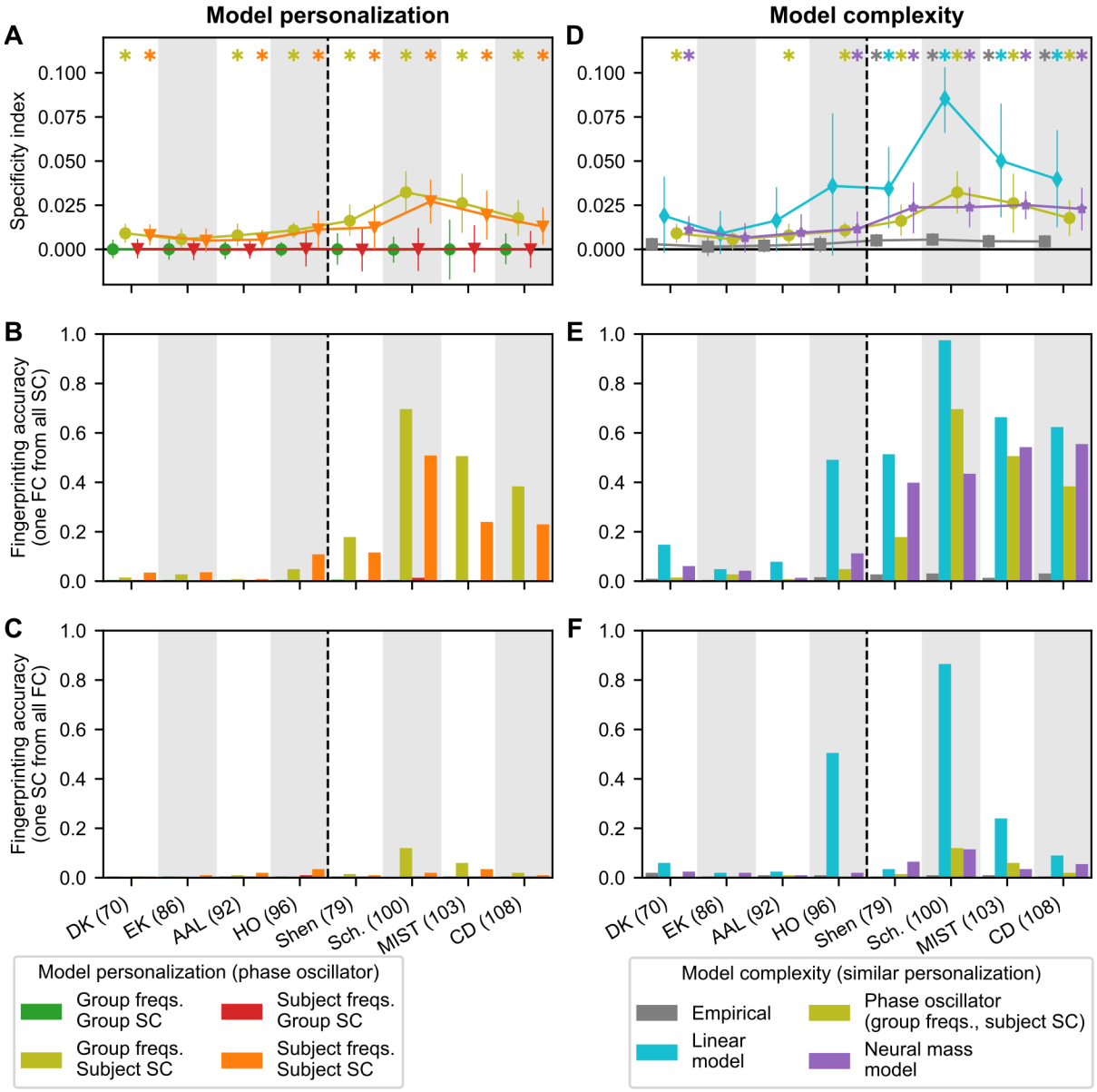

Fig. 4.5. Impact of the brain atlas, model personalization and model complexity on the subject specificity of the structure-function relationships being the correlations between the empirical SC and the empirical and simulated FC. **(A)** Specificity indices (Eq. 4.15) of the cross-modal correlations of the empirical SC with the simulated FC for the parcellations considered in this study; see Table 4.1. The extent of model personalization as given by the combinations of the subject-specific or group-averaged natural frequencies (freqs.) and SC is indicated in the legend (bottom left). The vertical dashed black line separates the brain atlases constructed on the basis of structural data (left block) from those based on functional data (right block). The symbols and error bars mark the medians and the (Bonferroni corrected) 95% confidence intervals across the 50,000 bootstrapped specificity index estimations, respectively. Asterisks indicate whether the lower bounds of these confidence intervals are higher than zero. **(B-C)** Fingerprinting accuracies determined by (B) identification of one simulated FC from all empirical SC based on the largest correlation between them and (C) by identification of one empirical SC from all simulated FC of the same modality for the parcellations considered in this study. **(D-F)** Same as panels A to C, but for varying levels of model complexity as reflected by the linear (least complex), phase oscillator (moderately complex) and neural mass (most complex) models with similar personalization levels and indicated in the legend shown in the lower right corner. The results for empirical FCs are also shown (gray).

SC resulted in structure-function specificity indices indistinguishable from zero (Fig. 4.5A, dark green and red). This finding indicated that models constructed on the basis of a personalized SC can embed subject-specific aspects from these structural connectomes into the simulated FC that in fact was fitted to the empirical FC. The fingerprinting accuracies further supported this claim (Fig. 4.5B-C). We also observed that the magnitude of the structure-function specificity indices were much lower than for the single-modal case (Fig. 4.4C vs. Fig. 4.5A,D).

Model personalization through the use of subject-specific frequency profiles induced a negative effect on the subject specificity of the structure-function relationship (Fig. 4.5A-C, orange vs. light green), which is very different from the single-modal FC correlations (Fig. 4.4). Model complexity did not seem to exert a clear effect on the structure-function subject specificity when considering the non-linear models (Fig. 4.5D-F). In addition, the fingerprinting accuracies hint towards a particular directionality of the structure-function fingerprinting concept when considering the non-linear models: The identification of the simulated FC from the empirical SC (Fig. 4.5B,E) resulted in much higher accuracies than the inverted case (Fig. 4.5C,F). Simultaneously, the fingerprinting confidences were mostly lower for the former than for the latter case (supplementary Fig. S4.23B-C and Fig. S4.24B-C). Interestingly, the subject specificity with which the simulated FCs incorporate the empirical SC patterns is larger for the functionally- than for the structurally-derived parcellations (Fig. 4.5).

The latter observation regarding the impact of parcellations was also true for the specificity indices and fingerprinting accuracies of the other considered models, in particular, the linear model that exhibited enhanced specificity relative to those of the non-linear models (Fig. 4.5D-F, blue). However, there appeared to be a less pronounced directionality with respect to the identification of individual subjects for the linear model. In this modeling case, the simulated FC can be identified from empirical SC, and also empirical SC can be identified from the simulated FC with high accuracy (Fig. 4.5E-F, blue). Such a simple model thus established very strong connections between empirical SC and simulated FC such that the connectome identification in both directions becomes equally possible.

Subsequently, we performed the same analyses for the model-fit correlations (Fig. 4.1, brown arrows). Even though the specificity indices of these correlations were significantly larger than zero for all tested modeling conditions (supplementary Fig. S4.25A), the values of the specificity indices and the fingerprinting accuracies determined from the model-fit correlations were relatively low (supplementary Fig. S4.25B-C). Thus, the models were not fitted so subject specific to the empirical data that individual subjects can be identified from their model-fit correlations with great accuracy. Model personalization but not model complexity could have a positive influence on the subject specificity of the model-fit correlations, although this effect was little consistent across both measures of subject specificity (supplementary Fig. S4.25A-C).

4.3.5 Subject specificity of similarity maps

Finally, we investigated how the model personalization may lead to the enhanced reliabilities of the model parameters. We hypothesized that model personalization has an effect on the similarity mappings (Eq. 4.1) that characterize the agreement between the empirical and simulated FC patterns as a function of the model parameters. Hence, we evaluated how well these similarity maps corresponded to one another between subjects and between distinct empirical FC realizations of the same subject by calculating their within- and between-subject correlations across parameter settings. The results showed that model personalization did not alter the within-subject correlations of the similarity maps consistently across parcellations, and correlation-based reliability of the similarity maps was very high for most of the parcellations (Fig. 4.6A). On the other hand, the influence of enhanced personalization on the specificity index and fingerprinting accuracy was positive for all atlases (Fig. 4.6B-C). Combined, these findings suggest that

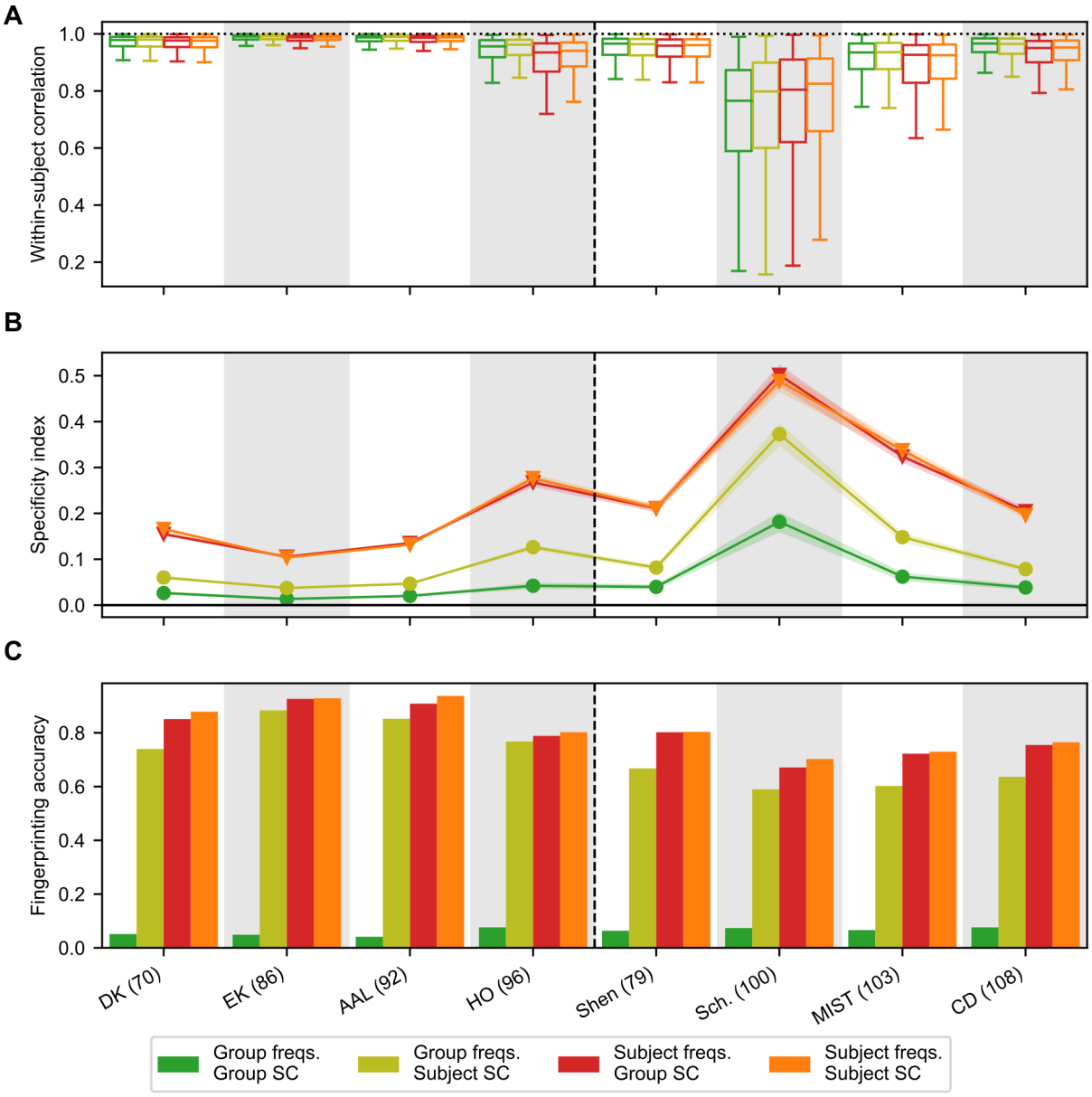

Fig. 4.6. Influence of parcellation and personalization of the phase oscillator model on the correspondences of the similarity mappings (Eq. 4.1). **(A)** Distributions of the within-subject correlations of the similarity maps calculated across parameter settings for the various parcellations considered in this study (Table 4.1). The extent of the model personalization as given by the combinations of the subject-specific or group-averaged natural frequencies (freqs.) and SC is indicated in the legend. The vertical dashed black line separates the brain atlases constructed on the basis of structural data (left block) from those based on functional data (right block). **(B)** Specificity indices (Eq. 4.15) calculated from the similarity mapping correlations. The symbols and shaded areas mark the medians and the (Bonferroni corrected) 95% confidence intervals across the 50,000 bootstrapped specificity index estimations, respectively. **(C)** Fingerprinting accuracy when identifying individual subjects by comparing the similarity mappings of one particular empirical FC with one another.

model personalization strongly enhanced subject-specific properties of the similarity maps that became less comparable across (but not within) subjects.

Given our previous findings, one might suspect that model complexity would then exert no consistent effect on the subject specificities of the similarity mappings (Eq. 4.1). However, we actually found that the distributions of the within-subject similarity map correlations could diverge considerably between model complexities depending on the parcellation (Fig. 4.7A). Moreover, the specificity indices of the similarity maps of the most complex model (the neural mass model) exceeded those of the less complex ones for all parcellations except for the Harvard-Oxford and Schaefer atlases (Fig. 4.7B), which are also characterized by a higher variability of the intra-subject correlations (reliability) of similarity maps (Fig. 4.7A). The fingerprinting accuracies of the similarity mappings were also increased for incrementing levels of model complexities for all atlases (Fig. 4.7C). These findings indicate that higher model complexity could lead to an enhanced subject specificity with respect to the similarity maps (Fig. 4.7B-C).

Analogous to the ICC of the model parameters (Fig. 4.3; supplementary Fig. S4.20), we verified whether these enhancements for more complex models could be explained by the absence of the signal latency in the network of the linear model. Again, we considered the non-linear models with zero global delay $\tau = 0$ in Eq. 4.4 and Eq. 4.8. Subsequently, we determined the similarity maps under this constraint and calculated the specificity indices and fingerprinting accuracies from the correlations between these one-parameter (global coupling) similarity maps. The results of this analysis showed that the ordering of the specificity index and fingerprinting accuracy for varying model complexity was preserved (supplementary Fig. S4.26). Hence, enhanced model complexity indeed yields similarity maps that are more subject specific.

We also checked whether the different types of specificity indices (single-modal, structure-function, model-fit, similarity maps) could be related to the goodness-of-fits of the model to the empirical data. Even though the tested relationships varied considerably in terms of variance explained, almost all of them were negative (supplementary Fig. S4.27). This indicates that a higher goodness-of-fit is more likely to reflect a less subject-specific model fit.

4.4 Discussion

In this study, we showed that dynamical whole-brain models may be fitted to the empirical data with a reliability ranging from ”poor” to ”good” depending on the exact implementation of the dynamical whole-brain modeling paradigm and brain parcellation utilized (Fig. 4.2; Fig. 4.3). Subsequently, we showed that the fits of the models might be established through diverging or converging simulated FC patterns, where the variability of the empirical data (FC) used for the model validation can either be enhanced or suppressed by the fitting process. We also demonstrated that simulated FC represented by individual edges or the entire connectivity patterns can be more reliable and subject-specific than the empirical FC (Fig. 4.2; Fig. 4.3; Fig. 4.4). We additionally demonstrated that the simulated FC may exhibit correlations with the empirical SC and empirical FC that exhibit significant subject specificity (Fig. 4.5; supplementary Fig. S4.25).

We observed that model personalization positively influences the reliability and subject specificity of the modeling results (Fig. 4.2; Fig. 4.4; Fig. 4.5; Fig. 4.6; supplementary Fig. S4.25). Furthermore, model complexity often did not affect the reliability or the subject specificity consistently across parcellations and measures when the fitted model parameters and simulated FCs were considered. A simple linear model can in some cases have enhanced reliability and subject specificity relative to more complex, non-linear models. Nevertheless, the similarity mappings were more subject specific for more complex models consistently for almost all considered parcellations (Fig. 4.7). We sampled all our results for 8 distinct, state-of-the-art brain atlases and demonstrated the pronounced parcellation-induced variation in the modeling results

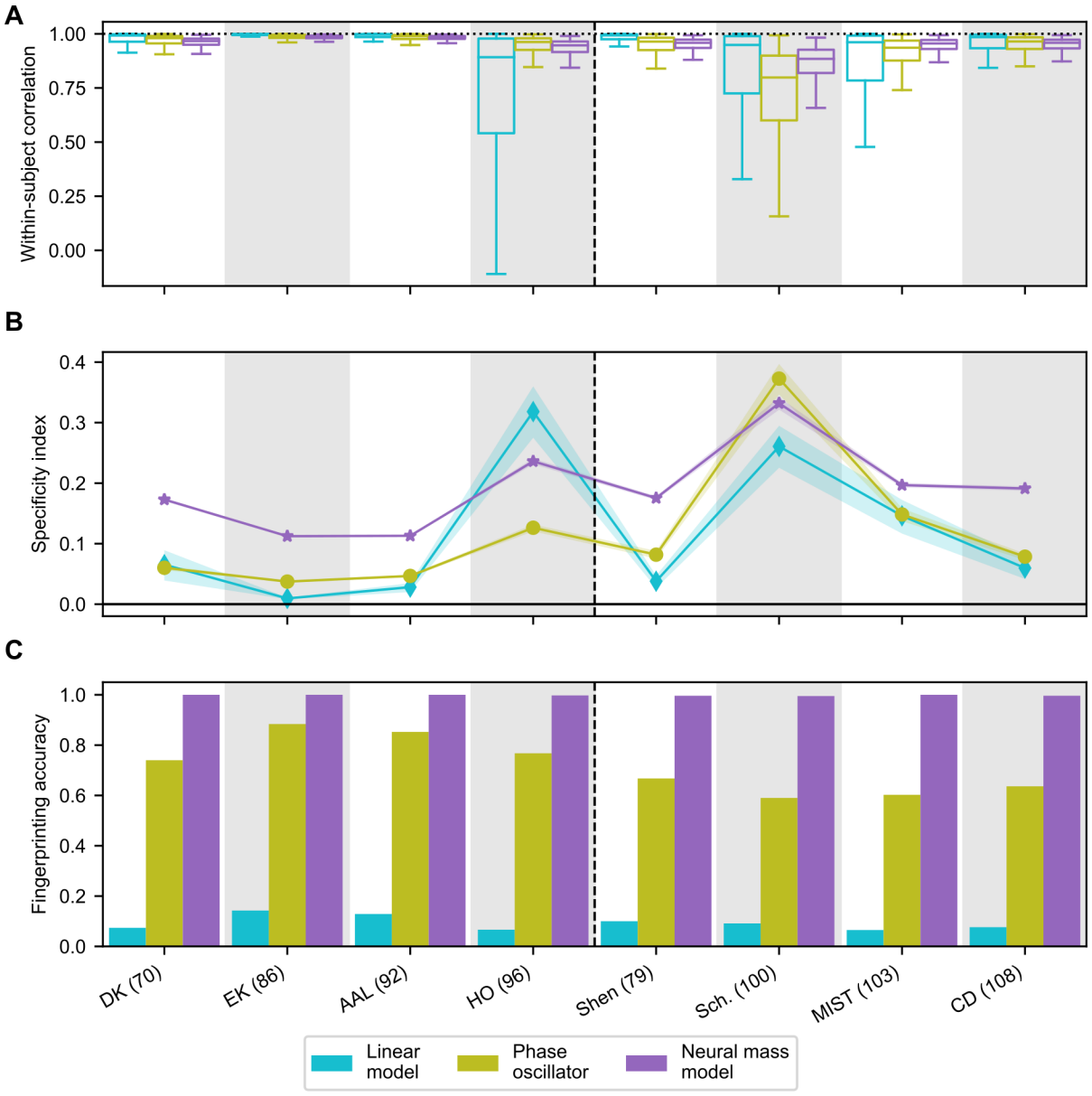

Fig. 4.7. Influence of parcellation and model complexity with similar model personalization on the correspondences of the similarity mappings (Eq. 4.1). **(A)** Distributions of the within-subject correlations of the similarity maps calculated across parameter settings for the various parcellations considered in this study (Table 4.1). The linear model (blue) corresponds to a low complexity, the phase oscillator model (green) to a moderate complexity, and neural mass model (purple) to a high complexity. The vertical dashed black line separates the brain atlases constructed on the basis of structural data (left block) from those based on functional data (right block). **(B)** Specificity indices (Eq. 4.15) calculated from the similarity mapping correlations. The symbols and shaded areas mark the medians and the (Bonferroni corrected) 95% confidence intervals across the 50,000 bootstrapped specificity index estimations, respectively. **(C)** Fingerprinting accuracy when identifying individual subjects by comparing the similarity mapping of one particular empirical FC with one another.

relative to the purely empirical results. Here, we discuss these findings in the broader scientific context and emphasize their relevance.

4.4.1 Reliability of modeling results

Even though the (test-retest) reliability has been actively investigated for the empirical FC (Birn et al., 2013; Noble et al., 2017, 2019; Pannunzi et al., 2017; Shehzad et al., 2009; Van Dijk et al., 2010), the literature lacks a comprehensive assessment of it for dynamical whole-brain models. One study nevertheless demonstrated their ”excellent” reliability for multiple realizations of the empirical SC (but not FC) for the same subject (Cicchetti & Sparrow, 1981; Muldoon et al., 2016), while another considered the within-subject correspondences of the fitted model parameters for only one subject, one parcellation and one type of model (Donnelly-Kehoe et al., 2019). Our study provided a comprehensive investigation of the reliability of the modeling results for a cohort of 200 subjects by considering the ICCs of several realizations of the optimal model parameters and simulated FCs fitted to the corresponding different realizations of the empirical FCs for the same subject. The obtained results demonstrated that the reliability of the simulated FC can be larger (and also smaller) than that of the empirical FC depending on the parcellation and exact model implementation (Fig. 4.2; Fig. 4.3). Here, our findings of the ”fair” reliability of the empirical FC agreed with the literature (Noble et al., 2017, 2019). As a next step, future studies may investigate how the simultaneous variation of the empirical SC and FC impacts the reliability of dynamical whole-brain modeling results. Our study and the study by Muldoon et al. (2016) may be used as a starting point for such an investigation, where our study in particular could be exploited for the selection of the modeling conditions to consider.

The results of this study, however, primarily suggest that the use of dynamical whole-brain models should be tightly connected with an estimate of the reliability of their results in order to enhance the interpretability of the observations. Despite the reported enhanced reliability of the modeling outcomes, our findings clearly indicate that the ICCs of the modeling results depend highly on the exact implementation of the dynamical whole-brain modeling paradigm. In fact, the reliability of the simulated FC edges was lower than that of the empirical FC edges when considering many of the tested conditions (Fig. 4.2; Fig. 4.3). Moreover, the model parameters often exhibited ”poor” reliability, which may also sometimes be the case for simulated FC, indicating they exhibit substantial variance for distinct empirical FC realizations of the same subject. We frequently observed such an unreliability and unspecificity for little personalized models with e.g., the group-averaged SC that is widely used in the literature. In the absence of other personalized factors, e.g., subject-specific natural frequencies, such models are hardly reliable and specific. These results are of importance for the neuroscientific conclusions derived from the dynamical whole-brain modeling practices published in the literature, which we adapted and used in this study; see below. They therefore raise the question how reliable published dynamical whole-brain modeling studies actually are.

The literature on dynamical whole-brain modeling is highly heterogeneous with respect to both the reconstruction of the empirical SC and FC from empirical MRI data as well as the model implementations. We, for instance, only covered three of many possible model descriptions that have regularly been used in the whole-brain modeling literature, which also included the (Landau-Stuart) limit-cycle oscillator model (Deco et al., 2017; Ghosh et al., 2008), the (reduced) Wong-Wang model (Deco, Ponce-Alvarez, et al., 2014; Wong & Wang, 2006) and other (more complex) biophysically-oriented models (Abeysuriya et al., 2018; Bick et al., 2020; Deco & Jirsa, 2012; E. C. A. Hansen et al., 2015; Honey et al., 2007; Naskar et al., 2021). Hence, the methodological procedures may vary considerably between dynamical whole-brain modeling studies, and for most of these variations it is still unclear whether they produce reliable modeling results. This notion further strengthens our recommendation that dynamical whole-brain modeling studies should explicitly estimate the reliability of the reported results. A consistent reporting of the reliability of results may also help identify best practices in dynamical whole-brain modeling.

4.4.2 Subject specificity of simulated functional connectivity patterns

Various studies validated the dynamical whole-brain models on the basis of a variety of statistics (Cabral et al., 2011; Deco et al., 2013, 2017, 2019; E. C. A. Hansen et al., 2015; Naskar et al., 2021). Nevertheless, the correlation between the empirical and simulated FC still seems to be the current state-of-the-art in whole-brain modeling (Abeysuriya et al., 2018; Aquino et al., 2022; Naskar et al., 2021; Saggio et al., 2016), and so we used this particular measure for model validation as well. However, by computing the within-subject, single-modal correlations, we demonstrated that this model fitting procedure can yield strongly diverging simulated FC patterns depending on the model implementation and parcellation (Fig. 4.4). Moreover, even when simulated FCs had similar connectivity motifs across different empirical FC realizations of the same subject, this could still reflect an unspecific increase in both the within- and between-subject single-modal correlations (Fig. 4.4).

On a positive note, the reliability and subject specificity of the model parameters and simulated FC can essentially be improved by enhancing the model personalization. Furthermore, the correspondences between the simulated FC and the empirical SC were subject specific, that is, their specificity indices were statistically distinguishable from zero, only if the personalized empirical SC was used for model construction (Fig. 4.5). Hence, this result demonstrated that some of these subject-specific SC patterns are embedded in the simulated FC after the model simulations. We also found that the model-fit correlations can be significantly subject-specific (supplementary Fig. S4.25). The dynamical whole-brain models thus seem to have the ability to integrate connectivity patterns from both the (personalized) empirical SC and FC, which may (in part) explain how they replicate resting-state brain activity at a personalized level (Bansal et al., 2018; Deco et al., 2017; Jirsa et al., 2017; Ritter et al., 2013; Sanz-Leon et al., 2015), and how they yield good subject classification results (Iravani et al., 2021; Zimmermann, Perry, et al., 2018).

Nevertheless, our results merely showed that model construction on the basis of the personalized empirical SC can introduce subject-specific subtleties in the simulated FC; they do not explicitly reveal to which (clinical) purposes this may be beneficial other than subject identification (Fig. 4.4; Fig. 4.5). Furthermore, the specificity indices of the structure-function and model-fit correlations involving a simulated FC had comparable and small scales, especially when comparing them to the much higher single-modal specificity indices (Fig. 4.4). This indicates that the models do not straightforwardly map the empirical SC to the simulated FC with high specificity. We therefore propose that the simulated FC assimilating a diversity of personalized information should be regarded as a separate connectome modality together with the empirical SC and empirical FC.

For the single-modal and structure-function correlations, we could apply the subject specificity analyses also to purely empirical data. Here, the specificity indices of the empirical structure-function relationship (Fig. 4.5) roughly agree with the study by Zimmermann, Griffiths, et al. (2018). In addition, we identified individual subjects based on the structure-function correlations by identifying one FC (empirical or simulated) from all empirical SC and by identifying one empirical SC from all FC. For the empirical FC, we found the computed fingerprinting accuracies resembling the results reported by Messé (2020). Also the identification of one FC from all SC manifested much higher success rates than vice versa when considering the non-linear models (Fig. 4.5). The latter result agrees with the problematic inference of the empirical SC from the empirical FC reported by Honey et al. (2009). The linear model was particularly different from the non-linear models with respect to the structure-function correlations. In particular, it exhibited large values of the structure-function specificity index, and could have enhanced fingerprinting accuracy irrespective of whether one simulated FC was identified from all empirical SC or the other way around (Fig. 4.5). Such a rigid connection between structure and function,

which may impair the flexibility of a variety of functions emerging from the same structure, was observed neither in the brain (Deco et al., 2011; E. C. A. Hansen et al., 2015; Honey et al., 2009; Ponce-Alvarez et al., 2015) nor in the non-linear models considered in this study.

Also the fingerprinting accuracies for the single-modal correlations of the empirical FC (Fig. 4.4) are in agreement with the literature (Finn et al., 2015; Li et al., 2021). However, the latter were rather variable across parcellations with a difference of up to 20% (Fig. 4.4). Even though the atlas granularity is known to influence the fingerprinting accuracy (Li et al., 2021; Peña-Gómez et al., 2018), we minimized this effect by selecting parcellations that contained roughly the same number of parcels. Our study therefore demonstrates the considerable effect of the parcellation technique in isolation on the fingerprinting analysis, which has not been assessed previously. With respect to the fingerprinting analysis, we also acknowledge that the limited number of subjects used in our study may lead to some positive bias in the fingerprinting accuracy (Li et al., 2021; Waller et al., 2017). Nevertheless, as we performed the same fingerprinting analysis for different modalities, this bias (if any) should be included in all results and hence does not render the comparison invalid.

4.4.3 Model implementations

Enhanced model personalization influenced the within-subject correlations of the similarity maps mildly at best, while it increased the specificity indices of these mappings (Fig. 4.6). Given Eq. 4.15, this implies a decrease in the correspondence of the similarity maps across subjects. Qualitatively, the latter finding agrees with the similarity maps shown in supplementary Figs. S4.3-S4.10 as well. The observed decrease in the inter-subject correspondence of the similarity mappings can also induce additional variation in the location of the maxima of these similarity mappings (optimal model parameters) between subjects. This is explicitly demonstrated by the enhancements of the between-subject variance in the optimal model parameters for enhanced model personalization (Fig. 4.2). Despite the relatively untouched within-subject correlations of the similarity maps, increased model personalization also somewhat enhanced the within-subject variance of the optimal model parameters, but not as much as the between-subject variance (Fig. 4.2). Given Eq. 4.14, this then leads to the higher ICC for enhanced model personalization. Taken together, we discovered that the higher reliability of the model parameters for more personalized dynamical whole-brain models is induced by a decrease in the comparability of the similarity maps between subjects. Future studies should confirm whether enhanced model personalization indeed improves the differentiability of modeling results across subjects in, for example, classification studies.

We sampled our results for 6 different model implementations that were based on two non-linear models and one linear model, which were all adapted from the literature (Deco et al., 2009; Galán, 2008; Ponce-Alvarez et al., 2015; Saggio et al., 2016). Here, we note that not all parameters of the considered models can straightforwardly be interpreted and associated with brain dynamics. We therefore consider them in the first approximation as model properties that may influence the quality of the model validation, reliability and specificity. Moreover, the literature also inspired the use of the grand-averaged and personalized empirical SCs for model construction and the wielding of the subject-specific frequency profiles in the simulations of the phase oscillator model. Iravani et al. (2021) and Zimmermann, Perry, et al. (2018), for instance, constructed their models on the basis of group-averaged and personalized empirical SCs, respectively, before using the modeling results for subject classifications. In addition, several recent studies embedded additional region-specific and potentially subject-specific data (among others, regional frequency profiles) in the dynamical whole-brain modeling workflow (Chapter 3; Deco, Cruzat, et al., 2018; Deco et al., 2019; Demirtaş et al., 2019; Donnelly-Kehoe et al., 2019; Jung et al., 2021; Kringelbach et al., 2020; Popovych et al., 2021). The investigation presented in this study may be extended by considering, for example, limit-cycle models (Deco

et al., 2017), where the additional model parameters controlling the oscillator amplitudes can be varied for further model personalization. A recent study also demonstrated that subject- and region-specific data can be incorporated into a neural mass model (Demirtaş et al., 2019), indicating that model personalization is in active investigation nowadays.

The two non-linear models (the Kuramoto and Wilson-Cowan models) were selected for three particular reasons. First, both models have frequently been used in previous investigations involving dynamical whole-brain models (Abeysuriya et al., 2018; Daffertshofer & van Wijk, 2011; Deco et al., 2009; Hellyer et al., 2016; Jung et al., 2021; Messé et al., 2014; Muldoon et al., 2016; Ponce-Alvarez et al., 2015; Popovych et al., 2021). Second, their dynamical behaviors under different parameter conditions can be understood and controlled well, because they are sufficiently reduced in terms of complexity and provided with good documentation (Kuramoto, 1984; Wilson & Cowan, 1972). Third, their underlying concepts and implementations in whole-brain modeling studies diverge considerably, which makes it more probable that differences are found between models. In particular, published studies used the Kuramoto model (just like a network of Landau-Stuart limit-cycle oscillators) to model the BOLD signal dynamics directly from the empirical SC (Chapter 3; Deco et al., 2017; Deco, Cabral, et al., 2018; Deco et al., 2019; Jung et al., 2021; Ponce-Alvarez et al., 2015; Popovych et al., 2021), whereas the Wilson-Cowan model requires a haemodynamic conversion model since it specifically models interactions between neural masses. However, the modeling of BOLD signal variations directly from the empirical SC does not reflect the neural dynamics underlying the BOLD signal, and hence future studies could check whether a transformation of the empirical SC matrix might be more appropriate in this case.

Furthermore, there were two reasons for the selection of the linear model. First, its analytical solution ensured that we could estimate the reliability of its global coupling parameter in the absence of any specifications associated with model simulations (Saggio et al., 2016). We actually found this reliability to be at about the same level as those of the global couplings of the non-linear models if signal latency was disregarded (supplementary Fig. S4.20). Second, as mentioned in Materials and methods, the model reflects the diffusion of noise across the empirical SC (Galán, 2008; Saggio et al., 2016). This process can be seen as a (linear) scaling of the direct dependencies included in the empirical SC to indirect dependencies, which are more compatible with the definition of the FC (Das et al., 2017; Liégeois et al., 2020). In most cases, we observed that model complexity did not exert a particular increasing or decreasing influence on the reliability or subject specificity of the results of the model fitting (Fig. 4.3; Fig. 4.4; supplementary Fig. S4.25). Also, there were no particular differences with respect to the goodness-of-fit (supplementary Fig. S4.11). In other words, with regard to (the reliability and specificity of) the wielded model fitting procedure, the Kuramoto and neural mass models in fact do not seem to outperform the linear model. On the contrary, the linear model sometimes demonstrated stronger reliability and subject-specificity than the non-linear models with the same level of personalization. However, the similarity mappings of more complex models appeared to exhibit much enhanced subject specificity as reflected by both the specificity index and the fingerprinting accuracy (Fig. 4.7). Also the results obtained for the structure-function relationship indicated that complex non-linear models can deliver more realistic results as discussed above. Therefore, the non-linear models appeared to have an increased potential in terms of modeling structure-function interactions and preserving and enhancing the reliability and subject specificity of empirical data as well as model personalization. However, the presented results may also indicate that the model validation procedure of fitting static empirical and simulated FCs is suboptimal in spite of being state-of-the-art as discussed above. Future studies may therefore scrutinize the influence of the model fitting procedure on the reliability and subject specificity of dynamical whole-brain modeling results and propose concrete procedures on how to improve this reliability. In particular, they could investigate whether multimodalities or degeneracy in the similarity maps, which can be observed in supplementary Figs. S4.3-S4.10 for some combina-

tions of parcellation and model, can affect the reliability and specificity of the model and should therefore be considered more explicitly when selecting the optimal model parameters. Alternatively, they could examine whether a completely different model fitting strategy, such as fitting the models on the basis of the dynamics of the FC (Brovelli et al., 2017; E. C. A. Hansen et al., 2015; Heitmann & Breakspear, 2018; Hutchison et al., 2013; Kong et al., 2021; Preti et al., 2017), yields more reliable results.

4.4.4 Atlas variation

A vast number of methods for parcellating the brain have been proposed in the literature (Amunts & Zilles, 2015; Eickhoff, Constable, & Yeo, 2018; Eickhoff, Yeo, & Genon, 2018). A lot of attention was devoted to the effect that the brain parcellation may have on the analyses of empirical data (Albers et al., 2021; Arslan et al., 2018; Messé, 2020; J. Wang et al., 2009; Zalesky et al., 2010) and recent modeling results (Chapter 3; Jung et al., 2021; Popovych et al., 2021). In this study, we put more emphasis on varying the parcellation method rather than the granularity (number of parcels included in the atlas) when investigating the effect of the parcellation on the modeling results. Previous studies support this focus: Even though granularity is a determining factor when considering statistical analyses of empirical data (Messé, 2020; J. Wang et al., 2009; Zalesky et al., 2010), parcellation-induced variations in the modeling results could not be explained by only considering this property of the parcellations. Instead, variations in the model fitting quality were primarily related to graph-theoretical network properties extracted from the empirical connectomes (Chapter 3) and to other data variables reflecting some statistical properties of the empirical data (Popovych et al., 2021).

In the variation of the parcellations, we balanced between parcellations derived from structural and functional data. Here, the included functionally-derived parcellations presumably optimize the regional homogeneity with respect to the voxel-wise FC (Craddock et al., 2012; Schaefer et al., 2018; Shen et al., 2013; Urchs et al., 2019). In contrast, the structurally-derived atlases have not been designed to do the same for the SC, but may for example follow the anatomical folding patterns of the cortex (Desikan et al., 2006; Frazier et al., 2005; Goldstein et al., 2007; Makris et al., 2006; Rolls et al., 2015; Scholtens et al., 2018; Tzourio-Mazoyer et al., 2002; von Economo & Koskinas, 1925). Our results portrayed distinctions between these structurally- and functionally-derived parcellations, especially when considering the structure-function correlations of the empirical SC with the simulated FC (Fig. 4.5). The reliability and the (single-modal) subject specificity of the simulated FC also demonstrated opposite tendencies for different parcellation groups, where the former is enhanced for the structurally-derived parcellations, while the latter is larger for the functionally-derived parcellations (Fig. 4.2; Fig. 4.3; Fig. 4.4). These distinctions between the structurally- and functionally-derived brain atlases demonstrate that the parcellation technique has a systematic impact on the modeling results, which can be organized according to particular parcellation principles. Even though relationships were found between the goodness-of-fits and the subject specificities across parcellations, the quality of these associations was rather variable across models (supplementary Fig. S4.27). Hence, the precision with which the reliability and subject specificity can be estimated from the goodness-of-fit, which is a proxy for the network properties of the empirical connectomes (Chapter 3) as well as the empirical structure-function relationship and other statistical properties (Popovych et al., 2021), is highly model-dependent.

We also observed notable model-dependent, parcellation-induced differences in the within-subject correlations of the similarity maps (Fig. 4.6; Fig. 4.7); see, for instance, the elongated boxes shown in Fig. 4.6 and Fig. 4.7 for the Schaefer atlas relative to the other parcellations. Since we found the reliability and specificity of the empirical FC to be relatively stable across parcellations (Fig. 4.2; Fig. 4.3; Fig. 4.4), we conclude that dynamical whole-brain models are sensitive to the choice of brain atlas; see also Chapter 3 and Popovych et al. (2021). In particular, these results imply that, even though the model is constructed from the same empirical SC,

variations of the empirical FC for the same subject may lead to considerably different similarity maps depending on the atlas (and model). We do not suggest that this is necessarily a negative facet of a particular brain atlas. When such parcellations are used for model construction, the fitted models may, for instance, characterize the distinct brain states or other information stored in the different resting-state empirical FC realizations of the same subject that are obscured by other parcellations (for a discussion, see Finn & Rosenberg, 2021; Finn, 2021). The negative relationships between the goodness-of-fits and specificity indices support this notion (supplementary Fig. S4.27), because these findings indicate that a better fit of the model to the empirical data is, in fact, more likely to reflect a more generic (hence not subject-specific) fit. All things considered, our study clearly demonstrates that the proper selection of the brain parcellation appears to be even more important for research using dynamical whole-brain models than studies straightforwardly analyzing the empirical data.

In sum, we extensively assessed the (test-retest) reliability and the subject specificity of the modeling results and their relation to the empirical data. We showed that the model parameters may be fitted to the empirical data with a reliability ranging from ”poor” to ”good” depending on the implementation of the dynamical whole-brain modeling paradigm. In addition, we demonstrated that more personalized models yield increasingly reliable and subject-specific modeling results. For some modeling conditions, we even found that the modeling results were more reliable and subject specific than the results only involving empirical data. We additionally illustrated that the simulated FC may concurrently adopt subject-specific connectivity patterns from both the empirical SC and the empirical FC through the model fitting procedure, which could support considering simulated FC as a separate connectome modality. Finally, we sampled all our findings for 8 state-of-the-art parcellations and demonstrated the substantial impact that a change of parcellation can have on the modeling results, which by far exceeded the parcellation-induced deflections in the results of the empirical data. Taken together, our findings provide an exploratory account on relevant methodological aspects of dynamical whole-brain modeling results. They contribute to the mechanistic understanding of (the personalization of) these models and reveal best practices. Hence, the presented results can be relevant for application of the whole-brain dynamical models and their further development.

Acknowledgements

We thank M. Kollmann for his consultation on the manuscript. The authors gratefully acknowledge the computing time granted through JARA on the supercomputer JURECA at Forschungszentrum Jülich. This study was made possible through the Portfolio Theme Supercomputing and Modeling for the Human Brain of the Helmholtz Association (https://www.helmholtz.de/en), and through the European Union’s Horizon 2020 Research and Innovation Program (grant agreements 785907 (HBP SGA2), 945539 (HBP SGA3) and 826421 (VirtualBrainCloud)). Open access publication was funded by the Deutsche Forschungsgemeinschaft (DFG, German Research Foundation) - 491111487. The funders had no role in study design, data collection and analysis, decision to publish, or preparation of the manuscript.

Supplementary figures

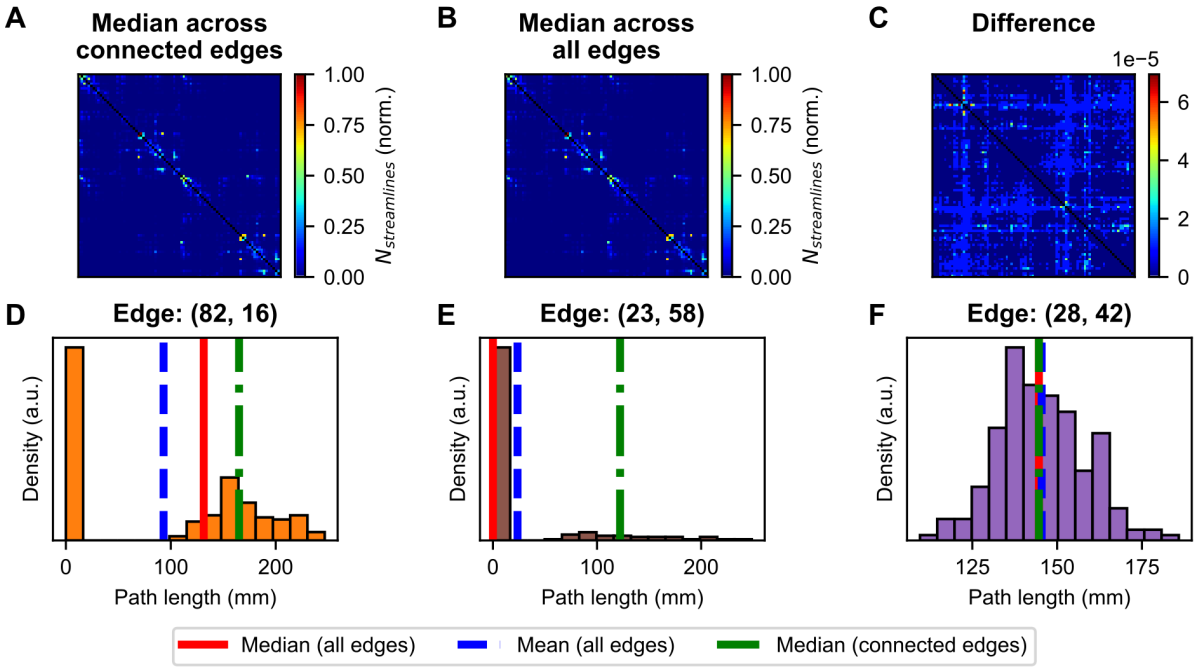

Fig. S4.1. Effect of a straightforward averaging of the empirical structural connectivity (SC) and path length (PL) matrices across subjects, and the grand-average approach proposed in this study; see "Empirical structural connectivity" in Materials and methods. The displayed connectomes were reconstructed using the von Economo-Koskinas atlas. **(A-B)** Group-averaged SC matrices derived (A) by taking the median of only the connected edges across subjects and (B) by straightforward averaging (median across connected and disconnected edges). Individual edges have been normalized by their maximum value across the group-averaged edges (edge that has the most influence on the group-averaged network dynamics). Diagonals are colored black, since they were not used for the model simulations. **(C)** The SC matrix shown in panel B subtracted from the one displayed in panel A. Note the substantial difference in scaling of the colors with respect to panels A and B as indicated by the color bars. **(D-F)** Examples of distributions of the path lengths of three distinct edges across subjects and their grand-averages over subjects. The lines depict the different types of group-averages as indicated in the legend. The medians calculated over all connected edges (green lines) were used in this study as proxies of the grand-averaged path lengths.

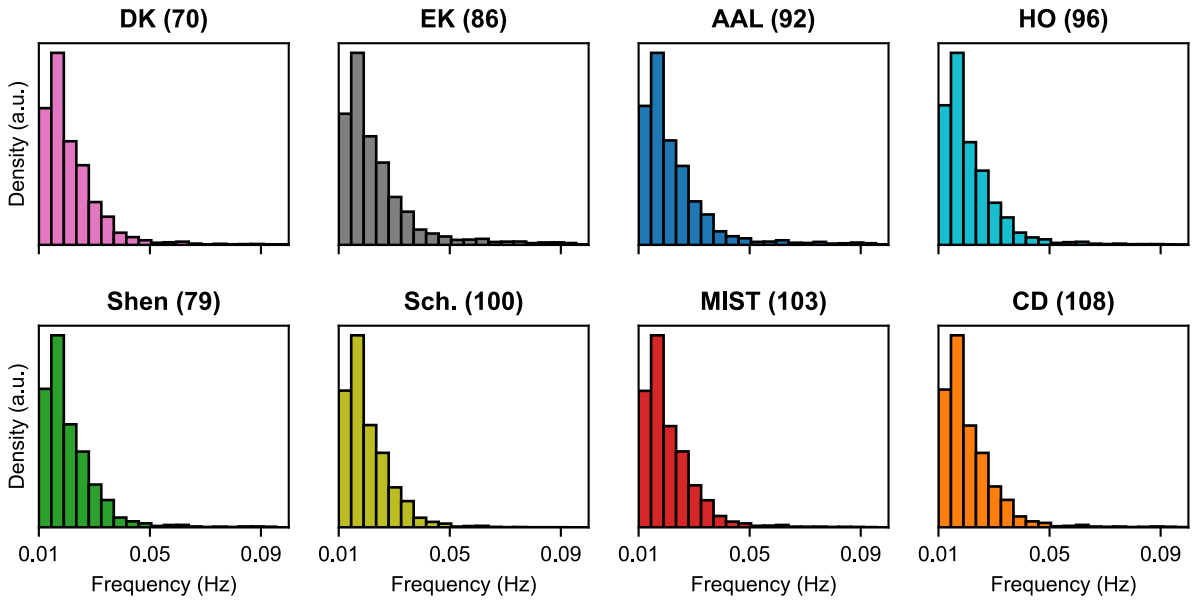

Fig. S4.2. Distributions of the natural frequencies determined from the blood-oxygen-level-dependent (BOLD) time series across all subjects and regions for the different parcellations considered in this study. Each plot corresponds to the parcellation described by the abbreviation included in the title; see Table 4.1.

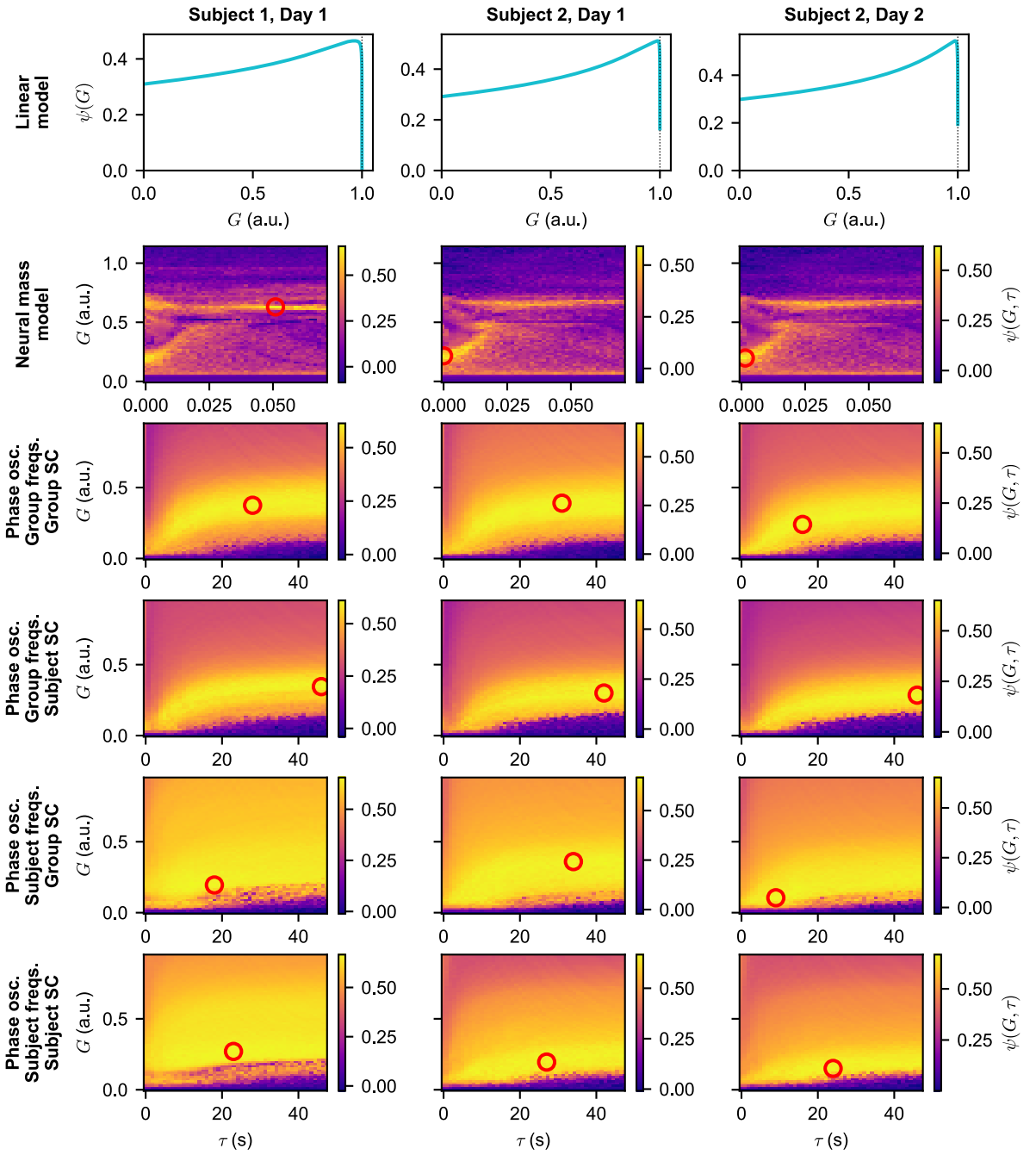

Fig. S4.3. Examples of the similarity maps $\psi(G, \tau)$ (Eq. 4.1) as a function of the global coupling G and delay τ parameter for three subject-session pairs when the Desikan-Killiany atlas (Table 4.1) was used for the reconstruction of the empirical connectomes. Each row corresponds to a different model as indicated by the labels on the left side of the plots. The black dotted lines in the plots of the linear model indicate the critical coupling $G = 1$; see "Linear model" in Materials and methods. The red circles in the plots of the non-linear models indicate the locations of the maxima. The first column corresponds to the first subject and the first day of fMRI data sampling, the second to the second subject and the first day of data sampling and the third to the second subject and the second day of data sampling. Hence, the first two columns may be compared for inter-subject variability, while the second and third may be checked for intra-individual differences. The fMRI data corresponding to the left-to-right phase-encoding direction were used for the acquisition of these plots. Abbreviations: a.u. = arbitrary unit, freqs. = frequencies, osc. = oscillator.

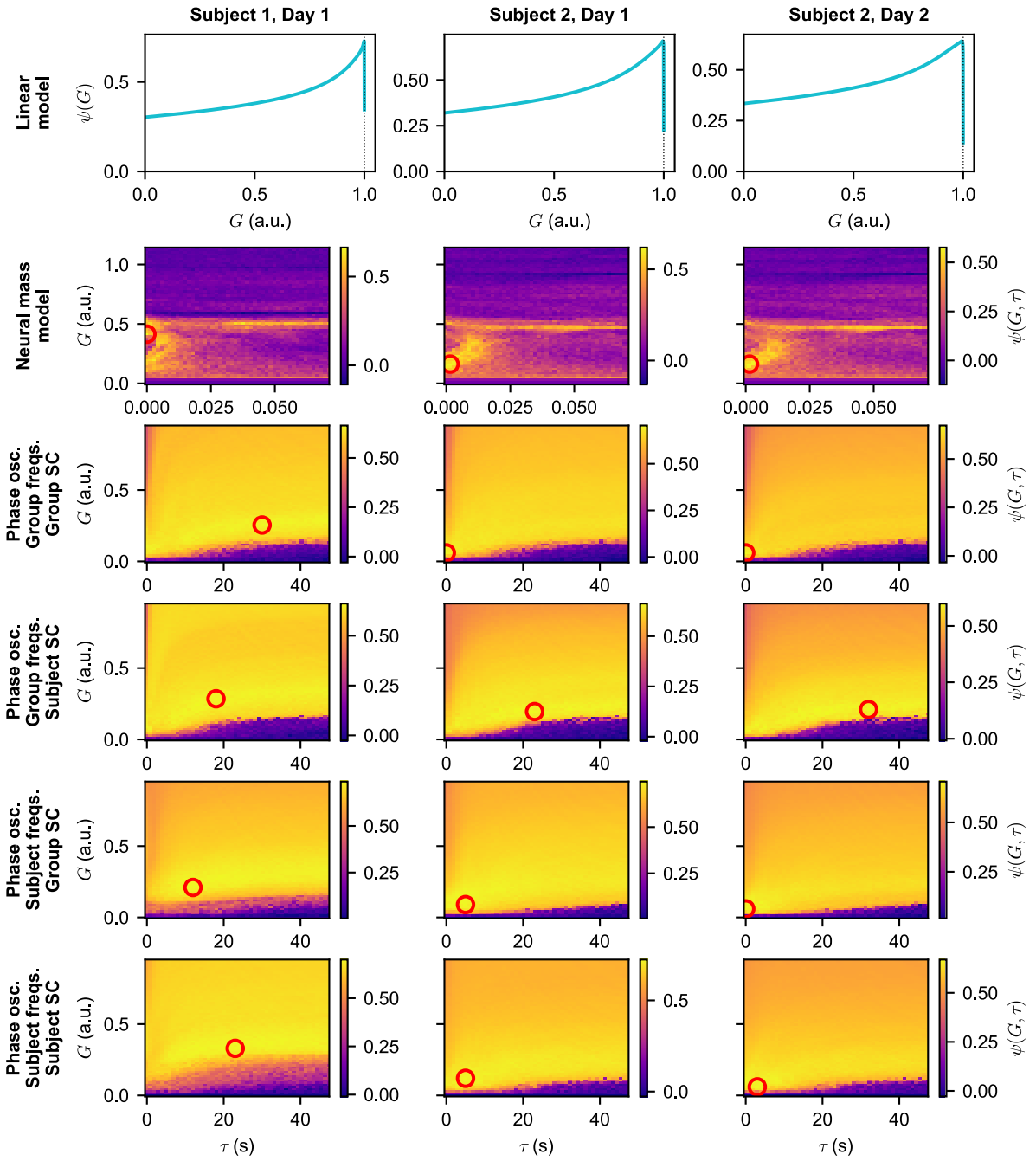

Fig. S4.4. Same as Fig. S4.3 but for the von Economo-Koskinas atlas (Table 4.1).

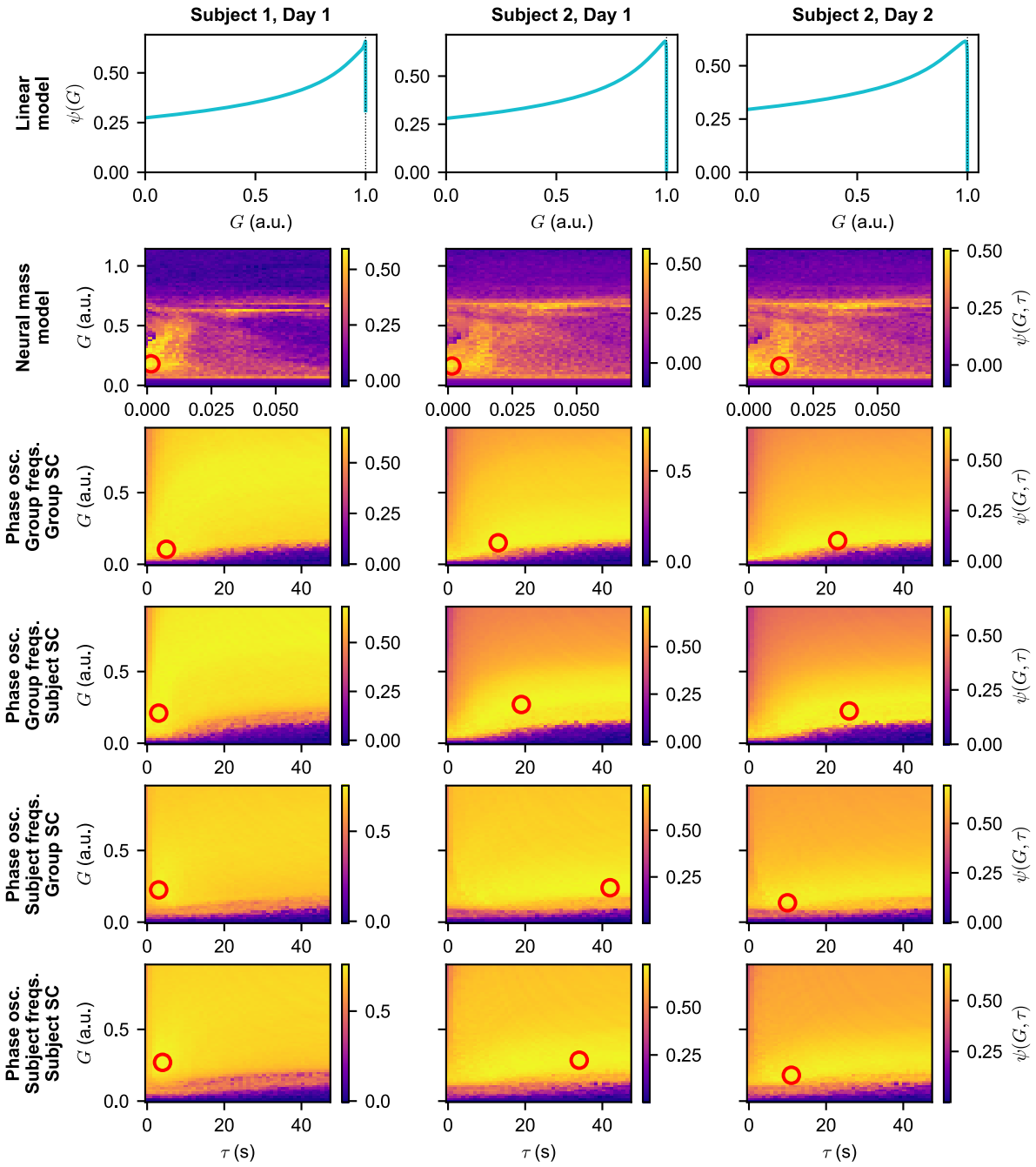

Fig. S4.5. Same as Fig. S4.3 but for the AAL atlas (Table 4.1).

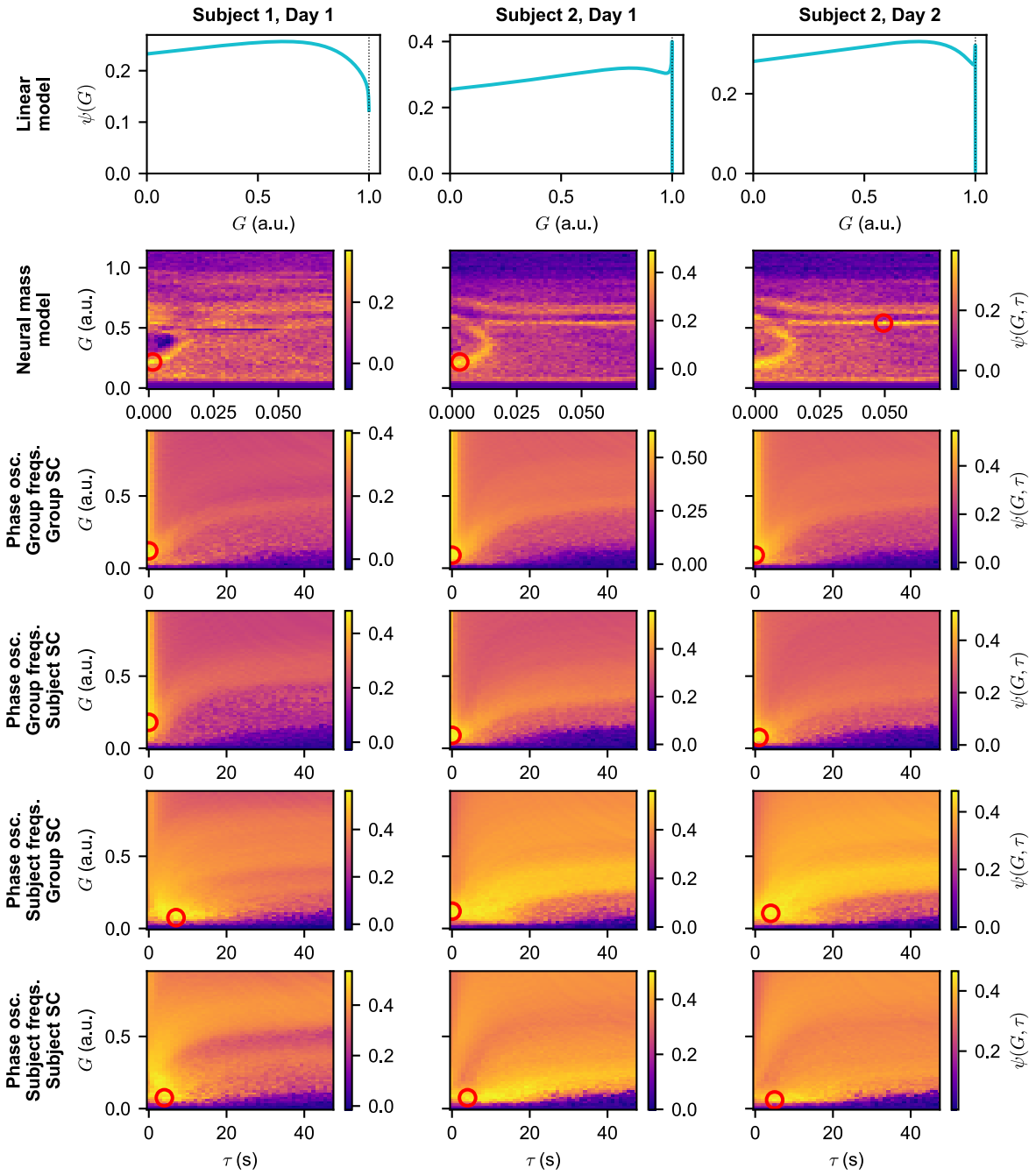

Fig. S4.6. Same as Fig. S4.3 but for the Harvard-Oxford atlas (Table 4.1).

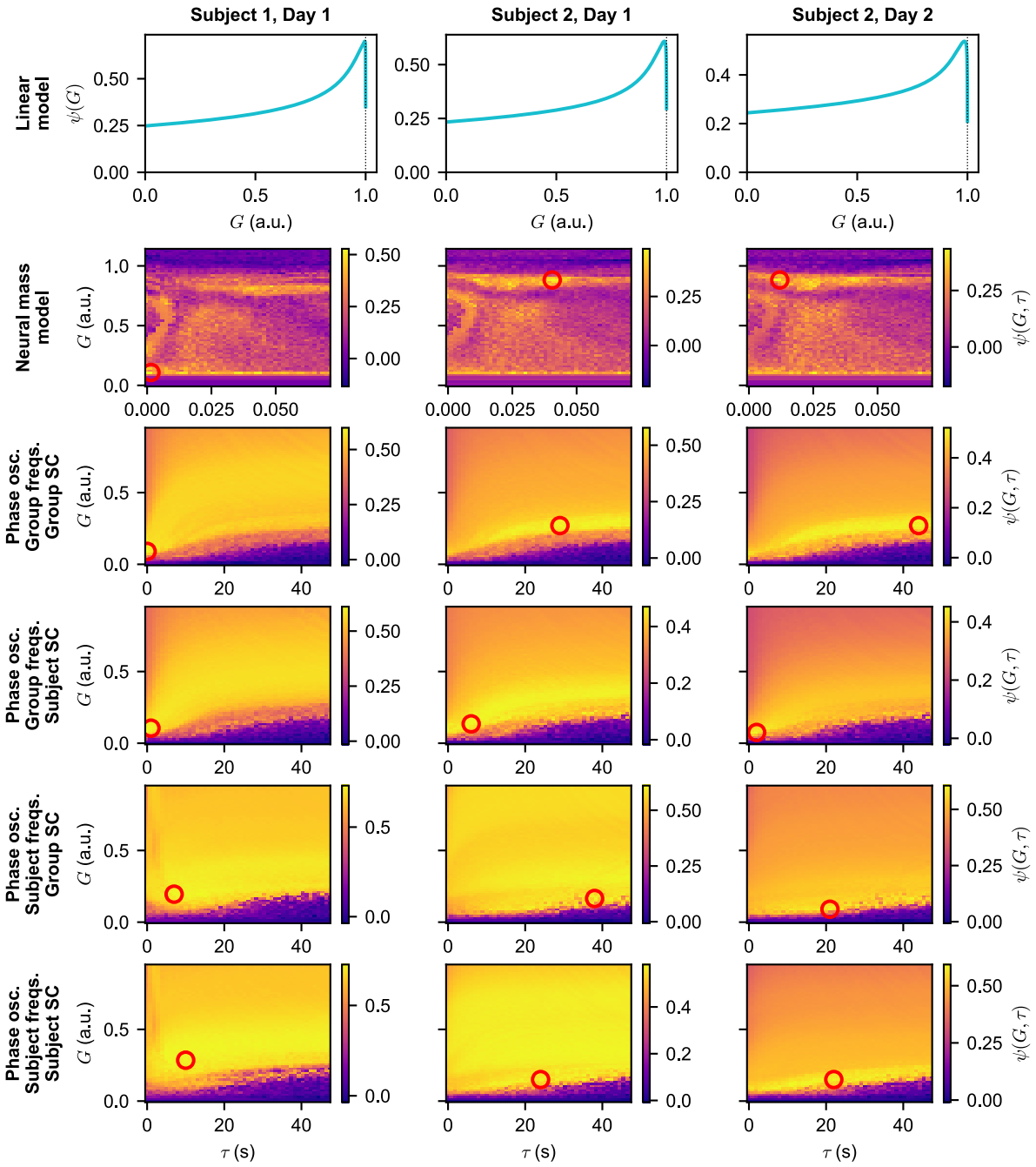

Fig. S4.7. Same as Fig. S4.3 but for the Shen atlas (Table 4.1).

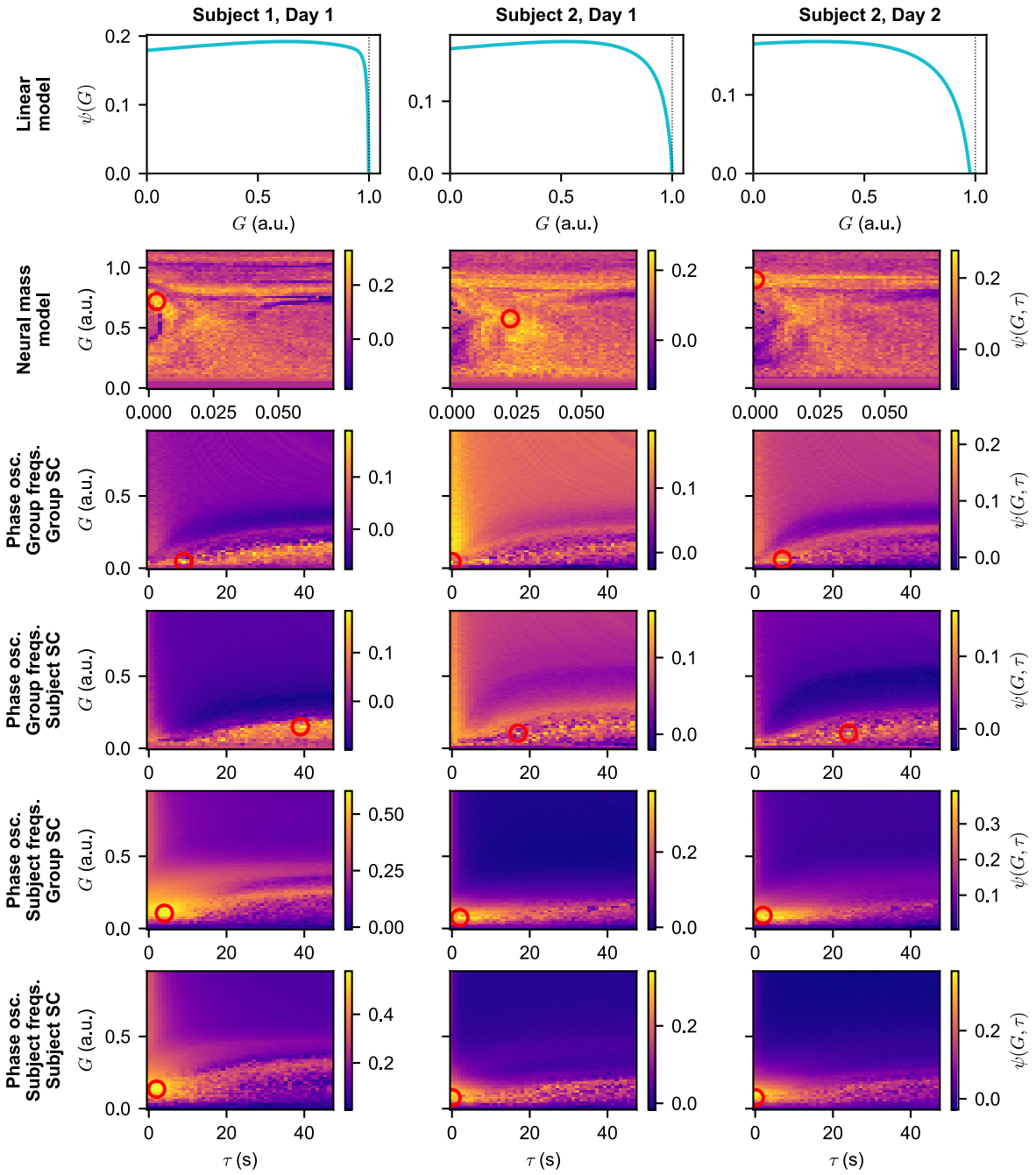

Fig. S4.8. Same as Fig. S4.3 but for the Schaefer atlas (Table 4.1).

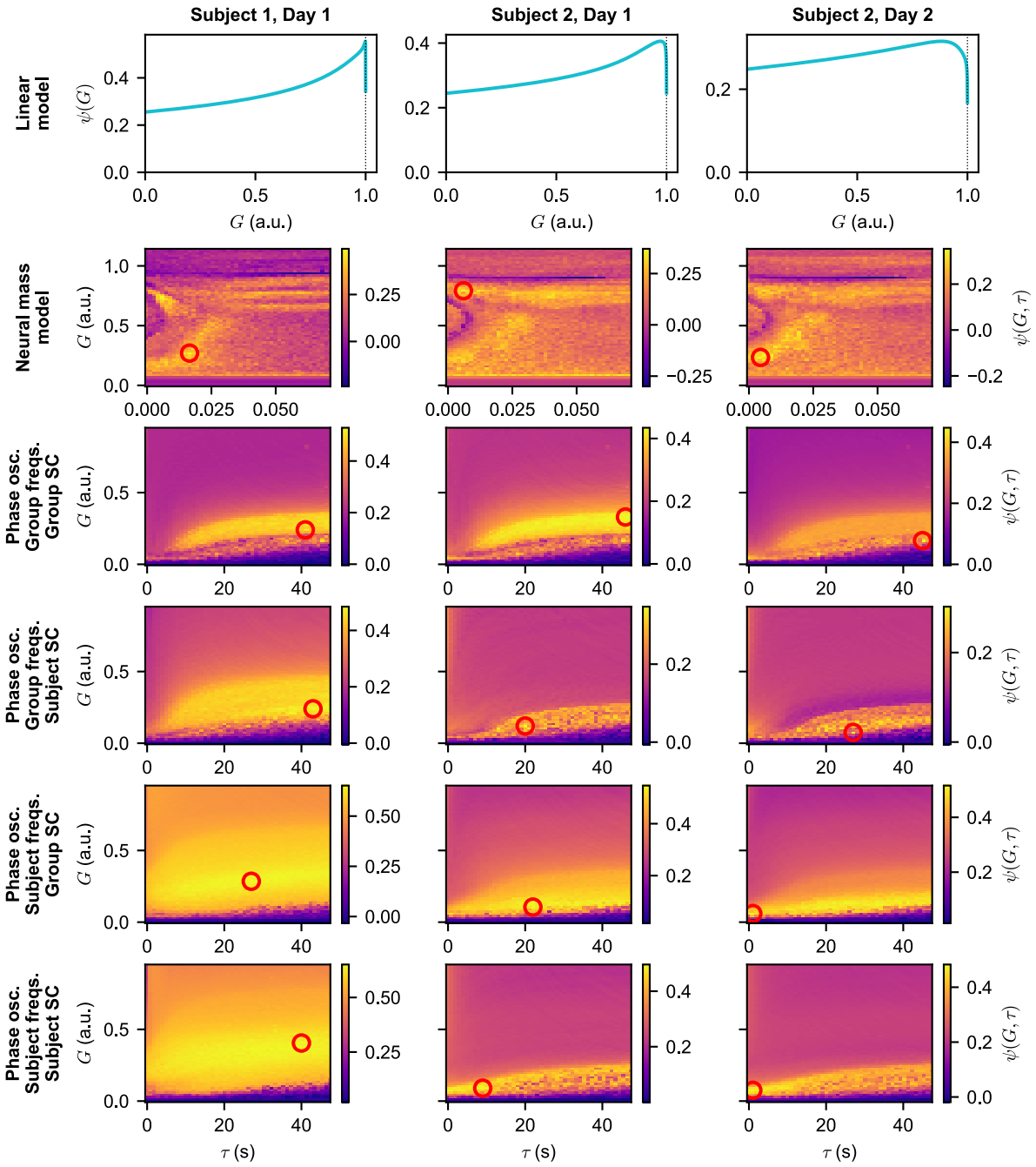

Fig. S4.9. Same as Fig. S4.3 but for the MIST atlas (Table 4.1).

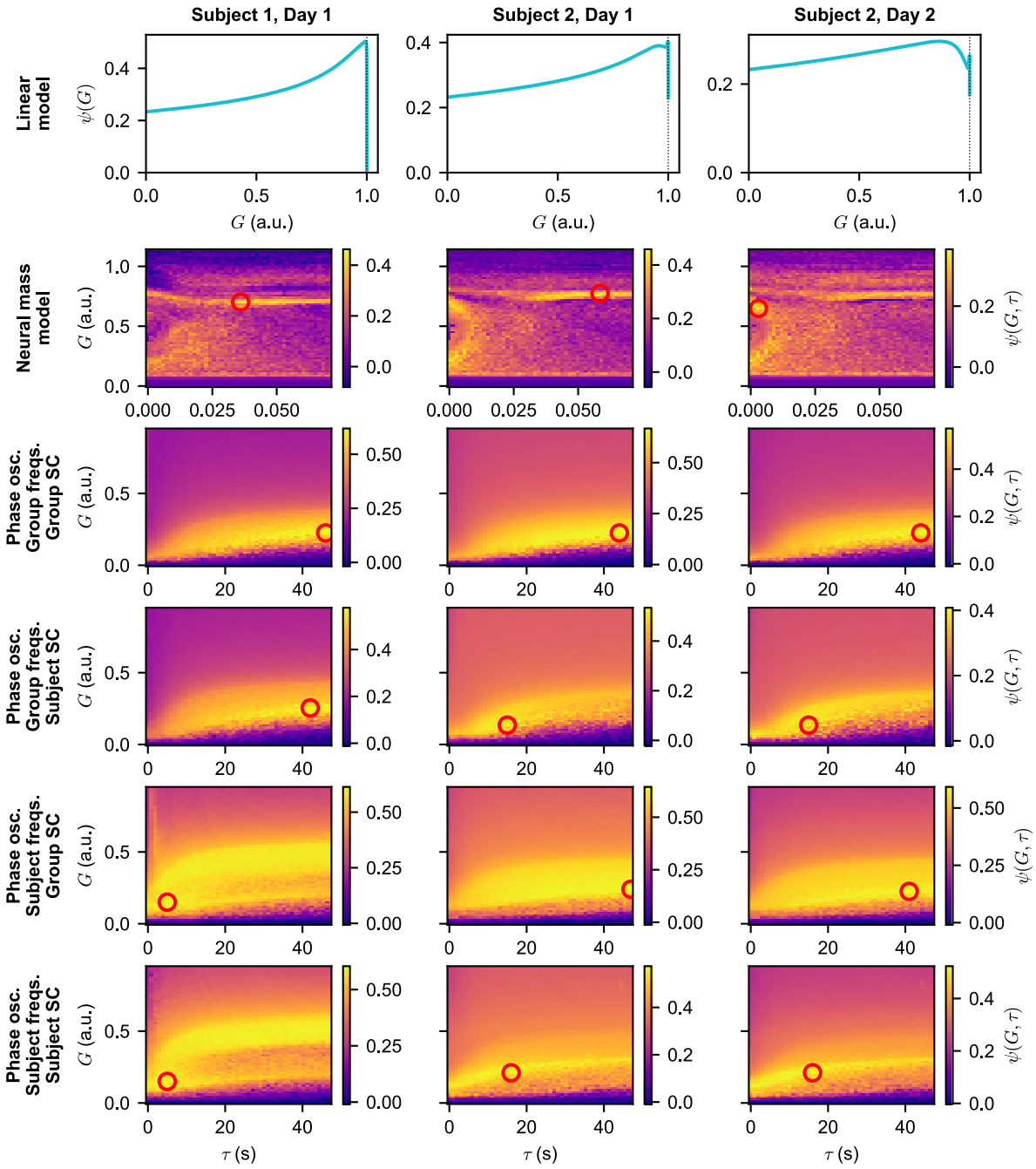

Fig. S4.10. Same as Fig. S4.3 but for the Craddock atlas (Table 4.1).

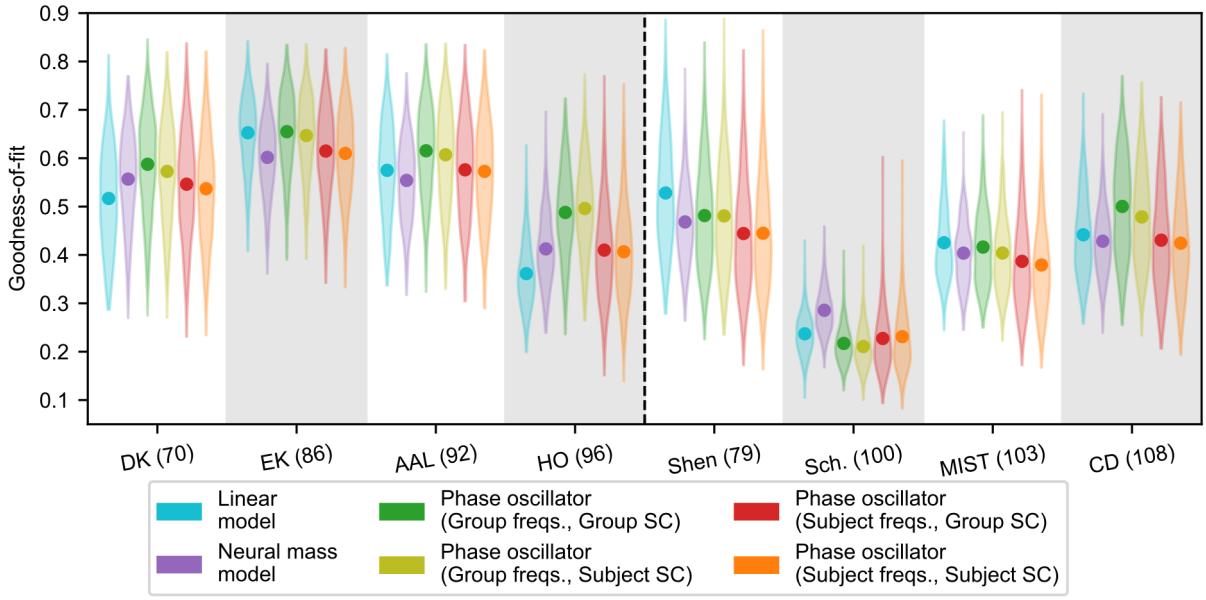

Fig. S4.11. Distribution of the goodness-of-fit values of the different model implementations as indicated in the legend and for the various parcellations used in this study as indicated on the horizontal axis (Table 4.1). Dots depict the means. The dashed black line separates the brain atlases constructed on the basis of structural data (left block) from those based on functional data (right block). Abbreviation: freqs. = (natural) frequencies.

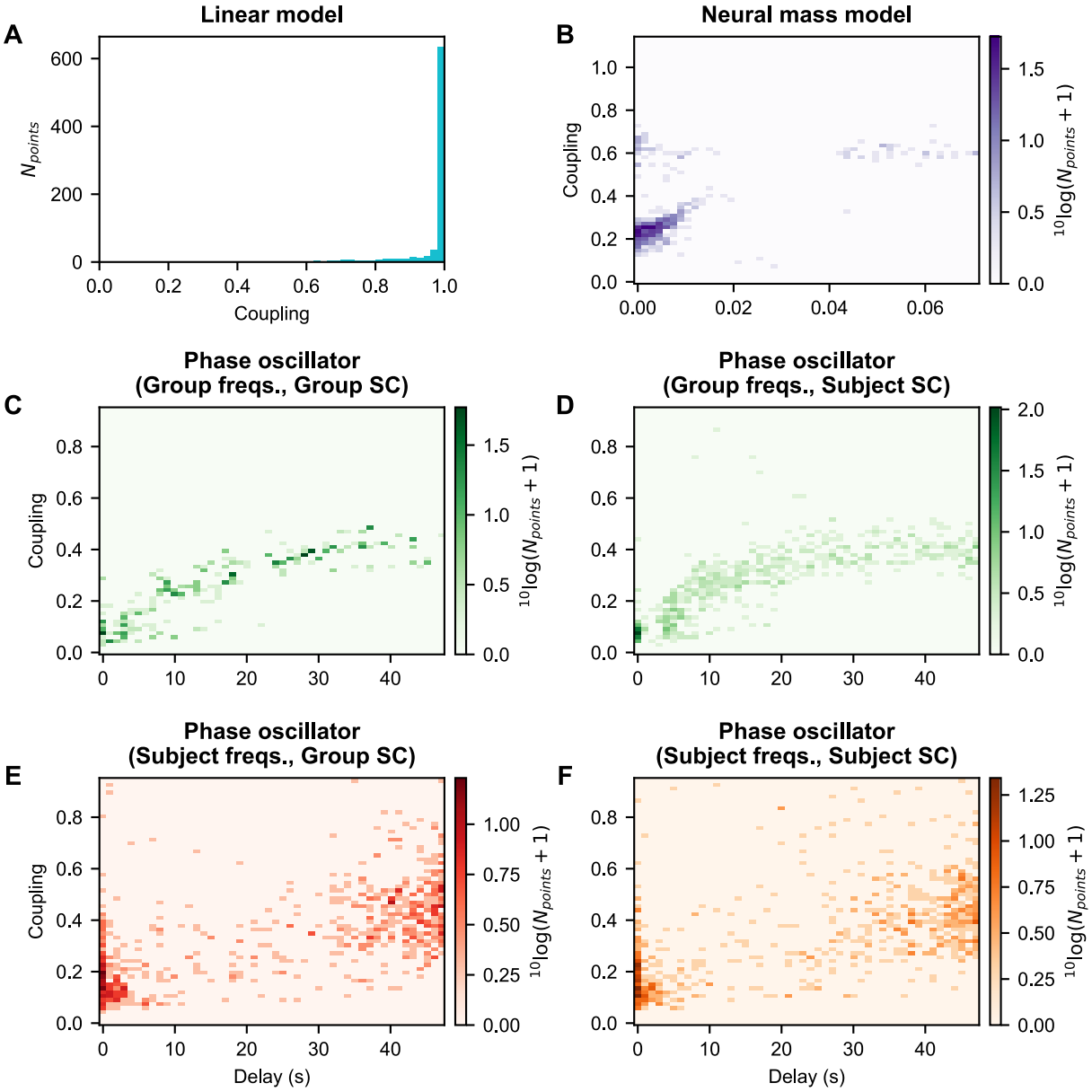

Fig. S4.12. Distributions of the optimal parameter settings for the Desikan-Killiany atlas (Table 4.1). **(A)** Distribution of the optimal coupling parameter for the linear model that was constructed using the personalized empirical structural connectivity (SC). **(B)** Distributions of the optimal coupling and delay parameters for the neural mass model that was constructed using the personalized empirical structural connectivity (SC). **(C-F)** Distributions of the optimal coupling and delay parameters for the phase oscillator model using group-averaged frequencies (C-D) and subject-specific frequencies (E-F). Models were constructed either on the basis of (C,E) the grand-averaged or (D,F) the personalized empirical SC.

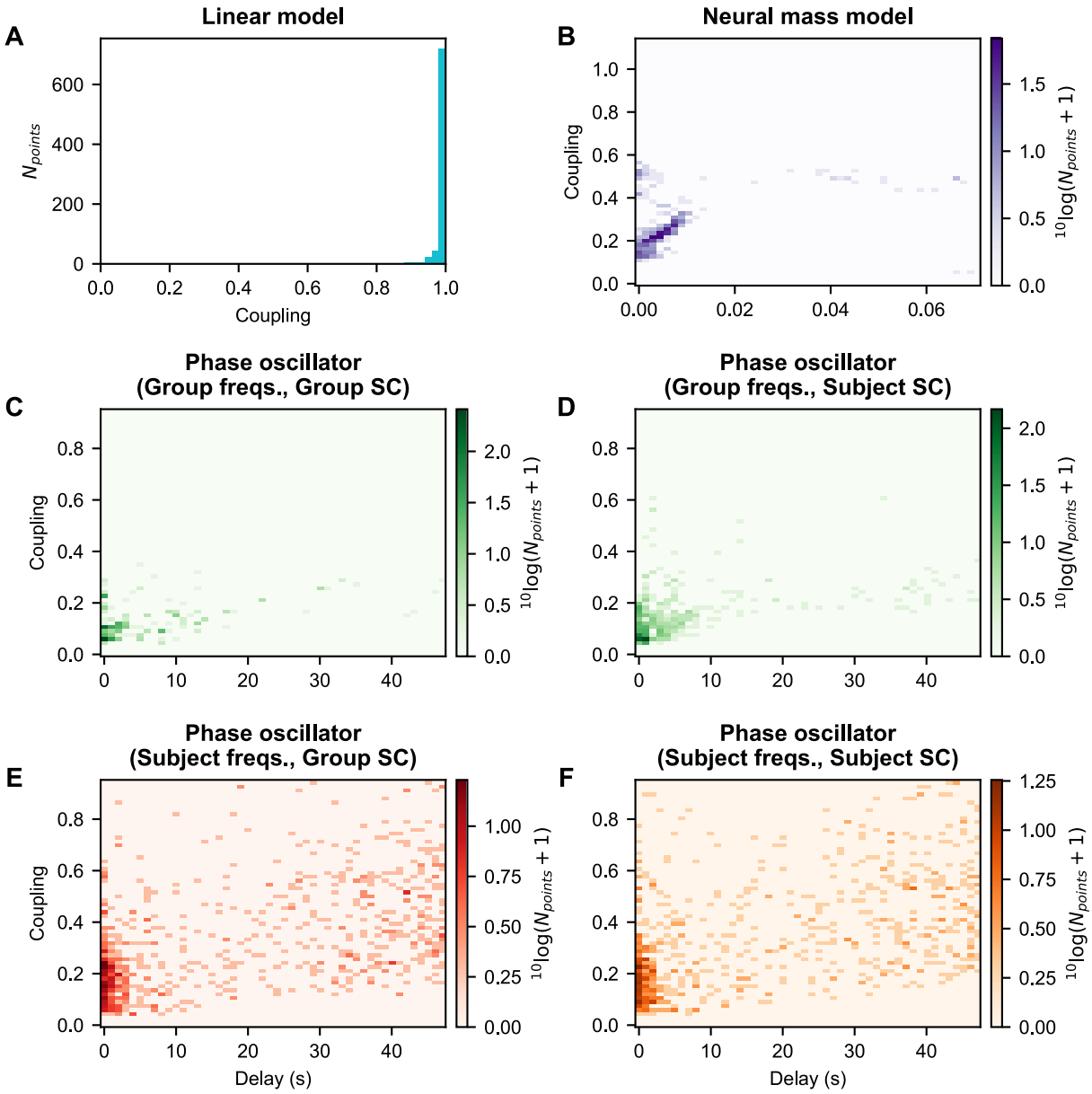

Fig. S4.13. Same as Fig. S4.12 but for the von Economo-Koskinas atlas (Table 4.1).

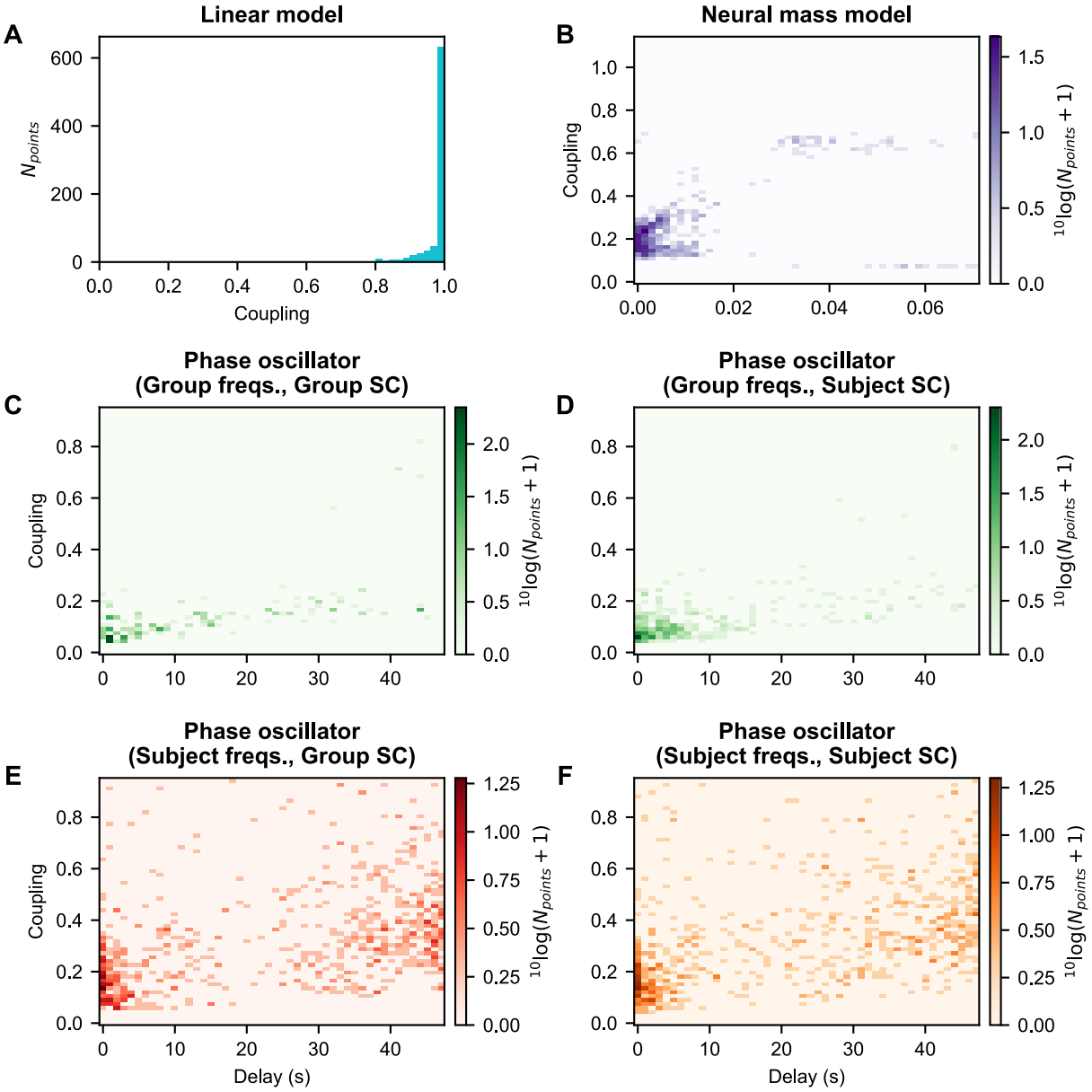

Fig. S4.14. Same as Fig. S4.12 but for the AAL atlas (Table 4.1).

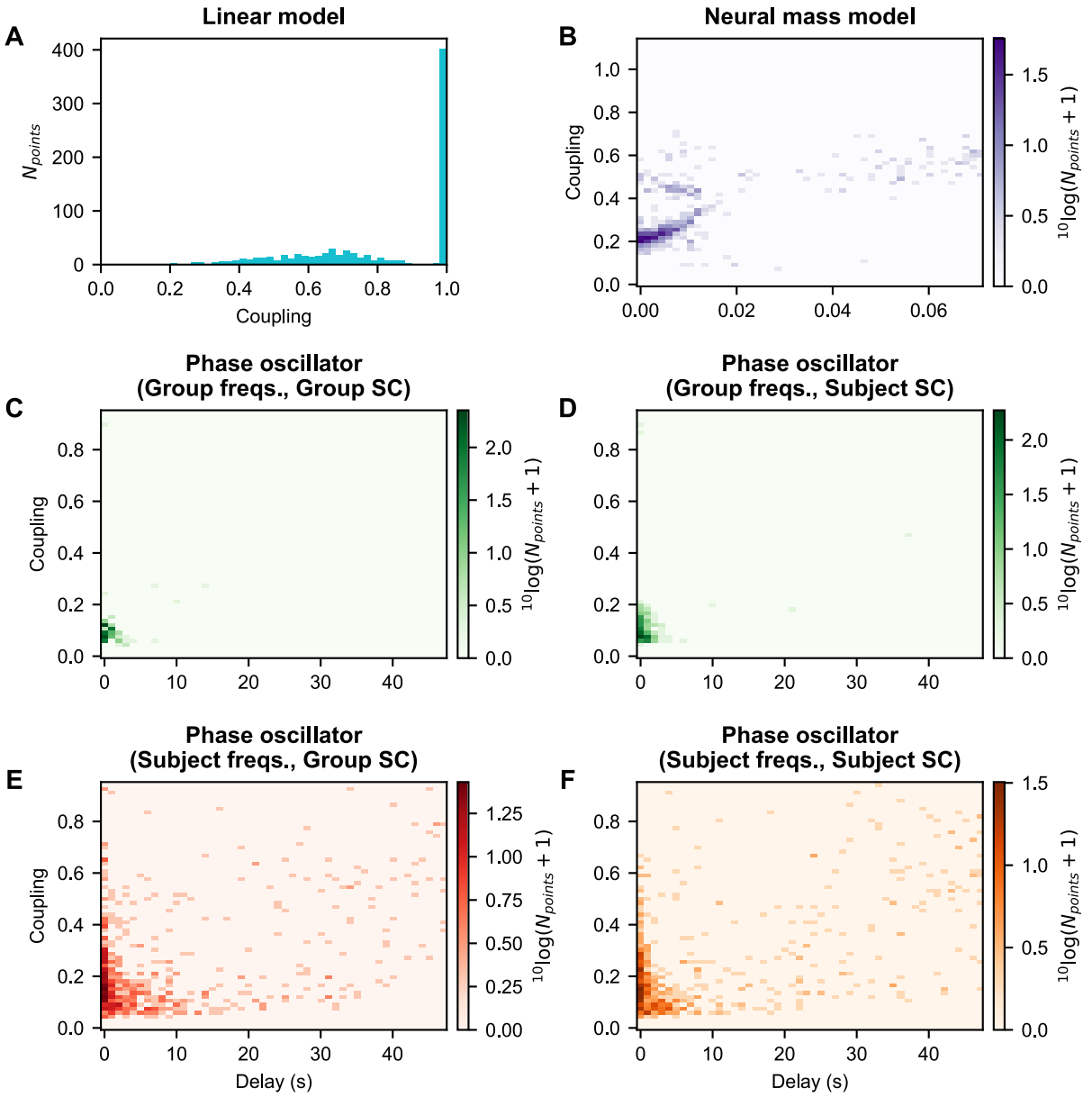

Fig. S4.15. Same as Fig. S4.12 but for the Harvard-Oxford atlas (Table 4.1).

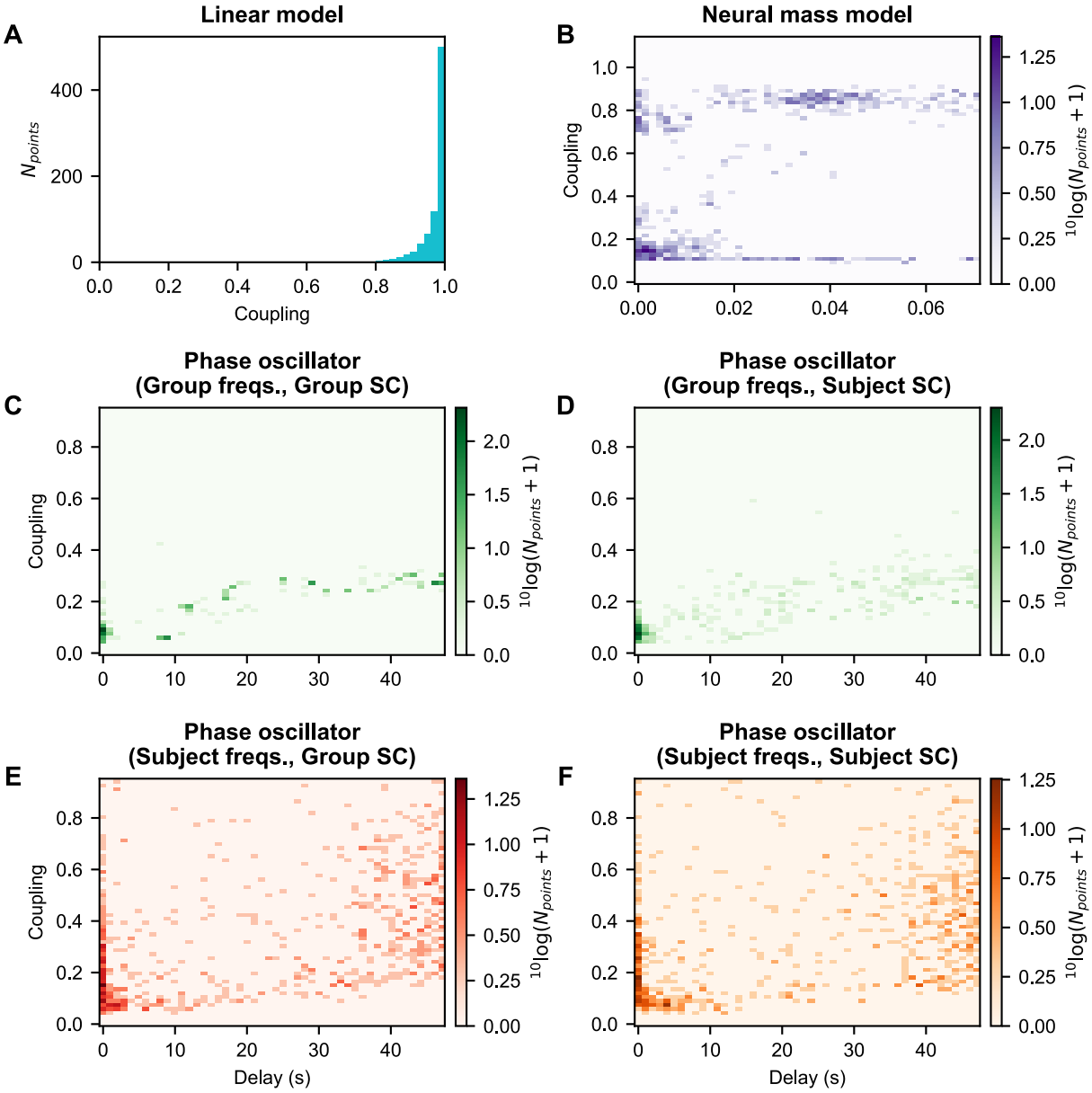

Fig. S4.16. Same as Fig. S4.12 but for the Shen atlas (Table 4.1).

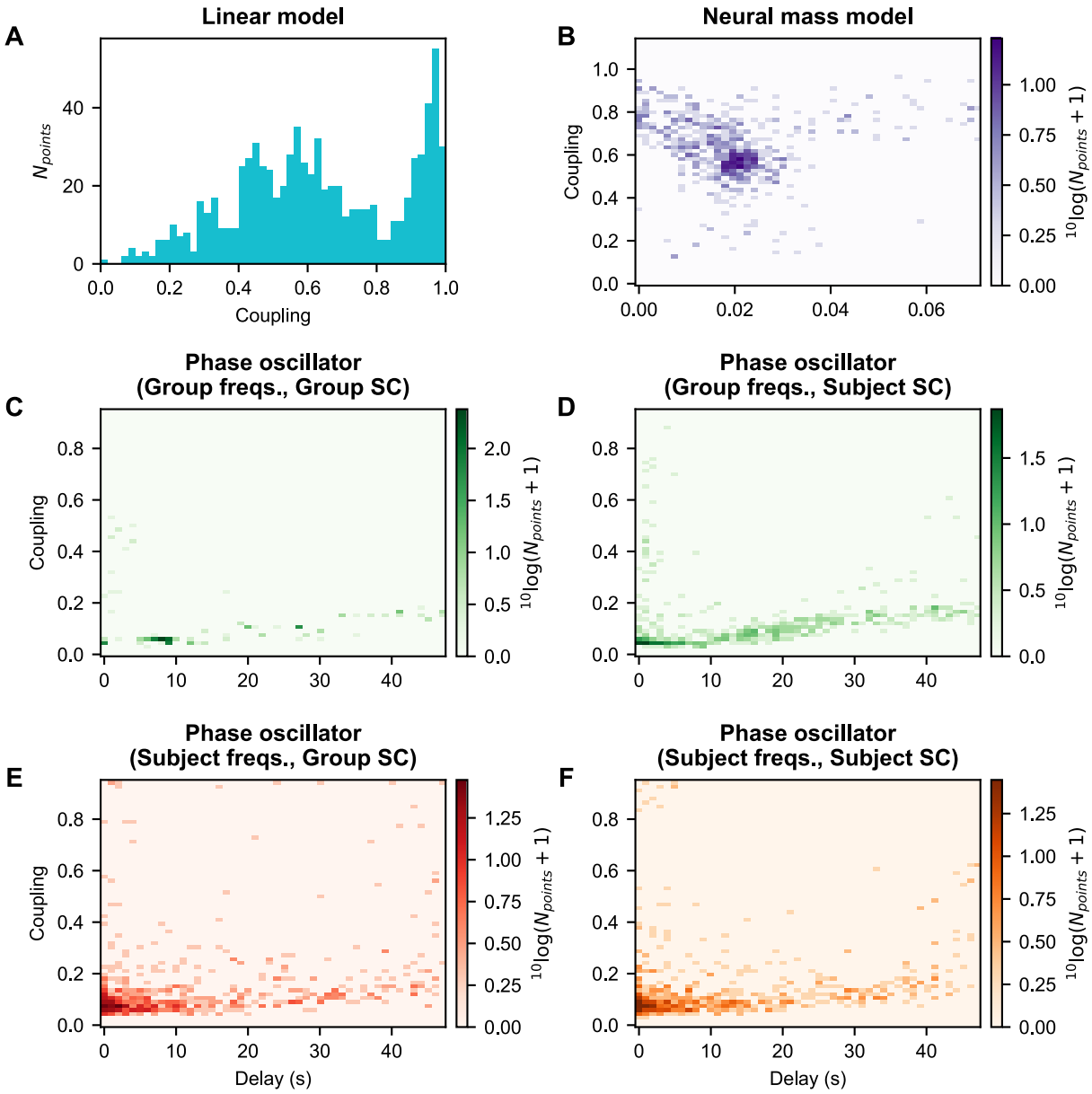

Fig. S4.17. Same as Fig. S4.12 but for the Schaefer atlas (Table 4.1).

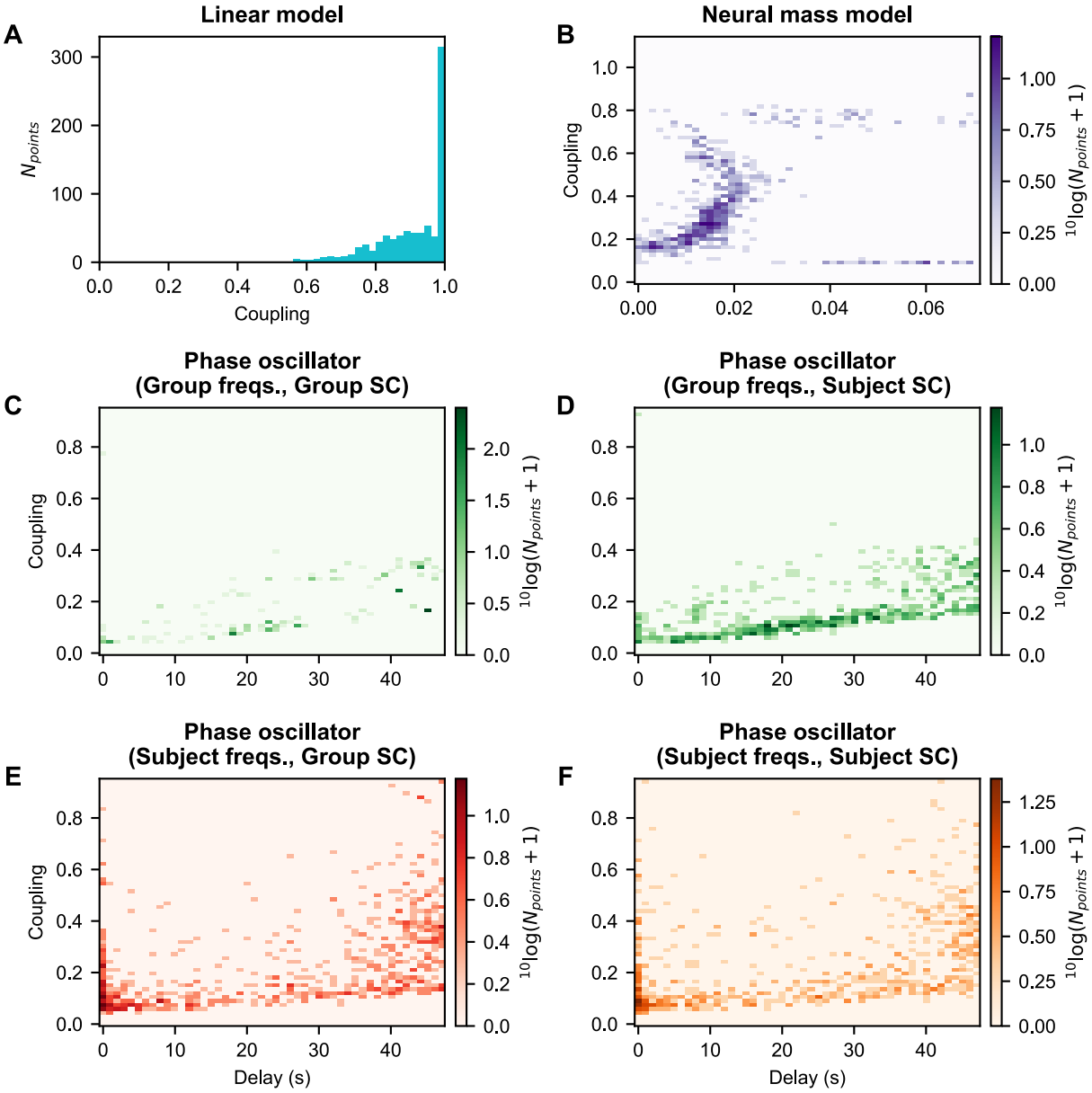

Fig. S4.18. Same as Fig. S4.12 but for the MIST atlas (Table 4.1).

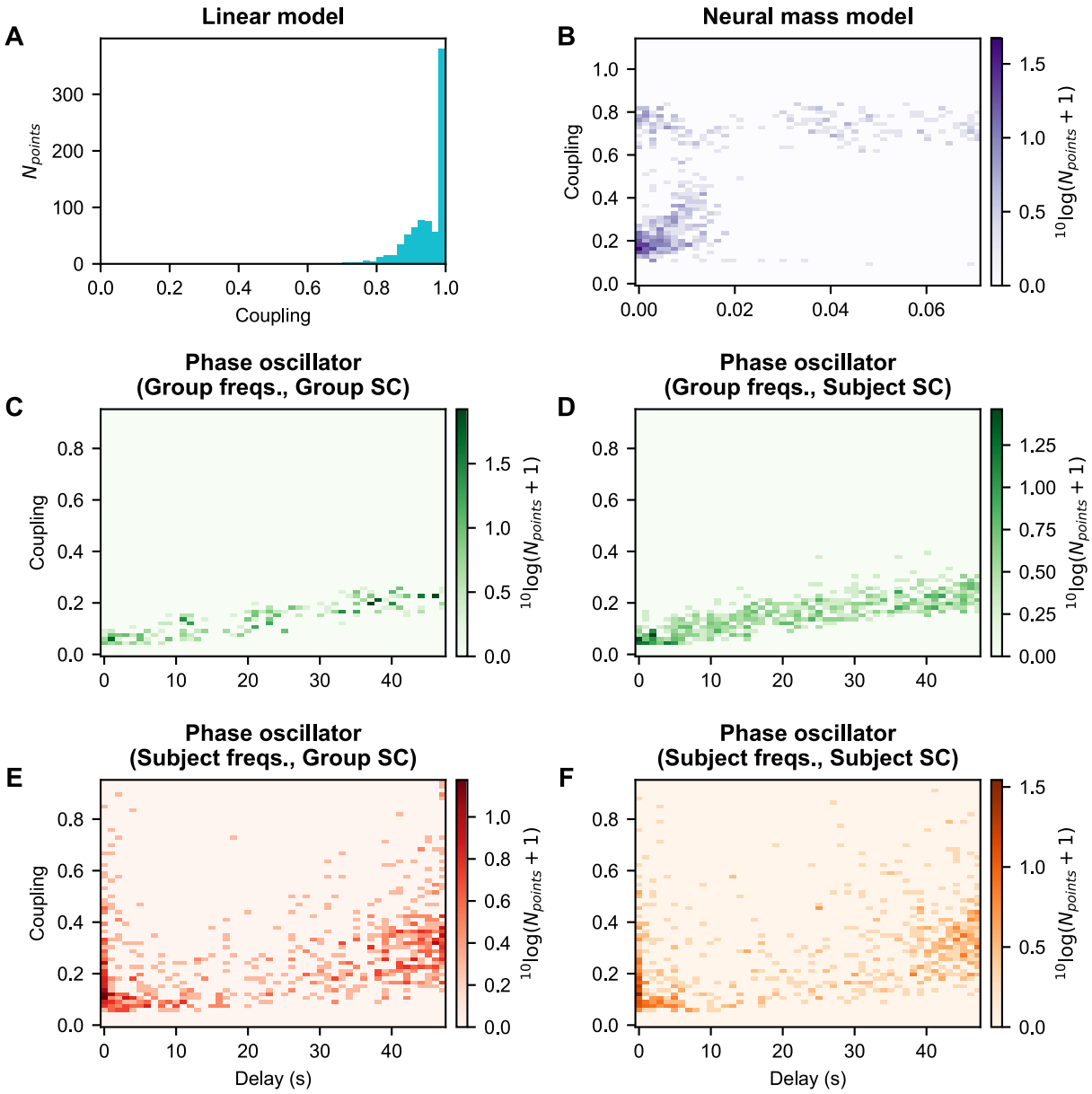

Fig. S4.19. Same as Fig. S4.12 but for the Craddock atlas (Table 4.1).

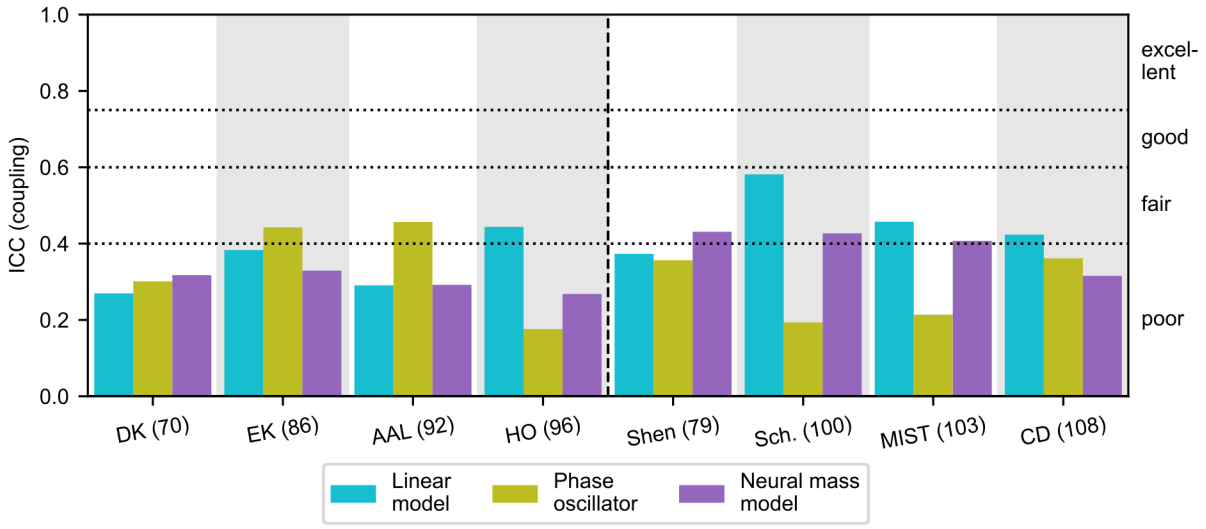

Fig. S4.20. Reliability of the coupling parameter for models with varying model complexity and similar model personalization when signal latency is disregarded in the models; see "Simulated functional connectivity" in Materials and methods. The plot shows the intraclass correlations (ICCs; Eq. 4.14) of the optimal coupling parameter G for all the atlases considered in this study (Table 4.1) under the constraint where the delay parameter is set to $\tau = 0$. The linear model (blue) corresponds to a low complexity, the phase oscillator model (green) to a moderate complexity and neural mass model (purple) to a high complexity as indicated in the legend. The labels "poor", "fair", "good" and "excellent" correspond to those proposed by Cicchetti & Sparrow (1981). The vertical dashed black line separates the brain atlases constructed on the basis of structural data (left block) from those based on functional data (right block). The ICCs of the coupling parameters corresponding to the linear model are the same as those shown in Fig. 4.3C.

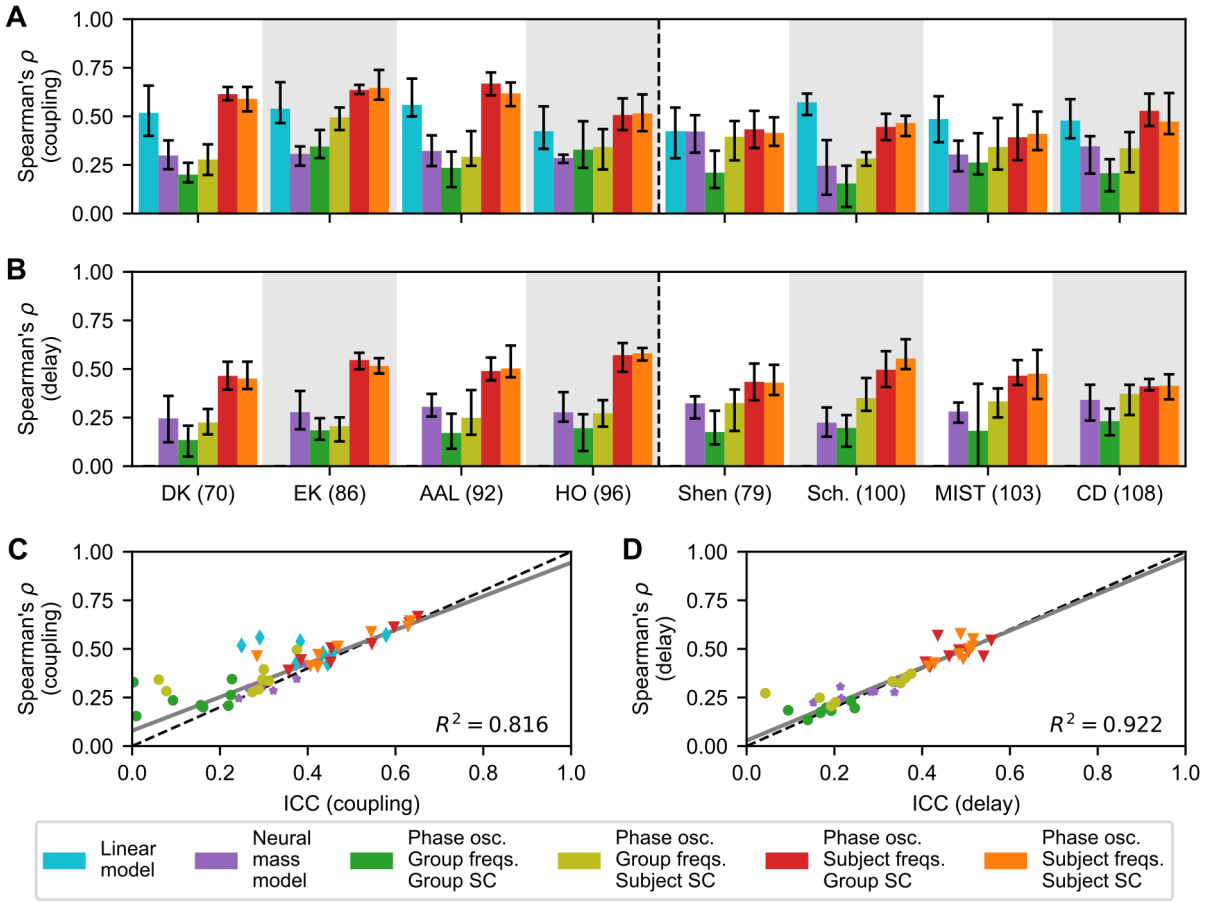

Fig. S4.21. Reliability of the model parameters as reflected by the test-retest Spearman correlation coefficient. First, vectors containing the 200 optimal coupling (delay) parameters of all subjects were constructed separately for all 4 individual fMRI data acquisition conditions; see "Empirical functional connectivity" in Materials and methods. Subsequently, the (test-retest) Spearman correlation coefficient between these vectors was calculated across subjects for all 6 combinations of these 4 vectors corresponding to the different fMRI sessions. **(A-B)** Test-retest Spearman correlation coefficients (Spearman's ρ) of (A) the optimal coupling parameters and (B) the delay parameters for all the atlases (Table 4.1, horizontal axis) and models (colors). The legend indicates the color coding of the models in the plots. The vertical dashed black lines separate the brain atlases constructed on the basis of structural data (left blocks) from those based on functional data (right blocks). Bars indicate the means, and the error bars the minimum and maximum values across the 6 combinations of fMRI data acquisition conditions. No data is available for the delay parameter of the linear model, since this model did not consider signal propagation latency (Eq. 4.2). **(C-D)** Scatter plot of the intraclass correlations (ICCs) and the test-retest Spearman correlations of (C) the optimal coupling and (D) the delay parameter. The plotted symbols represent parcellations and models as indicated in the legend. The dashed black lines represent $x = y$ for comparison. The gray solid lines represent the linear regressions between the measures, which explain the amounts of variance (R^2) that are depicted in the separate plots. Abbreviations: freqs. = (natural) frequencies, osc. = oscillator.

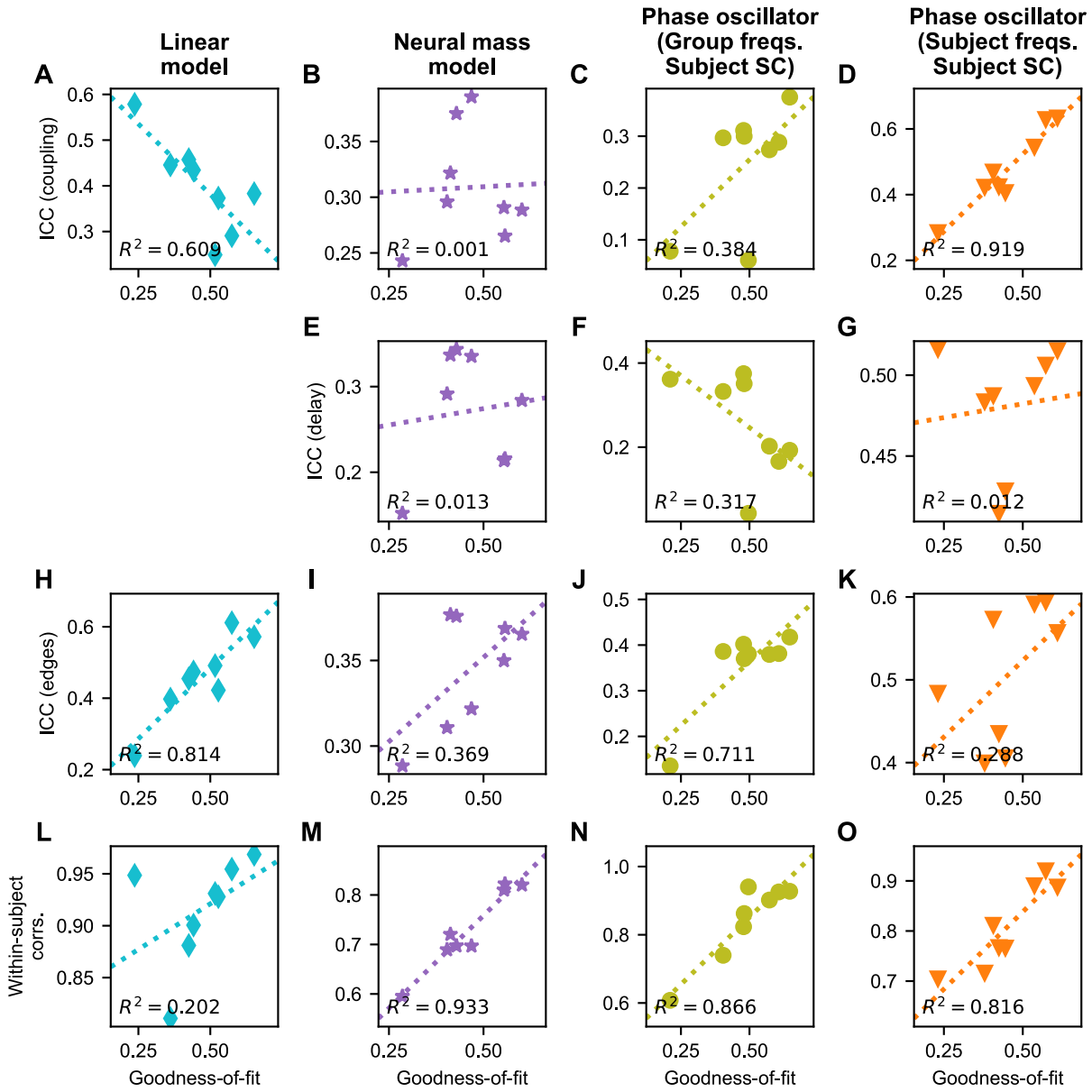

Fig. S4.22. Relation between the parcellation-induced variances in the reliability measures and the goodness-of-fit for four models considered in this study. **(A-D)** Scatter plots of the intraclass correlation (ICC) of the coupling parameter (Fig. 4.2C; Fig. 4.3C) against the mean goodness-of-fit of the model to the empirical FC (Fig. S4.11, dots) for (A) the linear model, (B) the neural mass model, (C) the phase oscillator model simulated using group-averaged frequencies and (D) the phase oscillator model simulated using subject-specific frequencies (freqs.). All models were constructed on the basis of the personalized empirical SC. Symbols represent individual parcellations, dotted lines reflect the linear regressions between the plotted quantities, and the variances explained by these regressions are shown at the bottom left corners of the plots. **(E-G)** Similar to panels B to D, but here the ICC of the delay is considered (Fig. 4.2D; Fig. 4.3D). As the linear model does not incorporate delay (Eq. 4.2), no ICC of the delay parameter and hence no plot is available for this model. **(H-K)** Similar to panels A to D, but here the mean edge ICC is considered (Fig. 4.2E; Fig. 4.3E). **(L-O)** Similar to panels A to D, but here the mean within-subject, single-modal correlations (corrs.) are considered (Fig. 4.4A-B).

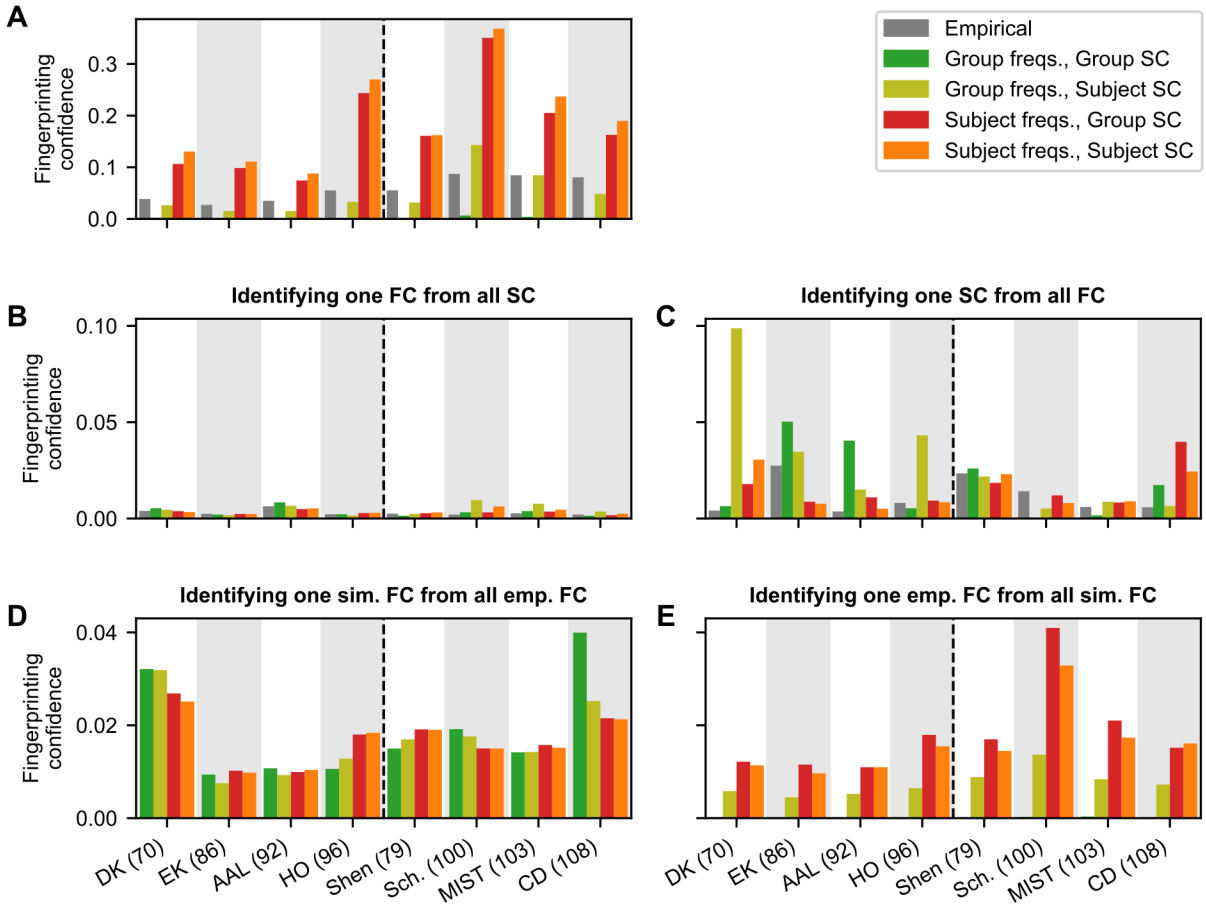

Fig. S4.23. Fingerprinting confidences for the various parcellations (Table 4.1) and fingerprinting analyses considered in the study while investigating varying (phase oscillator) model personalization. **(A)** Fingerprinting confidence when identifying individual subjects by comparing one of their empirical (simulated) FCs against all other empirical (simulated) FCs by the single-modal connectome correlation. The extent of the model personalization as given by the combinations of the subject-specific or group-averaged natural frequencies (freqs.) and SC is indicated in the legend. Less personalization corresponds to the model simulated using group-averaged frequency profiles and constructed on the basis of grand-averaged (dark green) and personalized empirical SC (light green). Then, more personalization relates to the versions of the phase oscillator model simulated using subject-specific frequency profiles and constructed on the basis of the grand-averaged (red) and personalized (orange) empirical SC. Results involving the empirical FC are colored gray. **(B-C)** Fingerprinting confidences determined by (B) correlating one FC (empirical or simulated) with all empirical SC and (C) by correlating one empirical SC with all FC of the same modality (empirical or simulated) for the parcellations considered in this study. **(D-E)** Fingerprinting confidences determined by (D) correlating one simulated FC with all empirical FC and (E) by correlating one empirical FC with all simulated FC.

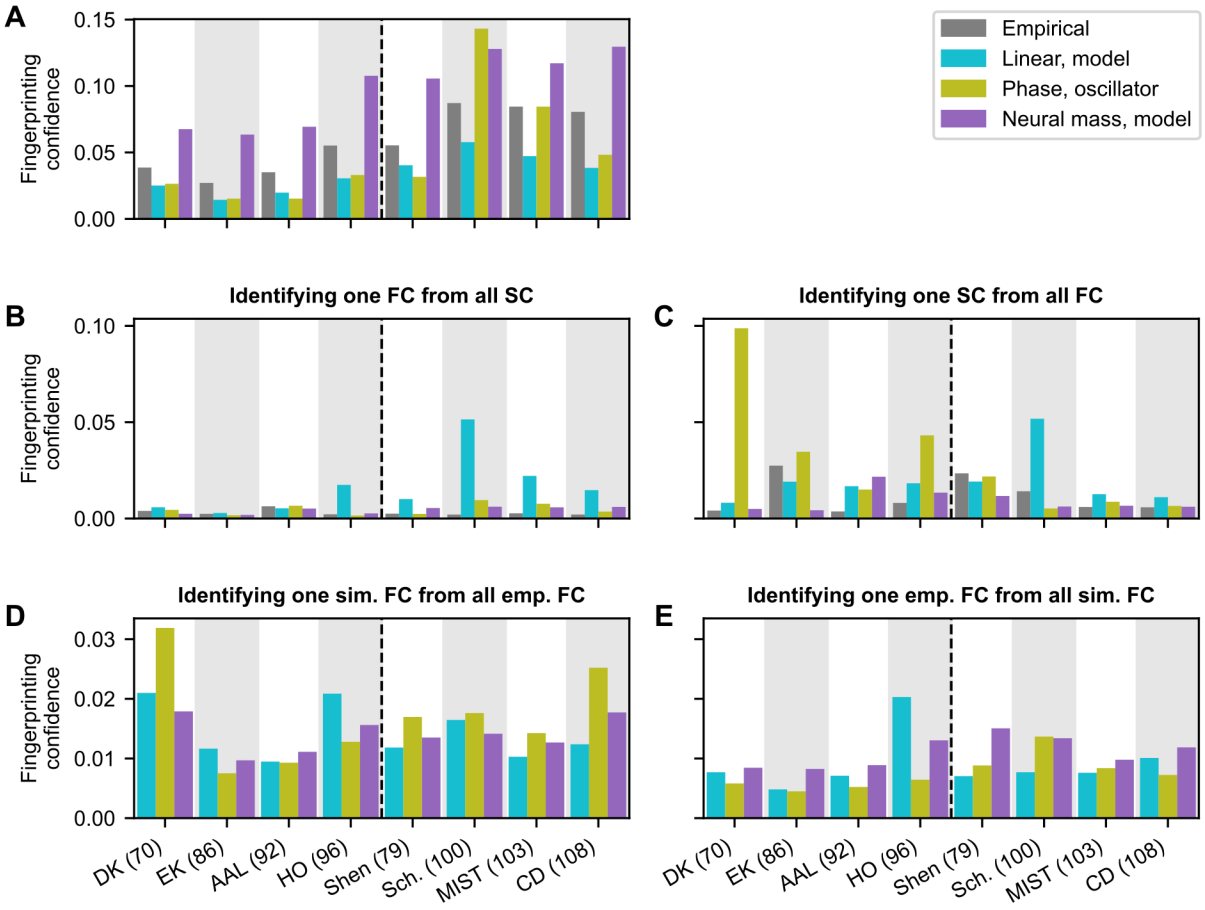

Fig. S4.24. Fingerprinting confidences for the various parcellations (Table 4.1) and fingerprinting analyses considered in the study while varying model complexity and keeping the same level of model personalization. **(A)** Fingerprinting confidence when identifying individual subjects by comparing one of their empirical (simulated) FCs against all other empirical (simulated) FCs by the single-modal connectome correlation. The linear model (blue) corresponds to a low complexity, the phase oscillator model (green) to a moderate complexity and neural mass model (purple) to a high complexity as indicated in the legend. Results involving the empirical FC are colored gray. **(B-C)** Fingerprinting confidences determined by (B) correlating one (empirical or simulated) FC with all empirical SC and (C) by correlating one empirical SC with all FC of the same modality (empirical or simulated) for the parcellations considered in this study. **(D-E)** Fingerprinting confidences determined by (D) correlating one simulated FC with all empirical FC and (E) by correlating one empirical FC with all simulated FC.

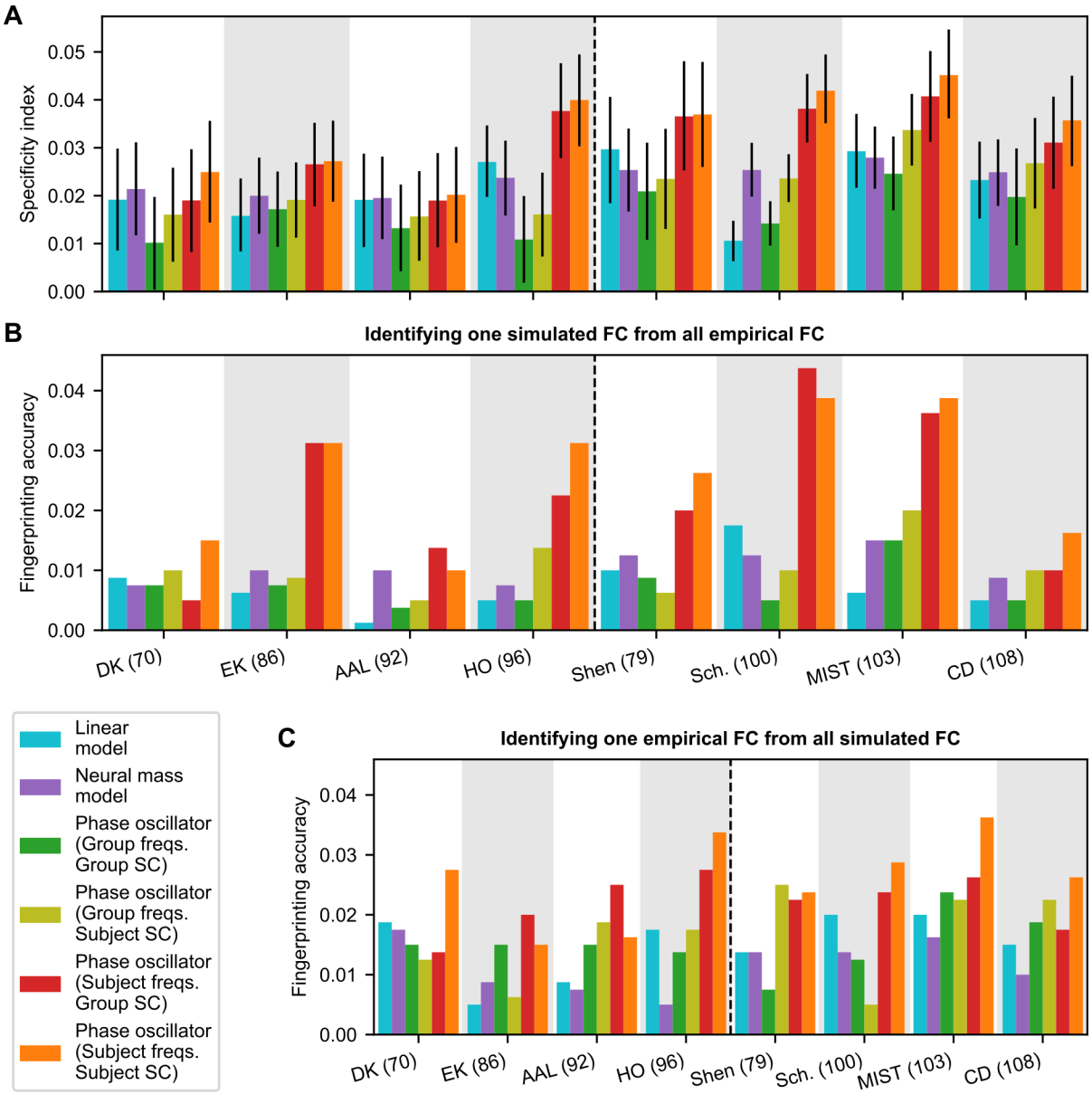

Fig. S4.25. Impact of the brain atlas and model implementation on the subject specificity of the model-fit correlations being the correlations between the empirical and the simulated FC. **(A)** Specificity indices (Eq. 4.15) of the cross-modal correlations of the empirical FC with the simulated FC for the parcellations considered in this study (Table 4.1). The legend indicates the color coding with respect to the various models considered in this study. The vertical dashed black line separates the brain atlases constructed on the basis of structural data (left block) from those based on functional data (right block). The bars and error bars mark the medians and the (Bonferroni corrected) 95% confidence intervals across the 50,000 bootstrapped specificity index estimations, respectively. **(B-C)** Fingerprinting accuracies determined by (B) correlating one simulated FC with all empirical FC and (C) by correlating one empirical FC with all simulated FC for the various parcellations considered in this study.

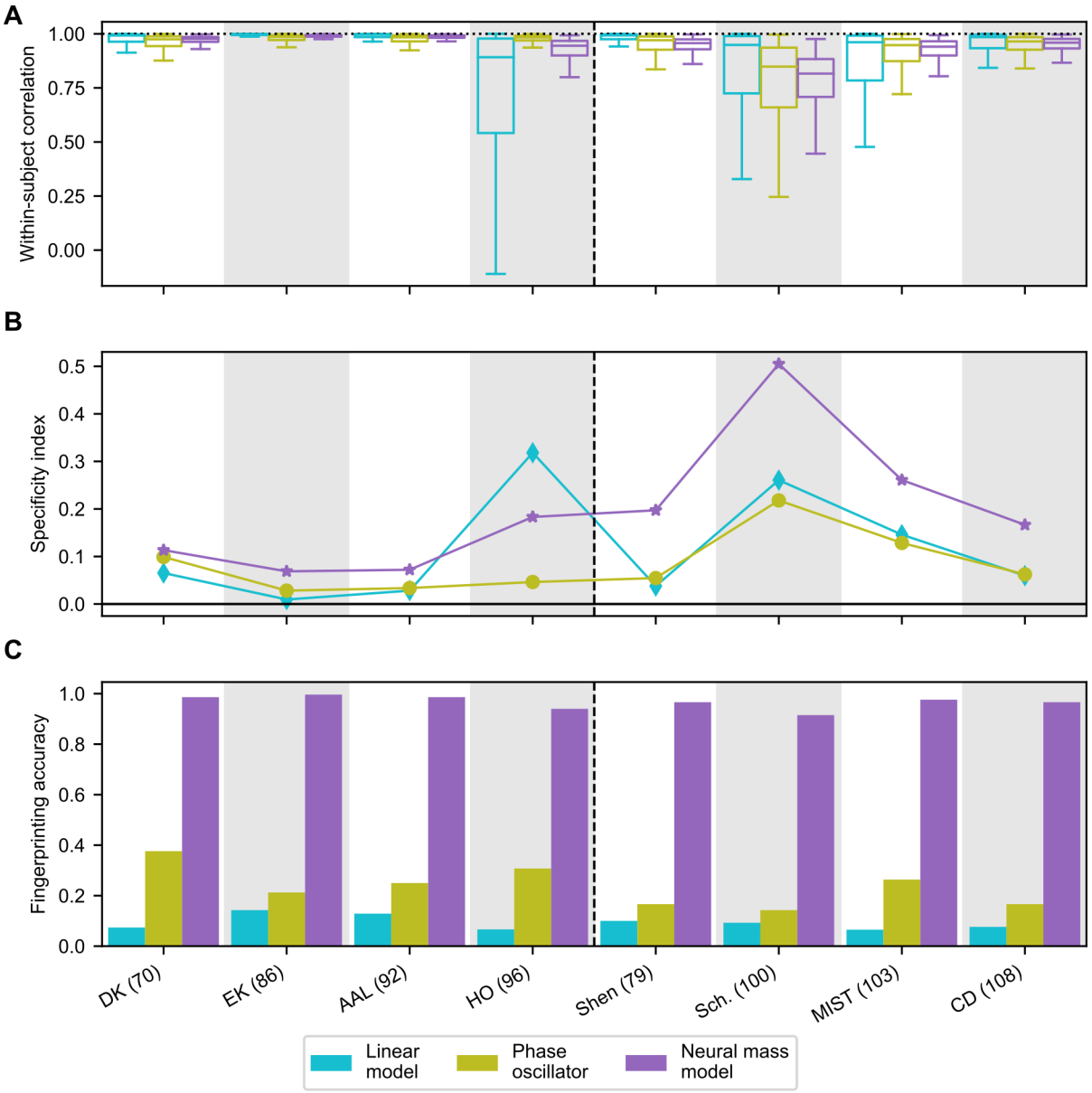

Fig. S4.26. Influence of parcellation and model complexity with similar model personalization on the correspondences of the similarity mappings (Eq. 4.1) when signal latency is disregarded in the model, that is, the delay parameter is set to $\tau = 0$; see "Simulated functional connectivity" in Materials and methods. **(A)** Distributions of the within-subject correlations of the similarity maps calculated across parameter settings for the various parcellations considered in this study (Table 4.1). The linear model (blue) corresponds to a low complexity, the phase oscillator model (green) to a moderate complexity and neural mass model (purple) to a high complexity. The vertical dashed black line separates the brain atlases constructed on the basis of structural data (left block) from those based on functional data (right block). **(B)** Specificity indices (Eq. 4.15) calculated from the similarity mapping correlations. The symbols and shaded areas mark the medians and the (Bonferroni corrected) 95% confidence intervals across the 50,000 bootstrapped specificity index estimations, respectively. **(C)** Fingerprinting accuracy when identifying individual subjects by comparing the similarity mapping of one particular empirical FC with one another.

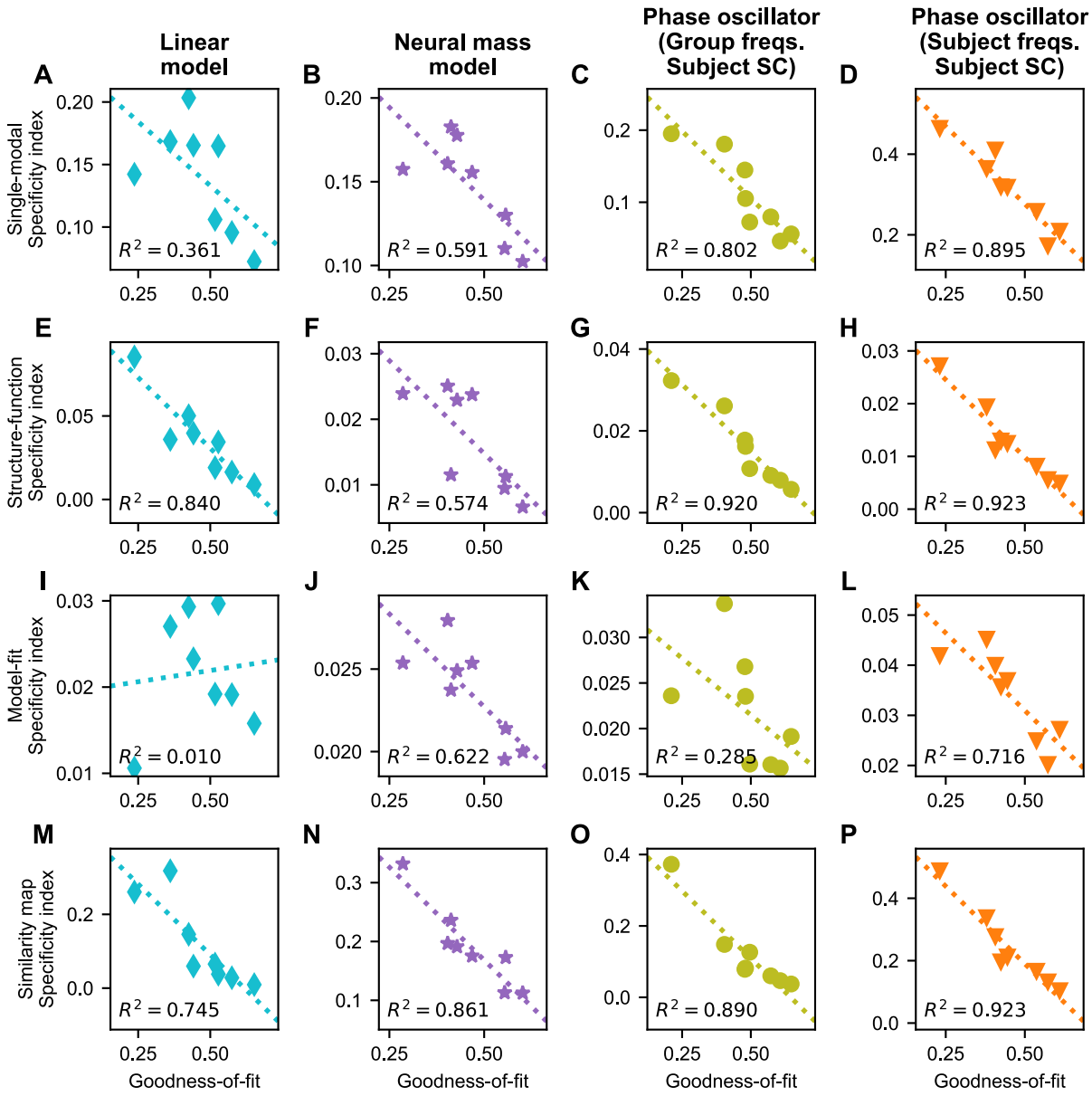

Fig. S4.27. Relation between the parcellation-induced variances in the specificity indices and the goodness-of-fit for four models considered in this study. **(A-D)** Scatter plots of the mean single-modal specificity index (Fig. 4.4) against the mean goodness-of-fit of the model to the empirical FC (Fig. S4.11, dots) for (A) the linear model, (B) the neural mass model, (C) the phase oscillator model simulated using group-averaged frequencies and (D) the phase oscillator model simulated using subject-specific frequencies. All models were constructed on the basis of the personalized empirical SC. Symbols represent individual parcellations, dotted lines reflect the linear regressions between the plotted quantities, and the variances explained by these regressions are shown at the bottom left corners of the plots. **(E-H)** Similar to panels A to D, but here the mean structure-function specificity indices are considered (Fig. 4.5). **(I-L)** Similar to panels A to D, but here the mean model-fit specificity indices are considered (Fig. S4.25). **(M-P)** Similar to panels A to D, but here the mean specificity indices of the similarity map correlations are considered (Fig. 4.6; Fig. 4.7).

Chapter 5

Overarching discussion

The two studies of this thesis have demonstrated how parcellations may influence distinct aspects of the dynamical whole-brain models.

The first study (Chapter 3) not only assessed how the parcellation influences the quality of model fit, but also investigated whether the parcellation-induced differences in this goodness-of-fit can be explained by statistics characterizing the network architectures of the empirical SC and FC. First, it was shown that a change of parcellation can considerably alter the network properties of the empirical structural and functional connectomes that are derived from dwMRI and fMRI data, respectively (Fig. 3.2, Fig. 3.3). Additionally, the consideration of a different parcellation could substantially affect the fit of the model to the empirical data as quantified by the maximized Pearson correlation coefficient calculated between the empirical and simulated FC (Fig. 3.6). For most of the computed network properties and qualities of model fit, the between-parcellation variance did not reflect a simple dependence on the granularity, that is, the number of parcels included in a parcellation (Fig. 3.4). Subsequently, it was shown that the model fitting qualities and graph-theoretical measures could be associated well to one another when considering group-averaged inter-parcellation differences (Fig. 3.7). Conversely, the within-parcellation, between-subject variations of the network properties and modeling results did not exhibit the same evident relationship (Fig. 3.8). Finally, the study showed that the network properties calculated from the empirical FC and the simulated FC may correlate with one another at both the level of the group and the individual subjects (Fig. 3.9, Fig. 3.10).

In the second study (Chapter 4), the reliability and the subject specificity of the modeling results and their dependence on the parcellation were evaluated. First, it was shown that the modeling results can be significantly more reliable than the empirical functional connectome (Fig. 4.2; Fig. 4.3). The reliability of the simulated FC could also be related to the reliabilities of the model parameters that were used for its generation (Fig. 4.2). Subsequently, it was demonstrated that the subject specificity of the simulated FC could exceed that of the empirical FC (Fig. 4.4). Interestingly, the cross-modal correlations between the simulated FC and the empirical SC that may be used for model construction could exhibit significant subject specificity as well, and were even shown to exceed the empirical structure-function relationship in this respect (Fig. 4.5). In addition, the cross-modal correlations between the simulated FC and the empirical FC used for model validation were also significantly subject specific (Fig. S4.25). All these findings depended critically on the model implementation and parcellation. Here, more personalized models yielded more reliable and subject-specific modeling results, and a change of parcellation could affect the modeling results to a much higher extent than the findings only involving empirical data (Chapter 4).

The results are generally discussed below. First, the relevance of these findings is emphasized (Section 5.1: Relevance of the results). Subsequently, the results are related to the many

variations of the dynamical whole-brain modeling workflow that have been reported in the literature (Section 5.2: Deviations in the dynamical whole-brain modeling workflow). This is followed by a discussion on the limitations of the models and the opportunities that may be explored in future investigations (Section 5.3: Limitations and opportunities). Finally, a discussion on the proper selection of the brain parcellation is provided (Section 5.4: The proper selection of the brain parcellation).

5.1 Relevance of the results

5.1.1 What the variation of the parcellations reveals about dynamical whole-brain models

The first study of this thesis (Chapter 3) complements the existing literature that investigates how the parcellation affects the empirical structural and functional connectomes and the dynamical whole-brain modeling results (Arslan et al., 2018; Popovych et al., 2021; Proix et al., 2016; J. Wang et al., 2009; Zalesky et al., 2010). In particular, Chapter 3 included parcellation-based graph-theoretical statistics and goodness-of-fit values that have not been reported previously. In addition, the study showed that some of the calculated network properties exhibited a pronounced relationship with the number of brain regions independently of the construction method of the parcellation (Fig. 3.4). Furthermore, it was explicitly shown that the other graph-theoretical measures and the goodness-of-fits could still vary considerably across parcellations after the granularity effect was regressed out of the results (Fig. S3.5).

The first study also demonstrated the sensitivity of the model fitting quality to distinct aspects of the empirical structural and functional networks. Only two principal axes in the feature space spanned by all extracted graph-theoretical measures could describe most of the parcellation-induced variations in the network properties (Fig. 3.7), which incidentally indicates a high amount of covariance among those different network properties under varying parcellation conditions. In turn, these two principal components could also explain a large portion of the parcellation-induced variance with regard to the quality of model fit (Fig. 3.7). Examining the loadings of these principal components subsequently revealed that the models prefer a heterogeneity in the nodal centralities of the empirical structural and functional networks (Fig. 3.7). In addition, they seem to favor an empirical SC that has a high potential for functional integration, and to have a slight preference for lower amounts of segregation in both the structural and functional connectomes (Fig. 3.7). These preferences may provide an insight into the mechanism that dynamical whole-brain models employ to link the empirical SC and FC together into one framework.

Subsequently, the second study of this thesis (Chapter 4) showed that the reliability of the FC simulated by dynamical whole-brain models can be considerably altered when the parcellation is varied. In particular, the simulated FC matrices were sampled more reliably when the structural parcellations were considered rather than the functional brain atlases (Fig. 4.2; Fig. 4.3). Furthermore, the second study also demonstrated that the subject specificities of the simulated FC and its cross-modal correlations with the empirical connectomes can be highly influenced by the choice of parcellation (Chapter 4). In contrast to the reliability, the use of the structural parcellations yielded modeling results that were less subject specific than when functional brain atlases were used to reconstruct the empirical connectomes (Fig. 4.4; Fig. 4.5). Hence, these results seem to hint towards a trade-off between reliability and subject specificity when selecting the brain parcellation in dynamical whole-brain modeling paradigms, which could be related to the discussion on the reliability and the predictive capacity of empirical functional connectomes by Finn & Rosenberg (2021). Also, it should be noted that the reliability and the subject specificity of the results that involved purely empirical data were in agreement with similar investigations reported in the (empirical) literature (Finn et al., 2015; Messé, 2020; Noble et al.,

2019; Li et al., 2021; Van Dijk et al., 2010; Zimmermann, Griffiths, et al., 2018). Furthermore, they were relatively stable across parcellation conditions when compared to the reliability and subject specificity of the modeling results (Fig. 4.2; Fig. 4.3; Fig. 4.4; Fig. 4.5).

In sum, the findings presented in Chapter 3 and Chapter 4 emphasize the importance of a well-informed choice of the parcellation in dynamical whole-brain modeling studies that is further discussed below (Section 5.4: The proper selection of the brain parcellation).

5.1.2 How the dynamical whole-brain model implementation shapes the results

The studies of Chapter 3 and Chapter 4 demonstrated that the model fitting quality can be rather stable across different models for local dynamics. The goodness-of-fits of the two non-linear model implementations considered in the first study, for example, correlated well with one another across parcellations, and their linear regression almost coincided with the ideal situation of $x = y$ (Fig. 3.6). Interestingly, removing the granularity effect from the fitting qualities of both models resulted in an even stronger relationship between them (Fig. S3.6). Using a different personalization of the phase oscillator model also did not result in very strong deviations with regard to the fitting coefficients (Fig. S4.11). These findings agree with a study that shows resemblances in the goodness-of-fits of the phase oscillator and a (Landau-Stuart) limit-cycle oscillator model (Deco et al., 2019; Popovych et al., 2021).

Even though the model fitting quality remains approximately the same when the model implementation varies, the network architecture of the simulated FC can still be considerably different for distinct models. This is explicitly shown by the graph-theoretical analysis of the simulated FC included in the first study of this thesis (Chapter 3). Indeed, not all network properties of the empirical and simulated functional connectomes could be related to one another (Fig. 3.9). Furthermore, the established relationships between the graph-theoretical measures of the empirical and simulated FC could be inaccurate and inconsistent across models (Fig. 3.9). In sum, although the selection of the model for local dynamics might not alter the goodness-of-fit, it can affect the network structure of the corresponding simulated FC to a large extent.

The proper selection of the model implementation is also non-trivial when considering the reliability and the subject specificity of the modeling results. The second study of this thesis showed that the FCs generated by the phase oscillator model could exhibit considerably higher reliability than those simulated by the neural mass model depending on the amount of model personalization of the former (Fig. 4.2; Fig. 4.3). In addition, the subject specificity of the modeling results could also be controlled well by the amount of personalized information embedded in the simulations of the dynamical whole-brain model (Fig. 4.4). A more personalized model could even be fitted more specifically to the empirical FC than its less personalized variant (Fig. S4.25). Moreover, it was shown that the model parameter spaces could be personalized when additional subject-specific information was used in the model simulations (Fig. 4.6). Hence, the exact implementation of the dynamical whole-brain modeling concept determines to a large extent the within- and between-subject reproducibility of the results.

Taken together, the choice of model implementation might not have consequences for the quality of the fit of the model to the empirical data. It is difficult, however, to generalize this statement for all models for local dynamics as a vast variety of dynamical whole-brain models have been reported in the literature; see Section 5.2: Deviations in the dynamical whole-brain modeling workflow. Moreover, the results presented in this thesis clearly demonstrate that the simulated FC can vary considerably across different model implementations in terms of its network architecture shared among subjects and its inter- and intra-individual differences. Hence, the exact implementation of the dynamical whole-brain modeling paradigm should be selected conscientiously.

5.2 Deviations in the dynamical whole-brain modeling workflow

5.2.1 Varying preprocessings of magnetic resonance imaging data

Two recent studies assessed how susceptible the dynamical whole-brain modeling results are to divergent dwMRI and fMRI data preprocessings (Aquino et al., 2022; Jung et al., 2021). Here, Jung et al. (2021) investigated how a variation of the number of streamlines that is used in the reconstruction of the SC can affect the fitting quality of dynamical whole-brain models. Interestingly, the optimal streamline count that maximized the goodness-of-fit was different for the two parcellations considered in that study (Jung et al., 2021). Furthermore, Aquino et al. (2022) showed that the fit of the dynamical whole-brain models to the empirical FC may be largely determined by fMRI signal fluctuations that involve a large portion of all the voxels constituting a volumetric brain image (also known as the *global signal*; Liu et al., 2017). Even though the conclusions of Aquino et al. (2022) were only based on one parcellation, the studies by Jung et al. (2021) and Aquino et al. (2022) clearly indicate that dynamical whole-brain modeling research could benefit greatly from an optimized and standardized MRI data preprocessing pipeline.

In spite of the present absence of such standardized pipelines, the quality of the work included in this thesis was ensured by the state-of-the-art tools and insights that were used to preprocess the dwMRI and fMRI data. The empirical connectomes used in the studies of this thesis, for instance, were reconstructed from MRI data collected by the Human Connectome Project (HCP) (Van Essen et al., 2012, 2013), which presumably are of high quality (Marcus et al., 2013). In addition, the data preprocessing steps were in agreement with published suggestions (Glasser et al., 2013; Salimi-Khorshidi et al., 2014; Tournier et al., 2019), and were performed by state-of-the-art software packages that are widely used and publicly available (Dale et al., 1999; Jenkinson et al., 2012; Tournier et al., 2019; Tustison et al., 2010); see also the data descriptor of J. W. M. Domhof et al. (2021). Additionally, as discussed in Chapter 3, the SC and PL matrices of individual subjects were reconstructed through whole-brain tractography calculations that sampled a rather high number of 10 million streamlines. Recent literature indeed argued that performing the tractography with such high streamline densities should benefit the accuracy of the resulting structural connectome, which potentially contains false positives and negatives (Bassett et al., 2011; Lindquist, 2020; Maier-Hein et al., 2017; Roine et al., 2019; Schilling et al., 2019; Sotiropoulos & Zalesky, 2019).

Additionally, the images of the parcellations used in this thesis were modified before they were used in the reconstructions of the empirical connectomes from the preprocessed MRI data. That is because the considered brain atlases were published in inconsistent formats. The Desikan-Killiany and Destrieux atlases (Desikan et al., 2006; Destrieux et al., 2010), for example, have been included as (cortical) surface-based parcellations in FreeSurfer (Dale et al., 1999), while the AAL parcellation (Rolls et al., 2015; Tzourio-Mazoyer et al., 2002) is provided as a volumetric image sampled in the Colin27 template space (C. J. Holmes et al., 1998). Therefore, the parcellation images were homogenized so that they all covered the same area of cortical grey matter, and were all sampled in the MNI152 non-linear template space (Grabner et al., 2006). The adjustments applied to the atlas images are listed in the Supplementary method of Chapter 3, and increased the likelihood that any observed parcellation-induced deviations were indeed related to differences in the method for brain atlas construction.

5.2.2 Reported models for local dynamics

The Kuramoto model of coupled phase oscillators (Kuramoto, 1984) and the Wilson-Cowan model (Wilson & Cowan, 1972) were selected for the sampling of the results presented in both studies of this thesis because of three reasons. In broad strokes, these three reasons are already listed in the second study of this thesis, where also a justification for the use of the (linear) Ornstein-Uhlenbeck model is included (Section 4.4.3: Model implementations). First of

all, these two models are well known (Breakspear et al., 2010; Breakspear, 2017), and have been used in previous investigations involving dynamical whole-brain models (Deco et al., 2009; Messé et al., 2014; Ponce-Alvarez et al., 2015). Second, they are conceptually distinct. The phase oscillator model can be used to describe any system of coupled phase oscillators, but is not biophysically-realistic in the sense that it approximates the neuronal interactions underlying brain dynamics (Acebrón et al., 2005; da Fonseca & Abud, 2018; Kuramoto, 1984; Strogatz, 2000). Conversely, the Wilson-Cowan model was designed to explicitly model the interplay between large groups of excitatory and inhibitory neurons, and thus enjoys a higher biological relevance (Wilson & Cowan, 1972). Finally, both models are sufficiently reduced in terms of complexity so that their dynamical behaviors can be understood and controlled well: The Kuramoto and Wilson-Cowan model use only one and two state variables per brain region, respectively, and their dynamics under different parameter conditions have been documented meticulously (Kuramoto, 1984; Wilson & Cowan, 1972).

The literature reports numerous models for local dynamics that can be used to investigate specific properties of the human brain. The Kuramoto model of coupled phase oscillators (Kuramoto, 1984), for instance, is well suited to investigate (temporal) synchronization patterns in the brain at rest (Cabral et al., 2011; Ponce-Alvarez et al., 2015). Additionally, the Wilson-Cowan model (Wilson & Cowan, 1972) can be used to effectively model the interactions between the excitatory and inhibitory neuron populations located in a particular brain region, which enhances the interpretability of results within the (neuro)biophysical context; see Section 2.3: Dynamical whole-brain models and Deco et al. (2009). Furthermore, a Landau-Stuart limit-cycle oscillator (Panteley et al., 2015), which is the normal form of a supercritical Hopf-bifurcation limit-cycle oscillator (Kuznetsov, 1998), can approximate the dynamics associated with individual brain regions transitioning from a noisy to an oscillatory behavior (Deco et al., 2017; Deco, Cabral, et al., 2018; Deco et al., 2019). Another example is the (reduced) Wong-Wang model (Deco, Ponce-Alvarez, et al., 2014; Wong & Wang, 2006), which may be used to explain variations in the FC over time (Deco et al., 2013; E. C. A. Hansen et al., 2015). A comparative analysis of the performances of many models for local dynamics was carried out by Messé et al. (2014) and Messé et al. (2015).

The dynamical whole-brain modeling concept hence is highly flexible in terms of the (mathematical) model descriptions and implementations. Recent endeavors exploited this flexibility in order to explain a variety of biophysical phenomena. A number of studies, for example, incorporated auxiliary region-specific data aside from the empirical SC and FC in the model simulations (Deco, Cruzat, et al., 2018; Deco et al., 2019; Demirtaş et al., 2019; Kringelbach et al., 2020). Chapter 4 indicated that this embedding can majorly influence the FC simulated by the models. Furthermore, one study extended the Wilson-Cowan model with a simple plasticity rule (Hellyer et al., 2016; Vogels et al., 2011) to investigate whether plasticity mechanisms may stabilize dynamical whole-brain modeling results (Abeysuriya et al., 2018). After all, such mechanisms of synaptic plasticity have been shown to adjust the strengths of the connections between individual neurons so that the desired pattern of neuronal activation is established (Cooke & Bliss, 2006; K. Fox & Wong, 2005; Hofer et al., 2006). Analogously, Naskar et al. (2021) expanded the model of Deco, Ponce-Alvarez, et al. (2014) with a kinetic receptor binding model (Destexhe et al., 1994a,b) to determine the role that neurotransmitter kinetics may play in resting-state brain dynamics. It is not clear whether the findings presented in this thesis also generalize to such more sophisticated dynamical whole-brain models that integrate processes with varying time scales.

5.2.3 Alternative strategies for model validation

The validity of the models can be assessed through a variety of methods. For instance, the resemblance between the empirical and simulated functional connectomes may be quantified

by different similarity measures. Indeed, the agreement of the model with the empirical data can be characterized by, among others, the Pearson correlation, the (Euclidean) distance, the Spearman correlation or the mutual information between the simulated and the empirical FC. In addition, several studies validated their dynamical whole-brain models on the basis of other paradigms than the similarity between the (static) empirical and simulated functional connectomes. When the variations of the empirical FC over time are investigated (Brovelli et al., 2017; Heitmann & Breakspear, 2018; Hutchison et al., 2013; Preti et al., 2017), for example, the empirical FC is no longer assumed to be static, and hence the dynamics of the empirical and simulated FC should be compared instead (Deco et al., 2013, 2017, 2019; E. C. A. Hansen et al., 2015). Moreover, just like in the first study of this thesis (Chapter 3), some dynamical whole-brain modeling studies used network properties extracted from the simulated functional connectome for the estimation of the model's performance (Cabral et al., 2012; Naskar et al., 2021).

In this thesis, the validation of the dynamical whole-brain models primarily involved the calculation of the Pearson correlation coefficient between the empirical and simulated FC. The literature provides two arguments to support this approach. First, it currently is still debated whether the time-dependent fluctuations of the empirical FC derived from fMRI data accurately capture (temporal) brain state variations (Hindriks et al., 2016; Honari et al., 2019; Leonardi & Van De Ville, 2015; Lurie et al., 2020; Zhang, Baum, et al., 2018). Throughout this thesis, it was therefore assumed that the functional connectome is static (Section 2.2.2: (Resting-state) functional connectivity). Because of this assumption, it was considered inappropriate to validate the models on the basis of the dynamics of the empirical and simulated FC and the resemblances between these kinetics. Second, the (Pearson) correlation between the (static) empirical and simulated FC has been used for model validation by many dynamical whole-brain modeling studies, and still seems to be the current standard (Abeysuriya et al., 2018; Aquino et al., 2022; Naskar et al., 2021). It therefore seemed appropriate to follow this standard as the primary measure for the validity of the model, especially since the main interest of this thesis is the influence of the parcellation rather than the effect of the model validation paradigm on the modeling results. However, it should be noted here that, in the first study of this thesis (Chapter 3), the network properties of the simulated FC were also used as a secondary measure for the ability of the models to reproduce the empirical FC. Additionally, as discussed in the second study (Section 4.4.3: Model implementations), the wielded static fitting of the simulated to the empirical FC may not be optimal since it could not capture the subject-specific subtleties in the parameter spaces of more complex models; see, for example, Fig. 4.3 vs. Fig. 4.7.

5.3 Limitations and opportunities

5.3.1 Computational costs

The dynamical whole-brain modeling paradigm bears high computational loads that arise from the vast number of calculations associated with the model simulations. After all, these simulations should first comprise an adequate amount of time T so that the corresponding simulated FC can be estimated accurately (Birn et al., 2013; H. E. Wang et al., 2014). Second, the size of the integration time step Δt should be be sufficiently small in order to approximate the dynamics at the individual network nodes with acceptable precision (Kim, 2014). Furthermore, it must be evaluated how the activities of the N individual brain regions influence one another at every single time step (Section 2.3: Dynamical whole-brain models). Hence, the number of computations required to simulate a dynamical whole-brain model increases proportionately with $N^2T/\Delta t$ when only one configuration of the model is considered in isolation.

However, the models also have some free parameters that require optimization, and these optimizations often involve grid searches (Deco et al., 2009; Zimmermann, Perry, et al., 2018;

Iravani et al., 2021). In grid searches, the individual free parameters are varied using predefined collections of values, and the model is simulated for all combinations of values between these collections. In the studies of this thesis, for instance, the global coupling and delay of the non-linear network models were varied using 64 and 48 different values, respectively, and hence the model was simulated for all their $64 \times 48 = 3{,}072$ combinations (Chapter 3; Chapter 4). Evidently, the computational costs accumulate with every additional model parameter configuration that is included in the grid search.

Even though the work presented in this thesis benefited greatly from computational resources provided by the Jülich Supercomputing Centre on the supercomputer JURECA (Jülich Supercomputing Centre, 2018), the computational load still imposed its limitations on the results. The simulations of the neural mass model, for example, were constrained in terms of the simulated time, which was a consequence of the relatively low integration step size that was required to precisely approximate the network dynamics of that model. Indeed, the model was designed so that the individual brain regions generated (alpha) oscillations with an oscillatory period of approximately $1/10$ Hz $= 100$ ms; see Section 2.3: Dynamical whole-brain models. Consequently, an integration step size of 2 ms was used in the simulations of this model in order to accurately sample (the interactions between) the activities of the individual network nodes (Chapter 3; Chapter 4). Preparatory investigations of the neural mass model prior to the large-scale sampling of modeling results revealed that time steps of 1 ms and 5 ms did not qualitatively change the modeling results. In addition, further increasing the time step to, e.g., 10 ms did not seem proper as the simulations then only sampled the activities of the brain regions on 100 ms$/$10 ms $= 10$ time points per oscillation. These two notions indicated that the 2 ms integration step size was indeed appropriate. Additional exploratory inquiries demonstrated that increasing the simulated time eligible for analyses, which was $T = 510$ s $- 150$ s $= 360$ s in both studies (Chapter 3; Chapter 4), also did not qualitatively alter the observations for the neural mass model.

The high computational load of the dynamical whole-brain modeling paradigm also limited the amount of results presented in this thesis in terms of both the numbers and the sizes of the parcellations considered (Chapter 3; Chapter 4). As indicated above, a rise in the number of brain regions quadratically increases the computational costs of the model simulations. Therefore, it is computationally unfeasible to sample modeling results for many large parcellations, that is, brain parcellations delineating a relatively high number of brain regions. Notably, studies assessing the influence of the brain atlas on analyses involving purely empirical data do not seem to suffer from this limitation (Albers et al., 2021; Arslan et al., 2018; Messé, 2020; Zalesky et al., 2010).

The computationally intensive simulation calculations were a constraining factor with respect to the model parameter optimizations as well. In both studies of this thesis, the other (non-linear) model parameters were set to the same fixed values for all subjects so that only the global coupling and delay parameters required optimization (Chapter 3; Chapter 4). Future dynamical whole-brain modeling studies, however, may benefit from a (subject-specific) fitting of other model parameters. After all, the second study of this thesis showed that more personalized models can be fitted to the empirical data with higher subject specificity than less personalized ones (Chapter 4). Moreover, it has been demonstrated that parameters reflecting the individualized neural excitation-inhibition balance may be used to distinguish patients with Alzheimer's disease from healthy subjects (Zimmermann, Perry, et al., 2018); see below.

Nevertheless, optimizing many model parameters via grid searches is computationally intractable. Indeed, from the discussion on the grid search above it follows that the number of parameter configurations to test increments tremendously with every additional free parameter that is included in the grid search if the density of the grid remains unaltered. Instead, the model parameters may also be optimized by employing dedicated, model-free optimization methods

that aim to find the optimal model parameter configuration while simulating the model as few times as possible. Examples of such algorithms include the Nelder-Mead algorithm (Nelder & Mead, 1965), particle swarm optimization (Eberhart & Kennedy, 1995; Kennedy & Eberhart, 1995), the covariance matrix adaptation evolution strategy (N. Hansen & Ostermeier, 1996) and Bayesian optimization (Jones et al., 1998; Snoek et al., 2012). Recently, a study assessed the performances of these four optimization schemes with regard to the dynamical whole-brain modeling workflow, and demonstrated that the latter two methods yield particularly good results (Wischnewski et al., 2022).

5.3.2 Personalization of the models

Several studies have demonstrated that the empirical FC of individuals can be highly subject specific (Amico & Goñi, 2018; Finn et al., 2015; Gratton et al., 2018; Li et al., 2021; Peña-Gómez et al., 2018; Sarar et al., 2021; Taxali et al., 2021; Waller et al., 2017), but it is not known how the personalization of that connectome is actually established. So far, it has been revealed that the empirical functional connectomes of a group of subjects share a common architecture, and that subject-specific deviations from this principal structure are stable in spite of daily variations (Amico & Goñi, 2018; Gratton et al., 2018). In addition, the empirical structure-function relationship (i.e., the correlation between the empirical SC and FC) may be significantly subject specific as well (Messé, 2020; Zimmermann, Griffiths, et al., 2018). However, the subject specificity of that relationship is considerably lower than that of the empirical FC itself (see, e.g., Messé, 2020 vs. Finn et al., 2015), and hence it is unclear to what extent the former contributes to the latter.

Dynamical whole-brain models may be a valuable tool for studies investigating the high subject specificity of the empirical FC and its underlying mechanism. After all, many model parameters can either be set to a fixed value for all subjects or derived from individualized empirical data. Then, by comparing the modeling results across different personalization conditions, it can be estimated how the personalization of a particular model parameter contributes to the subject specificity of the empirical FC. The second study of this thesis showcased this approach by using subject-specific regional frequency profiles and empirical SC matrices as well as their group-averages in the simulations of the phase oscillator model (Chapter 4). The results of this study demonstrated that the subject specificity of the simulated FC can indeed be enhanced (Fig. 4.4), and that the fit of the model to the empirical FC may be more subject specific when a more personalized model is considered (Fig. S4.25).

The results of the second study also provide new information about (the personalization of) dynamical whole-brain models that may affect the interpretation of contemporary modeling results. First, they provide a nuanced perspective on the notion that the models can approximate the resting-state brain dynamics of individual subjects at a personalized level (Aerts et al., 2020; Bansal et al., 2018; Deco et al., 2017; Ritter et al., 2013; Sanz-Leon et al., 2015). On the one hand, the results presented in Chapter 4 confirm the premise of the modeling results being subject specific (Fig. 4.4; Fig. S4.25). On the other hand, the same findings also show that the correspondence between the simulated and the empirical FC is far less subject specific than the (single-modal) correspondence among the empirical functional connectomes (Fig. 4.4 vs. Fig. S4.25). Hence, instead of being an accurate, individualized reproduction of the empirical FC itself, the simulated FC appears to merely adopt certain subject-specific aspects from the empirical FC.

Second, the results of Chapter 4 indicate that the degree of model personalization can have consequences for studies comparing optimal parameter settings across (groups of) subjects (Donnelly-Kehoe et al., 2019; Iravani et al., 2021; Zimmermann, Perry, et al., 2018). The mappings of the similarity between the empirical and simulated FC that are sampled by the

grid search exhibit decreasing between-subject correspondences for an increasing amount of model personalization (Fig. 4.6) In other words, the parameters of more personalized models can become less comparable in the sense that the same parameter setting in divergent models can yield simulated FCs exhibiting vastly different similarities with the empirical FCs. The extent to which this between-subject comparability of the similarity maps has to be preserved is unclear, and the answer to this question may depend on the goal of the study at hand. Until this matter is resolved by future investigations, studies comparing fitted parameter values across subjects should therefore explicitly report the extent to which the wielded models are personalized in order to safeguard the appropriate interpretation of the results.

5.3.3 Differentiation of clinical patients from healthy cohorts

Currently, there is a strong focus on the prediction of behavioral, clinical and demographic subject traits from various type of MRI data (Arbabshirani et al., 2017; Rashid et al., 2020; Yoo et al., 2018; Zhang, Dougherty, et al., 2018). The empirical FC derived from (resting-state) fMRI sequences, for instance, has been used as a predictor for autism spectrum disorder (Hull et al., 2017). That type of connectivity may also be utilized to discriminate between healthy controls and patients suffering from schizophrenia and Parkinson's disease (Y. Chen et al., 2015; Kottaram et al., 2018; Pläschke et al., 2017). In addition, behavioral characteristics of individual subjects like cognition and emotion have been successfully related to inter-individual differences in the empirical resting-state and task-based functional connectomes (Finn & Bandettini, 2021). Demographic examples include the prediction of age and sex from the empirical FC and structural brain images (Dinsdale et al., 2021; La Corte et al., 2016; Pläschke et al., 2017; Zhang, Dougherty, et al., 2018).

Recent advances have shown that also dynamical whole-brain models may be used to detect behavioral and clinical traits. Iravani et al. (2021), for instance, used the dynamical whole-brain modeling paradigm to distinguish between healthy controls and individuals with attention deficit hyperactivity disorder (ADHD). Moreover, the models enabled the identification of distinct subtypes expressing particular phenotypical behaviors within the full cohort of ADHD subjects (Iravani et al., 2021). A different study used between-group differences in the parameters providing the best fit of the model to empirical data to discriminate between healthy subjects and patients suffering from Alzheimer's disease (Zimmermann, Perry, et al., 2018). The latter study even provided evidence that dynamical whole-brain modeling results may outperform empirical connectomes when predicting the clinical statuses of individual subjects (Zimmermann, Perry, et al., 2018).

It is unclear what specific aspects of the dynamical whole-brain models facilitate the reported identification of clinical subgroups and improved predictive capacity relative to classification studies that exclusively use empirical data. Nevertheless, the second study of this thesis (Chapter 4) seems to give valuable information that can be used when investigating this mechanism. The results of that study, for instance, showed that the modeling results can be sampled with a higher reliability than the empirical FC depending on the parcellation and the exact implementation of the dynamical whole-brain modeling paradigm (Fig. 4.2; Fig. 4.3). In other words, when compared to the empirical FC to which the model is fitted, the modeling results in the form of the (fitted) simulated FC or model parameter configuration can exhibit increased within-subject consistency relative to the inter-individual variability. Follow-up investigations demonstrated that the dynamical whole-brain models can realize these enhanced reliabilities by integrating the inter-individual differences included in a variety of sources (Fig. 4.5; Fig. 4.6; Fig. S4.25). Furthermore, the increased reliability also leads to simulated FCs that are more subject specific than their empirical counterparts (Fig. 4.4). Whether these enhancements of the reliability and the subject specificity indeed could contribute to a high predictive capacity should however be confirmed by additional investigations.

Finally, it should be noted that the computational load associated with dynamical whole-brain models (Section 5.3.1: Computational costs) drastically constrains the extent to which modeling results can be employed in prediction studies. That is because machine learning paradigms require large sample sizes in order to avoid inflated and uncertain classification accuracies (Poldrack et al., 2020; Varoquaux, 2018). Studies predicting characteristics of individuals from modeling results should hence have access to suitable computational infrastructures like the JURECA high-performance computing cluster (Jülich Supercomputing Centre, 2018), so that modeling results can be sampled for an acceptable number of subjects (Chapter 3; Chapter 4; Jung et al., 2021; Popovych et al., 2021; Zimmermann, Perry, et al., 2018). If appropriate computing power is not available, the number of calculations can be reduced by using alternative modeling strategies. For instance, instead of constructing one model for every individual subject, Iravani et al. (2021) constructed a single model based on the group-averaged empirical SC matrix. Consequently, the model simulations did not include one grid search per subject, but merely comprised one grid search for the entire cohort. Evidently, the computational costs are considerably reduced by such an approach, but this reduction comes at the expense of the degree of model personalization (Section 5.3.2: Personalization of the models), and hence also affects the reliability of the modeling results as demonstrated in Chapter 4. Future investigations should therefore study the effect of model personalization on the conclusions of (clinical) prediction studies.

5.4 The proper selection of the brain parcellation

5.4.1 The importance of a well-informed selection of the brain atlas

The two studies comprising this thesis clearly demonstrate that the choice of parcellation is far from trivial in dynamical whole-brain modeling studies. First of all, the quality of the fit of the model to the empirical data may strongly diverge when the parcellation differs (Fig. 3.6). Second, the parcellation largely determines how well the goodness-of-fit can be related to network properties calculated from the empirical connectomes when considering the within-parcellation, between-subject variations of these quantities (Fig. 3.8). Moreover, while a change of parcellation seems to have almost no effect on the reliability of the empirical FC, the atlas appears to be a determining factor with respect to the reliability of the modeling results (Fig. 4.2). Likewise, the subject specificities of the single-modal and cross-modal correlations involving the simulated FC may also be particularly affected by a change of parcellation (Fig. 4.4; Fig. 4.5; Fig. S4.25). The latter finding implies that the brain atlas can even influence the extent to which the simulated FC adopts subject-specific connectivity patterns from the empirical SC and the empirical FC that are used for model construction and validation, respectively.

Future investigations that make use of dynamical whole-brain models may exploit the results presented in this thesis for a well-informed selection of the brain atlas. In addition, the findings reveal potential issues that may arise when the parcellation is poorly chosen. For instance, the second study of this thesis as well as the literature show that the modeling results seem to be rather reliable when the empirical connectomes are reconstructed on the basis of a structurally-derived parcellation (Fig. 4.2; Cammoun et al., 2012; Donnelly-Kehoe et al., 2019; Muldoon et al., 2016; Tzourio-Mazoyer et al., 2002). Conversely, this reliability appears to be lower for a functionally-derived atlas (Fig. 4.2). In other words, the results presented in this thesis indicate that a change of parcellation may lead to conflicting conclusions, which is in agreement with recent work (Jung et al., 2021).

Because of this pronounced influence of the parcellation on various aspects of modeling studies, inquiries involving dynamical whole-brain models should declare explicitly why a particular parcellation was used to sample the reported results. In particular, the granularity and the construction method of the parcellation are important factors to consider in this respect; see below.

In addition, it is highly recommended that modeling studies discuss or even examine whether their messages are critically dependent on the selected brain atlas.

5.4.2 Parcellation method, granularity and empirical connectomes

The neurobiological basis of a brain atlas can be a motivation to select a particular parcellation. As discussed in Section 2.1: Brain atlases or parcellations, brain atlases can be derived from various types of biological data reflecting the brain's spatial organization (Eickhoff, Constable, & Yeo, 2018; Eickhoff, Yeo, & Genon, 2018). The Desikan-Killiany, Destrieux and von Economo-Koskinas atlases, for instance, divide the brain into areas based on structural information such as cortical folding patterns and cytoarchitecture (Desikan et al., 2006; Destrieux et al., 2010; von Economo & Koskinas, 1925). Alternatively, brain regions have also been delineated on the basis of functional aspects of brain organization, which include cortical patterns of functional connectivity (Schaefer et al., 2018) and function mappings (Dadi et al., 2020). One particular parcellation was even constructed by considering both structural and functional brain features (Glasser et al., 2016). These conceptual differences between brain atlases may lead to varying neurobiological interpretations of observations, and hence could be a reason to prefer one parcellation over another.

However, the notion that atlases may be based on divergent principles of brain organization does not only have semantic consequences, but can actually result in empirical connectomes with varying network architectures. The first study of this thesis plainly demonstrated that the parcellation can have a prominent effect on graph-theoretical measures extracted from the empirical SC and the empirical FC (Fig. 3.2; Fig. 3.3), which is in accordance with the literature (Arslan et al., 2018; J. Wang et al., 2009; Zalesky et al., 2010). Moreover, many of the calculated network properties did not exhibit a simple dependence on the number of parcels (Fig. 3.4), which indeed indicates that the construction method of the parcellation can substantially influence the empirical structural and functional connectomes. One study investigating the empirical FC presented qualitatively similar observations in the sense that granularity does not explain all differences in the network properties between parcellations (Arslan et al., 2018).

Nevertheless, the number of brain regions included in a parcellation influences the results of analyses involving purely empirical data as well. For example, the correspondence between the empirical SC and the empirical FC can be related well to the number of parcels of a brain atlas (Messé, 2020), which is congruent with the results presented in this thesis (Fig. 3.4). Likewise, some network properties extracted from empirical connectomes are strongly related to the parcellation granularity (Arslan et al., 2018; Zalesky et al., 2010). The first study of this thesis agrees with the latter observation for some of the calculated graph-theoretical measures (Fig. 3.4).

In sum, the results of this thesis agree with the literature that both the granularity and parcellation method can considerably alter the empirical SC, the empirical FC and their relationship.

5.4.3 Considerations for the selection of the parcellation in modeling studies

The modeling results are sensitive to the parcellation method as well, and this sensitivity may be even higher than for the empirical results. The quality of the fit of the model to the empirical FC, for example, varied considerably across parcellations, and this variation could not be explained by only considering the parcellation granularity (Fig. 3.4; Fig. 3.6; Fig. 3.7). Recently reported modeling results seem to agree with these findings (Popovych et al., 2021). Consequently, the second study of this thesis used a selection of brain atlases that had similar numbers of parcels and were constructed on a variety of biological data and parcellation techniques (Chapter 4). It showed that, in terms of their reliability and subject specificity, the modeling results and the empirical data were highly and weakly affected by a change of brain atlas, respectively (Fig. 4.2;

Fig. 4.4). Furthermore, some of the results exhibited clear distinctions between the structurally- and the functionally-derived parcellations (Fig. 4.2; Fig. 4.4; Fig. 4.5; Fig. S4.25).

Nevertheless, the influence of the granularity on the modeling results is not negligible. Fig. 3.4 indeed demonstrated that almost half of the parcellation-induced variance in the model fitting quality could be explained by the reciprocal of the number of parcels when the neural mass model was considered. However, this portion was much lower for the phase oscillator model: With respect to this model, the granularity could only explain a fifth of the between-parcellation variance in the goodness-of-fit (Fig. 3.4). Hence, these results indicate that, analogous to the empirical structure-function relationship (Messé, 2020), the quality of model fit may exhibit a dependency on the number of parcels that is inversely proportional. Nonetheless, the strength of this association may vary between dynamical whole-brain model implementations.

Taken together, analogous to investigations involving purely empirical data (see above), modeling studies should deliberately consider which brain atlas best fits their investigation in terms of both the granularity and the construction method of the parcellation. Admittedly, relatively small parcellations substantially cut the computational costs of the model simulations (Section 5.3.1: Computational costs), and yield high model fitting qualities (Chapter 3). However, because small parcellations contain a low number of parcels, the included brain regions cover rather large portions of the cerebral cortex, and may therefore oversimplify the organization of the brain (Eickhoff, Constable, & Yeo, 2018). Furthermore, as discussed above, the construction method of a brain atlas can be a determining factor with regard to relevant methodological considerations like the reliability and interpretability of results, and should hence be considered in addition to the granularity of the parcellation.

In conclusion, the selection of the parcellation for a dynamical whole-brain modeling study should be carefully deliberated. It could involve a compromise between various methodological facets like the computational load of the simulations, the neurobiological interpretation of the results and the reliability of the simulated data.

Chapter 6

Conclusion

Brain atlases or parcellations divide the brain into several areas based on particular facets of its spatial organization (Section 2.1: Brain atlases or parcellations). The delineated brain regions can subsequently be used to reconstruct the region-based structural (SC) and functional connectivity (FC), which characterize how the individual brain areas are coupled to one another by anatomical connections and synchronized co-activations, respectively (Section 2.2: Brain connectivity). Nevertheless, because brain atlases can be based on a wide variety of neurobiological data and parcellation techniques (Amunts & Zilles, 2015; Eickhoff, Constable, & Yeo, 2018; Eickhoff, Yeo, & Genon, 2018), the network architectures of the empirical structural and functional connectomes may vary considerably when different parcellations are used for their derivations from MRI data (Chapter 3; Arslan et al., 2018; J. Wang et al., 2009; Zalesky et al., 2010). Yet, even though dynamical whole-brain models have been used to study the relationship between the empirical SC and empirical FC from a biophysical perspective (Section 2.3: Dynamical whole-brain models), there has been no systematic investigation as to whether the parcellation-induced differences in the empirical connectomes can also lead to substantial variations in the modeling results. This thesis therefore assessed the influence of the brain atlas on various aspects of the dynamical whole-brain models.

First, it was examined how a variation of the parcellation affects the goodness-of-fit that characterizes how well a model replicates the empirical FC. The results of this investigation showed that a change of the brain atlas can indeed drastically alter the model fitting quality (Fig. 3.6). Moreover, the observed group-averaged, between-parcellation variations in the goodness-of-fit were related to parcellation-induced differences in the network properties of the empirical connectomes (Fig. 3.7). Furthermore, the network properties of the simulated FC providing the best fit of the model to the empirical FC can exhibit considerable variations across parcellations as well (Fig. 3.9). Taken together, these findings showed that a change of brain atlas may drastically impact the modeling results at a global group level.

In addition, other findings presented in this thesis showed that the parcellation can also influence how the modeling results of individual subjects relate to one another. For example, the patterns of the goodness-of-fit values across subjects could vary substantially between pairs of parcellations (Fig. 3.6). Additionally, the relationships between the network properties and the model fitting qualities of individuals were rather variable across brain atlases (Fig. 3.8). Furthermore, the reliability of the modeling results depended very much on the choice of the parcellation as well (Fig. 4.2; Fig. 4.3), and also the subject specificity of the simulated FC varied considerably across brain atlases (Fig. 4.4). Moreover, the parcellation could largely determine the extent to which the simulated FC adopted subject-specific connectivity patterns from the empirical SC and the empirical FC (Fig. 4.5; Fig. S4.25). Finally, it should be noted that the brain atlas often

exercised a larger influence on the modeling results than on findings involving purely empirical data (Fig. 4.2; Fig. 4.3; Fig. 4.4; Fig. 4.5).

In sum, the parcellation influences the modeling results at the global group as well as the single-subject level. Moreover, the effect of the parcellation can be much more pronounced for results related to dynamical whole-brain models than for findings directly calculated from the empirical data. The proper selection of the brain parcellation thus seems to be particularly important for studies using these models. Such studies should hence carefully contemplate on which parcellation to use for the sampling of their results, and subsequently document their considerations with respect to the chosen brain atlas meticulously. As discussed in Section 5.4: The proper selection of the brain parcellation, the appropriate selection of the parcellation for modeling studies might in the end involve a compromise between distinct methodological aspects such as the reliability, the subject specificity and the neurobiological interpretability of the modeling results and the computational costs required to acquire them.

References

Abdollahzadeh, A., Belevich, I., Jokitalo, E., Tohka, J., & Sierra, A. (2019). Automated 3D Axonal Morphometry of White Matter. *Scientific Reports*, *9*(1), 6084. https://doi.org/10.1038/s41598-019-42648-2

Abeysuriya, R. G., Hadida, J., Sotiropoulos, S. N., Jbabdi, S., Becker, R., Hunt, B. A. E., … Woolrich, M. W. (2018). A biophysical model of dynamic balancing of excitation and inhibition in fast oscillatory large-scale networks. *PLOS Computational Biology*, *14*(2), e1006007. https://doi.org/10.1371/journal.pcbi.1006007

Acebrón, J. A., Bonilla, L. L., Pérez Vicente, C. J., Ritort, F., & Spigler, R. (2005). The Kuramoto model: A simple paradigm for synchronization phenomena. *Reviews of Modern Physics*, *77*(1), 137–185. https://doi.org/10.1103/RevModPhys.77.137

Achard, S., & Bullmore, E. (2007). Efficiency and Cost of Economical Brain Functional Networks. *PLOS Computational Biology*, *3*(2), e17. https://doi.org/10.1371/journal.pcbi.0030017

Aerts, H., Schirner, M., Dhollander, T., Jeurissen, B., Achten, E., Van Roost, D., … Marinazzo, D. (2020). Modeling brain dynamics after tumor resection using The Virtual Brain. *NeuroImage*, *213*, 116738. https://doi.org/10.1016/j.neuroimage.2020.116738

Albers, K. J., Ambrosen, K. S., Liptrot, M. G., Dyrby, T. B., Schmidt, M. N., & Mørup, M. (2021). Using connectomics for predictive assessment of brain parcellations. *NeuroImage*, *238*, 118170. https://doi.org/10.1016/j.neuroimage.2021.118170

Ambrosen, K. S., Eskildsen, S. F., Hinne, M., Krug, K., Lundell, H., Schmidt, M. N., … Dyrby, T. B. (2020). Validation of structural brain connectivity networks: The impact of scanning parameters. *NeuroImage*, *204*, 116207. https://doi.org/10.1016/j.neuroimage.2019.116207

Amico, E., & Goñi, J. (2018). The quest for identifiability in human functional connectomes. *Scientific Reports*, *8*(1), 8254. https://doi.org/10.1038/s41598-018-25089-1

Amunts, K., Mohlberg, H., Bludau, S., & Zilles, K. (2020). Julich-Brain: A 3D probabilistic atlas of the human brain's cytoarchitecture. *Science*, *369*(6506), 988–992. https://doi.org/10.1126/science.abb4588

Amunts, K., & Zilles, K. (2015). Architectonic Mapping of the Human Brain beyond Brodmann. *Neuron*, *88*(6), 1086–1107. https://doi.org/10.1016/j.neuron.2015.12.001

Aquino, K. M., Fulcher, B., Oldham, S., Parkes, L., Gollo, L., Deco, G., & Fornito, A. (2022). On the intersection between data quality and dynamical modelling of large-scale fMRI signals. *NeuroImage*, *256*, 119051. https://doi.org/10.1016/j.neuroimage.2022.119051

Arbabshirani, M. R., Plis, S., Sui, J., & Calhoun, V. D. (2017). Single subject prediction of brain disorders in neuroimaging: Promises and pitfalls. *NeuroImage*, *145*, 137–165. https://doi.org/10.1016/j.neuroimage.2016.02.079

Arslan, S., Ktena, S. I., Makropoulos, A., Robinson, E. C., Rueckert, D., & Parisot, S. (2018). Human brain mapping: A systematic comparison of parcellation methods for the human cerebral cortex. *NeuroImage*, *170*, 5–30. https://doi.org/10.1016/j.neuroimage.2017.04.014

Attwell, D., & Laughlin, S. B. (2001). An Energy Budget for Signaling in the Grey Matter of the Brain. *Journal of Cerebral Blood Flow & Metabolism*, *21*(10), 1133–1145. https://doi.org/10.1097/00004647-200110000-00001

Auzias, G., Coulon, O., & Brovelli, A. (2016). MarsAtlas: A cortical parcellation atlas for functional mapping. *Human Brain Mapping*, *37*(4), 1573–1592. https://doi.org/10.1002/hbm.23121

Auzias, G., Lefèvre, J., Le Troter, A., Fischer, C., Perrot, M., Régis, J., & Coulon, O. (2013). Model-Driven Harmonic Parameterization of the Cortical Surface: HIP-HOP. *IEEE Transactions on Medical Imaging*, *32*(5), 873–887. https://doi.org/10.1109/TMI.2013.2241651

Avena-Koenigsberger, A., Misic, B., & Sporns, O. (2018). Communication dynamics in complex brain networks. *Nature Reviews Neuroscience*, *19*(1), 17–33. https://doi.org/10.1038/nrn.2017.149

Ayesha, S., Hanif, M. K., & Talib, R. (2020). Overview and comparative study of dimensionality reduction techniques for high dimensional data. *Information Fusion*, *59*, 44–58. https://doi.org/10.1016/j.inffus.2020.01.005

Bandettini, P. A., Jesmanowicz, A., Wong, E. C., & Hyde, J. S. (1993). Processing strategies for time-course data sets in functional mri of the human brain. *Magnetic Resonance in Medicine*, *30*(2), 161–173. https://doi.org/10.1002/mrm.1910300204

Bandettini, P. A., Wong, E. C., Hinks, R. S., Tikofsky, R. S., & Hyde, J. S. (1992). Time course EPI of human brain function during task activation. *Magnetic Resonance in Medicine*, *25*(2), 390–397. https://doi.org/10.1002/mrm.1910250220

Bansal, K., Nakuci, J., & Muldoon, S. F. (2018). Personalized brain network models for assessing structure–function relationships. *Current Opinion in Neurobiology*, *52*, 42–47. https://doi.org/10.1016/j.conb.2018.04.014

Baria, A. T., Baliki, M. N., Parrish, T., & Apkarian, A. V. (2011). Anatomical and Functional Assemblies of Brain BOLD Oscillations. *Journal of Neuroscience*, *31*(21), 7910–7919. https://doi.org/10.1523/JNEUROSCI.1296-11.2011

Bartko, J. J. (1966). The Intraclass Correlation Coefficient as a Measure of Reliability. *Psychological Reports*, *19*(1), 3–11. https://doi.org/10.2466/pr0.1966.19.1.3

Bassett, D. S., Brown, J. A., Deshpande, V., Carlson, J. M., & Grafton, S. T. (2011). Conserved and variable architecture of human white matter connectivity. *NeuroImage*, *54*(2), 1262–1279. https://doi.org/10.1016/j.neuroimage.2010.09.006

Bastiani, M., & Roebroeck, A. (2015). Unraveling the multiscale structural organization and connectivity of the human brain: the role of diffusion MRI. *Frontiers in Neuroanatomy*, *9*, 77. https://doi.org/10.3389/fnana.2015.00077

Behrens, T. E. J., Johansen-Berg, H., Woolrich, M. W., Smith, S. M., Wheeler-Kingshott, C. A. M., Boulby, P. A., … Matthews, P. M. (2003). Non-invasive mapping of connections between human thalamus and cortex using diffusion imaging. *Nature Neuroscience*, *6*(7), 750–757. https://doi.org/10.1038/nn1075

Betzel, R. F., & Bassett, D. S. (2017). Multi-scale brain networks. *NeuroImage*, *160*, 73–83. https://doi.org/10.1016/j.neuroimage.2016.11.006

Bick, C., Goodfellow, M., Laing, C. R., & Martens, E. A. (2020). Understanding the dynamics of biological and neural oscillator networks through exact mean-field reductions: a review. *The Journal of Mathematical Neuroscience*, *10*(1), 9. https://doi.org/10.1186/s13408-020-00086-9

Birn, R. M., Molloy, E. K., Patriat, R., Parker, T., Meier, T. B., Kirk, G. R., … Prabhakaran, V. (2013). The effect of scan length on the reliability of resting-state fMRI connectivity estimates. *NeuroImage*, *83*, 550–558. https://doi.org/10.1016/j.neuroimage.2013.05.099

Bishop, C. (2006). *Pattern Recognition and Machine Learning*. New York: Springer-Verlag.

Biswal, B., Yetkin, F. Z., Haughton, V. M., & Hyde, J. S. (1995). Functional connectivity in the motor cortex of resting human brain using echo-planar mri. *Magnetic Resonance in Medicine*, *34*(4), 537–541. https://doi.org/10.1002/mrm.1910340409

Biswal, B. B. (2012). Resting state fMRI: A personal history. *NeuroImage*, *62*(2), 938–944. https://doi.org/10.1016/j.neuroimage.2012.01.090

Blondel, V. D., Guillaume, J.-L., Lambiotte, R., & Lefebvre, E. (2008). Fast unfolding of communities in large networks. *Journal of Statistical Mechanics: Theory and Experiment*, *2008*(10), P10008. https://doi.org/10.1088/1742-5468/2008/10/P10008

Bolt, T., Nomi, J. S., Rubinov, M., & Uddin, L. Q. (2017). Correspondence between evoked and intrinsic functional brain network configurations. *Human Brain Mapping*, *38*(4), 1992–2007. https://doi.org/10.1002/hbm.23500

Borgatti, S. P. (2005). Centrality and network flow. *Social Networks*, *27*(1), 55–71. https://doi.org/10.1016/j.socnet.2004.11.008

Borgatti, S. P., & Everett, M. G. (2006). A Graph-theoretic perspective on centrality. *Social Networks*, *28*(4), 466–484. https://doi.org/10.1016/j.socnet.2005.11.005

Brandes, U. (2001). A faster algorithm for betweenness centrality. *The Journal of Mathematical Sociology*, *25*(2), 163–177. https://doi.org/10.1080/0022250X.2001.9990249

Breakspear, M. (2017). Dynamic models of large-scale brain activity. *Nature Neuroscience*, *20*(3), 340–352. https://doi.org/10.1038/nn.4497

Breakspear, M., Heitmann, S., & Daffertshofer, A. (2010). Generative models of cortical oscillations: neurobiological implications of the Kuramoto model. *Frontiers in Human Neuroscience*, *4*, 190. https://doi.org/10.3389/fnhum.2010.00190

Brodmann, K. (1909). *Vergleichende Lokalisationslehre der Grosshirnrinde in ihren Prinzipien dargestellt auf Grund des Zellenbaues*. Barth.

Brovelli, A., Badier, J.-M., Bonini, F., Bartolomei, F., Coulon, O., & Auzias, G. (2017). Dynamic Reconfiguration of Visuomotor-Related Functional Connectivity Networks. *Journal of Neuroscience*, *37*(4), 839–853. https://doi.org/10.1523/JNEUROSCI.1672-16.2016

Bullmore, E., & Sporns, O. (2009). Complex brain networks: graph theoretical analysis of structural and functional systems. *Nature Reviews Neuroscience*, *10*(3), 186–198. https://doi.org/10.1038/nrn2575

Buzsáki, G. (2006). *Rhythms of the Brain*. New York: Oxford University Press. https://doi.org/10.1093/acprof:oso/9780195301069.001.0001

Cabral, J., Hugues, E., Kringelbach, M. L., & Deco, G. (2012). Modeling the outcome of structural disconnection on resting-state functional connectivity. *NeuroImage*, *62*(3), 1342–1353. https://doi.org/10.1016/j.neuroimage.2012.06.007

Cabral, J., Hugues, E., Sporns, O., & Deco, G. (2011). Role of local network oscillations in resting-state functional connectivity. *NeuroImage*, *57*(1), 130–139. https://doi.org/10.1016/j.neuroimage.2011.04.010

Cabral, J., Kringelbach, M. L., & Deco, G. (2014). Exploring the network dynamics underlying brain activity during rest. *Progress in Neurobiology*, *114*, 102–131. https://doi.org/10.1016/j.pneurobio.2013.12.005

Cammoun, L., Gigandet, X., Meskaldji, D., Thiran, J. P., Sporns, O., Do, K. Q., … Hagmann, P. (2012). Mapping the human connectome at multiple scales with diffusion spectrum MRI. *Journal of Neuroscience Methods*, *203*(2), 386–397. https://doi.org/10.1016/j.jneumeth.2011.09.031

Campbell, A. (1905). *Histological studies on the localization of cerebral function.* Oxford, England: Univ. Press.

Chen, G., Taylor, P. A., Haller, S. P., Kircanski, K., Stoddard, J., Pine, D. S., … Cox, R. W. (2018). Intraclass correlation: Improved modeling approaches and applications for neuroimaging. *Human Brain Mapping*, *39*(3), 1187–1206. https://doi.org/https://doi.org/10.1002/hbm.23909

Chen, Y., Yang, W., Long, J., Zhang, Y., Feng, J., Li, Y., & Huang, B. (2015). Discriminative Analysis of Parkinson's Disease Based on Whole-Brain Functional Connectivity. *PLOS ONE*, *10*(4), e0124153. https://doi.org/10.1371/journal.pone.0124153

Cherkassky, B. V., Goldberg, A. V., & Radzik, T. (1996). Shortest paths algorithms: Theory and experimental evaluation. *Mathematical Programming*, *73*(2), 129–174. https://doi.org/10.1007/BF02592101

Chiavaras, M. M., LeGoualher, G., Evans, A., & Petrides, M. (2001). Three-Dimensional Probabilistic Atlas of the Human Orbitofrontal Sulci in Standardized Stereotaxic Space. *NeuroImage*, *13*(3), 479–496. https://doi.org/10.1006/nimg.2000.0641

Chiavaras, M. M., & Petrides, M. (2000). Orbitofrontal sulci of the human and macaque monkey brain. *Journal of Comparative Neurology*, *422*(1), 35–54. https://doi.org/10.1002/(SICI)1096-9861(20000619)422:1<35::AID-CNE3>3.0.CO;2-E

Cicchetti, D. V., & Sparrow, S. A. (1981). Developing criteria for establishing interrater reliability of specific items: applications to assessment of adaptive behavior. *American Journal of Mental Deficiency*, *86*(2), 127–137.

Cohen, M. X. (2017). Where Does EEG Come From and What Does It Mean? *Trends in Neurosciences*, *40*(4), 208–218. https://doi.org/10.1016/j.tins.2017.02.004

Cole, M. W., Bassett, D. S., Power, J. D., Braver, T. S., & Petersen, S. E. (2014). Intrinsic and Task-Evoked Network Architectures of the Human Brain. *Neuron*, *83*(1), 238–251. https://doi.org/10.1016/j.neuron.2014.05.014

Conturo, T. E., Lori, N. F., Cull, T. S., Akbudak, E., Snyder, A. Z., Shimony, J. S., … Raichle, M. E. (1999). Tracking neuronal fiber pathways in the living human brain. *Proceedings of the National Academy of Sciences*, *96*(18), 10422–10427. https://doi.org/10.1073/pnas.96.18.10422

Cooke, S. F., & Bliss, T. V. P. (2006). Plasticity in the human central nervous system. *Brain*, *129*(7), 1659–1673. https://doi.org/10.1093/brain/awl082

Craddock, R. C., James, G. A., Holtzheimer, P. E., Hu, X. P., & Mayberg, H. S. (2012). A whole brain fMRI atlas generated via spatially constrained spectral clustering. *Human Brain Mapping*, *33*(8), 1914–1928. https://doi.org/10.1002/hbm.21333

Craddock, R. C., Jbabdi, S., Yan, C.-G., Vogelstein, J. T., Castellanos, F. X., Di Martino, A., … Milham, M. P. (2013). Imaging human connectomes at the macroscale. *Nature Methods*, *10*(6), 524–539. https://doi.org/10.1038/nmeth.2482

Crofts, J. J., & Higham, D. J. (2009). A weighted communicability measure applied to complex brain networks. *Journal of The Royal Society Interface*, *6*(33), 411–414. https://doi.org/10.1098/rsif.2008.0484

Cumin, D., & Unsworth, C. P. (2007). Generalising the Kuramoto model for the study of neuronal synchronisation in the brain. *Physica D: Nonlinear Phenomena*, *226*(2), 181–196. https://doi.org/10.1016/j.physd.2006.12.004

Dadi, K., Varoquaux, G., Machlouzarides-Shalit, A., Gorgolewski, K. J., Wassermann, D., Thirion, B., & Mensch, A. (2020). Fine-grain atlases of functional modes for fMRI analysis. *NeuroImage*, *221*, 117126. https://doi.org/10.1016/j.neuroimage.2020.117126

Daffertshofer, A., & van Wijk, B. C. M. (2011). On the influence of amplitude on the connectivity between phases. *Frontiers in Neuroinformatics*, *5*, 6. https://doi.org/10.3389/fninf.2011.00006

da Fonseca, J. D., & Abud, C. V. (2018). The Kuramoto model revisited. *Journal of Statistical Mechanics: Theory and Experiment*, *2018*(10), 103204. https://doi.org/10.1088/1742-5468/aadb05

Dale, A. M., Fischl, B., & Sereno, M. I. (1999). Cortical Surface-Based Analysis: I. Segmentation and Surface Reconstruction. *NeuroImage*, *9*(2), 179–194. https://doi.org/10.1006/nimg.1998.0395

Danon, L., Díaz-Guilera, A., Duch, J., & Arenas, A. (2005). Comparing community structure identification. *Journal of Statistical Mechanics: Theory and Experiment*, *2005*(9), P09008. https://doi.org/10.1088/1742-5468/2005/09/P09008

Das, A., Sampson, A. L., Lainscsek, C., Muller, L., Lin, W., Doyle, J. C., … Sejnowski, T. J. (2017). Interpretation of the Precision Matrix and Its Application in Estimating Sparse Brain Connectivity during Sleep Spindles from Human Electrocorticography Recordings. *Neural Computation*, *29*(3), 603–642. https://doi.org/10.1162/NECO_a_00936

Dawid, A. P. (1979). Conditional Independence in Statistical Theory. *Journal of the Royal Statistical Society: Series B (Methodological)*, *41*(1), 1–15. https://doi.org/10.1111/j.2517-6161.1979.tb01052.x

Deco, G., Cabral, J., Saenger, V. M., Boly, M., Tagliazucchi, E., Laufs, H., … Kringelbach, M. L. (2018). Perturbation of whole-brain dynamics in silico reveals mechanistic differences between brain states. *NeuroImage*, *169*, 46–56. https://doi.org/10.1016/j.neuroimage.2017.12.009

Deco, G., Cruzat, J., Cabral, J., Knudsen, G. M., Carhart-Harris, R. L., Whybrow, P. C., … Kringelbach, M. L. (2018). Whole-Brain Multimodal Neuroimaging Model Using Serotonin Receptor Maps Explains Non-linear Functional Effects of LSD. *Current Biology*, *28*(19), 3065–3074.e6. https://doi.org/10.1016/j.cub.2018.07.083

Deco, G., Cruzat, J., Cabral, J., Tagliazucchi, E., Laufs, H., Logothetis, N. K., & Kringelbach, M. L. (2019). Awakening: Predicting external stimulation to force transitions between different brain states. *Proceedings of the National Academy of Sciences*, *116*(36), 18088–18097. https://doi.org/10.1073/pnas.1905534116

Deco, G., Jirsa, V., McIntosh, A. R., Sporns, O., & Kötter, R. (2009). Key role of coupling, delay, and noise in resting brain fluctuations. *Proceedings of the National Academy of Sciences*, *106*(25), 10302–10307. https://doi.org/10.1073/pnas.0901831106

Deco, G., & Jirsa, V. K. (2012). Ongoing Cortical Activity at Rest: Criticality, Multistability, and Ghost Attractors. *Journal of Neuroscience*, *32*(10), 3366–3375. https://doi.org/10.1523/JNEUROSCI.2523-11.2012

Deco, G., Jirsa, V. K., & McIntosh, A. R. (2011). Emerging concepts for the dynamical organization of resting-state activity in the brain. *Nature Reviews Neuroscience*, *12*(1), 43–56. https://doi.org/10.1038/nrn2961

Deco, G., & Kringelbach, M. L. (2014). Great Expectations: Using Whole-Brain Computational Connectomics for Understanding Neuropsychiatric Disorders. *Neuron*, *84*(5), 892–905. https://doi.org/10.1016/j.neuron.2014.08.034

Deco, G., Kringelbach, M. L., Arnatkeviciute, A., Oldham, S., Sabaroedin, K., Rogasch, N. C., … Fornito, A. (2021). Dynamical consequences of regional heterogeneity in the brain's transcriptional landscape. *Science Advances*, *7*(29), eabf4752. https://doi.org/10.1126/sciadv.abf4752

Deco, G., Kringelbach, M. L., Jirsa, V. K., & Ritter, P. (2017). The dynamics of resting fluctuations in the brain: metastability and its dynamical cortical core. *Scientific Reports*, *7*(1), 3095. https://doi.org/10.1038/s41598-017-03073-5

Deco, G., McIntosh, A. R., Shen, K., Hutchison, R. M., Menon, R. S., Everling, S., … Jirsa, V. K. (2014). Identification of Optimal Structural Connectivity Using Functional Connectivity and Neural Modeling. *Journal of Neuroscience*, *34*(23), 7910–7916. https://doi.org/10.1523/JNEUROSCI.4423-13.2014

Deco, G., Ponce-Alvarez, A., Hagmann, P., Romani, G. L., Mantini, D., & Corbetta, M. (2014). How Local Excitation–Inhibition Ratio Impacts the Whole Brain Dynamics. *Journal of Neuroscience*, *34*(23), 7886–7898. https://doi.org/10.1523/JNEUROSCI.5068-13.2014

Deco, G., Ponce-Alvarez, A., Mantini, D., Romani, G. L., Hagmann, P., & Corbetta, M. (2013). Resting-State Functional Connectivity Emerges from Structurally and Dynamically Shaped Slow Linear Fluctuations. *Journal of Neuroscience*, *33*(27), 11239–11252. https://doi.org/10.1523/JNEUROSCI.1091-13.2013

Deco, G., Senden, M., & Jirsa, V. (2012). How anatomy shapes dynamics: a semi-analytical study of the brain at rest by a simple spin model. *Frontiers in Computational Neuroscience*, *6*, 68. https://doi.org/10.3389/fncom.2012.00068

DeFelipe, J. (2010). From the Connectome to the Synaptome: An Epic Love Story. *Science*, *330*(6008), 1198–1201. https://doi.org/10.1126/science.1193378

Deligianni, F., Carmichael, D. W., Zhang, G. H., Clark, C. A., & Clayden, J. D. (2016). NODDI and Tensor-Based Microstructural Indices as Predictors of Functional Connectivity. *PLOS ONE*, *11*(4), e0153404. https://doi.org/10.1371/journal.pone.0153404

Demirtaş, M., Burt, J. B., Helmer, M., Ji, J. L., Adkinson, B. D., Glasser, M. F., … Murray, J. D. (2019). Hierarchical Heterogeneity across Human Cortex Shapes Large-Scale Neural Dynamics. *Neuron*, *101*(6), 1181–1194.e13. https://doi.org/10.1016/j.neuron.2019.01.017

Dempster, A. P. (1972). Covariance Selection. *Biometrics*, *28*(1), 157–175. https://doi.org/10.2307/2528966

de Reus, M. A., & van den Heuvel, M. P. (2013). The parcellation-based connectome: Limitations and extensions. *NeuroImage*, *80*, 397–404. https://doi.org/10.1016/j.neuroimage.2013.03.053

Desikan, R. S., Ségonne, F., Fischl, B., Quinn, B. T., Dickerson, B. C., Blacker, D., … Killiany, R. J. (2006). An automated labeling system for subdividing the human cerebral cortex on MRI scans into gyral based regions of interest. *NeuroImage*, *31*(3), 968–980. https://doi.org/10.1016/j.neuroimage.2006.01.021

Destexhe, A., Mainen, Z. F., & Sejnowski, T. J. (1994a). An Efficient Method for Computing Synaptic Conductances Based on a Kinetic Model of Receptor Binding. *Neural Computation*, *6*(1), 14–18. https://doi.org/10.1162/neco.1994.6.1.14

Destexhe, A., Mainen, Z. F., & Sejnowski, T. J. (1994b). Synthesis of models for excitable membranes, synaptic transmission and neuromodulation using a common kinetic formalism. *Journal of Computational Neuroscience*, *1*(3), 195–230. https://doi.org/10.1007/BF00961734

Destrieux, C., Fischl, B., Dale, A., & Halgren, E. (2010). Automatic parcellation of human cortical gyri and sulci using standard anatomical nomenclature. *NeuroImage*, *53*(1), 1–15. https://doi.org/10.1016/j.neuroimage.2010.06.010

Diallo, B., Dolidon, F., Travere, J.-M., & Mazoyer, B. (1998). VoxeLine: a software program for 3D real-time visualization of biomedical images. *Computerized Medical Imaging and Graphics*, *22*(4), 275–289. https://doi.org/10.1016/S0895-6111(98)00040-8

Diestel, R. (2012). *Graph Theory* (4th ed.). Heidelberg: Springer.

Dinsdale, N. K., Bluemke, E., Smith, S. M., Arya, Z., Vidaurre, D., Jenkinson, M., & Namburete, A. I. L. (2021). Learning patterns of the ageing brain in MRI using deep convolutional networks. *NeuroImage*, *224*, 117401. https://doi.org/10.1016/j.neuroimage.2020.117401

Domhof, J. (2021). *Parcellation modelling, https://jugit.fz-juelich.de/inm7/parcellation-modelling.*

Domhof, J. W. M., Jung, K., Eickhoff, S. B., & Popovych, O. V. (2021). Parcellation-based structural and resting-state functional brain connectomes of a healthy cohort [Dataset]. EBRAINS. https://doi.org/10.25493/81EV-ZVT

Domhof, J. W. M., Jung, K., Eickhoff, S. B., & Popovych, O. V. (2022). Parcellation-based resting-state blood-oxygen-level-dependent (BOLD) signals of a healthy cohort (v1.0) [Dataset]. EBRAINS. https://doi.org/10.25493/F9DP-WCQ

Domhof, J. W. M., & Tiesinga, P. H. E. (2021). Flexible Frequency Switching in Adult Mouse Visual Cortex Is Mediated by Competition Between Parvalbumin and Somatostatin Expressing Interneurons. *Neural Computation*, *33*(4), 926–966. https://doi.org/10.1162/neco_a_01369

Donnelly-Kehoe, P., Saenger, V. M., Lisofsky, N., Kühn, S., Kringelbach, M. L., Schwarzbach, J., … Deco, G. (2019). Reliable local dynamics in the brain across sessions are revealed by whole-brain modeling of resting state activity. *Human Brain Mapping*, *40*(10), 2967–2980. https://doi.org/10.1002/hbm.24572

Douglas, R. J., & Martin, K. A. C. (2004). Neuronal circuits of the neocortex. *Annual Review of Neuroscience*, *27*(1), 419–451. https://doi.org/10.1146/annurev.neuro.27.070203.144152

Eberhart, R., & Kennedy, J. (1995). A new optimizer using particle swarm theory. In *MHS'95. Proceedings of the Sixth International Symposium on Micro Machine and Human Science* (pp. 39–43). https://doi.org/10.1109/MHS.1995.494215

Edlow, B. L., Mareyam, A., Horn, A., Polimeni, J. R., Witzel, T., Tisdall, M. D., … van der Kouwe, A. (2019). 7 Tesla MRI of the ex vivo human brain at 100 micron resolution. *Scientific Data*, *6*(1), 244. https://doi.org/10.1038/s41597-019-0254-8

Eickhoff, S. B., Constable, R. T., & Yeo, B. T. T. (2018). Topographic organization of the cerebral cortex and brain cartography. *NeuroImage*, *170*, 332–347. https://doi.org/10.1016/j.neuroimage.2017.02.018

Eickhoff, S. B., Yeo, B. T. T., & Genon, S. (2018). Imaging-based parcellations of the human brain. *Nature Reviews Neuroscience*, *19*(11), 672–686. https://doi.org/10.1038/s41583-018-0071-7

Faillenot, I., Heckemann, R. A., Frot, M., & Hammers, A. (2017). Macroanatomy and 3D probabilistic atlas of the human insula. *NeuroImage*, *150*, 88–98. https://doi.org/10.1016/j.neuroimage.2017.01.073

Fan, L., Li, H., Zhuo, J., Zhang, Y., Wang, J., Chen, L., … Jiang, T. (2016). The Human Brainnetome Atlas: A New Brain Atlas Based on Connectional Architecture. *Cerebral Cortex*, *26*(8), 3508–3526. https://doi.org/10.1093/cercor/bhw157

Farahani, F. V., Karwowski, W., & Lighthall, N. R. (2019). Application of Graph Theory for Identifying Connectivity Patterns in Human Brain Networks: A Systematic Review. *Frontiers in Neuroscience*, *13*, 585. https://doi.org/10.3389/fnins.2019.00585

Felleman, D. J., & Van Essen, D. C. (1991). Distributed Hierarchical Processing in the Primate Cerebral Cortex. *Cerebral Cortex*, *1*(1), 1–47. https://doi.org/10.1093/cercor/1.1.1-a

Fields, R. D. (2010). Change in the Brain's White Matter. *Science*, *330*(6005), 768–769. https://doi.org/10.1126/science.1199139

Fillard, P., Descoteaux, M., Goh, A., Gouttard, S., Jeurissen, B., Malcolm, J., … Poupon, C. (2011). Quantitative evaluation of 10 tractography algorithms on a realistic diffusion MR phantom. *NeuroImage*, *56*(1), 220–234. https://doi.org/10.1016/j.neuroimage.2011.01.032

Finn, E. S. (2021). Is it time to put rest to rest? *Trends in Cognitive Sciences*, *25*(12), 1021–1032. https://doi.org/10.1016/j.tics.2021.09.005

Finn, E. S., & Bandettini, P. A. (2021). Movie-watching outperforms rest for functional connectivity-based prediction of behavior. *NeuroImage*, *235*, 117963. https://doi.org/10.1016/j.neuroimage.2021.117963

Finn, E. S., & Rosenberg, M. D. (2021). Beyond fingerprinting: Choosing predictive connectomes over reliable connectomes. *NeuroImage*, *239*, 118254. https://doi.org/10.1016/j.neuroimage.2021.118254

Finn, E. S., Shen, X., Scheinost, D., Rosenberg, M. D., Huang, J., Chun, M. M., … Constable, R. T. (2015). Functional connectome fingerprinting: identifying individuals using patterns of brain connectivity. *Nature Neuroscience*, *18*(11), 1664–1671. https://doi.org/10.1038/nn.4135

Fisher, R. A. (1915). Frequency Distribution of the Values of the Correlation Coefficient in Samples from an Indefinitely Large Population. *Biometrika*, *10*(4), 507–521. https://doi.org/10.2307/2331838

Fisher, R. A. (1921). On the "Probable Error" of a Coefficient of Correlation Deduced from a Small Sample. *Metron*, *1*, 3–32.

Flechsig, P. E. (1920). *Anatomie des menschlichen Gehirns und Rückenmarks auf myelogenetischer Grundlage. v. 1* (Vol. 1). G. Thieme.

Foster, J. J., Sutterer, D. W., Serences, J. T., Vogel, E. K., & Awh, E. (2017). Alpha-Band Oscillations Enable Spatially and Temporally Resolved Tracking of Covert Spatial Attention. *Psychological Science*, *28*(7), 929–941. https://doi.org/10.1177/0956797617699167

Fox, K., & Wong, R. O. L. (2005). A Comparison of Experience-Dependent Plasticity in the Visual and Somatosensory Systems. *Neuron*, *48*(3), 465–477. https://doi.org/10.1016/j.neuron.2005.10.013

Fox, M. D., & Greicius, M. (2010). Clinical applications of resting state functional connectivity. *Frontiers in Systems Neuroscience*, *4*, 19. https://doi.org/10.3389/fnsys.2010.00019

Fraga González, G., Smit, D. J. A., van der Molen, M. J. W., Tijms, J., Stam, C. J., de Geus, E. J. C., & van der Molen, M. W. (2018). EEG Resting State Functional Connectivity in Adult Dyslexics Using Phase Lag Index and Graph Analysis. *Frontiers in Human Neuroscience*, *12*, 341. https://doi.org/10.3389/fnhum.2018.00341

Frazier, J. A., Chiu, S., Breeze, J. L., Makris, N., Lange, N., Kennedy, D. N., … Biederman, J. (2005). Structural Brain Magnetic Resonance Imaging of Limbic and Thalamic Volumes in Pediatric Bipolar Disorder. *American Journal of Psychiatry*, *162*(7), 1256–1265. https://doi.org/10.1176/appi.ajp.162.7.1256

Freeman, L. C. (1978). Centrality in social networks conceptual clarification. *Social Networks*, *1*(3), 215–239. https://doi.org/10.1016/0378-8733(78)90021-7

Freud, E., Plaut, D. C., & Behrmann, M. (2016). 'What' Is Happening in the Dorsal Visual Pathway. *Trends in Cognitive Sciences*, *20*(10), 773–784. https://doi.org/10.1016/j.tics.2016.08.003

Friston, K. J. (2011). Functional and Effective Connectivity: A Review. *Brain Connectivity*, *1*(1), 13–36. https://doi.org/10.1089/brain.2011.0008

Friston, K. J., Harrison, L., & Penny, W. (2003). Dynamic causal modelling. *NeuroImage*, *19*(4), 1273–1302. https://doi.org/10.1016/S1053-8119(03)00202-7

Galán, R. F. (2008). On How Network Architecture Determines the Dominant Patterns of Spontaneous Neural Activity. *PLOS ONE*, *3*(5), e2148. https://doi.org/10.1371/journal.pone.0002148

Ghosh, A., Rho, Y., McIntosh, A. R., Kötter, R., & Jirsa, V. K. (2008). Noise during Rest Enables the Exploration of the Brain's Dynamic Repertoire. *PLOS Computational Biology*, *4*(10), e1000196. https://doi.org/10.1371/journal.pcbi.1000196

Gilson, M., Moreno-Bote, R., Ponce-Alvarez, A., Ritter, P., & Deco, G. (2016). Estimation of Directed Effective Connectivity from fMRI Functional Connectivity Hints at Asymmetries of Cortical Connectome. *PLOS Computational Biology*, *12*(3), e1004762. https://doi.org/10.1371/journal.pcbi.1004762

Glasser, M. F., Coalson, T. S., Robinson, E. C., Hacker, C. D., Harwell, J., Yacoub, E., … Van Essen, D. C. (2016). A multi-modal parcellation of human cerebral cortex. *Nature*, *536*(7615), 171–178. https://doi.org/10.1038/nature18933

Glasser, M. F., Sotiropoulos, S. N., Wilson, J. A., Coalson, T. S., Fischl, B., Andersson, J. L., … Jenkinson, M. (2013). The minimal preprocessing pipelines for the Human Connectome Project. *NeuroImage*, *80*, 105–124. https://doi.org/10.1016/j.neuroimage.2013.04.127

Goldstein, J. M., Seidman, L. J., Makris, N., Ahern, T., O'Brien, L. M., Caviness, V. S., … Tsuang, M. T. (2007). Hypothalamic Abnormalities in Schizophrenia: Sex Effects and Genetic Vulnerability. *Biological Psychiatry*, *61*(8), 935–945. https://doi.org/10.1016/j.biopsych.2006.06.027

Gordon, E. M., Laumann, T. O., Adeyemo, B., Huckins, J. F., Kelley, W. M., & Petersen, S. E. (2016). Generation and Evaluation of a Cortical Area Parcellation from Resting-State Correlations. *Cerebral Cortex*, *26*(1), 288–303. https://doi.org/10.1093/cercor/bhu239

Gousias, I. S., Rueckert, D., Heckemann, R. A., Dyet, L. E., Boardman, J. P., Edwards, A. D., & Hammers, A. (2008). Automatic segmentation of brain MRIs of 2-year-olds into 83 regions of interest. *NeuroImage*, *40*(2), 672–684. https://doi.org/10.1016/j.neuroimage.2007.11.034

Goñi, J., van den Heuvel, M. P., Avena-Koenigsberger, A., Velez de Mendizabal, N., Betzel, R. F., Griffa, A., … Sporns, O. (2014). Resting-brain functional connectivity predicted by analytic measures of network communication. *Proceedings of the National Academy of Sciences*, *111*(2), 833–838. https://doi.org/10.1073/pnas.1315529111

Grabner, G., Janke, A. L., Budge, M. M., Smith, D., Pruessner, J., & Collins, D. L. (2006). Symmetric Atlasing and Model Based Segmentation: An Application to the Hippocampus in Older Adults. In R. Larsen, M. Nielsen, & J. Sporring (Eds.), *Medical Image Computing and Computer-Assisted Intervention – MICCAI 2006* (pp. 58–66). Berlin, Heidelberg: Springer. https://doi.org/10.1007/11866763_8

Graham, D., & Rockmore, D. (2011). The Packet Switching Brain. *Journal of Cognitive Neuroscience*, *23*(2), 267–276. https://doi.org/10.1162/jocn.2010.21477

Gratton, C., Laumann, T. O., Nielsen, A. N., Greene, D. J., Gordon, E. M., Gilmore, A. W., … Petersen, S. E. (2018). Functional Brain Networks Are Dominated by Stable Group and Individual Factors, Not Cognitive or Daily Variation. *Neuron*, *98*(2), 439–452.e5. https://doi.org/10.1016/j.neuron.2018.03.035

Grienberger, C., & Konnerth, A. (2012). Imaging Calcium in Neurons. *Neuron*, *73*(5), 862–885. https://doi.org/10.1016/j.neuron.2012.02.011

Griffanti, L., Salimi-Khorshidi, G., Beckmann, C. F., Auerbach, E. J., Douaud, G., Sexton, C. E., … Smith, S. M. (2014). ICA-based artefact removal and accelerated fMRI acquisition for improved resting state network imaging. *NeuroImage*, *95*, 232–247. https://doi.org/10.1016/j.neuroimage.2014.03.034

Guye, M., Bettus, G., Bartolomei, F., & Cozzone, P. J. (2010). Graph theoretical analysis of structural and functional connectivity MRI in normal and pathological brain networks. *Magnetic Resonance Materials in Physics, Biology and Medicine*, *23*(5), 409–421. https://doi.org/10.1007/s10334-010-0205-z

Hagberg, A., Swart, P., & S Chult, D. (2008). *Exploring network structure, dynamics, and function using networkx* (Tech. Rep. No. LA-UR-08-05495; LA-UR-08-5495). Retrieved 2020-11-03, from https://www.osti.gov/biblio/960616-exploring-network-structure-dynamics-function-using-networkx

Hahn, G., Skeide, M. A., Mantini, D., Ganzetti, M., Destexhe, A., Friederici, A. D., & Deco, G. (2019). A new computational approach to estimate whole-brain effective connectivity from functional and structural MRI, applied to language development. *Scientific Reports*, *9*(1), 8479. https://doi.org/10.1038/s41598-019-44909-6

Hammers, A., Allom, R., Koepp, M. J., Free, S. L., Myers, R., Lemieux, L., … Duncan, J. S. (2003). Three-dimensional maximum probability atlas of the human brain, with particular reference to the temporal lobe. *Human Brain Mapping*, *19*(4), 224–247. https://doi.org/https://doi.org/10.1002/hbm.10123

Hansen, E. C. A., Battaglia, D., Spiegler, A., Deco, G., & Jirsa, V. K. (2015). Functional connectivity dynamics: Modeling the switching behavior of the resting state. *NeuroImage*, *105*, 525–535. https://doi.org/10.1016/j.neuroimage.2014.11.001

Hansen, N., & Ostermeier, A. (1996). Adapting arbitrary normal mutation distributions in evolution strategies: the covariance matrix adaptation. In *Proceedings of IEEE International Conference on Evolutionary Computation* (pp. 312–317). https://doi.org/10.1109/ICEC.1996.542381

Harris, J. J., Jolivet, R., & Attwell, D. (2012). Synaptic Energy Use and Supply. *Neuron*, *75*(5), 762–777. https://doi.org/10.1016/j.neuron.2012.08.019

Havlicek, M., Roebroeck, A., Friston, K., Gardumi, A., Ivanov, D., & Uludag, K. (2015). Physiologically informed dynamic causal modeling of fMRI data. *NeuroImage*, *122*, 355–372. https://doi.org/10.1016/j.neuroimage.2015.07.078

Heitmann, S., & Breakspear, M. (2018). Putting the "dynamic" back into dynamic functional connectivity. *Network Neuroscience*, *02*(02), 150–174. https://doi.org/10.1162/netn_a_00041

Hellyer, P. J., Jachs, B., Clopath, C., & Leech, R. (2016). Local inhibitory plasticity tunes macroscopic brain dynamics and allows the emergence of functional brain networks. *NeuroImage*, *124*, 85–95. https://doi.org/10.1016/j.neuroimage.2015.08.069

Hindriks, R., Adhikari, M. H., Murayama, Y., Ganzetti, M., Mantini, D., Logothetis, N. K., & Deco, G. (2016). Can sliding-window correlations reveal dynamic functional connectivity in resting-state fMRI? *NeuroImage*, *127*, 242–256. https://doi.org/10.1016/j.neuroimage.2015.11.055

Hofer, S. B., Mrsic-Flogel, T. D., Bonhoeffer, T., & Hübener, M. (2006). Lifelong learning: ocular dominance plasticity in mouse visual cortex. *Current Opinion in Neurobiology*, *16*(4), 451–459. https://doi.org/10.1016/j.conb.2006.06.007

Holmes, A. J., Hollinshead, M. O., O'Keefe, T. M., Petrov, V. I., Fariello, G. R., Wald, L. L., … Buckner, R. L. (2015). Brain Genomics Superstruct Project initial data release with structural, functional, and behavioral measures. *Scientific Data*, *2*(1), 150031. https://doi.org/10.1038/sdata.2015.31

Holmes, C. J., Hoge, R., Collins, L., Woods, R., Toga, A. W., & Evans, A. C. (1998). Enhancement of MR Images Using Registration for Signal Averaging. *Journal of Computer Assisted Tomography*, *22*(2), 324–333.

Honari, H., Choe, A. S., Pekar, J. J., & Lindquist, M. A. (2019). Investigating the impact of autocorrelation on time-varying connectivity. *NeuroImage*, *197*, 37–48. https://doi.org/10.1016/j.neuroimage.2019.04.042

Honey, C. J., Kötter, R., Breakspear, M., & Sporns, O. (2007). Network structure of cerebral cortex shapes functional connectivity on multiple time scales. *Proceedings of the National Academy of Sciences*, *104*(24), 10240–10245. https://doi.org/10.1073/pnas.0701519104

Honey, C. J., Sporns, O., Cammoun, L., Gigandet, X., Thiran, J. P., Meuli, R., & Hagmann, P. (2009). Predicting human resting-state functional connectivity from structural connectivity. *Proceedings of the National Academy of Sciences*, *106*(6), 2035–2040. https://doi.org/10.1073/pnas.0811168106

Hotelling, H. (1936). Relations Between Two Sets of Variates. *Biometrika*, *28*(3/4), 321–377. https://doi.org/10.2307/2333955

Hull, J. V., Dokovna, L. B., Jacokes, Z. J., Torgerson, C. M., Irimia, A., & Van Horn, J. D. (2017). Resting-State Functional Connectivity in Autism Spectrum Disorders: A Review. *Frontiers in Psychiatry*, *7*, 205. https://doi.org/10.3389/fpsyt.2016.00205

Hutchison, R. M., Womelsdorf, T., Allen, E. A., Bandettini, P. A., Calhoun, V. D., Corbetta, M., … Chang, C. (2013). Dynamic functional connectivity: Promise, issues, and interpretations. *NeuroImage*, *80*, 360–378. https://doi.org/10.1016/j.neuroimage.2013.05.079

Huth, A. G., de Heer, W. A., Griffiths, T. L., Theunissen, F. E., & Gallant, J. L. (2016). Natural speech reveals the semantic maps that tile human cerebral cortex. *Nature*, *532*(7600), 453–458. https://doi.org/10.1038/nature17637

Huth, A. G., Griffiths, T. L., Theunissen, F. E., & Gallant, J. L. (2015). PrAGMATiC: a Probabilistic and Generative Model of Areas Tiling the Cortex. *arXiv:1504.03622 [q-bio]*.

Iravani, B., Arshamian, A., Fransson, P., & Kaboodvand, N. (2021). Whole-brain modelling of resting state fMRI differentiates ADHD subtypes and facilitates stratified neuro-stimulation therapy. *NeuroImage*, *231*, 117844. https://doi.org/10.1016/j.neuroimage.2021.117844

Jansen, B. H., & Rit, V. G. (1995). Electroencephalogram and visual evoked potential generation in a mathematical model of coupled cortical columns. *Biological Cybernetics*, *73*(4), 357–366. https://doi.org/10.1007/BF00199471

Jansen, B. H., Zouridakis, G., & Brandt, M. E. (1993). A neurophysiologically-based mathematical model of flash visual evoked potentials. *Biological Cybernetics*, *68*(3), 275–283. https://doi.org/10.1007/BF00224863

Jbabdi, S., Sotiropoulos, S. N., Haber, S. N., Van Essen, D. C., & Behrens, T. E. (2015). Measuring macroscopic brain connections in vivo. *Nature Neuroscience*, *18*(11), 1546–1555. https://doi.org/10.1038/nn.4134

Jenkinson, M., Beckmann, C. F., Behrens, T. E. J., Woolrich, M. W., & Smith, S. M. (2012). FSL. *NeuroImage*, *62*(2), 782–790. https://doi.org/10.1016/j.neuroimage.2011.09.015

Jeurissen, B., Tournier, J.-D., Dhollander, T., Connelly, A., & Sijbers, J. (2014). Multi-tissue constrained spherical deconvolution for improved analysis of multi-shell diffusion MRI data. *NeuroImage*, *103*, 411–426. https://doi.org/10.1016/j.neuroimage.2014.07.061

Jirsa, V. K., Proix, T., Perdikis, D., Woodman, M. M., Wang, H., Gonzalez-Martinez, J., … Bartolomei, F. (2017). The Virtual Epileptic Patient: Individualized whole-brain models of epilepsy spread. *NeuroImage*, *145*, 377–388. https://doi.org/10.1016/j.neuroimage.2016.04.049

Joliot, M., Jobard, G., Naveau, M., Delcroix, N., Petit, L., Zago, L., … Tzourio-Mazoyer, N. (2015). AICHA: An atlas of intrinsic connectivity of homotopic areas. *Journal of Neuroscience Methods*, *254*, 46–59. https://doi.org/10.1016/j.jneumeth.2015.07.013

Jones, D. R., Schonlau, M., & Welch, W. J. (1998). Efficient Global Optimization of Expensive Black-Box Functions. *Journal of Global Optimization*, *13*(4), 455–492. https://doi.org/10.1023/A:1008306431147

Ju, N.-S., Guan, S.-C., Tao, L., Tang, S.-M., & Yu, C. (2021). Orientation Tuning and End-stopping in Macaque V1 Studied with Two-photon Calcium Imaging. *Cerebral Cortex*, *31*(4), 2085–2097. https://doi.org/10.1093/cercor/bhaa346

Jung, K., Eickhoff, S. B., & Popovych, O. V. (2021). Tractography density affects whole-brain structural architecture and resting-state dynamical modeling. *NeuroImage*, *237*, 118176. https://doi.org/10.1016/j.neuroimage.2021.118176

Jülich Supercomputing Centre. (2018). JURECA: Modular supercomputer at Jülich Supercomputing Centre. *Journal of large-scale research facilities*, *4*(A132). https://doi.org/10.17815/jlsrf-4-121-1

Kadirvelu, B., Hayashi, Y., & Nasuto, S. J. (2017). Inferring structural connectivity using Ising couplings in models of neuronal networks. *Scientific Reports*, *7*(1), 8156. https://doi.org/10.1038/s41598-017-05462-2

Kale, P., Zalesky, A., & Gollo, L. L. (2018). Estimating the impact of structural directionality: How reliable are undirected connectomes? *Network Neuroscience*, *02*(02), 259–284. https://doi.org/10.1162/netn_a_00040

Kennedy, J., & Eberhart, R. (1995). Particle swarm optimization. In *Proceedings of ICNN'95 - International Conference on Neural Networks* (Vol. 4, pp. 1942–1948 vol.4). https://doi.org/10.1109/ICNN.1995.488968

Kim, S. (2014). Issues on the Choice of a Proper Time Step in Molecular Dynamics. *Physics Procedia*, *53*, 60–62. https://doi.org/10.1016/j.phpro.2014.06.027

Kleist, K. (1934). *Gehirnpathologie : vornehmlich auf Grund der Kriegserfahrungen*. Leipzig: Barth.

Kong, X., Kong, R., Orban, C., Wang, P., Zhang, S., Anderson, K., … Yeo, B. T. T. (2021). Sensory-motor cortices shape functional connectivity dynamics in the human brain. *Nature Communications*, *12*(1), 6373. https://doi.org/10.1038/s41467-021-26704-y

Koo, T. K., & Li, M. Y. (2016). A Guideline of Selecting and Reporting Intraclass Correlation Coefficients for Reliability Research. *Journal of Chiropractic Medicine*, *15*(2), 155–163. https://doi.org/10.1016/j.jcm.2016.02.012

Kopell, N., Ermentrout, G. B., Whittington, M. A., & Traub, R. D. (2000). Gamma rhythms and beta rhythms have different synchronization properties. *Proceedings of the National Academy of Sciences*, *97*(4), 1867–1872. https://doi.org/10.1073/pnas.97.4.1867

Kottaram, A., Johnston, L., Ganella, E., Pantelis, C., Kotagiri, R., & Zalesky, A. (2018). Spatio-temporal dynamics of resting-state brain networks improve single-subject prediction of schizophrenia diagnosis. *Human Brain Mapping*, *39*(9), 3663–3681. https://doi.org/10.1002/hbm.24202

Kringelbach, M. L., Cruzat, J., Cabral, J., Knudsen, G. M., Carhart-Harris, R., Whybrow, P. C., … Deco, G. (2020). Dynamic coupling of whole-brain neuronal and neurotransmitter systems. *Proceedings of the National Academy of Sciences*, *117*(17), 9566–9576. https://doi.org/10.1073/pnas.1921475117

Kuramoto, Y. (1984). *Chemical oscillations, waves, and turbulence*. Berlin: Springer.

Kuznetsov, Y. (1998). *Elements of Applied Bifurcation Theory* (2nd ed.). New York: Springer-Verlag. https://doi.org/10.1007/b98848

Kwong, K. K., Belliveau, J. W., Chesler, D. A., Goldberg, I. E., Weisskoff, R. M., Poncelet, B. P., … Turner, R. (1992). Dynamic magnetic resonance imaging of human brain activity during primary sensory stimulation. *Proceedings of the National Academy of Sciences*, *89*(12), 5675–5679. https://doi.org/10.1073/pnas.89.12.5675

La Corte, V., Sperduti, M., Malherbe, C., Vialatte, F., Lion, S., Gallarda, T., … Piolino, P. (2016). Cognitive Decline and Reorganization of Functional Connectivity in Healthy Aging: The Pivotal Role of the Salience Network in the Prediction of Age and Cognitive Performances. *Frontiers in Aging Neuroscience*, *8*, 204. https://doi.org/10.3389/fnagi.2016.00204

Larson-Prior, L. J., Oostenveld, R., Della Penna, S., Michalareas, G., Prior, F., Babajani-Feremi, A., … Snyder, A. Z. (2013). Adding dynamics to the Human Connectome Project with MEG. *NeuroImage*, *80*, 190–201. https://doi.org/10.1016/j.neuroimage.2013.05.056

Latora, V., & Marchiori, M. (2001). Efficient Behavior of Small-World Networks. *Physical Review Letters*, *87*(19), 198701. https://doi.org/10.1103/PhysRevLett.87.198701

Le Bihan, D. (2003). Looking into the functional architecture of the brain with diffusion MRI. *Nature Reviews Neuroscience*, *4*(6), 469–480. https://doi.org/10.1038/nrn1119

Le Bihan, D., Breton, E., Lallemand, D., Aubin, M. L., Vignaud, J., & Laval-Jeantet, M. (1988). Separation of diffusion and perfusion in intravoxel incoherent motion MR imaging. *Radiology*, *168*(2), 497–505. https://doi.org/10.1148/radiology.168.2.3393671

Leonardi, N., & Van De Ville, D. (2015). On spurious and real fluctuations of dynamic functional connectivity during rest. *NeuroImage*, *104*, 430–436. https://doi.org/10.1016/j.neuroimage.2014.09.007

Li, K., Wisner, K., & Atluri, G. (2021). Feature selection framework for functional connectome fingerprinting. *Human Brain Mapping*, *42*(12), 3717–3732. https://doi.org/10.1002/hbm.25379

Liljequist, D., Elfving, B., & Roaldsen, K. S. (2019). Intraclass correlation – A discussion and demonstration of basic features. *PLOS ONE*, *14*(7), e0219854. https://doi.org/10.1371/journal.pone.0219854

Lindquist, M. (2020). Neuroimaging results altered by varying analysis pipelines. *Nature*, *582*(7810), 36–37. https://doi.org/10.1038/d41586-020-01282-z

Liu, T. T., Nalci, A., & Falahpour, M. (2017). The global signal in fMRI: Nuisance or Information? *NeuroImage*, *150*, 213–229. https://doi.org/10.1016/j.neuroimage.2017.02.036

Liégeois, R., Santos, A., Matta, V., Van De Ville, D., & Sayed, A. H. (2020). Revisiting correlation-based functional connectivity and its relationship with structural connectivity. *Network Neuroscience*, *4*(4), 1235–1251. https://doi.org/10.1162/netn_a_00166

Lurie, D. J., Kessler, D., Bassett, D. S., Betzel, R. F., Breakspear, M., Kheilholz, S., … Calhoun, V. D. (2020). Questions and controversies in the study of time-varying functional connectivity in resting fMRI. *Network Neuroscience*, *4*(1), 30–69. https://doi.org/10.1162/netn_a_00116

Lv, H., Wang, Z., Tong, E., Williams, L. M., Zaharchuk, G., Zeineh, M., … Wintermark, M. (2018). Resting-State Functional MRI: Everything That Nonexperts Have Always Wanted to Know. *American Journal of Neuroradiology*, *39*(8), 1390–1399. https://doi.org/10.3174/ajnr.A5527

Lynall, M.-E., Bassett, D. S., Kerwin, R., McKenna, P. J., Kitzbichler, M., Muller, U., & Bullmore, E. (2010). Functional Connectivity and Brain Networks in Schizophrenia. *Journal of Neuroscience*, *30*(28), 9477–9487. https://doi.org/10.1523/JNEUROSCI.0333-10.2010

MacKay, D. J. C. (2003). *Information Theory, Inference and Learning Algorithms*. Cambridge University Press.

Maier-Hein, K. H., Neher, P. F., Houde, J.-C., Côté, M.-A., Garyfallidis, E., Zhong, J., … Descoteaux, M. (2017). The challenge of mapping the human connectome based on diffusion tractography. *Nature Communications*, *8*(1), 1349. https://doi.org/10.1038/s41467-017-01285-x

Makris, N., Goldstein, J. M., Kennedy, D., Hodge, S. M., Caviness, V. S., Faraone, S. V., … Seidman, L. J. (2006). Decreased volume of left and total anterior insular lobule in schizophrenia. *Schizophrenia Research*, *83*(2), 155–171. https://doi.org/10.1016/j.schres.2005.11.020

Makris, N., Worth, A. J., Papadimitriou, G. M., Stakes, J. W., Caviness, V. S., Kennedy, D. N., … Davis, T. L. (1997). Morphometry of in vivo human white matter association pathways with diffusion-weighted magnetic resonance imaging. *Annals of Neurology*, *42*(6), 951–962. https://doi.org/10.1002/ana.410420617

Mann, K., Gallen, C. L., & Clandinin, T. R. (2017). Whole-Brain Calcium Imaging Reveals an Intrinsic Functional Network in Drosophila. *Current Biology*, *27*(15), 2389–2396.e4. https://doi.org/10.1016/j.cub.2017.06.076

Marcus, D. S., Harms, M. P., Snyder, A. Z., Jenkinson, M., Wilson, J. A., Glasser, M. F., … Van Essen, D. C. (2013). Human Connectome Project informatics: Quality control, database services, and data visualization. *NeuroImage*, *80*, 202–219. https://doi.org/10.1016/j.neuroimage.2013.05.077

Marrelec, G., Messé, A., Giron, A., & Rudrauf, D. (2016). Functional Connectivity's Degenerate View of Brain Computation. *PLOS Computational Biology*, *12*(10), e1005031. https://doi.org/10.1371/journal.pcbi.1005031

Mayhew, S. D., Ostwald, D., Porcaro, C., & Bagshaw, A. P. (2013). Spontaneous EEG alpha oscillation interacts with positive and negative BOLD responses in the visual–auditory cortices and default-mode network. *NeuroImage*, *76*, 362–372. https://doi.org/10.1016/j.neuroimage.2013.02.070

McGraw, K. O., & Wong, S. P. (1996). Forming inferences about some intraclass correlation coefficients. *Psychological Methods*, *1*(1), 30–46. https://doi.org/10.1037/1082-989X.1.1.30

Melzer, S., & Monyer, H. (2020). Diversity and function of corticopetal and corticofugal GABAergic projection neurons. *Nature Reviews Neuroscience*, *21*(9), 499–515. https://doi.org/10.1038/s41583-020-0344-9

Messé, A. (2020). Parcellation influence on the connectivity-based structure–function relationship in the human brain. *Human Brain Mapping*, *41*(5), 1167–1180. https://doi.org/10.1002/hbm.24866

Messé, A., Rudrauf, D., Benali, H., & Marrelec, G. (2014). Relating Structure and Function in the Human Brain: Relative Contributions of Anatomy, Stationary Dynamics, and Non-stationarities. *PLOS Computational Biology*, *10*(3), e1003530. https://doi.org/10.1371/journal.pcbi.1003530

Messé, A., Rudrauf, D., Giron, A., & Marrelec, G. (2015). Predicting functional connectivity from structural connectivity via computational models using MRI: An extensive comparison study. *NeuroImage*, *111*, 65–75. https://doi.org/10.1016/j.neuroimage.2015.02.001

Mišić, B., Betzel, R. F., de Reus, M. A., van den Heuvel, M. P., Berman, M. G., McIntosh, A. R., & Sporns, O. (2016). Network-Level Structure-Function Relationships in Human Neocortex. *Cerebral Cortex*, *26*(7), 3285–3296. https://doi.org/10.1093/cercor/bhw089

Mišić, B., Betzel, R. F., Nematzadeh, A., Goñi, J., Griffa, A., Hagmann, P., … Sporns, O. (2015). Cooperative and Competitive Spreading Dynamics on the Human Connectome. *Neuron*, *86*(6), 1518–1529. https://doi.org/10.1016/j.neuron.2015.05.035

Muldoon, S. F., Pasqualetti, F., Gu, S., Cieslak, M., Grafton, S. T., Vettel, J. M., & Bassett, D. S. (2016). Stimulation-Based Control of Dynamic Brain Networks. *PLOS Computational Biology*, *12*(9), e1005076. https://doi.org/10.1371/journal.pcbi.1005076

Naskar, A., Vattikonda, A., Deco, G., Roy, D., & Banerjee, A. (2021). Multiscale dynamic mean field (MDMF) model relates resting-state brain dynamics with local cortical excitatory–inhibitory neurotransmitter homeostasis. *Network Neuroscience*, *5*(3), 757–782. https://doi.org/10.1162/netn_a_00197

Nelder, J. A., & Mead, R. (1965). A Simplex Method for Function Minimization. *The Computer Journal*, *7*(4), 308–313. https://doi.org/10.1093/comjnl/7.4.308

Newman, M. E. J. (2003). The Structure and Function of Complex Networks. *SIAM Review*, *45*(2), 167–256. https://doi.org/10.1137/S003614450342480

Newman, M. E. J. (2006). Modularity and community structure in networks. *Proceedings of the National Academy of Sciences*, *103*(23), 8577–8582. https://doi.org/10.1073/pnas.0601602103

Newman, M. E. J., & Girvan, M. (2004). Finding and evaluating community structure in networks. *Physical Review E*, *69*(2), 026113. https://doi.org/10.1103/PhysRevE.69.026113

Noble, S., Scheinost, D., & Constable, R. T. (2019). A decade of test-retest reliability of functional connectivity: A systematic review and meta-analysis. *NeuroImage*, *203*, 116157. https://doi.org/10.1016/j.neuroimage.2019.116157

Noble, S., Spann, M. N., Tokoglu, F., Shen, X., Constable, R. T., & Scheinost, D. (2017). Influences on the Test–Retest Reliability of Functional Connectivity MRI and its Relationship with Behavioral Utility. *Cerebral Cortex*, *27*(11), 5415–5429. https://doi.org/10.1093/cercor/bhx230

Ogawa, S., Tank, D. W., Menon, R., Ellermann, J. M., Kim, S. G., Merkle, H., & Ugurbil, K. (1992). Intrinsic signal changes accompanying sensory stimulation: functional brain mapping with magnetic resonance imaging. *Proceedings of the National Academy of Sciences*, *89*(13), 5951–5955. https://doi.org/10.1073/pnas.89.13.5951

Ohki, K., Chung, S., Ch'ng, Y. H., Kara, P., & Reid, R. C. (2005). Functional imaging with cellular resolution reveals precise micro-architecture in visual cortex. *Nature*, *433*(7026), 597–603. https://doi.org/10.1038/nature03274

Oizumi, M., Albantakis, L., & Tononi, G. (2014). From the Phenomenology to the Mechanisms of Consciousness: Integrated Information Theory 3.0. *PLOS Computational Biology*, *10*(5), e1003588. https://doi.org/10.1371/journal.pcbi.1003588

Olivas, N. D., Quintanar-Zilinskas, V., Nenadic, Z., & Xu, X. (2012). Laminar circuit organization and response modulation in mouse visual cortex. *Frontiers in Neural Circuits*, *6*, 70. https://doi.org/10.3389/fncir.2012.00070

Onnela, J.-P., Saramäki, J., Kertész, J., & Kaski, K. (2005). Intensity and coherence of motifs in weighted complex networks. *Physical Review E*, *71*(6), 065103. https://doi.org/10.1103/PhysRevE.71.065103

Pang, R., Lansdell, B. J., & Fairhall, A. L. (2016). Dimensionality reduction in neuroscience. *Current Biology*, *26*(14), R656–R660. https://doi.org/10.1016/j.cub.2016.05.029

Pannunzi, M., Hindriks, R., Bettinardi, R. G., Wenger, E., Lisofsky, N., Martensson, J., … Deco, G. (2017). Resting-state fMRI correlations: From link-wise unreliability to whole brain stability. *NeuroImage*, *157*, 250–262. https://doi.org/10.1016/j.neuroimage.2017.06.006

Panteley, E., Loria, A., & Ati, A. E. (2015). On the Stability and Robustness of Stuart-Landau Oscillators. *IFAC-PapersOnLine*, *48*(11), 645–650. https://doi.org/10.1016/j.ifacol.2015.09.260

Pearson, K. (1901). On lines and planes of closest fit to systems of points in space. *The London, Edinburgh, and Dublin Philosophical Magazine and Journal of Science*, *2*(11), 559–572. https://doi.org/10.1080/14786440109462720

Peña-Gómez, C., Avena-Koenigsberger, A., Sepulcre, J., & Sporns, O. (2018). Spatiotemporal Network Markers of Individual Variability in the Human Functional Connectome. *Cerebral Cortex*, *28*(8), 2922–2934. https://doi.org/10.1093/cercor/bhx170

Pfeffer, C. K., Xue, M., He, M., Huang, Z. J., & Scanziani, M. (2013). Inhibition of inhibition in visual cortex: the logic of connections between molecularly distinct interneurons. *Nature Neuroscience*, *16*(8), 1068–1076. https://doi.org/10.1038/nn.3446

Pijnenburg, R., Scholtens, L. H., Ardesch, D. J., de Lange, S. C., Wei, Y., & van den Heuvel, M. P. (2021). Myelo- and cytoarchitectonic microstructural and functional human cortical atlases reconstructed in common MRI space. *NeuroImage*, *239*, 118274. https://doi.org/10.1016/j.neuroimage.2021.118274

Pläschke, R. N., Cieslik, E. C., Müller, V. I., Hoffstaedter, F., Plachti, A., Varikuti, D. P., … Eickhoff, S. B. (2017). On the integrity of functional brain networks in schizophrenia, Parkinson's disease, and advanced age: Evidence from connectivity-based single-subject classification. *Human Brain Mapping*, *38*(12), 5845–5858. https://doi.org/10.1002/hbm.23763

Poldrack, R. A., Huckins, G., & Varoquaux, G. (2020). Establishment of Best Practices for Evidence for Prediction: A Review. *JAMA Psychiatry*, *77*(5), 534–540. https://doi.org/10.1001/jamapsychiatry.2019.3671

Ponce-Alvarez, A., Deco, G., Hagmann, P., Romani, G. L., Mantini, D., & Corbetta, M. (2015). Resting-State Temporal Synchronization Networks Emerge from Connectivity Topology and Heterogeneity. *PLOS Computational Biology*, *11*(2), e1004100. https://doi.org/10.1371/journal.pcbi.1004100

Popovych, O. V., Jung, K., Manos, T., Diaz-Pier, S., Hoffstaedter, F., Schreiber, J., … Eickhoff, S. B. (2021). Inter-subject and inter-parcellation variability of resting-state whole-brain dynamical modeling. *NeuroImage*, *236*, 118201. https://doi.org/10.1016/j.neuroimage.2021.118201

Popovych, O. V., Manos, T., Hoffstaedter, F., & Eickhoff, S. B. (2019). What Can Computational Models Contribute to Neuroimaging Data Analytics? *Frontiers in Systems Neuroscience*, *12*, 68. https://doi.org/10.3389/fnsys.2018.00068

Preti, M. G., Bolton, T. A. W., & Van De Ville, D. (2017). The dynamic functional connectome: State-of-the-art and perspectives. *NeuroImage*, *160*, 41–54. https://doi.org/10.1016/j.neuroimage.2016.12.061

Proix, T., Spiegler, A., Schirner, M., Rothmeier, S., Ritter, P., & Jirsa, V. K. (2016). How do parcellation size and short-range connectivity affect dynamics in large-scale brain network models? *NeuroImage*, *142*, 135–149. https://doi.org/10.1016/j.neuroimage.2016.06.016

Rashid, M., Singh, H., & Goyal, V. (2020). The use of machine learning and deep learning algorithms in functional magnetic resonance imaging—A systematic review. *Expert Systems*, *37*(6), e12644. https://doi.org/10.1111/exsy.12644

Ritter, P., Schirner, M., McIntosh, A. R., & Jirsa, V. K. (2013). The Virtual Brain Integrates Computational Modeling and Multimodal Neuroimaging. *Brain Connectivity*, *3*(2), 121–145. https://doi.org/10.1089/brain.2012.0120

Robinson, P. A. (2012). Interrelating anatomical, effective, and functional brain connectivity using propagators and neural field theory. *Physical Review E*, *85*(1), 011912. https://doi.org/10.1103/PhysRevE.85.011912

Robinson, P. A., Sarkar, S., Pandejee, G. M., & Henderson, J. A. (2014). Determination of effective brain connectivity from functional connectivity with application to resting state connectivities. *Physical Review E*, *90*(1), 012707. https://doi.org/10.1103/PhysRevE.90.012707

Rodrigues, F. A., Peron, T. K. D., Ji, P., & Kurths, J. (2016). The Kuramoto model in complex networks. *Physics Reports*, *610*, 1–98. https://doi.org/10.1016/j.physrep.2015.10.008

Rogers, B. P., Morgan, V. L., Newton, A. T., & Gore, J. C. (2007). Assessing functional connectivity in the human brain by fMRI. *Magnetic Resonance Imaging*, *25*(10), 1347–1357. https://doi.org/10.1016/j.mri.2007.03.007

Roine, T., Jeurissen, B., Perrone, D., Aelterman, J., Philips, W., Sijbers, J., & Leemans, A. (2019). Reproducibility and intercorrelation of graph theoretical measures in structural brain connectivity networks. *Medical Image Analysis*, *52*, 56–67. https://doi.org/10.1016/j.media.2018.10.009

Rolls, E. T., Huang, C.-C., Lin, C.-P., Feng, J., & Joliot, M. (2020). Automated anatomical labelling atlas 3. *NeuroImage*, *206*, 116189. https://doi.org/10.1016/j.neuroimage.2019.116189

Rolls, E. T., Joliot, M., & Tzourio-Mazoyer, N. (2015). Implementation of a new parcellation of the orbitofrontal cortex in the automated anatomical labeling atlas. *NeuroImage*, *122*, 1–5. https://doi.org/10.1016/j.neuroimage.2015.07.075

Rubinov, M., Knock, S. A., Stam, C. J., Micheloyannis, S., Harris, A. W. F., Williams, L. M., & Breakspear, M. (2009). Small-world properties of nonlinear brain activity in schizophrenia. *Human Brain Mapping*, *30*(2), 403–416. https://doi.org/10.1002/hbm.20517

Rubinov, M., & Sporns, O. (2010). Complex network measures of brain connectivity: Uses and interpretations. *NeuroImage*, *52*(3), 1059–1069. https://doi.org/10.1016/j.neuroimage.2009.10.003

Rubinov, M., & Sporns, O. (2011). Weight-conserving characterization of complex functional brain networks. *NeuroImage*, *56*(4), 2068–2079. https://doi.org/10.1016/j.neuroimage.2011.03.069

Saenger, V. M., Kahan, J., Foltynie, T., Friston, K., Aziz, T. Z., Green, A. L., … Deco, G. (2017). Uncovering the underlying mechanisms and whole-brain dynamics of deep brain stimulation for Parkinson's disease. *Scientific Reports*, *7*(1), 9882. https://doi.org/10.1038/s41598-017-10003-y

Saggio, M. L., Ritter, P., & Jirsa, V. K. (2016). Analytical Operations Relate Structural and Functional Connectivity in the Brain. *PLOS ONE*, *11*(8), e0157292. https://doi.org/10.1371/journal.pone.0157292

Saleeba, C., Dempsey, B., Le, S., Goodchild, A., & McMullan, S. (2019). A Student's Guide to Neural Circuit Tracing. *Frontiers in Neuroscience*, *13*, 897. https://doi.org/10.3389/fnins.2019.00897

Salimi-Khorshidi, G., Douaud, G., Beckmann, C. F., Glasser, M. F., Griffanti, L., & Smith, S. M. (2014). Automatic denoising of functional MRI data: Combining independent component analysis and hierarchical fusion of classifiers. *NeuroImage*, *90*, 449–468. https://doi.org/10.1016/j.neuroimage.2013.11.046

Sanchez-Panchuelo, R. M., Francis, S., Bowtell, R., & Schluppeck, D. (2010). Mapping Human Somatosensory Cortex in Individual Subjects With 7T Functional MRI. *Journal of Neurophysiology*, *103*(5), 2544–2556. https://doi.org/10.1152/jn.01017.2009

Sanz-Leon, P., Knock, S. A., Spiegler, A., & Jirsa, V. K. (2015). Mathematical framework for large-scale brain network modeling in The Virtual Brain. *NeuroImage*, *111*, 385–430. https://doi.org/10.1016/j.neuroimage.2015.01.002

Sarar, G., Rao, B., & Liu, T. (2021). Functional connectome fingerprinting using shallow feedforward neural networks. *Proceedings of the National Academy of Sciences*, *118*(15), e2021852118. https://doi.org/10.1073/pnas.2021852118

Schaefer, A., Kong, R., Gordon, E. M., Laumann, T. O., Zuo, X.-N., Holmes, A. J., … Yeo, B. T. T. (2018). Local-Global Parcellation of the Human Cerebral Cortex from Intrinsic Functional Connectivity MRI. *Cerebral Cortex*, *28*(9), 3095–3114. https://doi.org/10.1093/cercor/bhx179

Scheeringa, R., Koopmans, P. J., van Mourik, T., Jensen, O., & Norris, D. G. (2016). The relationship between oscillatory EEG activity and the laminar-specific BOLD signal. *Proceedings of the National Academy of Sciences*, *113*(24), 6761–6766. https://doi.org/10.1073/pnas.1522577113

Schilling, K. G., Nath, V., Hansen, C., Parvathaneni, P., Blaber, J., Gao, Y., … Landman, B. A. (2019). Limits to anatomical accuracy of diffusion tractography using modern approaches. *NeuroImage*, *185*, 1–11. https://doi.org/10.1016/j.neuroimage.2018.10.029

Schmahmann, J. D., Doyon, J., McDonald, D., Holmes, C., Lavoie, K., Hurwitz, A. S., … Petrides, M. (1999). Three-Dimensional MRI Atlas of the Human Cerebellum in Proportional Stereotaxic Space. *NeuroImage*, *10*(3), 233–260. https://doi.org/10.1006/nimg.1999.0459

Schmidt-Rohr, K. (2020). Oxygen Is the High-Energy Molecule Powering Complex Multicellular Life: Fundamental Corrections to Traditional Bioenergetics. *ACS Omega*, *5*(5), 2221–2233. https://doi.org/10.1021/acsomega.9b03352

Scholtens, L. H., de Reus, M. A., de Lange, S. C., Schmidt, R., & van den Heuvel, M. P. (2018). An MRI Von Economo – Koskinas atlas. *NeuroImage*, *170*, 249–256. https://doi.org/10.1016/j.neuroimage.2016.12.069

Shehzad, Z., Kelly, A. M. C., Reiss, P. T., Gee, D. G., Gotimer, K., Uddin, L. Q., … Milham, M. P. (2009). The Resting Brain: Unconstrained yet Reliable. *Cerebral Cortex*, *19*(10), 2209–2229. https://doi.org/10.1093/cercor/bhn256

Shen, X., Tokoglu, F., Papademetris, X., & Constable, R. T. (2013). Groupwise whole-brain parcellation from resting-state fMRI data for network node identification. *NeuroImage*, *82*, 403–415. https://doi.org/10.1016/j.neuroimage.2013.05.081

Shi, J., & Malik, J. (2000). Normalized cuts and image segmentation. *IEEE Transactions on Pattern Analysis and Machine Intelligence*, *22*(8), 888–905. https://doi.org/10.1109/34.868688

Shrout, P. E., & Fleiss, J. L. (1979). Intraclass correlations: uses in assessing rater reliability. *Psychological Bulletin*, *86*(2), 420–428. https://doi.org/10.1037//0033-2909.86.2.420

Smith, G. E. (1907). A New Topographical Survey of the Human Cerebral Cortex, being an Account of the Distribution of the Anatomically Distinct Cortical Areas and their Relationship to the Cerebral Sulci. *Journal of Anatomy and Physiology*, *41*(Pt 4), 237–254.

Smitha, K. A., Akhil Raja, K., Arun, K. M., Rajesh, P. G., Thomas, B., Kapilamoorthy, T. R., & Kesavadas, C. (2017). Resting state fMRI: A review on methods in resting state connectivity analysis and resting state networks. *The Neuroradiology Journal*, *30*(4), 305–317. https://doi.org/10.1177/1971400917697342

Snoek, J., Larochelle, H., & Adams, R. P. (2012). Practical Bayesian Optimization of Machine Learning Algorithms. In F. Pereira, C. J. C. Burges, L. Bottou, & K. Q. Weinberger (Eds.), *Advances in Neural Information Processing Systems* (Vol. 25). Curran Associates, Inc.

Sotiropoulos, S. N., & Zalesky, A. (2019). Building connectomes using diffusion MRI: why, how and but. *NMR in Biomedicine*, *32*(4), e3752. https://doi.org/https://doi.org/10.1002/nbm.3752

Spitoni, G. F., Cimmino, R. L., Bozzacchi, C., Pizzamiglio, L., & Di Russo, F. (2013). Modulation of spontaneous alpha brain rhythms using low-intensity transcranial direct-current stimulation. *Frontiers in Human Neuroscience*, *7*, 529. https://doi.org/10.3389/fnhum.2013.00529

Sporns, O., Tononi, G., & Kötter, R. (2005). The Human Connectome: A Structural Description of the Human Brain. *PLOS Computational Biology*, *1*(4), e42. https://doi.org/10.1371/journal.pcbi.0010042

Stewart, G. W. (1992, April). *On the early history of the singular value decomposition.* Retrieved 2021-09-27, from http://conservancy.umn.edu/handle/11299/1868

Stiefel, K. M., & Ermentrout, G. B. (2016). Neurons as oscillators. *Journal of Neurophysiology*, *116*(6), 2950–2960. https://doi.org/10.1152/jn.00525.2015

Stosiek, C., Garaschuk, O., Holthoff, K., & Konnerth, A. (2003). In vivo two-photon calcium imaging of neuronal networks. *Proceedings of the National Academy of Sciences*, *100*(12), 7319–7324. https://doi.org/10.1073/pnas.1232232100

Strogatz, S. H. (2000). From Kuramoto to Crawford: exploring the onset of synchronization in populations of coupled oscillators. *Physica D: Nonlinear Phenomena*, *143*(1), 1–20. https://doi.org/10.1016/S0167-2789(00)00094-4

Stucht, D., Danishad, K. A., Schulze, P., Godenschweger, F., Zaitsev, M., & Speck, O. (2015). Highest Resolution In Vivo Human Brain MRI Using Prospective Motion Correction. *PLOS ONE*, *10*(7), e0133921. https://doi.org/10.1371/journal.pone.0133921

Suárez, L. E., Markello, R. D., Betzel, R. F., & Misic, B. (2020). Linking Structure and Function in Macroscale Brain Networks. *Trends in Cognitive Sciences*, *24*(4), 302–315. https://doi.org/10.1016/j.tics.2020.01.008

Taxali, A., Angstadt, M., Rutherford, S., & Sripada, C. (2021). Boost in Test–Retest Reliability in Resting State fMRI with Predictive Modeling. *Cerebral Cortex*, *31*(6), 2822–2833. https://doi.org/10.1093/cercor/bhaa390

Thirion, B., Varoquaux, G., Dohmatob, E., & Poline, J.-B. (2014). Which fMRI clustering gives good brain parcellations? *Frontiers in Neuroscience*, *8*, 167. https://doi.org/10.3389/fnins.2014.00167

Tiesinga, P., & Sejnowski, T. J. (2009). Cortical Enlightenment: Are Attentional Gamma Oscillations Driven by ING or PING? *Neuron*, *63*(6), 727–732. https://doi.org/10.1016/j.neuron.2009.09.009

Toker, D., & Sommer, F. T. (2019). Information integration in large brain networks. *PLOS Computational Biology*, *15*(2), e1006807. https://doi.org/10.1371/journal.pcbi.1006807

Tong, F. (2003). Primary visual cortex and visual awareness. *Nature Reviews Neuroscience*, *4*(3), 219–229. https://doi.org/10.1038/nrn1055

Tournier, J.-D., Calamante, F., & Connelly, A. (2010). Improved probabilistic streamlines tractography by 2nd order integration over fibre orientation distributions. *Proceedings of the International Society for Magnetic Resonance in Medicine*, *1670*.

Tournier, J.-D., Smith, R., Raffelt, D., Tabbara, R., Dhollander, T., Pietsch, M., … Connelly, A. (2019). MRtrix3: A fast, flexible and open software framework for medical image processing and visualisation. *NeuroImage*, *202*, 116137. https://doi.org/10.1016/j.neuroimage.2019.116137

Tremblay, R., Lee, S., & Rudy, B. (2016). GABAergic Interneurons in the Neocortex: From Cellular Properties to Circuits. *Neuron*, *91*(2), 260–292. https://doi.org/10.1016/j.neuron.2016.06.033

Tustison, N. J., Avants, B. B., Cook, P. A., Zheng, Y., Egan, A., Yushkevich, P. A., & Gee, J. C. (2010). N4ITK: Improved N3 Bias Correction. *IEEE Transactions on Medical Imaging*, *29*(6), 1310–1320. https://doi.org/10.1109/TMI.2010.2046908

Tzourio-Mazoyer, N., Landeau, B., Papathanassiou, D., Crivello, F., Etard, O., Delcroix, N., … Joliot, M. (2002). Automated Anatomical Labeling of Activations in SPM Using a Macroscopic Anatomical Parcellation of the MNI MRI Single-Subject Brain. *NeuroImage*, *15*(1), 273–289. https://doi.org/10.1006/nimg.2001.0978

Urchs, S., Armoza, J., Moreau, C., Benhajali, Y., St-Aubin, J., Orban, P., & Bellec, P. (2019). MIST: A multi-resolution parcellation of functional brain networks [version 2; peer review: 4 approved]. *MNI Open Research*, *1*, 3. https://doi.org/10.12688/mniopenres.12767.2

Uğurbil, K., Xu, J., Auerbach, E. J., Moeller, S., Vu, A. T., Duarte-Carvajalino, J. M., … Yacoub, E. (2013). Pushing spatial and temporal resolution for functional and diffusion MRI in the Human Connectome Project. *NeuroImage*, *80*, 80–104. https://doi.org/10.1016/j.neuroimage.2013.05.012

Valdes-Sosa, P. A., Roebroeck, A., Daunizeau, J., & Friston, K. (2011). Effective connectivity: Influence, causality and biophysical modeling. *NeuroImage*, *58*(2), 339–361. https://doi.org/10.1016/j.neuroimage.2011.03.058

van den Heuvel, M. P., & Hulshoff Pol, H. E. (2010). Exploring the brain network: A review on resting-state fMRI functional connectivity. *European Neuropsychopharmacology*, *20*(8), 519–534. https://doi.org/10.1016/j.euroneuro.2010.03.008

van den Heuvel, M. P., & Sporns, O. (2019). A cross-disorder connectome landscape of brain dysconnectivity. *Nature Reviews Neuroscience*, *20*(7), 435–446. https://doi.org/10.1038/s41583-019-0177-6

van den Heuvel, M. P., Stam, C. J., Kahn, R. S., & Hulshoff Pol, H. E. (2009). Efficiency of Functional Brain Networks and Intellectual Performance. *Journal of Neuroscience*, *29*(23), 7619–7624. https://doi.org/10.1523/JNEUROSCI.1443-09.2009

van der Walt, S., Colbert, S. C., & Varoquaux, G. (2011). The NumPy Array: A Structure for Efficient Numerical Computation. *Computing in Science Engineering*, *13*(2), 22–30. https://doi.org/10.1109/MCSE.2011.37

Van Dijk, K. R. A., Hedden, T., Venkataraman, A., Evans, K. C., Lazar, S. W., & Buckner, R. L. (2010). Intrinsic Functional Connectivity As a Tool For Human Connectomics: Theory, Properties, and Optimization. *Journal of Neurophysiology*, *103*(1), 297–321. https://doi.org/10.1152/jn.00783.2009

Van Essen, D. C., Smith, S. M., Barch, D. M., Behrens, T. E. J., Yacoub, E., & Ugurbil, K. (2013). The WU-Minn Human Connectome Project: An overview. *NeuroImage*, *80*, 62–79. https://doi.org/10.1016/j.neuroimage.2013.05.041

Van Essen, D. C., Ugurbil, K., Auerbach, E., Barch, D., Behrens, T. E. J., Bucholz, R., … Yacoub, E. (2012). The Human Connectome Project: A data acquisition perspective. *NeuroImage*, *62*(4), 2222–2231. https://doi.org/10.1016/j.neuroimage.2012.02.018

Varikuti, D. P., Genon, S., Sotiras, A., Schwender, H., Hoffstaedter, F., Patil, K. R., … Eickhoff, S. B. (2018). Evaluation of non-negative matrix factorization of grey matter in age prediction. *NeuroImage*, *173*, 394–410. https://doi.org/10.1016/j.neuroimage.2018.03.007

Varoquaux, G. (2018). Cross-validation failure: Small sample sizes lead to large error bars. *NeuroImage*, *180*, 68–77. https://doi.org/10.1016/j.neuroimage.2017.06.061

Vergara, R. C., Jaramillo-Riveri, S., Luarte, A., Moënne-Loccoz, C., Fuentes, R., Couve, A., & Maldonado, P. E. (2019). The Energy Homeostasis Principle: Neuronal Energy Regulation Drives Local Network Dynamics Generating Behavior. *Frontiers in Computational Neuroscience*, *13*, 49. https://doi.org/10.3389/fncom.2019.00049

Verstraelen, P., Van Dyck, M., Verschuuren, M., Kashikar, N. D., Nuydens, R., Timmermans, J.-P., & De Vos, W. H. (2018). Image-Based Profiling of Synaptic Connectivity in Primary Neuronal Cell Culture. *Frontiers in Neuroscience*, *12*, 389. https://doi.org/10.3389/fnins.2018.00389

Vijayan, S., & Kopell, N. J. (2012). Thalamic model of awake alpha oscillations and implications for stimulus processing. *Proceedings of the National Academy of Sciences*, *109*(45), 18553–18558. https://doi.org/10.1073/pnas.1215385109

Viriyopase, A., Memmesheimer, R.-M., & Gielen, S. (2016). Cooperation and competition of gamma oscillation mechanisms. *Journal of Neurophysiology*, *116*(2), 232–251. https://doi.org/10.1152/jn.00493.2015

Virtanen, P., Gommers, R., Oliphant, T. E., Haberland, M., Reddy, T., Cournapeau, D., … van Mulbregt, P. (2020). SciPy 1.0: fundamental algorithms for scientific computing in Python. *Nature Methods*, *17*(3), 261–272. https://doi.org/10.1038/s41592-019-0686-2

Vogels, T. P., Sprekeler, H., Zenke, F., Clopath, C., & Gerstner, W. (2011). Inhibitory Plasticity Balances Excitation and Inhibition in Sensory Pathways and Memory Networks. *Science*, *334*(6062), 1569–1573. https://doi.org/10.1126/science.1211095

von Economo, C., & Koskinas, G. N. (1925). *Die Cytoarchitektonik der Hirnrinde des erwachsenen Menschen*. Wien: Springer.

von Luxburg, U. (2007). A tutorial on spectral clustering. *Statistics and Computing*, *17*(4), 395–416. https://doi.org/10.1007/s11222-007-9033-z

Vázquez-Rodríguez, B., Suárez, L. E., Markello, R. D., Shafiei, G., Paquola, C., Hagmann, P., … Misic, B. (2019). Gradients of structure–function tethering across neocortex. *Proceedings of the National Academy of Sciences*, *116*(42), 21219–21227. https://doi.org/10.1073/pnas.1903403116

Wall, M. E., Rechtsteiner, A., & Rocha, L. M. (2003). Singular Value Decomposition and Principal Component Analysis. In D. P. Berrar, W. Dubitzky, & M. Granzow (Eds.), *A Practical Approach to Microarray Data Analysis* (pp. 91–109). Boston, MA: Springer US. https://doi.org/10.1007/0-306-47815-3_5

Waller, L., Walter, H., Kruschwitz, J. D., Reuter, L., Müller, S., Erk, S., & Veer, I. M. (2017). Evaluating the replicability, specificity, and generalizability of connectome fingerprints. *NeuroImage*, *158*, 371–377. https://doi.org/10.1016/j.neuroimage.2017.07.016

Wang, H. E., Bénar, C. G., Quilichini, P. P., Friston, K. J., Jirsa, V. K., & Bernard, C. (2014). A systematic framework for functional connectivity measures. *Frontiers in Neuroscience*, *8*, 405. https://doi.org/10.3389/fnins.2014.00405

Wang, H. E., Friston, K. J., Bénar, C. G., Woodman, M. M., Chauvel, P., Jirsa, V., & Bernard, C. (2018). MULAN: Evaluation and ensemble statistical inference for functional connectivity. *NeuroImage*, *166*, 167–184. https://doi.org/10.1016/j.neuroimage.2017.10.036

Wang, J., Wang, L., Zang, Y., Yang, H., Tang, H., Gong, Q., … He, Y. (2009). Parcellation-dependent small-world brain functional networks: A resting-state fMRI study. *Human Brain Mapping*, *30*(5), 1511–1523. https://doi.org/10.1002/hbm.20623

Wang, Z., Xin, J., Wang, Z., Yao, Y., Zhao, Y., & Qian, W. (2021). Brain functional network modeling and analysis based on fMRI: a systematic review. *Cognitive Neurodynamics*, *15*(3), 389–403. https://doi.org/10.1007/s11571-020-09630-5

Watts, D. J., & Strogatz, S. H. (1998). Collective dynamics of 'small-world' networks. *Nature*, *393*(6684), 440–442. https://doi.org/10.1038/30918

Wilson, H. R., & Cowan, J. D. (1972). Excitatory and Inhibitory Interactions in Localized Populations of Model Neurons. *Biophysical Journal*, *12*(1), 1–24. https://doi.org/10.1016/S0006-3495(72)86068-5

Wischnewski, K. J., Eickhoff, S. B., Jirsa, V. K., & Popovych, O. V. (2022). Towards an efficient validation of dynamical whole-brain models. *Scientific Reports*, *12*(1), 4331. https://doi.org/10.1038/s41598-022-07860-7

Wong, K.-F., & Wang, X.-J. (2006). A Recurrent Network Mechanism of Time Integration in Perceptual Decisions. *Journal of Neuroscience*, *26*(4), 1314–1328. https://doi.org/10.1523/JNEUROSCI.3733-05.2006

Woolrich, M. W., & Stephan, K. E. (2013). Biophysical network models and the human connectome. *NeuroImage*, *80*, 330–338. https://doi.org/10.1016/j.neuroimage.2013.03.059

Yeh, C.-H., Jones, D. K., Liang, X., Descoteaux, M., & Connelly, A. (2021). Mapping Structural Connectivity Using Diffusion MRI: Challenges and Opportunities. *Journal of Magnetic Resonance Imaging*, *53*(6), 1666–1682. https://doi.org/https://doi.org/10.1002/jmri.27188

Yoo, K., Rosenberg, M. D., Hsu, W.-T., Zhang, S., Li, C.-S. R., Scheinost, D., … Chun, M. M. (2018). Connectome-based predictive modeling of attention: Comparing different functional connectivity features and prediction methods across datasets. *NeuroImage*, *167*, 11–22. https://doi.org/10.1016/j.neuroimage.2017.11.010

Yu, S. X., & Shi, J. (2003). Multiclass spectral clustering. In *Proceedings Ninth IEEE International Conference on Computer Vision* (pp. 313–319 vol.1). https://doi.org/10.1109/ICCV.2003.1238361

Zalesky, A., Fornito, A., Cocchi, L., Gollo, L. L., van den Heuvel, M. P., & Breakspear, M. (2016). Connectome sensitivity or specificity: which is more important? *NeuroImage*, *142*, 407–420. https://doi.org/10.1016/j.neuroimage.2016.06.035

Zalesky, A., Fornito, A., Harding, I. H., Cocchi, L., Yücel, M., Pantelis, C., & Bullmore, E. T. (2010). Whole-brain anatomical networks: Does the choice of nodes matter? *NeuroImage*, *50*(3), 970–983. https://doi.org/10.1016/j.neuroimage.2009.12.027

Zhan, L., Zhou, J., Wang, Y., Jin, Y., Jahanshad, N., Prasad, G., … Thompson, P. M. (2015). Comparison of nine tractography algorithms for detecting abnormal structural brain networks in Alzheimer's disease. *Frontiers in Aging Neuroscience*, *7*, 48. https://doi.org/10.3389/fnagi.2015.00048

Zhang, C., Baum, S. A., Adduru, V. R., Biswal, B. B., & Michael, A. M. (2018). Test-retest reliability of dynamic functional connectivity in resting state fMRI. *NeuroImage*, *183*, 907–918. https://doi.org/10.1016/j.neuroimage.2018.08.021

Zhang, C., Dougherty, C. C., Baum, S. A., White, T., & Michael, A. M. (2018). Functional connectivity predicts gender: Evidence for gender differences in resting brain connectivity. *Human Brain Mapping*, *39*(4), 1765–1776. https://doi.org/10.1002/hbm.23950

Zimmermann, J., Griffiths, J., Schirner, M., Ritter, P., & McIntosh, A. R. (2018). Subject specificity of the correlation between large-scale structural and functional connectivity. *Network Neuroscience*, *3*(1), 90–106. https://doi.org/10.1162/netn_a_00055

Zimmermann, J., Perry, A., Breakspear, M., Schirner, M., Sachdev, P., Wen, W., … Solodkin, A. (2018). Differentiation of Alzheimer's disease based on local and global parameters in personalized Virtual Brain models. *NeuroImage: Clinical*, *19*, 240–251. https://doi.org/10.1016/j.nicl.2018.04.017

Appendix

List of acronyms

AAL	Automated Anatomical Labeling
ADHD	attention deficit hyperactivity disorder
ANOVA	analysis of variance
ATP	adenosine triphosphate
BOLD	blood-oxygen-level-dependent
DK	Desikan-Killiany
dwMRI	diffusion-weighted MRI
EEG	electroencephalography
EK	von Economo-Koskinas
FC	functional connectivity
fMRI	functional MRI
HCP	Human Connectome Project
HO	Harvard-Oxford
ICC	intraclass correlation
MIST	Multiresolution Intrinsic Segmentation Template
MRI	magnetic resonance imaging
PC	principal component
PC1	first principal component
PC2	second principal component
PL	path length
SC	structural connectivity
Sch.	Schaefer
Shen	Shen 2013
WBT	whole-brain tractography

List of figures

List of publications

Domhof, J. W. M., Jung, K., Eickhoff, S. B., & Popovych, O. V. (2021). Parcellation-based structural and resting-state functional brain connectomes of a healthy cohort [Data set]. EBRAINS. https://doi.org/10.25493/81EV-ZVT

Domhof, J. W. M., Jung, K., Eickhoff, S. B., & Popovych, O. V. (2021). Parcellation-induced variation of empirical and simulated brain connectomes at group and subject levels. *Network Neuroscience*, 5(3), 798–830. https://doi.org/10.1162/netn_a_00202

Domhof, J. W. M., Jung, K., Eickhoff, S. B., & Popovych, O. V. (2022). Parcellation-based resting-state blood-oxygen-level-dependent (BOLD) signals of a healthy cohort (v1.0) [Data set]. EBRAINS. https://doi.org/10.25493/F9DP-WCQ

Domhof, J. W. M., Eickhoff, S. B., & Popovych, O. V. (2022). Reliability and subject specificity of personalized whole-brain dynamical models. *NeuroImage*, 257, 119321. https://doi.org/10.1016/j.neuroimage.2022.119321

Domhof, J. W. M., Eickhoff, S. B., & Popovych, O. V. (2022). Parcellation-based functional connectivity simulated by personalized whole-brain dynamical models (1.0) [Data set]. EBRAINS. https://doi.org/10.25493/CBE0-EQV

List of tables